TRANSACTIONS
OF THE ASME
Series B

Journal of ENGINEERING FOR INDUSTRY

August 1960

Divisions: AVIATION • MACHINE DESIGN • MANAGEMENT • PROCESS INDUSTRIES
MAINTENANCE AND PLANT ENGINEERING • RAILROAD • PRODUCTION ENGINEERING
MATERIALS HANDLING • RUBBER AND PLASTICS • PETROLEUM • SAFETY • TEXTILE
WOOD INDUSTRIES • Research Committees: METAL PROCESSING • FLOW OF
BULK MATERIALS • ELEVATORS • MECHANICAL SPRINGS

Published Quarterly by
THE AMERICAN SOCIETY OF MECHANICAL ENGINEERS

TRANSACTIONS OF THE ASME
Series B

Journal of
ENGINEERING FOR INDUSTRY

VOLUME 82 • SERIES B • NUMBER 3

August 1960

EDITORIAL DEPARTMENT

Editor, J. J. JAKLITSCH, JR.
Consulting Editor, LEO BLODGETT
Production, JEAN NORTH
Art Editor, HENRY BALFOUR

OFFICERS OF THE ASME

President, W. L. CISLER
Secretary, O. B. SCHIER, II
Treasurer, E. J. KATES
Assistant Treasurer, H. J. BAUER

PUBLICATIONS COMMITTEE

Chairman, B. G. A. SKROTZKI
HENDLEY N. BLACKMON
R. D. MINDLIN
MARTIN GOLAND
VITO L. SALERNO

Junior Representatives
A. S. GOLDSTEIN
J. W. FOLLANSBEE

REGIONAL ADVISORY BOARD

Region I, H. M. ROGERS, JR.
Region II, GLENN R. FRYLING
Region III, F. J. KEINZE
Region IV, FRANCIS C. SMITH
Region V, H. M. CATHER
Region VI, C. R. EARLE
Region VII, M. S. UMBENHAUER
Region VIII, CARL J. ECKHARDT

Published quarterly by The American Society of Mechanical Engineers. Publication office at 20th and Northampton Streets, Easton, Pa. The editorial department is located at the headquarters of the Society, 29 West Thirty-Ninth Street, New York 18, N. Y. Cable address, "Mechaneer," New York. Price $3.00 a copy, $10.00 annually; to members, $1.50 a copy, $5.00 annually. Add 50 cents for postage to all countries outside the United States and Canada. Changes of address must be received at Society headquarters seven weeks before they are to be effective on the mailing list. Please send old as well as new address. . . . By-Law: The Society shall not be responsible for statements or opinions advanced in papers or . . . printed in its publications (B13, Par. 4). . . . Second-class mail privileges authorized at Easton, Penna. . . . This publication is authorized to be mailed at the special rates of postage prescribed by Section 132 . . . © Copyrighted, 1960, by The American Society of Mechanical Engineers. Permission from this publication may be made on condition that full credit be given the TRANSACTIONS OF THE ASME, Series B—Journal of Engineering for Industry, and the author, and that date of publication be stated.

TRANSACTIONS OF THE ASME
Indexed by the Engineering Index, Inc.

CONTENTS

173 **Synthesis of Epicyclic Gear Trains Using the Velocity Ratio Spectrum**
R. C. Brewer

179 **Helixform Bevel and Hypoid Gears**
G. M. Spear, C. B. King, and M. L. Baxter, Jr.

191 **The Twinworm Drive—A Self-Locking Worm-Gear Transmission of High Efficiency**
B. Popper and D. W. Pessen

200 **Determination of Cutter Trajectories for Contoured Turbine Buckets**
R. G. DeBiase

205 **An Analysis of Factors Used for Strength Rating Helical Gears**
E. J. Wellauer

213 **Bending Strength of Gear Teeth by Cantilever-Plate Theory**
E. J. Wellauer and A. Seireg

223 **Rocket Motor Gear Tooth Analysis (Hertzian Contact Stresses and Times)**
E. K. Gatcombe and R. W. Prowell

231 **Analysis of Power Spinning of Cones**
B. Avitzur and C. T. Yang

246 **Some Problems of Press Forging Lead and Aluminum**
A. G. MacDonald, S. Kobayashi, and E. G. Thomsen

253 **The Deformation Process in Metal-Cutting**
W. J. McDonald and B. F. Murphey

259 **Influence Coefficients and Pressure Vessel Analysis**
G. D. Galletly

270 **Tube Metal Temperatures for Structural Design**
E. E. Ungar and L. A. Mekler

277 **Supersonic-Wind-Tunnel Air-Drying-System Design**
T. W. Macios

TRANSACTIONS
Series C

Journal of
HEAT TRANSFER
Vol. 82 • Series C • No. 3

CONTENTS FOR AUGUST, 1960

155 Rocket Heat-Transfer Literature
170 Unsteady Turbulent Heat Transfer in Tubes, by E. M. Sparrow and R. Siegel. (59—HT-16)
181 Improved Lumped Parameter Method for Transient Heat Conduction Calculations, by H. G. Elrod, Jr. (59—HT-28)
189 Local and Average Heat Transfer and Pressure Drop for Refrigerants Evaporating in Horizontal Tubes, by M. Altman, R. H. Norris, and F. W. Staub. (59—A-278)
199 Heat-Transfer and Flow-Friction Characteristics of Crossed-Rod Matrices, by A. L. London, J. W. Mitchell, and W. A. Sutherland. (59—A-168)
214 Experiments on Heat Transfer From Spheres Including Combined Natural and Forced Convection, by T. Yuge. (59—A-123)
221 Heat Transfer to Freon 12 Near the Critical State in a Natural-Circulation Loop, by J. P. Holman and J. H. Boggs. (59—A-142)
227 Combined Free and Forced-Convection Heat-Generating Laminar Flow Inside Vertical Pipes With Circular Sector Cross Sections, by Pau-Chang Lu. (59—A-145)
233 On Combined Free and Forced Convection in Channels, by L. N. Tao. (59—A-77)
239 The Role of the Skin in Heat Transfer, by A. M. Stoll. (59—A-138)
243 The Prediction of Human Thermal Tolerance When Using a Ventilating Garment With An Anti-exposure Suit, by J. W. McCutchan. (59—A-114)

TECHNICAL BRIEFS

252 Heat Transfer by Laminar Flow From a Rotating Cone, by C. L. Tien.
253 Apparent Emissivity and Heat Transfer in a Long Cylindrical Hole, by E. M. Sparrow and L. U. Albers.
255 On the Variable-Density Single-Fluid Model for Two-Phase Flow, by Novak Zuber.
258 Nearly Quasi-Steady Free Convection Heat Transfer in Gases, by E. M. Sparrow and J. L. Gregg.
260 The Effect of Mass Transfer on Free Convection, by R. Eichhorn.
263 An Interferometric Method of Studying Boundary Layer Oscillations, by J. P. Holman, H. E. Gartrell, and E. E. Soehngen.

TRANSACTIONS
Series D

Journal of
BASIC ENGINEERING
Vol. 82 • Series D • No. 2

CONTENTS FOR JUNE, 1960

251 The Fluids Engineering Laboratory at the University of Michigan, by G. V. Edmonson. (59—Hyd-16)
257 Flow Parameters in Hydrostatic Lubrication for Several Bearing Shapes, by S. Raynor and A. Charnes. (59—SA-61)
265 A General Method for Correlating Labyrinth-Seal Leak-Rate Data, by F. E. Heffner. (59—Lub-7)
276 Hydrostatic Gas Bearings, by J. H. Laub. (59—Lub-1)
287 Effect of Hardness, Surface Finish, and Grain Size on Rolling-Contact Fatigue Life of M-50 Bearing Steel, by R. A. Baughman. (59—Lub-11)
295 The Importance of Spinning Friction in Thrust-Carrying Ball Bearings, by G. S. Reichenbach. (59—Lub-9)
302 The Effect of Ball Bearing Steel Structure on Rolling Friction and Contact Plastic Deformation, by R. C. Drutowski and E. B. Mikus. (59—Lub-2)
309 A General Theory for Elastically Constrained Ball and Radial Roller Bearings Under Arbitrary Load and Speed Conditions, by A. B. Jones. (59—Lub-10)
321 A Sommerfeld Solution for Finite Bearings With Circumferential Grooves, by J. V. Fedor. (59—Lub-4)
327 Bearing Oil-Ring Performance, by D. C. Lemmon and E. R. Booser. (59—Lub-5)
335 Torque Produced by Misalignment of Hydrodynamic Gas-Lubricated Journal Bearings, by J. S. Ausman. (59—Lub-3)
342 Friction Characteristics of Sliding Surfaces Undergoing Subsurface Plastic Flow, by M. C. Shaw, A. Ber, and P. A. Mamin.
347 Machining Characteristics of Leaded Steel, by F. L. Bagley, Jr., and R. Mennell.
360 A General Flow Graph Technique for the Solution of Multiloop Sampled Systems, by R. Ash, W. H. Kim, and G. M. Kranc. (59—NAC-1)
371 Control System Analysis and Design Via the "Second Method "of Lyapunov, Part I, by R. E. Kalman and J. E. Bertram. (59—NAC-2)
394 Control System Analysis and Design Via the "Second Method" of Lyapunov, Part II, by R. E. Kalman and J. E. Bertram. (59—NAC-3)
401 Relations Between the Notch Tensile Strength of Cylindrical and Prismatic Specimens of Titanium Alloys and Heat-Treated Steels, by G. Sachs, J. G. Sessler, R. F. Pray, and T. H. Yeh. (59—Met-2)
411 Nonmetallic Inclusions and Fracture Behavior of Steels, by S. Yukawa. (59—Met-10)
417 Fracture Mode Transition for a Crack Traversing a Plate, by G. R. Irwin.
426 Use of the Moiré Effect to Measure Plastic Strains, by A. Vinckier and R. Dechaene. (59—Met-7)
435 A Generalization of Cumulative Damage, by R. M. Mains. (59—Met-1)
441 Effect of Relaxation on the Behavior of Materials Under Combined Alternating and Static Stress, by F. H. Vitovec. (59—Met-3)
447 Cyclic Operation of Pressure Piping With γ Heating, by K. R. Merckx. (59—Met-4)
453 Creep Rupture Tests for Design of High-Pressure Steam Equipment, by E. A. Davis. (59—Met-14)
462 Steady Creep of a Tube Under Combined Bending and Internal Pressure, by Iain Finnie. (59—Met-5)
465 Effect of Wall Thickness on Stress-Rupture Life of Tubular Specimens, by J. T. Tucker, Jr., E. E. Coulter, and L. F. Kooistra. (59—Met-11)
477 Design of Pressurized Cylinders for High-Temperature Applications, by J. F. Traexler. (59—Met-8)
482 The Response of a Pressure-Sensing System, by R. P. Benedict. (59—A-289)
489 Dynamics of Heat Exchangers and Their Models, by Herman Thal-Larsen. (59—A-117)

TRANSACTIONS OF THE ASME Series A

Journal of
ENGINEERING FOR POWER

Volume 82 • Series A • Number 3

CONTENTS FOR JULY, 1960

169 An Experimental Investigation of Fuel Additives in a Supercharged Boiler, by R. J. Zoschak and R. W. Bryers. (59—A-160)

181 External Corrosion of Superheaters in Boilers Firing High-Alkali Coals, by P. Sedor, E. K. Diehl, and D. H. Barnhart. (59—A-76)

194 Corrosion of Superheaters and Reheaters of Pulverized-Coal-Fired Boilers, by Wharton Nelson and Carl Cain, Jr. (59—A-89)

205 Considerations for the Reduction of Noise in Ship Installations of Gas Turbines, by E. M. Herrmann. (59—A-238)

215 A Torsional Vibration Problem as Associated With Synchronous Motor Driven Machines, by R. N. Brown. (59—A-141)

221 Design Control of Overcompression in Rotary-Vane Compressors, by E. O. Bransford and R. A. Stein. (59—A-109)

227 Operation of Steam Turbines to Minimize Shell Cracking, by S. B. Coulter and R. L. Jackson. (59—Pwr-10)

TRANSACTIONS OF THE ASME Series E

Journal of
APPLIED MECHANICS

Volume 82 • Series E • No. 2

CONTENTS FOR JUNE, 1960

TECHNICAL PAPERS

223 Note on the Assessment of Flow Disturbances at a Blunt Body Traveling at Supersonic Speeds Owing to Flow Disturbances in Free Stream, M. V. Morkovin. (60—APM-10)

230 Possible Similarity Solutions for Laminar Free Convection on Vertical Plates and Cylinders, Kwang-Tzu Yang. (59—A-86)

237 On the Annular Damper for a Freely Precessing Gyroscope, G. F. Carrier and J. W. Miles. (59—A-44)

241 Heat Transfer for Laminar Flow in Ducts With Arbitrary Time Variations in Wall Temperature, Robert Siegel. (59—APMW-21)

250 A Study of the Stability of Externally Pressurized Gas Bearings, Lazar Licht and Harold Elrod. (60—APM-5)

259 On the Theoretical Analysis of a Dynamic Thermocouple: 2—The Continuous Area Interface, W. F. Hughes and E. W. Gaylord. (60—APM-19)

263 Normal Modes of Nonlinear Dual-Mode Systems, R. M. Rosenberg. (59—A-93)

269 Classical Normal Modes in Damped Linear Dynamic Systems, T. K. Caughey. (59—A-62)

272 The Vibration Response of a Linear Undamped System Resting on a Nonlinear Spring, P. R. Paslay and M. E. Gurtin. (60—APM-6)

275 The Approximate Analysis of Certain Boundary-Value Problems, H. D. Conway. (59—A-80)

278 Stresses in a Slab Having a Spherical Cavity Under Circular Bending, Chih-Bing Ling and Chen-Peng Tsai. (59—A-64)

283 Elastic Equilibrium of a Plate With a Reinforced Elliptical Hole, Eugene Levin. (59—A-45)

289 A Method of Solution for the Elastic Quarter-Plane, M. Hetényi. (59—A-92)

297 Thermal Stress in a Viscoelastic-Plastic Plate With Temperature-Dependent Yield Stress, H. G. Landau, J. H. Weiner, and E. E. Zwicky, Jr. (59—A-33)

303 Prediction of Creep Failure Time for Pressure Vessels, F. P. J. Rimrott, E. J. Mills, and Joseph Marin. (60—APM-7)

309 On the Plastic Behavior of Rotating Cylinders, F. P. J. Rimrott. (59—A-65)

316 On the Optimum Design of Shells, R. T. Shield. (59—A-47)

323 Yield Conditions for Rotationally Symmetric Shells Under Axisymmetric Loading, P. G. Hodge, Jr. (59—A-129)

332 An Approximate Analysis of the Influence of Aerodynamic Heating and Initial Twist on the Torsional Stiffness of Thin Wings, L. S. Han. (60—APM-13)

335 Postbuckling Behavior of Rectangular Plates With Small Initial Curvature Loaded in Edge Compression—(continued), Noboru Yamaki. (59—APMW-22)

343 The Junction Problem of Solid-Slotted Cylindrical Shells, D. H. Cheng and N. A. Weil. (60—APM-2)

BRIEF NOTES

350 Method of Numerical Evaluation of a Large Determinant, F. R. E. Crossley and U. Germen. 352 On the Griffith-Irwin Theory, J. L. Sanders, Jr. 353 On the Flexure of Plastic Plates, S. Lerner and W. Prager. 355 Induced Velocities in Two-Dimensional Cascade Theory, J. Polasek. 356 Relation Between Stress Concentration and Boundary Displacement, J. S. Brock. 357 Bending of an Isotropic Triangular Plate, B. D. Aggarwala. 358 Simplified Analysis of a Thrust-Augmentation System, K. L. Bergman. 359 Stress Concentration in a Rotating Disk, Ta-Cheng Ku.

DISCUSSION

361 Discussion of previously published papers by M. K. Newman; M. V. Morkovin; P. G. Hodge, Jr., and R. Sankaranarayanan; Joseph Marin; R. R. Berlot; Norman Davids; T. Gillespie and A. W. Gunter; J. W. Dally, W. F. Riley, and A. J. Durelli; T. K. Caughey; H. H. Bleich and O. W. Dillon, Jr.; H. D. Conway; P. S. Theocaris; D. S. Johnson; R. P. Kanwal; Yi-Yuan Yu; C. W. Nelson; A. E. Bryson

377 BOOK REVIEWS

Synthesis of Epicyclic Gear Trains Using the Velocity Ratio Spectrum

R. C. BREWER

Lecturer in Mechanical Engineering, The Imperial College of Science and Technology, University of London, London, England

For a simple epicyclic train, the controlling element is almost invariably fixed, i.e., prevented from rotating by being connected, in some way, to the frame. Such trains are easy to synthesize because there are a limited number of variations of the three basic elements and, normally, six equations will define all possible velocity ratios. For a compound epicyclic train, the number of equations is considerably increased.

A method of synthesizing compound epicyclic trains is developed using the concept of a velocity ratio spectrum. To facilitate the application of this concept, only one train in a compound epicyclic train is regarded as basic; all others are considered as merely serving the purpose of modifying the motion of the controlling element in the basic train.

Introduction

THERE IS LITTLE LITERATURE to guide anyone who has to design an epicyclic train to satisfy some given conditions. With gear trains, as with other mechanisms, it is normally true that synthesis presents more problems than analysis and, apart from the fact that there is rarely a unique solution, the method of approach usually has to sacrifice some elegance for the sake of expedience.

In this present discussion, consideration will only be given to trains having annular or ring wheels but the treatment itself is general and could be altered to suit other types of epicyclic gear train. Consider Fig. 1 which shows diagrammatically a simple epicyclic gear train consisting of an annular or ring wheel, A, a carrier C for the planet wheels (of which P is one), and a sun wheel, S. Let the ratio (number of teeth on A/ number of teeth on S) = R. Then a tabular solution may be effected for tnis train (see Table 1) where the capital letters refer to numbers of teeth on the corresponding wheels. Any one of the three elements, sun wheel, carrier, or annular wheel, may be fixed or may be the driving element thus giving a total of 6 fundamental velocity ratios.

The theoretical limits of R are unity and infinity but, in practice, the extreme values are very unlikely to exceed the limits 1.8 and 11. If these limiting values are substituted into the expressions for the six velocity ratios, they will determine the practical range of velocity ratio for each type of train. The results of this are shown in Table 2. (The designation referred to in the table is merely a convenient way of indicating the driving, driven, and fixed elements in that order.)

The figures in the last two columns of Table 2 are shown graphically in Fig. 2 which may be termed "the velocity ratio spectrum." It will be noted that, although the theoretical ranges cover the whole of the spectrum from $-\infty$ to $+\infty$, the practical ranges are such as to leave several "dead zones" in the spectrum, i.e., velocity ratios for which a simple epicyclic train cannot be designed. Five of these zones occur between velocity ratios of approximately -2 and $+3$; in this range, an ordinary

Contributed by the Machine Design Division and presented at the Annual Meeting, Atlantic City, N. J., November 29–December 4, 1959, of THE AMERICAN SOCIETY OF MECHANICAL ENGINEERS.

NOTE: Statements and opinions advanced in papers are to be understood as individual expressions of their authors and not those of the Society. Manuscript received at ASME Headquarters, March 13, 1959. Paper No. 59—A-22.

Table 1

No.	Operation	A	C	S
1	Fix C and give A + 1 rev	+1	0	$-A/S = -R$
2	Fix A, i.e., line (1) − 1	0	−1	$-(1 + R)$
3	Fix S, i.e., line (1) + R	$1 + R$	R	0

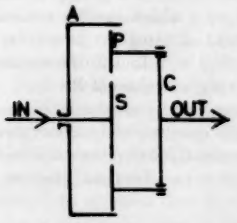

Fig. 1 A simple epicyclic gear train

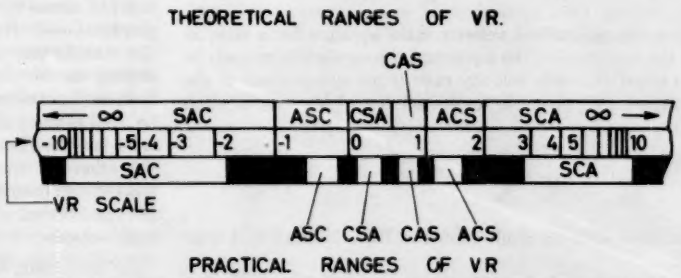

Fig. 2 The velocity ratio spectrum showing the theoretical and practical ranges for each type of train

Table 2

Element			Designation	Velocity ratio	Range of velocity ratio	
Driving	Driven	Fixed			Theoretical	Practical
S	A	C	SAC	$-R$	$-\infty$ to -1	−11.00 to −1.8
A	S	C	ASC	$-1/R$	−1 to 0	−0.56 to −0.09
C	S	A	CSA	$1/1 + R$	0 to $^1/_2$	0.08 to 0.36
C	A	S	CAS	$R/1 + R$	$^1/_2$ to 1	0.64 to 0.92
A	C	S	ACS	$1 + R/R$	1 to 2	1.10 to 1.56
S	C	A	SCA	$1 + R$	2 to ∞	2.80 to 12.00

fixed carrier train could be employed. The other two dead zones are for positive and negative velocity ratios of approximately 10 to infinity; again, use could be made of a type of train known to lend itself to high velocity ratios (one such type is discussed later).

As a simple example, suppose that a train having a single velocity ratio of 3.5 were required. Inspection of the velocity ratio spectrum shows that an SCA train is needed, the velocity ratio for which is $1 + R$, i.e., $1 + R = 3.5$, $R = 2.5$ say 60/24 for A/S; furthermore, the designation SCA means that the sun wheel is the driving element, the carrier is the driven element, and the annular wheel is stationary.

It should be borne in mind, however, that if more than one planet pinion is used to improve the balance of the carrier assembly, then there are certain conditions regarding tooth numbers which have to be complied with in order to permit the gear train to be assembled. This appears to have been pointed out first by Plint[1] and, more recently, by Benford.[2]

The Concept of a Compound Epicyclic Train

Now consider the train shown in Fig. 1 under "free" conditions, i.e., with none of the elements fixed.[3] The equation giving the relationship between the various angular velocities is most easily derived from the fact that the speeds of the sun wheel and annular wheel *relative to the carrier* are in the inverse ratio of their numbers of teeth, i.e.,

$$\frac{\text{speed of sun wheel relative to carrier}}{\text{speed of annular wheel relative to carrier}} = \frac{N_s - N_c}{N_a - N_c} = -\frac{A}{S} = -R$$

or
$$N_s - N_c = R(N_c - N_a) \qquad (1)$$

From this, the ratio of any two speeds may be deduced; as an example, the ratio of the speed of the sun wheel to that of the carrier may be found as follows:

Dividing equation (1) by N_c,

$$\frac{N_s}{N_c} - 1 = R\left(1 - \frac{N_a}{N_c}\right)$$

or
$$\frac{N_s}{N_c} = 1 + R\left(1 - \frac{N_a}{N_c}\right) \qquad (2)$$

This is the generalized velocity ratio equation for a train in which the sun wheel is the input and the carrier the output; it will be noted that this velocity ratio is not independent of the output speed (N_c) except in the special case of $N_a = 0$, in which event,

$$\frac{N_s}{N_c} = 1 + R,$$

in accordance with the result quoted in Table 2 for an SCA type of train.

Fig. 3 shows the velocity ratio (N_s/N_c) as a function of (N_a/N_c) for several discrete values of R within the practical range of 1.8 to 11. Although the curves of Fig. 3 satisfy equation (2), they do not represent the only way in which the information of equation

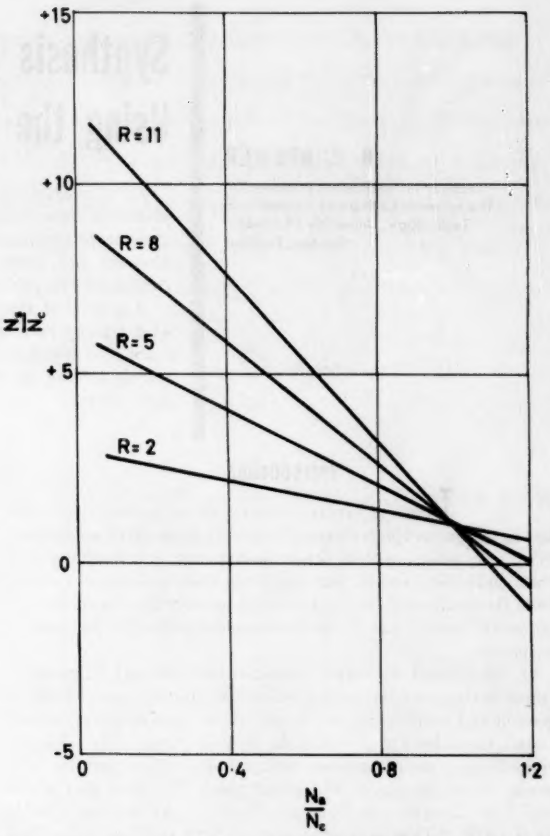

Fig. 3 The relationship between N_s/N_c and N_a/N_c for an SCA type of train

(2) may be presented; to be more precise, Fig. 3 is in a form which may be useful for synthesizing trains having the sun wheel as the input and the carrier as the output but it is ill-suited to the synthesis of the other five types of train.

This need for six sets of curves and the tedium of interpolating for nonplotted values of R, together with the simplicity of equation (1), means that an analytical approach is to be preferred to a graphical one. Hence, the main virtue of Fig. 3 is to illustrate the considerable effect on (N_s/N_c) which can be achieved by driving the annular wheel instead of fixing it. It will be noted that, within the range of (N_a/N_c) = 0 to 1.2, the variation in (N_s/N_c) is much greater for the higher values of R.

So far, the discussion has been largely academic and no consideration has been given to the question of how the third element should be driven. Clearly, the third element could be driven from an external source (constant or variable speed) for one of two main reasons:

(*a*) To obtain, from an epicyclic gear train, a velocity ratio within one of the dead zones; for example, the normally unobtainable velocity ratio of 2 may be achieved with an SCA type of train, by driving the annular wheel at a speed

$$N_a = \frac{R - 1}{R} \cdot N_c, \text{ where } R \text{ has its usual meaning.}$$

(*b*) To obtain an infinitely variable velocity ratio within some given range. In either of these cases, the chances that a non-epicyclic type of train would be more practical are fairly high.

However, if the third element is driven from within the train

[1] M. A. Plint, "Designing Epicyclic Gear Trains for Equal Planet Pinion Spacing," *Machinery (London)*, vol. 79, pp. 727–728.

[2] R. L. Benford, "Numerical Rules for Designing Planetary Gears," *Machine Design*, August 21, 1958, pp. 129–135.

[3] It is preferable now to stop using the term "fixed element" and to adopt the designation "input element, output element, and *third* element."

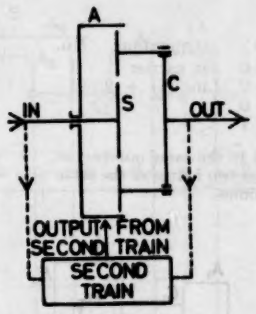

Fig. 4 Diagrammatic representation showing how a second train may drive the annular wheel of the first train

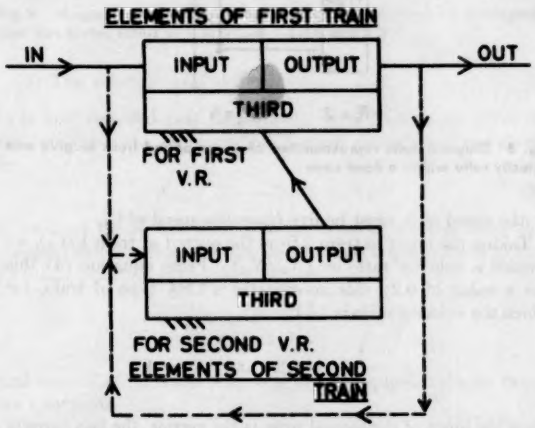

Fig. 5 Block diagram showing a generalized double-compound train and how the two ratios are derived

itself, a more interesting situation is perceived. Evidently, the third element can only be driven from either the input element or the output element; furthermore, the required speed of the third element will not, in general, be equal to either the input or output speeds and hence, a second gear train will be required to *transform* the speed derived from the first, or basic, train to that required for the third element. This is shown diagrammatically in Fig. 4 for an SCA type of train and in Fig. 5 for a generalized system.

The introduction of such a second train is justifiable *if a two-speed gear-box is required*, the two velocity ratios being obtained by fixing the third element of (*a*) the first train and (*b*) the second train. Such a train may be called a compound epicyclic train or, more specifically, a double compound epicyclic train since it has two constituent simple trains. In this paper, the first train will be referred to as the *basic train* and the second (and any further) trains as *modifying trains*.

It should be stressed that the foregoing description has been given because it is the basis of the present approach to the synthesis of compound epicyclic trains; there may well be other approaches.

Synthesis of Compound Epicyclic Trains

Consider now the case of a train which is to be designed to give velocity ratios of +4 and +3, the numbers being chosen thus merely to simplify arithmetical working.

The first, or basic, train may be allotted either the +3 or the +4 ratio. Taking, say, the +4 ratio, the velocity ratio spectrum shows that an SCA type of train is needed, i.e., the sun wheel is the input, the carrier the output, and the annulus the fixed element. From Table 2, the velocity ratio of an SCA type of train is $(1 + R)$ and hence, if R_1 be the specific value of R for the first train,

$$1 + R_1 = 4 \text{ or } R_1 = 3$$

In practice, S_1 and C_1 must remain the input and output elements (or, at least, coupled to these elements) and hence, having determined a specific value for R_1 (with the annulus fixed), the train shown in Fig. 4 can only now give a different velocity ratio (in this instance +3) if A_1 is driven at a speed determined by equation (1). Since the tooth numbers have not been altered, R_1 still has the value 3,

$$\text{i.e., } N_{a1} - N_{c1} = 3(N_{c1} - N_{s1})$$

Dividing by N_{c1} and writing $N_{s1}/N_{c1} = 3$ (this being the desired ratio)

$$3 - 1 = 3(1 - N_{s1}/N_{c1})$$

or

$$\frac{N_{c1}}{N_{a1}} = 3 \qquad (3)$$

If A_1 were driven, by any means, at one third the speed of C_1 then the desired ratio of 3 would be obtained. As discussed previously, the input to train 2 may be derived from either the input or output of train 1 as represented diagrammatically in Fig. 4. The output of train 2 is used to drive the annular wheel of train 1.

Thus a second train is needed such that its output will cause A_1 to rotate at one third of the speed of C_1 (and hence one ninth of the speed of S_1).

Case 1. Taking the Input to Train 2 From the Output of Train 1. The output of train 1 (C_1) now provides the input to train 2 and the output of train 2 drives A_1 thus modifying the motion. The velocity ratio of train 2 is thus given by N_{a1}/N_{s1}, which from equation (3) has the value 3. This requires an SCA type of train (see Table 2) whose velocity ratio is given by $1 + R \therefore 1 + R_2 = 3$ or $R_2 = 2$.

To determine the two couplings between trains 1 and 2, we know that, as train 2 is of type SCA, the sun wheel S_2 is the input and the carrier C_2 the output. Therefore, S_2 is coupled to C_1 (the output of train 1) and C_2 is coupled to A_1. This train is shown diagrammatically in Fig. 6(*a*).

Case 2. Taking the Input to Train 2 From the Input of Train 1. The input to train 2 is now derived from S_1 (the input of train 1) but the output of train 2 still drives A_1. Thus the velocity ratio of the second train must now be:

$$\frac{N_{a1}}{N_{s1}} = \frac{N_{a1}}{N_{c1}} \cdot \frac{N_{c1}}{N_{s1}} = 3 \times 3 = 9$$

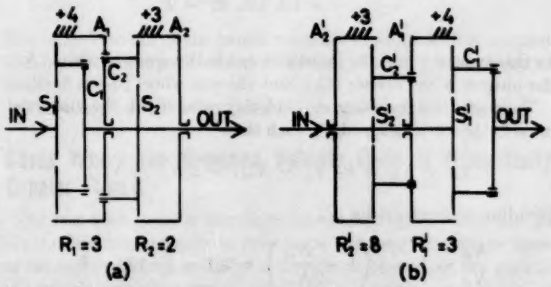

Fig. 6 Diagrammatic representation of a compound train to give velocity ratios of +4 and +3, the basic train giving the +4 ratio. The input for the second train is taken from (a) the output and (b) the input of train 1.

Table 3

No.	Operation	A_1	S_1	C_1	A_2	S_2	C_2	Operation	No.
1	Fix carrier	+1	−3	0	+1	−2	0	Fix carrier	I
2	Line (1) × 2	+2	−6	0	+3	0	+2	Line (I) + 2	II
3	Line (2) − 2, i.e., A_1 fixed	0	−8	−2	+1	−2	0		
4	Line (3) − 1, i.e., A_2 fixed	−1	−9	−3	0	−3	−1		

The coupled elements (A_1 and C_2; C_1 and S_2) having been brought to the same numbers of revolutions in lines 2 and II, it is no longer necessary to consider the two halves of the table separately and the remarks in the left-hand table apply to all 6 columns.

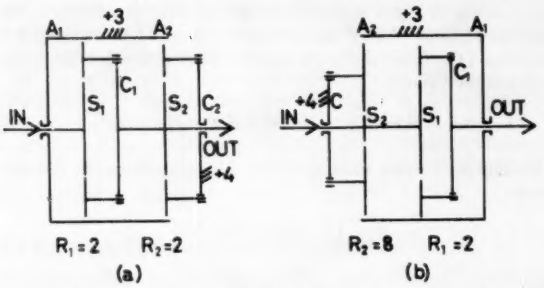

Fig. 7 The same case as shown in Fig. 6 but with the basic train giving the +3 ratio

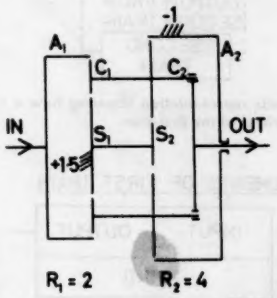

Fig. 8 Diagrammatic representation of a compound train to give one velocity ratio within a dead zone

[N_{s1}/N_{a1} from equation (3); N_{s1}/N_{c1} is the desired velocity ratio, 3.]

A velocity ratio of 9 requires an SCA type of train, whose tooth ratio $R_2' = 8$ (q.v., Table 2). This designation shows that S_2' is the input and must be coupled to S_1 (the input of train 1); also that C_2' is the output and must be coupled to A_1. This train is shown in Fig. 6(*b*). It should be noted that $R_2' = 8$ is rather high and, given suitable alternatives, would possibly be rejected. It should also be remembered that there are still the two trains for which the +3 ratio is taken for the basic train. Synthesis in these cases, leads to the solutions shown in Figs. 7(*a* and *b*).

Table 3 is the analysis for the train in Fig. 4(*a*), thus providing a check on the synthesis done previously.

Similar tables may be drawn up to show that the other syntheses are correct.

A Case Where One of the Velocity Ratios Lies Within a Dead Zone

Consider the case of a double-compound epicyclic train which is to be designed to give ratios of +1.5 and −1.0. Since the −1.0 ratio lies in a dead zone, there is no longer an arbitrary choice of ratio for the basic train.

This basic train, to give a velocity ratio of +1.5, must be an ACS type of train and the tooth ratio R_1 is given by

$$\frac{1 + R_1}{R_1} = 1.5, \text{ i.e., } R_1 = 2$$

In this type of train, the input element is the annular wheel (A_1), the output is the carrier (C_1), and the sun wheel (S_1) is fixed.

To enable this train to give a velocity ratio of −1, the sun wheel must be driven at a speed N_{s1} such that

$$N_{s1} - N_{c1} = R_1(N_{c1} - N_{a1}) = 2(N_{c1} - N_{a1})$$

Dividing throughout by N_{c1}

$$\frac{N_{s1}}{N_{c1}} - 1 = 2\left(1 - \frac{N_{a1}}{N_{c1}}\right) = 2(1 - (-1)) = 4$$

or

$$\frac{N_{a1}}{N_{c1}} = 5 \qquad (4)$$

$\therefore$ the speed of S_1 must be five times the speed of C_1.

Taking the input to train 2 from the output of train 1 (C_1), we require a velocity ratio = (N_{c1}/N_{s1}). From equation (4) this has a value of 0.2; this necessitates a CSA type of train, for which the velocity ratio is $1/(1 + R)$.

$$\therefore \frac{1}{1 + R_2} = 0.2 \quad \text{and} \quad R_2 = 4.$$

Since the input of the second train is the carrier, the two carriers are coupled together. The other coupling is from the output of the second train (S_2) to the sun wheel of the first train, the complete train being as shown in Fig. 8.

Thus, in this case, the presence of a ratio in the dead zone is no obstacle to synthesis of the train. In general, this will be true and cases where one ratio in a dead zone prevents synthesis may be regarded as exceptional.

Application to a Multispeed Box

One of the best-known applications of multispeed epicyclic gear boxes is to the automobile (sometimes known then as *preselector boxes*), the common arrangement being three or four forward gears and one reverse gear. Since it is customary to obtain top gear by direct drive, i.e., by "locking" the whole train, a four-speed box consists, in effect, of only three epicyclic trains for forward gears plus one additional train for the reverse gear.

To illustrate the method of synthesis which has been described previously in the paper consider a gear-box in which velocity ratios of +4, +2.5, +1.43, and −5 are required. The stages in the synthesis are:

(1) The velocity ratio of +4:

This is the basic train and, by consulting Table 2, it is seen that an SCA type of train is needed; further the velocity ratio is given by (1 + R) so that the tooth ratio for the first train, R_1, must satisfy

$$1 + R_1 = 4 \quad \text{or} \quad R_1 = 3.$$

The sun wheel S_1 is the input, the carrier C_1 the output, and the annular wheel A_1 is fixed for this ratio.

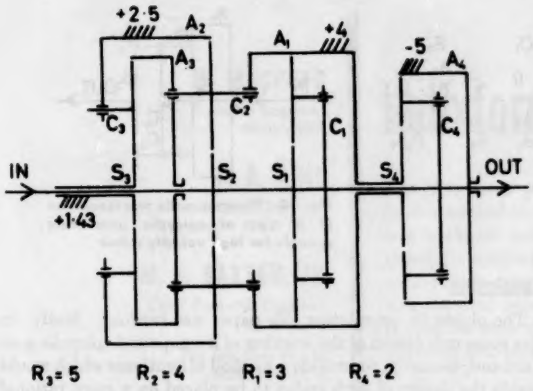

Fig. 9 Diagrammatic representation of an automobile type of multispeed gear box giving ratios of +4, +2.5, +1.43, and −5

(2) The velocity ratio +2.5:

It is now required that the velocity ratio N_{s1}/N_{c1} be +2.5, to achieve which, the annular wheel A_1 must rotate at a speed given by

$$N_{s1} - N_{c1} = 3(N_{c1} - N_{a1}) \qquad (5)$$

If we drive the second train from the input of the first train, the required velocity ratio for the second train is given by N_{s1}/N_{a1}. Dividing equation (5) by N_{s1}

$$1 - \frac{N_{c1}}{N_{s1}} = 3\left(\frac{N_{c1}}{N_{s1}} - \frac{N_{a1}}{N_{s1}}\right)$$

and since N_{s1}/N_{a1} is the reciprocal of the required velocity ratio, we may write

$$1 - 0.4 = 3\left(0.4 - \frac{N_{a1}}{N_{s1}}\right)$$

giving $N_{a1}/N_{s1} = 0.2$. Thus, $N_{s1}/N_{a1} = 5$

which is the required ratio for the second train. Hence this is also an SCA type of train in which $1 + R_2 = 5$ or $R_2 = 4$.

The input element of the second train is the sun wheel S_2 which is thus coupled to S_1. The output is the carrier C_2 and this should be coupled to the annular wheel A_1 (see Fig. 9).

(3) The velocity ratio +1.43:

Since the basic train has not been altered physically, equation (5) must still be true, but we now require that $N_{s1}/N_{c1} = +1.43$. Dividing equation (5) by N_{s1},

$$1 - \frac{N_{c1}}{N_{s1}} = 3\left(\frac{N_{c1}}{N_{s1}} - \frac{N_{a1}}{N_{s1}}\right)$$

Substituting $N_{c1}/N_{s1} = 1/1.43 = 0.7$

$$1 - 0.7 = 3\left(0.7 - \frac{N_{a1}}{N_{s1}}\right)$$

giving $$\frac{N_{a1}}{N_{s1}} = 0.6 \quad \text{or} \quad \frac{N_{a1}}{N_{a1}} = \frac{10}{6} = 1.67$$

Thus we require the second train to give a velocity ratio of +1.67; since it has already been designed to give a velocity ratio of +5 (with A_2 fixed), it can only give a ratio of +1.67 if A_2 is driven, by a third train, at a speed N_{a2} given by the basic equation for a "free" train, i.e., equation (1) with $R = R_2 = 5$.

This leads to the equation:

$$N_{s2} - N_{c2} = 5(N_{c2} - N_{a2}). \qquad (6)$$

Let us take the input for this third train from the output of the second train, i.e., the carrier C_2. Then, dividing equation (6) by N_{c2}

$$\frac{N_{s2}}{N_{c2}} - 1 = 5\left(1 - \frac{N_{a2}}{N_{c2}}\right)$$

and since we desire that $N_{s2}/N_{c2} = 1.67$

$$1.67 - 1 = 5\left(1 - \frac{N_{a2}}{N_{c2}}\right)$$

giving $$\frac{N_{a2}}{N_{c2}} = \frac{5}{6} \quad \text{or} \quad \frac{N_{c2}}{N_{a2}} = 1.2$$

Thus, by Table 2, the third train must be an ACS type of train, the velocity ratio for which is $\left(\frac{1+R}{R}\right)$ in terms of the tooth ratio. Calling this tooth ratio R_3 for the third train,

$$\frac{1 + R_3}{R_3} = 1.2 \quad \text{or} \quad R_3 = 5.$$

The couplings are:

A_3 (input of train 3) to C_2 (output of train 2) and C_3 (output of train 3) to A_2 (the previously fixed element of train 2). These are shown in Fig. 9.

(4) The velocity ratio −5:

It is assumed that this fourth ratio, since it is not a forward gear, will be obtained by modifying the motion of the basic train directly and not via the second and third trains.

Once again, equation (5) must hold but we now require that $N_{s1}/N_{c1} = -5$. Dividing equation (5) by N_{c1},

$$\frac{N_{s1}}{N_{c1}} - 1 = 3\left(1 - \frac{N_{a1}}{N_{c1}}\right)$$

or $$-5 - 1 = 3\left(1 - \frac{N_{a1}}{N_{c1}}\right)$$

giving $$\frac{N_{a1}}{N_{c1}} = 3 \quad \text{or} \quad \frac{N_{c1}}{N_{a1}} = \frac{1}{3}.$$

We now need a fourth train which will derive its motion from the output of the first train (C_1) and modify it so that A_1 is driven at three times the speed of C_1, i.e., we require a train whose velocity ratio is 1/3 = 0.33. For this a CSA type of train is needed and its tooth ratio R_4 is given by

$$\frac{1}{1 + R_4} = \frac{1}{3} \quad \text{or} \quad R_4 = 2$$

The input element of the fourth train is C_4 (which is thus coupled to C_1) and the output element is the sun wheel S_4 (which must be coupled to A_1).

The complete train is shown diagrammatically in Fig. 9.

Cases Where the Required Velocity Ratio Is Numerically Greater Than 8

As has been seen, a double compound epicyclic train can be synthesized theoretically in four ways. In practice, one or more of these may be impossible of achievement because of the gaps in the velocity ratio spectrum. Normally, of course, one solution is suitable but if a high ratio has to be dealt with, the best type of train is that shown in Fig. 10, which is really a special case of a

Table 4

No.	Operation	S_1	A_1	P_1 and P_2	C_1	S_2
1	Fix C_1 and give +1 rev to A_1	$-\frac{A_1}{S_1}$	$+1$	$+\frac{A_1}{P_1}$	0	$-\frac{A_1}{P_1}\cdot\frac{P_2}{S_2}$
2	Fix S_1, i.e., line (1) + A_1/S_1.	0	$1+\frac{A_1}{S_1}$	$\frac{A_1}{P_1}+\frac{A_1}{S_1}$	$\frac{A_1}{S_1}$	$\frac{A_1}{S_1}-\frac{A_1P_2}{P_1S_2}$

double compound train in which C_1 and C_2 are common and either A_2 or S_2 is omitted (in Fig. 10, it is A_2 which is omitted).

Table 4 gives the solution for this train and, evidently, with either A_1 or C_1 as input and S_2 as output, the velocity ratio for S_1 fixed has, as its denominator, the speed of S_2, i.e.,

$$N_{s2} = \frac{A_1}{S_1} - \frac{A_1P_2}{P_1S_2} = \frac{A_1}{P_1S_1S_2}(P_1S_2 - P_2S_1)$$

The term in brackets can, theoretically, be made to tend to zero thus giving a velocity ratio which tends to infinity. In practice, of course, there are limitations, the principal of which is the fact that the number of teeth on a wheel must be an integer. The difference term in the denominator (referred to above) is rather deceptive in the form quoted since only three of the four parameters are independent and it is probably better to combine this difference with the geometrical condition

$$S_1 + P_1 = S_2 + P_2$$

to give
$$P_1S_2 - P_2S_1 = P_1(S_1 + P_1 - P_2) - P_2S_1$$
$$= (P_1 - P_2)(S_1 + P_1).$$

Hence, as the difference in the numbers of teeth on P_1 and P_2 diminishes, the velocity ratio increases.

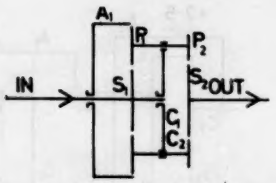

Fig. 10 Diagrammatic representation of a type of epicyclic gear train suitable for high velocity ratios

Conclusion

The object in formulating this paper was twofold; firstly, to give some conception of the working of a compound epicyclic gear train and, secondly, to provide a method of synthesis which would enable the design of such trains to be placed on a more rational basis.

In the field of linkage mechanisms, Richard de Jonge has repeatedly stressed the undue emphasis which has, in the past, been placed on analysis to the exclusion of synthesis. This is also true in the field of epicyclic gear trains but, in this case, it has also led to a state of almost complete ignorance regarding the way in which compound epicyclic gear trains work—a glance through several American and British standard textbooks failed to disclose any kind of explanation of the action of compound trains.

The paper gives some account of the way in which compound epicyclic gear trains work and has proposed one method of synthesis for such trains.

G. M. SPEAR
Research Engineer.
Mem. ASME

C. B. KING
Associate Chief Research Engineer. Mem. ASME

M. L. BAXTER, JR.
Chief Research Engineer.
Mem. ASME

The Gleason Works,
Rochester, N. Y.

Helixform Bevel and Hypoid Gears

The Helixform[1] process is a recent development in the art of gear cutting. Gears made by this method are classified as nongenerated which means that the workpiece remains at rest while the teeth are being cut. Cutting the gear without generation is a process especially adapted to high production and accurate machining and is the method used to manufacture most automotive spiral bevel and hypoid gears. Pinions which match nongenerated gears are of course produced with generating motion, that is, the tools cutting the teeth of the pinion are mounted on a machine element which, while the teeth are being cut, turns in concord with the turning of the pinion on its axis.

General Description and Geometry

OBJECTIVES SOUGHT in the development of the Helixform process were:

1 To produce gears and pinions by a method which gives basically correct tooth bearings with conjugate tooth action within the practical limits of manufacturing tolerances and deflections.

2 To produce gears and pinions by a process which maintains the depthwise taper of the teeth which is the established standard of design for spiral bevel and hypoid gears.

3 To maintain the production advantages of the nongenerated type of gear.

4 In so far as heat-treatment distortions will allow, to eliminate empirical methods of obtaining desired tooth bearings.

5 To achieve mathematical simplicity in both theory and calculation.

When the gear is made without generation there are but two processes by which spiral bevel and hypoid gears have been produced, using face-mill cutters, with teeth completely conjugate in the strictly mathematical sense. With one of these processes, the gear tooth surfaces are spherical concave and convex surfaces and the method is adaptable to teeth of tapering depth. The other uses conical gear teeth but, to obtain mathematical or absolute conjugacy, the many advantages of the tapering depth tooth must be relinquished. Neither of these processes, nor any process which produces completely conjugate teeth, is suitable for the production of practical gear pairs because without mismatch there could be no tolerances in manufacture or assembly, and consequently no adjustment and no accommodation to load and deflection.

The Helixform process is a simple direct means of making gear pairs practically conjugate, that is, with the mismatch necessary to allow for tolerance and deflection. Tooth bearings are produced at the initial cutting which are correctly shaped for the delivery of uniform motion.

This is so because Helixform pinions are generated with machine set ups by which a face-mill cutter and machine cradle carrying the cutter represent the counterpart of the mating gear except for the difference in cutter curvature which provides the desired lengthwise mismatch.

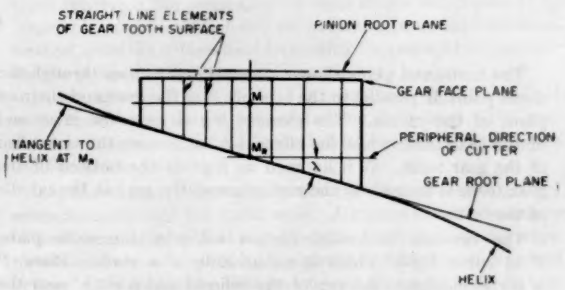

Fig. 1

Most automotive gears are currently manufactured by the Formate[1] process which also produces gear sets that are practically conjugate. However, with the Formate process which uses conical gear tooth surfaces, the method of obtaining practical conjugacy is less direct. It involves substantial differences between the imaginary generating gear for the pinion and the mating gear itself. These differences are achieved by modification in the machine set up for the pinion.

With the Helixform process, the surfaces of the gear teeth are basically involute helicoids. As such they are made up of straight line elements and are ruled, developable, synclastic surfaces. Involute helicoidal gear tooth surfaces can also be thought of as being made up of an infinite series of helices in the longitudinal direction. With Helixform gears, the helices of the tooth surfaces are slightly inclined to the peripheral direction of the cutter by the lead angle λ. This is illustrated in Fig. 1 which is a schematic representation of the gear tooth surface as seen from the center of the gear tooth space. M is the central or mean point where spiral angles and pressure angles are specified. M_R is the root mean point and lies directly below M in a direction perpendicular to the face plane of the gear. The lead L of the helicoidal gear tooth surface is chosen so that the root helix is tangent to the root plane direction at point M_R. The straight line elements of the gear tooth surface are perpendicular to the trace of the gear face plane with the drawing plane.

Fig. 2 is a three-dimensional representation of the involute helicoidal gear tooth surface and the conical surface which is the surface of the cutter used to generate the mating pinion. The straight dotted lines represent the straight line elements of the conical pinion cutter and adjacent to each is shown a straight line element of the gear tooth surface.

[1] Registered trade mark.

Contributed by the Machine Design Division and presented at the Annual Meeting, Atlantic City, N. J., November 29–December 4, 1959, of THE AMERICAN SOCIETY OF MECHANICAL ENGINEERS.

NOTE: Statements and opinions advanced in papers are to be understood as individual expressions of their authors and not those of the Society. Manuscript received at ASME Headquarters, August 13, 1959. Paper No. 59—A-90.

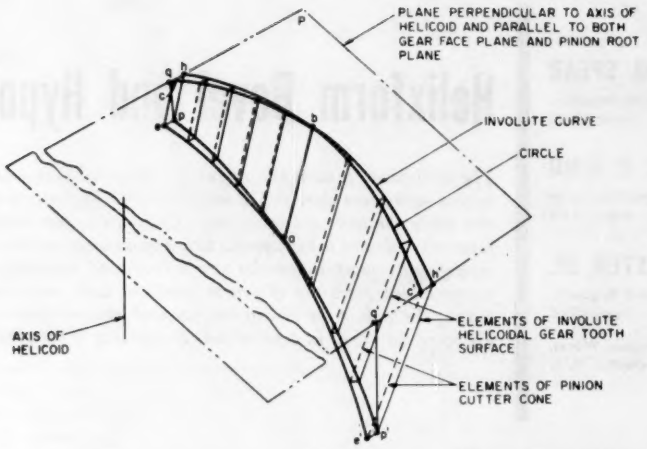
PLANE PERPENDICULAR TO AXIS OF HELICOID AND PARALLEL TO BOTH GEAR FACE PLANE AND PINION ROOT PLANE
INVOLUTE CURVE
CIRCLE
ELEMENTS OF INVOLUTE HELICOIDAL GEAR TOOTH SURFACE
ELEMENTS OF PINION CUTTER CONE
AXIS OF HELICOID

Fig. 2

The horizontal plane shown is considered to pass through the mean point M parallel to the face plane of the gear and the root plane of the pinion. The element h-p is near the inner end of the gear teeth while the element h'-p' is near the outer end of the gear teeth. A helix such as p-p' at the bottom of the gear teeth is tangent to the root plane of the gear at the middle of the teeth.

The involute helicoidal surface h-h'-p'-p intersects plane P in curve h-p-h' which is an involute of a circle. Plane P is perpendicular to the axis of the helicoid and point p' near the outer tooth end has a greater negative elevation from P than point p which is at the inner end of the teeth.

The conical surface of the pinion cutter c-c'-e'-e intersects plane P in the circle c-c'. The axis of the pinion cutter is usually parallel to the axis of the helicoid and perpendicular to plane P.

At the middle of the tooth, the element of the pinion cutter cone coincides with the element of the involute helicoid. At the ends there is shown the separation between the surfaces which is required for lengthwise mismatch.

Cutting the Helixform Gear Tooth Surface

The helicoidal gear tooth is produced by face-mill cutters such as shown in Fig. 3. Indexing of the work is done when a gap in the cutter is in a position to permit the work to be turned on its axis. The index gap of the cutter usually includes three blade pitches, and the cutters contain both outside cutting blades and inside cutting blades alternately spaced. A concave tooth surface and a convex tooth surface which are the two sides of the tooth slot are finished with each turn of the cutter. As each blade of the Helixform cutter passes through the tooth slot, the cutter is advanced axially and then returned before entry of the subsequent blade. The cutters producing the gear tooth surface thus have combined rotational and reciprocating motion. The reciprocating motion which is a function of the rotation can be represented by the following equation during the cutting portion of the cycle

$$X = LK\theta \tag{1}$$

where

X = axial position of cutter spindle
L = lead of helicoid
K = constant
θ = angle through which spindle is rotated

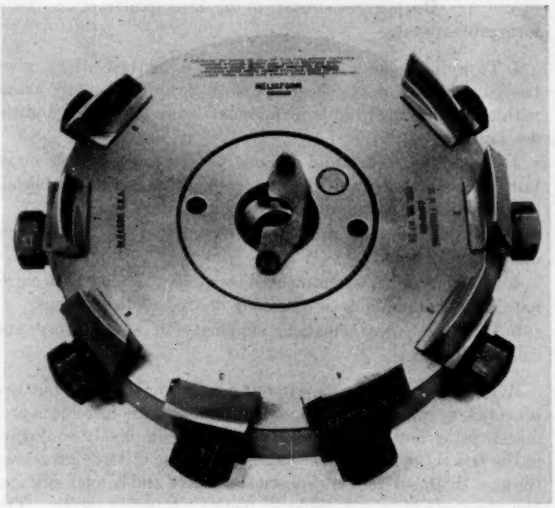

Fig. 3 Helixform gear finishing cutter

It can be seen from equation (1) that the velocity of the axial motion is uniform and equal to the constant LK. A straight cutting edge lying in a plane tangent to the base cylinder, as shown in Fig. 4, sweeps out an involute helicoid when given this type of motion. The involute curve illustrated in Fig. 4 which is the intersection of the involute helicoid and the plane of rotation of the cutter can be considered to unwind from the base circle shown. The axis of the cutter is, of course, the axis of the helicoid and the axis of the base circle and the base cylinders.

The base cylinders for the two sides of the teeth are slightly different in diameter and the involute curves unwind from them in opposite directions.

Cutting the Pinion Tooth Surface

The Gleason 116 Generator and the 106 Generator are used to finish Helixform pinions. With these machines the cradle carrying the cutter represents the mating gear. A tilting cutter spindle and swiveling housing permit the conical pinion cutter to be positioned in space so that it is tangent to the imaginary mating gear surface at the middle of the teeth exactly as illustrated in Fig. 2. The axis of the pinion cutter is usually parallel to the axis of the involute helicoidal gear tooth surfaces.

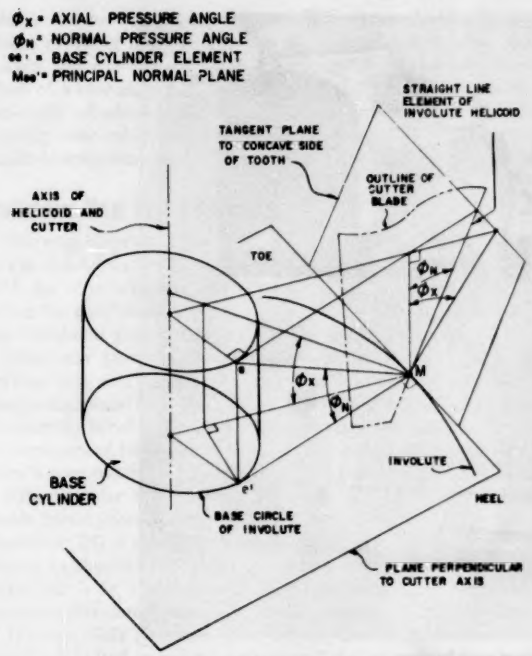

Fig. 4 Involute base cylinder and principal normal plane

The pinion is usually placed in space in exactly the position it would occupy if it were to mesh with the imaginary mating gear. The cradle and workpiece are turned about their respective axes with uniform velocities proportional to the numbers of teeth.

Since the straight line element of the pinion cutter cone coincides with the straight line element of the gear tooth surface at the middle of the face, the pinion teeth are free from bias and except for the lengthwise mismatch are conjugate to the gear teeth. The gear and pinion are thus *practically conjugate.*

Mathematics and Machine Setup

The basic mathematics of machine setup and surface curvature of the involute helicoid is found in the Appendix. The fundamental co-ordinates of the cutters relative to the gear and pinion are shown. From the fundamental cutter co-ordinates, the actual machine setup may be derived.

Design of Blanks for Helixform Cutting

Blanks used for Helixform cutting are exactly the same as those designed for the Formate process. Spiral angles and pressure angles are maintained very close to the corresponding values for Formate gears.

Helixform Tooth Bearings

The customary and very practical way of judging the contact of gear teeth is by observing the tooth bearing, which is the pattern produced in a marking compound on the tooth surfaces when the gears run together. In order to accurately interpret these patterns it is necessary to understand something about how they are produced.

Fully conjugate gear teeth contact at any instant along an oblique line of contact which moves across the surfaces as rotation progresses. Under load, of course, a line of contact spreads out to become a band of finite width, but its direction is substantially unchanged. Under very light load with a marking compound the line of contact can be observed, and also appears to have a finite width, due chiefly to the grain size of the marking material; as rotation progresses the marking progresses across the entire meshing areas, and we see a "full tooth bearing."

If the teeth of one member of this conjugate pair are modified so that the surface is unchanged along a specified line but is eased-off in a continuous manner on each side of this line, we have "singly mismatched" teeth. Correct motion will continue to be transmitted by point contact, the point moving along the unaltered line in the tooth surface. The contact mark which appears on the tooth will not however be a point, but an elongated ellipse with its major axis substantially in the direction of the original lines of contact. The dimensions of such a contact mark may be estimated by assuming that marking will fade out when the theoretical separation between the surfaces exceeds 0.00025 in.

Fig. 7 illustrates two cases of singly mismatched teeth. In one case the path of the contact points is essentially along the profile; the contact marks are shown as dotted ellipses, and the tooth bearing is the summation of these marks and is seen to be "square." This condition results naturally from the Helixform method, since the cutters used for cutting the gear and for generating the pinion have a common element.

In the right-hand part of Fig. 7 is seen a case where the path of contact, and hence the entire tooth bearing, is inclined. This condition is known as "bias." Control of bias comes naturally with the Helixform method.

It is also of great importance to observe the tooth bearing when contact occurs near the tooth ends. A square central bearing is in itself no guarantee that a good contact will be obtained when mounting errors or applied loads cause the contact to shift to heel or toe. It is customary therefore to run the gears with slightly altered shaft offset (V) and pinion axial position (H) in such combination that the bearing can be observed near the tooth ends. The amount of displacement required is a measure of the amount of mismatch, and the V/H ratio is an indication of the kind of adjustability it provides.

Helixform pairs show a square bearing at toe and heel under the V-and-H check, both as calculated and as seen on the testing machine. There is however a difference in length of bearing from toe to heel, the heel bearing being ordinarily the shorter. This difference is caused by the changing curvature of the involute helicoid as shown in Fig. 2, and can be compensated if desired by using a nonuniform lead on the gear as previously mentioned. Fig. 8 shows the relative lengths of the bearings at toe and heel before and after modification. The desired relationship for a particular installation depends largely on the nature of the deflections under load, and it is seldom sufficient to simply compensate for the theoretical third-order component of the involute.

It has been found that the bearings at toe and heel are not only square but that motion transmission remains uniform, even though the gears are actually being operated substantially out of their correct position. A typical extreme rotational error is 0.00005 in.; and this is of such a nature as to simply constitute a minute amount of profile mismatch.

The Helixform Gear Finishing Machine

Gears are finished on the Gleason No. 112 Hypoid Helixform Gear Finisher, which is shown in Fig. 5. The cutter head assembly of this machine is illustrated in Fig. 6. A stroke cam transmits axial motion to the cutter spindle by means of an adjustable hardened steel guide plate which can be set to deliver from 0 to 58 per cent of the cam motion.

The work head and cutter head are mounted on a combination of ways to permit both vertical and horizontal adjustments with respect to one another. The work head can also be rotated about

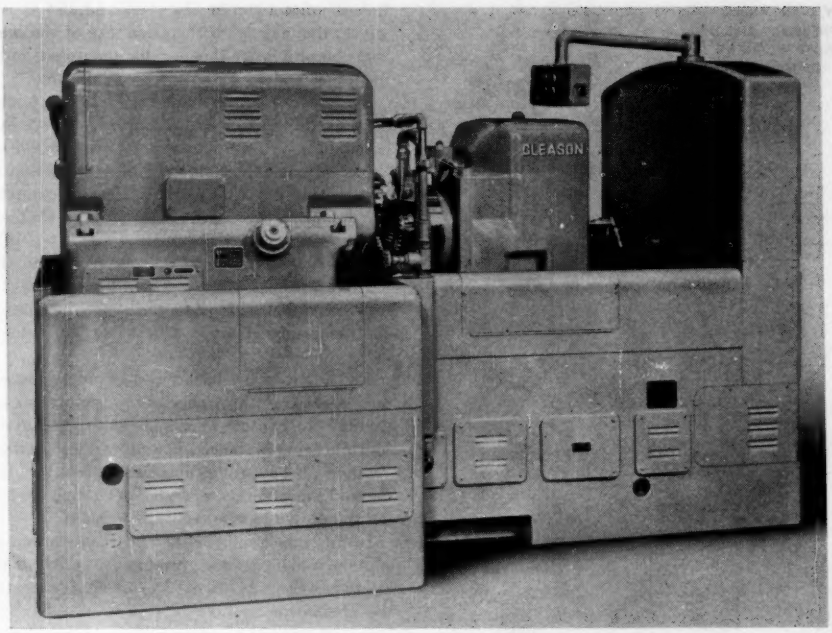

Fig. 5 No. 112 Helixform gear finisher

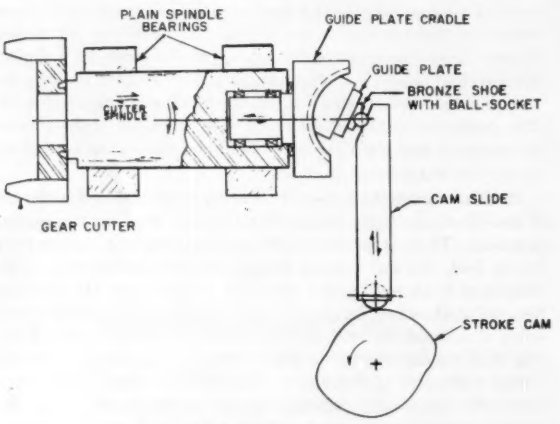

Fig. 6 Cutter head mechanism

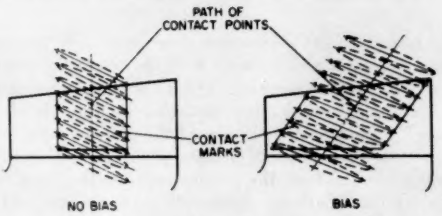

Fig. 7

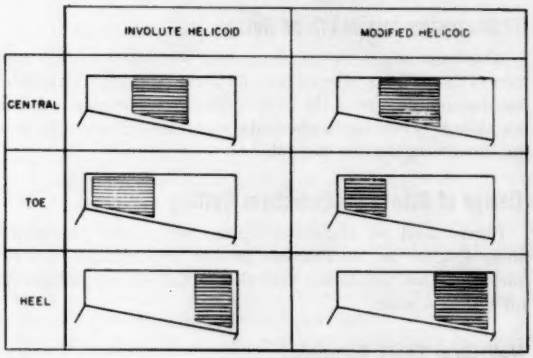

Fig. 8

a vertical axis to make a root angle setting. Hydraulic clamps automatically lock this head to the frame when it is in the cutting position.

Rapid indexing of the work is accomplished by using a plate-type indexing mechanism having a modified Geneva driver. The work spindle is unclamped before the beginning of the index cycle by a cam-actuated hydraulic system. Immediately after completion of the index cycle the spindle is again clamped to insure maximum rigidity during cutting and to reduce forces transmitted to the index mechanism.

Helixform Gear Roughing

A companion machine to the gear finishing machine roughs gears in a manner similar to Formate gear roughing. The cutter consists of alternate side and bottom cutting blades and is fed by a cam motion in the direction of the cutter axis until the full depth position is reached. Since gear roughing can be done at speeds that are comparable to gear finishing, the combination of a roughing and finishing machine readily lends itself to automation.

A rigid machine construction combined with a large volume of coolant flow through pipes directed behind and in front of the area of cutting help to increase production capacity as much as 50 per cent.

Helixform Pinion Roughing

Pinions are roughed by the ratio change method with which the convex side of the teeth are cut on the up roll and the concave

side on the down roll. An automatic set-over mechanism in the pinion roughing machine changes the ratio of roll between the convex and concave sides which produces the secondary taper effect of a change of generating pressure angle. This method is especially effective with the Helixform process since bias is initially removed in the gear and it is therefore now possible to rough pinions close to the finished tooth surface.

Helixform Gear Finishing Cutter

The angular pitch of the blades of the ten-stroke cutter shown in Fig. 3 is 36 deg. There are four inside and four outside blades with the remaining space being used as the index gap through which the gear blank is rotated. The blades are stepped in both the radial and axial direction to take a precalculated chip load.

Helixform gear cutters are sharpened in the conventional manner with only a side rake angle. The cutter blade surface and sharpening plane intersect to form the cutting edge necessary to produce the involute helicoid. The difference between the radius of curvature of the involute helicoid in the axial and normal sections is very small. A typical 9-in. OD automotive gear cut with a 9-in. diameter cutter having 28-deg outside blade and 10-deg inside blade pressure angles requires a lead of about 2.5 inch. Equation (70) of the Appendix shows that the radius of curvature for the axial section of the drive side is 65×10^4 inches while the coast side is 11×10^3 inches. The curvature of the helicoidal surface is therefore insensitive to small errors in cutter sharpening.

Inserted blade Helixform gear cutters have large blade shanks which are bolted in ground slots around the periphery of a thick cutter head. A center clamping screw is used to secure the cutter on the spindle and to eject the cutter evenly and rapidly when used with an ejection plate.

Helixform Stroke Cam

The stroke cam is designed with two lead and return paths (Fig. 6) and rotates five times for each revolution of the cutter. The proportion of lead to return path is approximately 3 to 1 which means that the maximum angular face width of the gear which can be cut is about 27 deg. Since the stroke cam has a timed relationship with the cutter, one lead path is always used to cut the coast side of the gear and the other lead path the drive side. This is an important feature of the cam design if it is decided to modify one or the other lead path to suit individual axle deflections and hardening distortions.

The involute of a circle, which is the intersection of the gear tooth surface and plane perpendicular to the cutter axis, is shown in Figs. 2 and 4. The conical cutter surface, which cuts the mating pinion tooth, intersects the reference plane in a circle which is tangent to the involute curve at the middle of the tooth. Since the radius of curvature of the involute changes lengthwise along the curve it is apparent that the tooth bearing will be longer at the toe end than at the heel. Should it be desirable to change the radius of curvature at the toe and heel to equalize the bearing lengths or to make the heel bearing longer than the toe bearing, then the stroke cam path must be modified. This can be done by the addition of a third-order change. The equation of the cutter axial motion would then become

$$X = LK\theta + LK_1\theta^3 \qquad (2)$$

The slope of this curve becomes the same as the slope of the curve of equation (1) when $\theta = 0$. This means that when the modification is small the central bearing at $\theta = 0$ would remain unchanged.

Modified and unmodified tooth bearings are described in a prior section.

The third-order change can be made on either the drive or coast sides, or both, depending on the requirements of a particular job. It has been found by trial that only two or three different cam modifications are sufficient to suit the range of gears which the machine can cut.

Conclusion

The Helixform method of producing gears is flexible in that it permits any of the conventional modifications in tooth shape necessary to compensate for heat-treatment and mounting deflections under load. Because of the mathematical correctness these modifications can be made without introducing undesirable secondary effects. Bearings remain substantially square whether placed at the toe or heel, permitting greater adjustment tolerances.

Gear finishing methods such as burnishing and lapping are readily adapted to Helixform gears. Burnishing gears are easily developed and because they can be made conjugate to the pinion, produce a completely burnished pinion tooth surface. The involute helicoid tooth surface of the gear is lapped by conventional lapping methods and usually requires less lapping time because of the exactness of the soft tooth-bearing development.

Helixform gears cut on the new Helixform Gear Finishing Machine combine the practical advantages of the involute helicoid tooth surface with increased production to produce gears of higher quality at decreased costs.

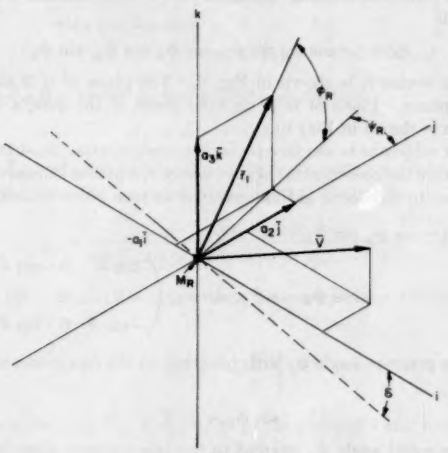

Fig. 9

APPENDIX

Symbols and Notation

The relationships which follow are treated in vector and matrix notation; the co-ordinate system used has right-handed orientation and is shown in Fig. 9.

In Fig. 9, $\bar{\imath}$, $\bar{j}$, $\bar{k}$ are unit vectors in the directions of the positive x, y, and z-axes. The "bar" superimposed will always designate a vector quantity. Thus $\bar{V}$ is a vector.

$\bar{V} = d_1\bar{\imath} + d_2\bar{j} + d_3\bar{k}$, where d_1, d_2, d_3 are the scalar magnitudes of the components of $\bar{V}$ in the $\bar{\imath}$, $\bar{j}$, $\bar{k}$-directions.

When convenient the vector $\bar{V}$ will also be written in row matrix form

$$\bar{V} = (d_1, d_2, d_3)$$

Omission of the bar will indicate a scalar quantity, thus V is the magnitude of vector $\bar{V}$, and so on.

Mathematics

The following equations give the basic machine setup for the gear and for the concave side of the pinion. See glossary for definitions of terms and symbols.

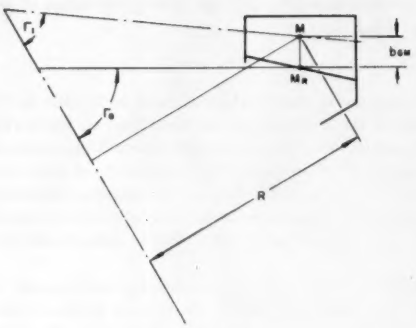

Fig. 10

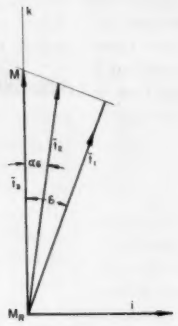

Fig. 11

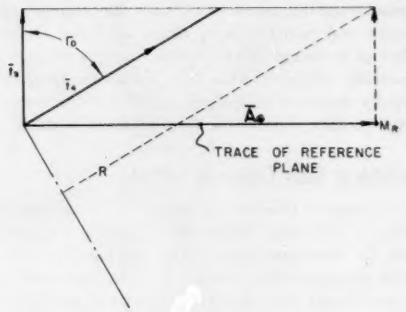

Fig. 12

Spiral Angle and Pressure Angle of Gear Referred to Face Plane of Gear. The angle between the face plane and the root plane of the gear, is

$$\delta = \Gamma_0 - \Gamma_R \tag{3}$$

A unit vector in the direction of the normal to the convex gear tooth surface, treating the gear as a conventional Formate gear is

$$\bar{r}_1 = (-\cos\phi_R \sin\psi_R, \cos\phi_R \cos\psi_R, \sin\phi_R) \tag{4}$$

The vector $\bar{r}_1$ is shown in Fig. 9. The plane of $\bar{i}\bar{j}$ is the gear root plane. Plane of $\bar{i}\bar{k}$ is an axial plane of the gear, a view of which is shown in Fig. 10.

For reference to the face plane, a transformation must be made to obtain the co-ordinates of unit vector $\bar{r}_2$ which is the unit vector normal to the tooth surface referred to face plane co-ordinates

$$\bar{r}_2 = (-\cos\phi_R \sin\psi_R, \cos\phi_R \cos\psi_R, \sin\phi_R) \begin{pmatrix} \cos\delta & 0 & \sin\delta \\ 0 & 1 & 0 \\ -\sin\delta & 0 & \cos\delta \end{pmatrix} \tag{5}$$

The pressure angle ϕ_f with reference to the face plane is given by

$$\sin\phi_f = \bar{r}_2 \cdot \bar{k} \tag{6}$$

The spiral angle ψ_f referred to the face plane is given by

$$\tan\psi_f = \frac{-\bar{r}_2 \cdot \bar{i}}{\bar{r}_2 \cdot \bar{j}} \tag{7}$$

The angle α_G is the difference between gear face angle and gear pitch angle

$$\alpha_G = \Gamma_0 - \Gamma_1 \tag{8}$$

The distance b_{GM} from mean point of reference M to the gear root plane may be obtained from the equation

$$\bar{l}_1 \cdot \bar{l}_2 = \bar{l}_1 \cdot \bar{l}_3 \quad \text{(see Fig. 10)} \tag{9}$$

See Figs. 10 and 11, where

$$\bar{l}_1 = \sin\delta\bar{i} + \cos\delta\bar{k} \tag{10a}$$

$$\bar{l}_2 = b_G \sin\alpha_G\bar{i} + b_G \cos\alpha_G\bar{k} \tag{10b}$$

$$\bar{l}_3 = b_{GM}\bar{k} \tag{10c}$$

A plane through the root mean point M_R parallel to the gear face plane is taken as a plane of reference. See Figs. 12 and 10.

The point of intersection of this datum plane and the gear axis is taken as a co-ordinate center for machine setup.

The magnitude A_G of vector $\bar{A}_G$ may be obtained from the equation $(\bar{A}_G + \bar{l}_3)\cdot\bar{l}_4 = R$

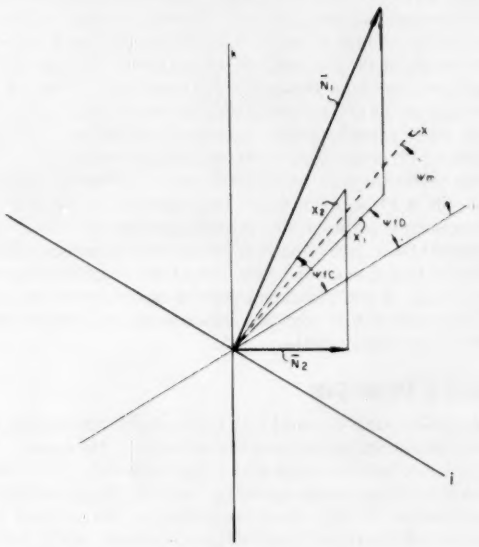

Fig. 13

where $$\bar{l}_4 = \sin\Gamma_0\bar{i} + \cos\Gamma_0\bar{k}. \tag{11}$$

$$A_G = \frac{R}{\sin\Gamma_0} - \frac{b_{GM}}{\tan\Gamma_0} \tag{12}$$

Equations (6) and (7) yield two values of ϕ_f and ψ_f, a set of values for the convex gear tooth surface and another set of values for the concave tooth surface treating the gear as a Formate gear. Fig. 13 shows the normal to the convex gear tooth surface $\bar{N}_1$ and the normal to the concave tooth surface $\bar{N}_2$. The plane of $\bar{i}$, $\bar{j}$ is parallel to the gear face plane. Lines X_1 and X_2 are the projections of the normals to the face plane and are inclined to the positive direction of the $\bar{j}$-axis by angles ψ_{fD} and ψ_{fC}, respectively. The line X is inclined to the $\bar{j}$-axis by the angle ψ_M where $\psi_M = {}^1/_2(\psi_{fD} + \psi_{fC})$. The plane P_1, determined by X and $\bar{k}$, contains the axis of the Helixform cutter. Usually, the axis of the Helixform gear cutter is inclined to $\bar{k}$ by an angle $\Delta\phi_G$ as illustrated in Fig. 15. We thus produce a Helixform gear close to the equivalent Formate gear in pressure angle and spiral angle at the mean point.

Machine Setup for Gear. The axial pressure angle of the helicoidal tooth sides are somewhat arbitrarily chosen and are designated by ϕ_x. These axial pressure angles are referred to the plane of rotation of the cutter, that is, to the plane perpendicular to the axis of the helicoid. Angle $\Delta\phi_G$ is given by the equation,

$$\Delta\phi_G = \phi_x - \phi_f \tag{13}$$

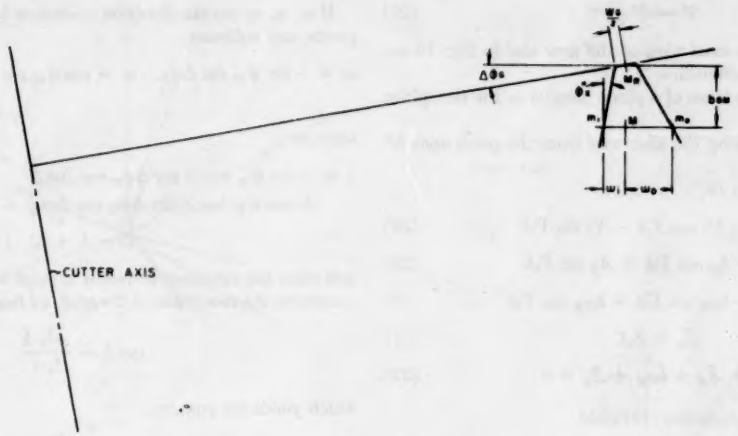

Fig. 14

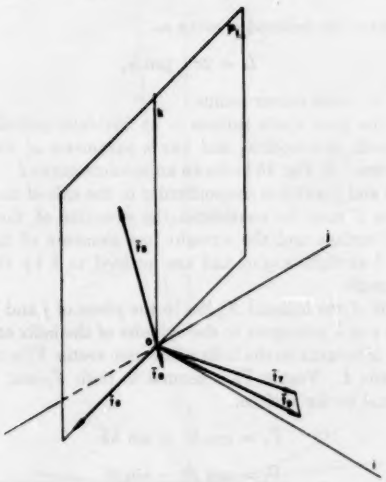

Fig. 15

The axial pressure angle of the helicoid referred to the face plane is then

$$\phi_x'' = \phi_x - \Delta\phi_G \qquad \text{(see Fig. 14)} \tag{14}$$

In Fig. 24, page 11, the datum plane through M_R is the plane of $\bar{\imath}$ and $\bar{j}$ and the plane of $\bar{\imath}$ and $\bar{k}$ contains the cutter axis.

We may write the radius vector of the cutter as

$$\bar{r} = (-r, 0, 0) \tag{15}$$

the and vector from M_R to 0 as

$$\bar{A}_G = (-A_G \sin \psi_M, -A_G \cos \psi_M, 0) \tag{16}$$

A unit vector in the direction of the gear axis is

$$\bar{x}_0 = (\cos \Gamma_0 \sin \psi_M, \cos \Gamma_0 \cos \psi_M, \sin \Gamma_0) \tag{17}$$

Since the cutter axis is inclined to $\bar{k}$ by $\Delta\phi_G$ we apply a rotational matrix to get

$$\bar{x}' = (\cos \Gamma_0 \sin \psi_M, \cos \Gamma_0 \cos \psi_M, \sin \Gamma_0) \begin{pmatrix} \cos \Delta\phi_G & 0 & -\sin \phi\Delta_G \\ 0 & 1 & 0 \\ \sin \Delta\phi_G & 0 & \cos \Delta\phi_G \end{pmatrix} \tag{18}$$

and

$$\bar{A}_{G'} = (-A_G \sin \psi_M, -A_G \cos \psi_M, 0) \begin{pmatrix} \cos \Delta\phi_G & 0 & -\sin \Delta\phi_G \\ 0 & 1 & 0 \\ \sin \Delta\phi_G & 0 & \cos \Delta\phi_G \end{pmatrix} \tag{19}$$

If $\Delta\bar{X}_M$ is a vector in the direction of $\bar{x}'$, then

$$\bar{A}_z = \bar{A}_{G'} - \Delta X_M \cdot \bar{x}' \tag{20}$$

If $\Delta\bar{X}_M$ is of magnitude sufficient to make vector $\bar{A}_z$ lie in plane of $\bar{\imath}$ and $\bar{j}$, then the $\bar{k}$ component of $\bar{A}_z = 0$ whence

$$\Delta X_M = \frac{-A_G \sin \psi_M \sin \Delta\phi_G}{\cos \Gamma_0 \sin \psi_M \sin \Delta\phi_G - \sin \Gamma_0 \cos \Delta\phi_G} \tag{21}$$

The projection of the gear axis to the $\bar{\imath}$ and $\bar{j}$-plane is inclined to j by ψ_z where

$$\tan \psi_z = \frac{\bar{x}' \cdot \bar{\imath}}{\bar{x}' \cdot \bar{j}} \tag{22}$$

The inclination Γ_M of vector $\bar{x}'$ to the plane of $\bar{\imath}$ and $\bar{j}$ is given by

$$\sin \Gamma_M = \bar{x}' \cdot \bar{k} \tag{23}$$

The angle of inclination of the gear axis to the plane perpendicular to the cutter axis is the angle Γ_M. This is a machine setting known as the machine root angle.

The vectors $\bar{r}$ and $\bar{A}_z$ are coplanar since $\bar{r}$ always lies in plane of $\bar{\imath}$ and $\bar{j}$.

In Fig. 25 if the co-ordinate center be taken at O_M, the radius vector to the cutter center is $\bar{S}$ where

$$\bar{S} = \bar{r} - \bar{A}_z = (b_1, b_2, b_3) \tag{24}$$

In the machine setup the axis of the work must lie in the plane of $\bar{\imath}$ and $\bar{k}$ so we apply a rotational matrix to get

$$\bar{S}' = (b_1, b_2, b_3) \begin{pmatrix} \sin \psi_z & -\cos \psi_z & 0 \\ \cos \psi_z & \sin \psi_z & 0 \\ 0 & 0 & 1 \end{pmatrix} \tag{25}$$

whence the horizontal co-ordinate in the number 112 machine is

$$H = \bar{S}' \cdot \bar{\imath} \tag{26}$$

and the vertical co-ordinate is

$$V = \bar{S}' \cdot \bar{j} \tag{27}$$

In Fig. 18 is shown an axial view of the gear and in Fig. 19 are shown the vector relationships.

The line $O\text{-}M_R$ is the trace of a plane parallel to the face plane through M_R.

Z_x is the distance along the gear axis from the pitch apex O' to the point O.

From vector diagram 19,

$$\bar{V}_1 = -V_1 \cos \Gamma_1 \bar{\imath} - V_1 \sin \Gamma_1 \bar{k} \tag{28}$$

$$\bar{A}_G = A_G \cos \Gamma_0 \bar{\imath} + A_G \sin \Gamma_0 \bar{k} \tag{29}$$

$$\bar{b}_{GM} = -b_{GM} \sin \Gamma_0 \bar{\imath} + b_{GM} \cos \Gamma_0 \bar{k} \tag{30}$$

$$\bar{Z}_x = Z_x \bar{\imath} \tag{31}$$

$$\bar{V}_1 + \bar{A}_G + \bar{b}_{GM} + \bar{Z}_x = 0 \tag{32}$$

These equations and equation (12) yield

$$Z_x = R \operatorname{ctn} \Gamma_1 + \frac{b_{GM}}{\sin \Gamma_0} - \frac{R}{\tan \Gamma_0} \tag{33}$$

Z_x is the distance along the gear axis from the pitch apex to the intersection of the datum plane.

The basic machine settings for the gear are

horizontal	H
vertical	V
machine root angle	Γ_M
machine center to back	X_M

where

$$X_M = \text{mounting distance of gear} + Z - Z_x + \Delta X_M \tag{34}$$

Lead and Surface Curvature Relationships. Fig. 14 shows an axial section of the gear cutter in the plane P_1, the plane of xk, Fig. 13.

The points of intersection m_o and m_i of the gear cutter and a plane through M parallel to the face plane are at distance w from M where,

$$w = \frac{W_G \cos \Delta\phi_G}{2} + \left(b_{GM} - \frac{W_G}{2} \sin \Delta\phi_G \right) \tan \phi_x'' \tag{35}$$

The distances of points m_o and m_i from the center of the cutter point width measured in a radial direction are

$$\Delta r = w \cos \Delta\phi_G + b_{GM} \sin \Delta\phi_G \tag{36}$$

Fig. 15, also, shows plane P_1. The unit vector $\bar{l}_5$ is parallel to the gear cutter axis and lies in plane P_1. The angle between unit vector $\bar{l}_5$ and unit vector $\bar{k}$ is $\Delta\phi_G$.

The unit vector $\bar{l}_6$ is collinear with the intersection of plane P_1 and the plane of $\bar{\imath}$ and $\bar{j}$.

$$\bar{l}_7 = \bar{l}_5 \times \bar{l}_6. \text{ The magnitude } l_7 \text{ is } \cos \Delta\phi_G. \tag{37}$$

If $\bar{l}_7$ be taken as proportional to an infinitesimal peripheral movement of a point on the cutter blade, then, since this point has helical motion about the cutter axis, there is an axial advance related to the peripheral motion.

If vector $\bar{l}_8$ represents the axial advance, the magnitude

$$t_8 = t_7 \tan \lambda. \tag{38}$$

Since $\bar{l}_5$ and $\bar{l}_8$ are collinear,

$$\bar{l}_5 \times \bar{l}_8 = 0 \tag{39}$$

$$\bar{l}_5 = \sin \Delta\phi_G \sin \psi_M \bar{\imath} - \sin \Delta\phi_G \cos \psi_M \bar{j} + \cos \Delta\phi_G \bar{k} \tag{40}$$

$$\bar{l}_6 = \sin \psi_M \bar{\imath} - \cos \psi_M \bar{j} \tag{41}$$

If a_1, a_2, a_3 are the direction cosines of $\bar{l}_8$, since $\bar{l}_5$ and $\bar{l}_8$ are opposite and collinear,

$$a_1 = -\sin \psi_M \sin \Delta\phi_G, \quad a_2 = \cos \psi_M \sin \Delta\phi_G, \quad a_3 = -\cos \Delta\phi_G \tag{42}$$

whence

$$\bar{l}_8 = -\sin \psi_M \tan \lambda \sin \Delta\phi_G \cos \Delta\phi_G \bar{\imath} + \cos \psi_M \tan \lambda \sin \Delta\phi_G \cos \Delta\phi_G \bar{j} - \tan \lambda \cos^2 \Delta\phi_G \bar{k} \tag{43}$$

$$\bar{l}_9 = \bar{l}_7 + \bar{l}_8 \tag{44}$$

and since the terminus of vector $\bar{l}_9$ must lie in a plane through j parallel to the root plane of the gear, we have

$$\tan \delta = \frac{-\bar{l}_9 \cdot \bar{k}}{\bar{l}_9 \cdot \bar{\imath}} \tag{45}$$

which yields the equation

$$\tan \lambda = \frac{\tan \delta \cos \psi_M}{\cos \Delta\phi_G + \tan \delta \sin \psi_M \sin \Delta\phi_G} \tag{46}$$

The lead of the helicoid is taken as

$$L = 2\pi r_c \tan \lambda, \tag{47}$$

where r_c = mean cutter radius.

When the gear tooth surface is an involute helicoid it is of course ruled, developable, and has a parameter of distribution equal to zero. In Fig. 16 is shown an involute curve I lying in the plane of $\bar{\imath}$ and $\bar{j}$ which is perpendicular to the axis of the helicoid. The curve I may be considered the directrix of the involute helicoidal surface and the straight line elements of the surface intersect I at right angles and are inclined to $\bar{k}$ by the normal pressure angle.

The axis of the helicoid X_h lies in the plane of $\bar{j}$ and $\bar{k}$ and the plane of $\bar{\imath}$ and $\bar{k}$ is tangent to the cylinder of the helix at O. Unit vector $\bar{V}_1$ is tangent to the helix while unit vector $\bar{V}_2$ is tangent to the directrix I. Vector $\bar{V}_3$ is normal to both $\bar{V}_1$ and $\bar{V}_2$ and is thus normal to the surface.

$$\bar{V}_1 = \cos \lambda \bar{\imath} + \sin \lambda \bar{k} \tag{48}$$

$$\bar{V}_2 = \cos \beta \bar{\imath} - \sin \beta \bar{j} \tag{49}$$

$$\bar{V}_3 = \bar{V}_2 \times \bar{V}_1 \tag{50}$$

$$\tan \phi_x = \frac{\bar{V}_3 \cdot \bar{k}}{-\bar{V}_3 \cdot \bar{j}} = \frac{\tan \beta}{\tan \lambda} \tag{51}$$

If W is the angle between $\bar{V}_1$ and $\bar{V}_2$ then

$$\cos W = \bar{V}_1 \cdot \bar{V}_2 = \cos \lambda \cos \beta \tag{52}$$

and

$$\bar{V}_3 \cdot \bar{k} = V_3 \sin \phi_n \tag{53}$$

where

$$V_3 = \sin W = \sqrt{1 - \cos^2 \lambda \cos^2 \beta} \tag{54}$$

Equations (51) and (52) yield

$$\tan \phi_n = \tan \phi_x \cos \beta \tag{55}$$

In Fig. 16, vector $\bar{V}_4 = \bar{V}_3 \times \bar{V}_2$ lies in the principal direction of minimum principal curvature; that is, the vector $\bar{V}_4$ is collinear with the straight line element of the surface at O.

$\bar{V}_2$ is in the direction of maximum principal curvature.

If the minimum principal radius of curvature is designated by ρ_G then the radius of curvature r_I of the involute I is given by theorem of Meunier.

$$r_I = \rho_G \cos \phi_n \tag{56}$$

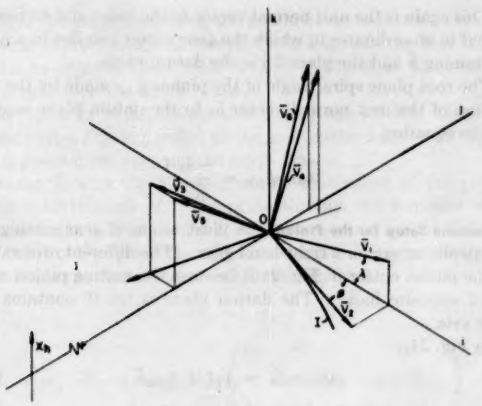

Fig. 16

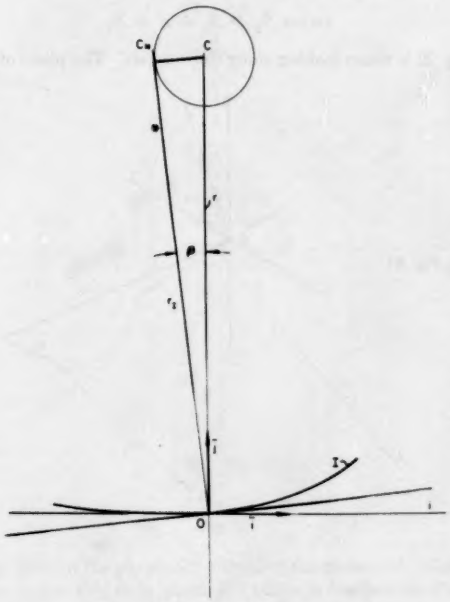

Fig. 17

From Fig. 17 it is seen that $r_I = r \cos \beta$ where r is the distance of the axis of the helicoid to point O. Hence

$$\rho_G = \frac{(r_c - \Delta r) \cos \beta}{\cos \phi_n} \tag{57}$$

Since $\bar{V}_1$ and $\bar{V}_2$ are unit vectors, an expression for the vector $\bar{V}_4$, which is collinear with the generatrix through O, may be written as

$$\bar{V}_4 = \bar{V}_3 \times \bar{V}_2 \tag{58}$$

and the magnitude

$$V_4 = V_3 = \sin W \tag{59}$$

See Fig. 16.

Vector $\bar{V}_6$ lies in the tangent plane to the surface at O and also in the plane of $\bar{j}$ and $\bar{k}$. Designating the vector $\bar{V}_6$ by

$$\bar{V}_6 = a_2\bar{j} + a_3\bar{k}, \tag{60}$$

since $\bar{V}_6$ is coplanar with $\bar{V}_1$ and $\bar{V}_2$, the scalar triple product

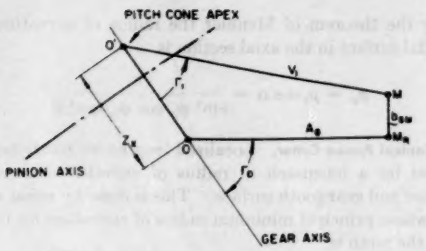

Fig. 18

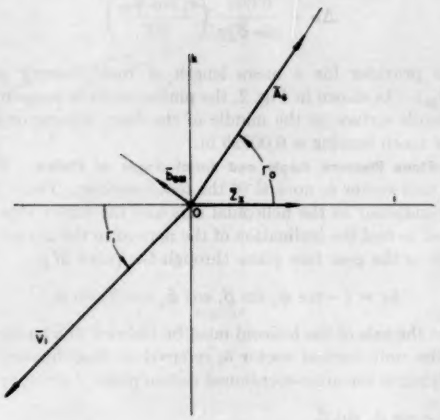

Fig. 19

$$\bar{V}_6 \cdot \bar{V}_1 \times \bar{V}_2 = 0 \tag{61}$$

Since $\bar{V}_6$ is a unit vector

$$a_2^2 + a_3^2 = 1 \tag{62}$$

Equations (61) and (62) yield the equations

$$a_2 = \sin \phi_x; \; a_3 = \cos \phi_x \tag{63}$$

which are the $\bar{j}$ and $\bar{k}$ components of unit vector $\bar{V}_6$

$$\bar{V}_5 = \bar{i} \times \bar{V}_6 \text{ is a unit vector normal to } \bar{V}_6 \tag{64}$$

From (51), (54), and (55)

$$\sin W = \frac{\cos \lambda \sin \beta}{\sin \phi_n} \tag{65}$$

The angle α between $\bar{V}_3$ and $\bar{V}_5$ is given by the equation

$$\bar{V}_3 \cdot \bar{V}_5 = V_3 \cos \alpha = \sin W \cos \alpha \tag{66}$$

which with (51) and (65) yields

$$\cos \alpha = \frac{\cos \beta \cos \phi_n}{\cos \phi_x} \tag{67}$$

Likewise the angle W_x between $\bar{V}_4$ and $\bar{V}_6$ may be determined from the equation

$$\sin W_x = -\bar{V}_6 \cdot \bar{V}_2 = \sin \phi_x \sin \beta \tag{68}$$

By the theorem of Euler, the radius of curvature in the plane of $\bar{V}_3$ and $\bar{V}_6$ is

$$\rho_i = \frac{r \cos \beta}{\cos \phi_n} \frac{1}{\sin^2 W_x} = \frac{r \cos \beta}{\cos \phi_n \sin^2 \phi_x \sin^2 \beta} \tag{69}$$

and by the theorem of Meunier the radius of curvature of the helicoidal surface in the axial section is

$$\rho_x = \rho_i \cos \alpha = \frac{r}{\sin^2 \phi_x \cos \phi_x \tan^2 \beta} \tag{70}$$

The Conical Pinion Cutter. Localized lengthwise tooth bearing is obtained by a mismatch in radius of curvature between pinion cutter and gear tooth surface. This is done by using a pinion cutter whose principal minimum radius of curvature for the drive side of the teeth is

$$\rho_p = \rho_G + \Delta\rho \tag{71}$$

where

$$\Delta\rho = \frac{0.002}{\cos \phi_{RP}} \left(\frac{r_c \cos \psi_M}{BF} \right)^2 \tag{72}$$

This provides for a mean length of tooth bearing of $BF/(\cos \psi_M)$. As shown in Fig. 2, the pinion cutter is tangent to the gear tooth surface at the middle of the face; separation at the ends of tooth bearing is 0.00025 in.

Root-Plane Pressure Angle and Spiral Angle of Pinion. Fig. 20 shows unit vector $\bar{n}_1$ normal to the tooth surface. The $\bar{\imath}$, $\bar{j}$-plane is perpendicular to the helicoidal axis and the cutter axis. It is required to find the inclination of the normal to the datum plane, parallel to the gear face plane through the point M_R

$$\bar{n}_1 = (-\cos \phi_n \sin \beta, \cos \phi_n \cos \beta, \sin \phi_n) \tag{73}$$

Since the axis of the helicoid must be inclined to $\bar{k}$ by the angle $\Delta\phi_G$, the unit normal vector $\bar{n}_2$ referred to co-ordinates with $\bar{\imath}$ and $\bar{j}$ lying in the afore-mentioned datum plane is given by

$$\bar{n}_2 = (-\cos \phi_n \sin \beta, \cos \phi_n \cos \beta, \sin \phi_n) \begin{pmatrix} 1 & 0 & 0 \\ 0 & \cos \Delta\phi_G & -\sin \Delta\phi_G \\ 0 & \sin \Delta\phi_G & \cos \Delta\phi_G \end{pmatrix} \tag{74}$$

This permits the determination of the normal pressure angle ϕ_{RP} of the helicoidal surface relative to the datum plane

$$\sin \phi_{RP} = \bar{n}_2 \cdot \bar{k} \tag{75}$$

ϕ_{RP} is the root-plane pressure angle of the pinion.

A further transformation of co-ordinates yields the vector

$$\bar{n}_3 = (-\cos \phi_n \sin \beta, \cos \phi_n \cos \beta, \sin \phi_n) \begin{pmatrix} 1 & 0 & 0 \\ 0 & \cos \Delta\phi_G & -\sin \Delta\phi_G \\ 0 & \sin \Delta\phi_G & \cos \Delta\phi_G \end{pmatrix} \begin{pmatrix} \cos \psi_M & \sin \psi_M & 0 \\ -\sin \psi_M & \cos \psi_M & 0 \\ 0 & 0 & 1 \end{pmatrix} \tag{76}$$

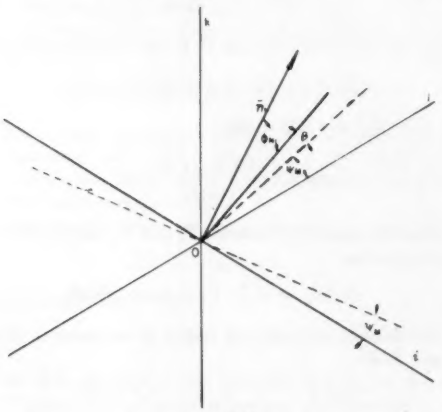

Fig. 20

This again is the unit normal vector to the helicoidal surface referred to co-ordinates in which the gear cutter axis lies in a plane containing $\bar{k}$ and the plane $\bar{\imath}$ $\bar{j}$ is the datum plane.

The root plane spiral angle of the pinion ψ_{RP} made by the projection of the unit normal vector $\bar{n}_3$ to the datum plane is given by the equation

$$\tan \psi_{RP} = \frac{-\bar{n}_3 \cdot \bar{\imath}}{\bar{n}_3 \cdot \bar{j}} \tag{77}$$

Machine Setup for the Pinion. In illustrations of gear cutting the setups shown are for a right-hand gear. The different orientation of the pinion cutter in Fig. 21 is because the mating pinion must be of opposite hand. The datum plane is iji, ik contains the gear axis.

In Fig. 21,

$$\text{vector } \bar{S}_2 = A_G \bar{\imath} + b_{GM} \bar{k} \tag{78}$$

$$\bar{w} = -w \sin \psi_M \bar{\imath} - w \cos \psi_M \bar{j} \tag{79}$$

$$\bar{S}_3 = -\rho_P \cos \phi_{RP} \sin \psi_{RP} \bar{\imath} - \rho_P \cos \phi_{RP} \cos \psi_{RP} \bar{j} - \sin \phi_{RP} \bar{k} \tag{80}$$

$$\text{vector } \bar{S}_K = \bar{S}_2 + \bar{w} + \bar{S}_3 \tag{81}$$

Fig. 22 is taken looking along the $-\bar{\imath}$ axis. The plane of $\bar{j}$, $\bar{k}$ is

Fig. 21

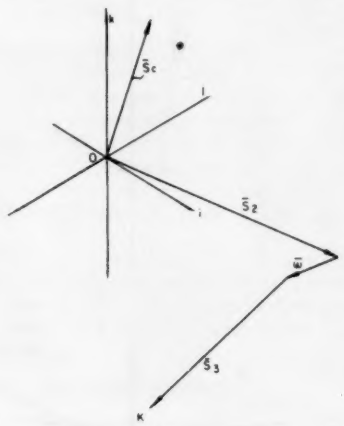

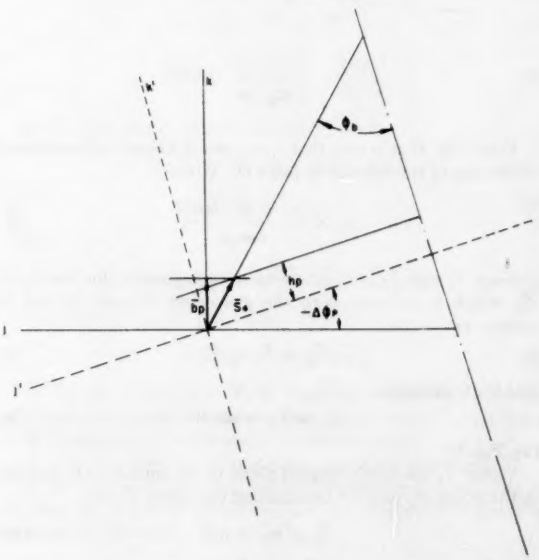

Fig. 22

taken as the plane containing the pinion cutter axis and $\bar{j}$ is taken as being parallel to the datum plane through M. In Fig. 22 the dotted co-ordinate lines show a C.W. rotation of co-ordinates about the $\bar{\imath}$ axis of amount $-\Delta\phi_P$.

The value of $-\Delta\phi_P$ is equal in magnitude to $\Delta\phi_G$ when the pinion cutter axis is parallel to the gear cutter axis; it is also in the opposite direction from the angle $\Delta\phi_G$.

Vector $\bar{S}_4$ is in the direction of a cone element of the pinion cutter cone through M. The plane through the terminus of $\bar{S}_4$ perpendicular to $\bar{k}$ is parallel to the datum plane and at distance b_P from M. The plane through the terminus $\bar{S}_4$ perpendicular to $\bar{k}'$ contains the tips of the pinion cutter blades.

$$\bar{S}_4 = -b_P \tan \phi_{RP}\bar{j} + b_P\bar{k} \tag{82}$$

$$\bar{S}_5 = (0, -b_P \tan \phi_{RP}, b_P)\begin{pmatrix} 1 & 0 & 0 \\ 0 & \cos\Delta\phi_P & -\sin\Delta\phi_P \\ 0 & \sin\Delta\phi_P & \cos\Delta\phi_P \end{pmatrix} \tag{83}$$

$$h_P = \bar{S}_6 \cdot \bar{k}$$

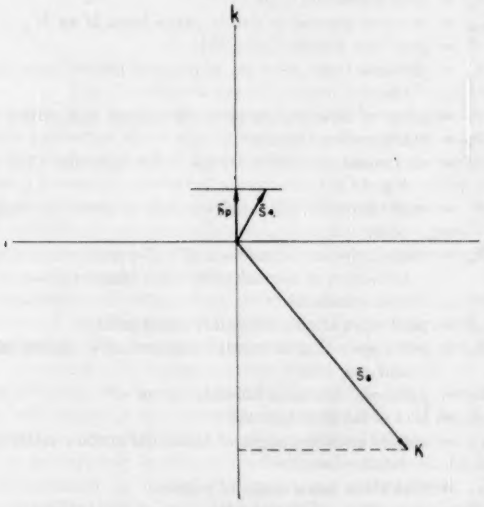

Fig. 23

Fig. 23 is for the purpose of obtaining the distance U_e along the pinion cutter axis from point K (which is the terminus of the normal vector $\bar{S}_3$, see Fig. 21) to the plane containing the pinion cutter blade tips. The magnitude of vector $\bar{S}_6$ is equal to the magnitude of vector $\bar{S}_3$, Fig. 21. The plane through the terminus of vector $\bar{h}_P$ perpendicular to $\bar{k}$ is the plane of the cutter blade tips.

$$U_e = -(\bar{S}_6 - \bar{h}_p)\cdot\bar{k} \tag{84}$$

where ϕ_b = blade angle and

$$\bar{S}_6 = -\rho_P \cos\phi_b\bar{\imath} - \rho_P \sin\phi_b\bar{k} \tag{85}$$

$$\bar{b}_p = b_p\bar{k} \tag{86}$$

Returning to Fig. 21, the vector $\bar{S}_e$ is of length U_e

$$\bar{S}_e = +U_e \sin\Delta\phi_P \sin\psi_m\bar{\imath} + U_e \sin\Delta\phi_P \cos\psi_m\bar{j} + U_e \cos\Delta\phi_P\bar{k} \tag{87}$$

The radius vector to the pinion cutter center is

$$\bar{S}_R = \bar{S}_K + \bar{S}_e \tag{88}$$

A transformation must be made on this vector to refer it to a co-ordinate system with $\bar{k}$ parallel to the cradle axis. The cradle axis is collinear with gear axis.

If from (88) $\quad \bar{S}_R = S_1\bar{\imath} + S_2\bar{j} + S_3\bar{k}, \tag{89}$

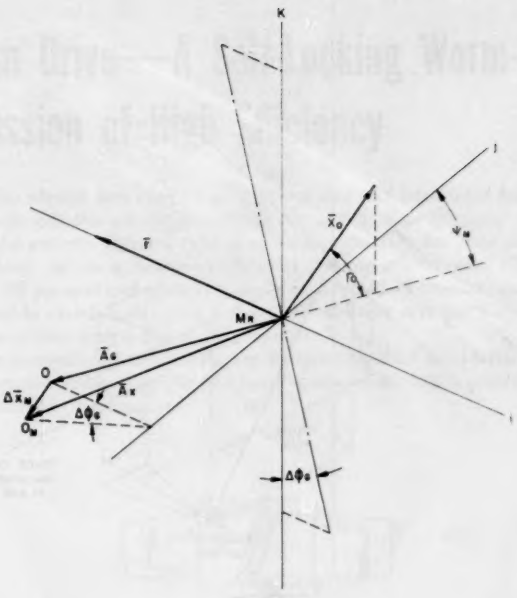

Fig. 24

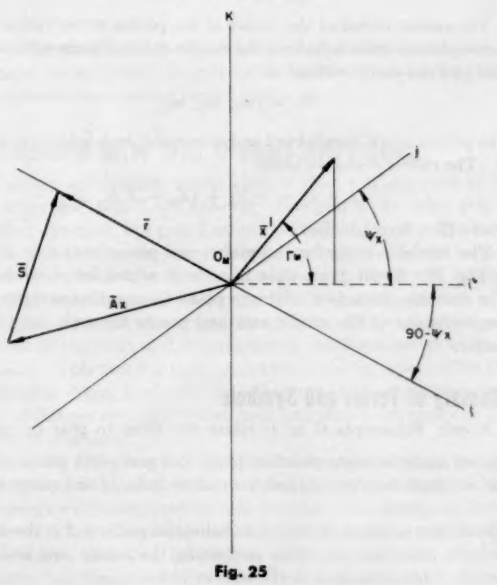

Fig. 25

after transformation

$$(m_1, m_2, m_3) = (S_1, S_2, S_3)\begin{pmatrix} \sin\Gamma_0 & 0 & \cos\Gamma_0 \\ 0 & 1 & 0 \\ -\cos\Gamma_0 & 0 & \sin\Gamma_0 \end{pmatrix} \tag{90}$$

The direction cosines of the unit vector $\bar{X}_e$ (parallel to $\bar{S}_e$ shown in Fig. 21) given by

$$(-\sin\Delta\phi_P \sin\psi_M, -\sin\Delta\phi_P \cos\psi_M, -\cos\Delta\phi_P)\begin{pmatrix} \sin\Gamma_0 & 0 & \cos\Gamma_0 \\ 0 & 1 & 0 \\ -\cos\Gamma_0 & 0 & \sin\Gamma_0 \end{pmatrix} \tag{91}$$

give the inclinations of the pinion cutter axis to the axes of the co-ordinate system.

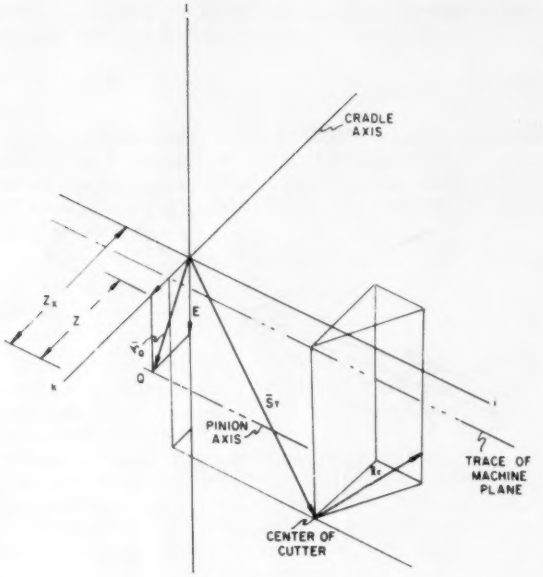

Fig. 26

The radius vector of the center of the pinion cutter referred to a co-ordinate system having the cradle axis collinear with the $\bar{k}$-axis and the $\bar{j}$-axis vertical is

$$\bar{S}_T = (m_1,\ m_2,\ m_3) \tag{92}$$

The pinion axis is parallel to $\bar{\imath}$ and intersects the $\bar{j}$, $\bar{k}$-plane at point Q. The radius vector to point

$$Q = \bar{r}_Q = -E\bar{j} + (Z_x - Z)\bar{k} \tag{93}$$

where E = hypoid offset.

The machine setup for the pinion and pinion cutter is shown in Fig. 26. Light guide lines have been added for clarification. The machine plane is a reference plane for machine setups; it is perpendicular to the cradle axis and passes through the cutter center.

Glossary of Terms and Symbols

NOTE: Subscripts G or P relate the term to gear or pinion

α_G = angle between gear face plane and gear pitch plane
α = angle between normal to involute helicoid and cutter axial plane
β = at a point on the involute helicoidal surface, β is the angle between the plane containing the cutter axis and the plane tangent to the base cylinder
Γ_0 = face angle of gear
Γ_1 = pitch angle of gear
Γ_R = root angle of gear
δ = difference between face angle and root angle of gear
λ = lead angle of helix
ρ_G = minimum principal radius of curvature of involute helicoid
ρ_P = minimum principal radius of curvature of conical pinion cutter
ρ_x = radius of curvature in axial section of involute helicoid
ϕ_R = pressure angle referred to root plane
ϕ_b = cutter blade angle
ϕ_n = normal pressure angle of involute helicoid
ϕ_f = pressure angle referred to face plane
ϕ_x = axial pressure angle of involute helicoid
ϕ_x'' = axial pressure angle of involute helicoid referred to datum plane

NOTE: Pressure angle is the angle between a tooth normal and reference plane.

$\Delta\phi_G$ = angle between cutter axis and perpendicular to datum plane
ψ_f = spiral angle referred to face plane
ψ_M = angle between plane containing gear cutter axis and normal to datum plane at M_R and plane containing tangent to gear peripheral direction and normal to datum plane at M_R
ψ_R = spiral angle referred to root plane of gear

NOTE: Spiral angle is measured in reference plane between projection of tooth normal and peripheral direction of gear at M.

w = see Fig. 14
A_G = distance in datum plane from intersection of gear axis to root mean point M_R
b_P = pinion dedendum at M
b_G = gear dedendum at M
b_{GM} = distance normal to datum plane from M to M_R
F = gear face width
h_p = distance from point m_i to plane of pinion cutter blade tips
K = point of intersection of tooth normal and cutter axis
r_c = cutter radius (mean)
Δr = decrement in cutter radius. See equation (36) and Fig. 14
W = angle between helix and involute of circle (in tangent plane)
W_x = angle between intersection of cutter axial plane and intersection of normal plane with tangent plane to involute helicoid
Z = pitch apex of gear beyond crossing point
Z_x = pitch apex of gear beyond intersection of datum plane and gear axis
W_G = point width of gear finishing cutter
L = lead of involute helicoid
ϕ_{RP} = normal pressure angle of helicoidal surface relative to datum plane
ψ_{RP} = root plane spiral angle of pinion
B = proportion of face width desired for bearing length
F = face width
ΔX_M = distance along gear axis between plane of blade tips and plane parallel to face plane through M_R
U_c = distance along pinion axis between plane of the blade tips and the intersection point of the normal to the involute helicoid

Bibliography

C. B. King and G. M. Spear, "Helixform: A Recent Development in Spiral Bevel and Hypoid Gears," The Institution of Mechanical Engineers, International Conference on Gearing, paper 11, London, England, 1958.

"Helixform Spiral Bevel and Hypoid Gears," abstract of paper, *Machinery*, vol. 65, no. 6, February, 1959.

U. S. Patent No. 2,857,819 to E. Wildhaber and C. B. King, October 28, 1958.

The following references may be useful to the reader of the Appendix:

A. Albert, "Solid Analytical Geometry," McGraw-Hill Book Company, Inc., New York, N. Y., 1949.

C. E. Weatherburn, "Differential Geometry of Three Dimensions," vol. 1, Cambridge University Press, Cambridge, England, 1955.

"Modern Mathematics for the Engineer," edited by E. Beckenbach, McGraw-Hill Book Company, Inc., New York, N. Y., 1955.

G. Hay, "Vector and Tensor Analysis," Dover Publications, 1953.

J. Gibbs, "Vector Analysis," Yale University Press, New Haven, Conn., 1929.

J. Kemeny, J. Snell, and G. Thompson, "Introduction to Finite Mathematics," Prentice-Hall, New York, N. Y., 1957.

The Twinworm Drive—A Self-Locking Worm-Gear Transmission of High Efficiency

B. POPPER
Israel Ministry of Defense,
Scientific Department,
Tel Aviv, Israel

D. W. PESSEN
Dept. of Mechanical Engineering,
Technion,
Israel Institute of Technology,
Haifa, Israel. Assoc. Mem. ASME

Up to the present, it has always been accepted as a proven and well-established fact that worm gears or screw threads that are self-locking are bound to have an efficiency of less than 50 per cent. An entirely different type of worm transmission has been developed which is self-locking, yet has a theoretical efficiency that can almost reach 100 per cent. Efficiencies of 90 per cent and above can easily be obtained in practice, and have, in fact, been obtained in models built by the authors. In addition, this new transmission exhibits a number of other unique and useful properties.

The paper describes the transmission and develops the theory upon which its operation is based. Design equations are derived for different operating conditions, and a number of possible uses and applications are discussed.

1 Introduction

THE TWINWORM DRIVE,[1] which is to be described in this paper, is a worm-gear transmission possessing a number of unique properties which should make it a valuable new machine element at the disposal of the machine designer. A conventional worm transmission consists of a worm driving a worm wheel, with their axes normal to one another. The Twinworm drive, however, consists of two worms in mesh, their axes *almost* parallel to each other, as shown in Fig. 1. The threads of the two worms are right and left-handed, respectively.

In conventional worm drives, the transmission ratio is generally very much smaller than one. With the Twinworm drive, the transmission ratio can be made smaller than one *or larger than one*, according to the requirements of the application. It can even be made exactly equal to one, something that is achieved only with difficulty with conventional worm drives. It should be pointed out, however, that the function of the Twinworm drive is not to provide very large speed reductions, as these can be more easily obtained by means of conventional worm drives. The purpose of the Twinworm drive is to produce self-locking, without any sacrifice in efficiency.

As already mentioned, the two worm axes of the Twinworm drive must be almost, but not quite, parallel to each other. The exact angle between the axes, together with the respective pitch angles of the two worms, must be computed according to definite design formulas. These formulas, together with the mathematical explanation of the Twinworm drive, will be derived later. Suffice it to say here that the unique properties of the drive are due to the fact that a completely different range of pitch angles and axes angles are utilized than in conventional worm drives.

Depending on the specific design formulas (and the resulting pitch angles) which are chosen, the Twinworm drive can be provided with a number of completely different properties. Which properties are desired depends, of course, on the given application. In general, however, Twinworm drives can be classified into two main groups: Those that possess ordinary self-locking characteristics; and those with so-called second-order self-locking, a completely new property which will be defined later. Before proceeding with the derivation of the theory and design formulas, we will briefly discuss the characteristics and some possible applications of each of these two groups.

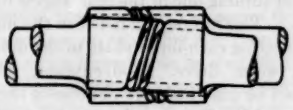

Fig. 1 Twinworm drive

2 Twinworm Drive With Ordinary Self-Locking

Ordinary self-locking means that, if gear 1 is designed to be the driver and gear 2 the follower, then gear 1 can drive gear 2 in either direction, but gear 2 cannot drive gear 1 in any direction.

This self-locking property serves as a valuable safety feature wherever loads have to be raised and lowered. As is well known, the efficiency of any conventional self-locking worm drive or self-locking power screw can never be more than the theoretical maximum of 50 per cent, and, in practice, is usually closer to 40 to 45 per cent. This fact has been accepted for a long time. With the Twinworm drive, however, the efficiency reaches a theoretical limit of 100 per cent, and 90 per cent and above can easily be obtained in practice.

Thus, the Twinworm drive permits the use of much smaller driving motors or power units, and also, of course, only about half the energy will be required to raise the load. The drive can therefor be used advantageously wherever loads must be raised, such as in hoists, elevators, lift trucks, lifting mechanisms, airplane actuator mechanisms, heavy drill presses, automatic garage doors, mechanisms for adjusting car seats or car windows, and so forth. Where loads must be raised manually, such as with screw jacks, hospital beds, and so forth, much lower turning effort will be required.

It should be noted here that, as will be proved later, the Twinworm drive can be designed according to either one of two different criteria: It can be designed so that the same input torque is required *both* for raising and for lowering the load (even if no counterweight is used). In this design, the power unit will be of the minimum possible size. Alternatively, the transmission can be designed so that the power consumption (for one complete cycle of raising and lowering the load) is at a minimum. In that case, however, the size of the power unit will be somewhat larger than in the first design. Design formulas for each of these two conditions will be derived.

[1] Patent applied for.

Contributed by the Machine Design Division and presented at the Annual Meeting, Atlantic City, N. J., November 29–December 4, 1959, of THE AMERICAN SOCIETY OF MECHANICAL ENGINEERS.

NOTE: Statements and opinions advanced in papers are to be understood as individual expressions of their authors and not those of the Society. Manuscript received at ASME Headquarters, August 4, 1959. Paper No. 59—A-75.

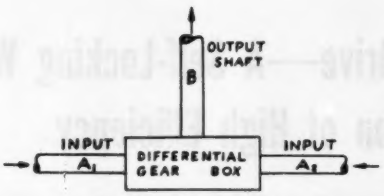

Fig. 2 Conventional differential

Another interesting application of the Twinworm drive concerns differential gears in computing mechanisms. Here the Twinworm drive can be used to prevent one input shaft from affecting the second input of a differential. Referring to Fig. 2, if we give input shaft A_2 one turn, we normally obtain a proportional number of turns at the output shaft B. If, however, the resisting torque at shaft B is sufficiently great, then shaft A_1 might turn slightly at the expense of shaft B. In the extreme case, shaft B might remain completely at rest with shaft A_1 getting all the motion. (This can be demonstrated by jacking up the rear end of a car and turning one of the rear wheels by hand, with the engine in gear.) This interaction between the inputs can be prevented by connecting each input shaft to the differential through a self-locking worm drive. Conventional self-locking worm drives would not be practical here because of their low efficiency. The Twinworm drive, however, could be used to advantage, especially for airborne computing mechanisms where the weight of the driving unit is of importance, or wherever small power loss is desired. The fact that the transmission ratio of the Twinworm drive can easily be made equal to one is an additional advantage for computer applications.

As an example of this application, Fig. 3 shows a Twinworm drive in actual use in a mechanical computer mechanism. The differential is shown in the right portion of the picture, above the integrating mechanism to which its output is connected. One of the input shafts is driven by a chain, and is connected to the differential through the Twinworm drive, as seen in the picture. The Twinworm drive, in this case, is designed to produce a 3:1 step-up in velocity, and, for that reason, the input (lower) worm is larger in diameter than the output (upper) worm. This particular Twinworm drive has an efficiency of 83 per cent, and it has been operating with good results for a considerable period of time.

3 Twinworm Drive With Second-Order Self-Locking

If so desired, the Twinworm drive can be designed to exhibit a unique new property, which, for want of a better name, will be called "second-order self-locking." To obtain this property, it is only necessary to choose the appropriate combination of pitch angles and axis angle, according to the proper design formulas for this condition.

Second-order self-locking includes all the properties of ordinary self-locking; i.e., if gear 1 is designed to be the driver, it can drive gear 2 in either direction, but gear 2 cannot drive gear 1 in any direction. In addition, however, as soon as gear 2 tries to go faster than it is being driven by gear 1 (i.e., if a force is applied to gear 2 which tends to "help" gear 1) *the whole transmission is immediately locked*, and comes to a stop as fast as the kinetic energy of the system can be converted into elastic energy.

To realize the full implications of this interesting property, let us consider the following case: Assume that a small flywheel is attached to the output shaft of a Twinworm drive with second-order self-locking. Assume further that the drive is turning at constant speed, and that the input force to the drive is suddenly made zero. At that moment, the input wheel 1 wants to stop, but the inertia of the flywheel attached to the output wheel 2 tends to make wheel 2 go faster than it is being driven by wheel 1. According to the definition of second-order self-locking, the whole transmission will immediately stop turning. Paradoxically, the inertia of the flywheel, instead of adding to the total inertia of the whole transmission, reduces its effective value almost to zero, *as long as the transmission is to be stopped*. When the transmission is to be started again, the flywheel will, of course, add slightly to the total inertia of the transmission.

The moment when the locking action begins can be influenced. Ordinarily, the drive would be locked as soon as the input acceleration becomes negative. If, however, the turning of the flywheel is opposed by some frictional resistance (leaf-spring rubbing against flywheel), then the drive will lock only if the de-

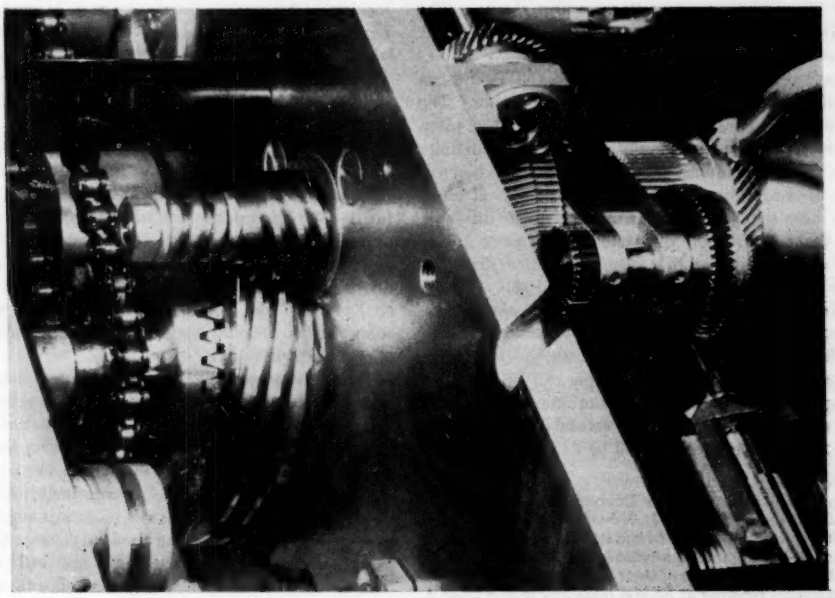

Fig. 3 Self-locking Twinworm drive in computing mechanism

celeration of the input shaft exceeds a certain value. Finally, if the flywheel is connected to the shaft in a flexible manner by means of a torsional spring, then the drive will be locked even before the acceleration of the input shaft becomes negative.

A demonstration model of a Twinworm drive displaying second-order self-locking is shown in Fig. 4. (The flywheel is not shown in the photo.) Experimental tests showed this drive to have an efficiency of 87 per cent, which already includes friction losses of the shaft bearings. (These tests were carried out by hanging weights on the input and output shafts until the drive barely turned.)

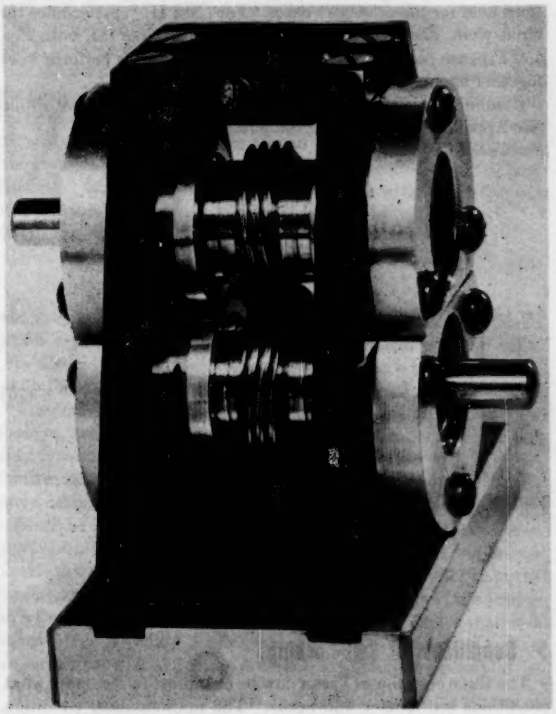

Fig. 4 Demonstration model of Twinworm drive with second-order self-locking

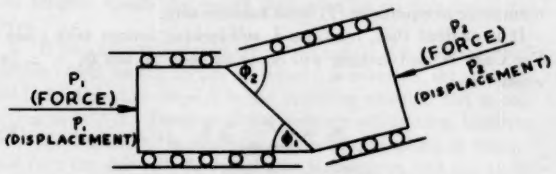

Fig. 5(a) Inclined-plane transmission

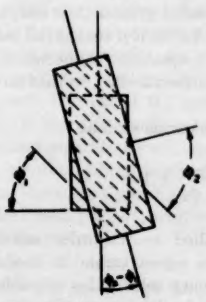

Fig. 5(b) Meshing worms

The described properties have a number of possible applications. For example, by connecting the drive to a position servomechanism, overshoot of the servo output can be completely prevented, so that the servo has almost perfect damping characteristics. The mechanism can thus replace conventional clutch and brake servos. By proper design, a servo can be built with a very high frequency response, not obtainable by other means such as conventional electric-servo motors.

Another possible application of second-order self-locking is in connection with hand-operated drills, contour milling machines, dental drills, and the like, where it may be desired to bring the drill or tool to an immediate stop should it penetrate an unintended area. The electric brakes or slip clutches used for this purpose are not always effective. Using a Twinworm drive with second-order self-locking and with a flywheel connected to the output worm, the tool will come to an immediate stop as soon as the driving force stops. Similarly, rotary switches, often rotating at considerable speeds, could be stopped quickly at any desired position by this method.

4 Force Equations for Inclined-Plane Transmission

The mathematical theory of the Twinworm drive will now be derived. The problem of analyzing the forces transmitted by meshing gears or screw threads can be simplified by considering only small contacting elements of surface of the meshing gears. The problem then reduces itself to the analysis of two inclined planes sliding one on the other. The generalized problem is represented in Fig. 5(a). The two planes are sliding freely, with the only friction being at the contact face between the two planes. This friction is denoted by μ, the coulomb (dry) friction coefficient. The contact faces make angles of ϕ_1 and ϕ_2, respectively, with the direction of motion of the planes. The driving and opposing forces are denoted by P_1 and P_2, and the respective displacements by p_1 and p_2. We arbitrarily define the forces and displacements as positive if they act in the direction of the respective arrows.

In order to help us visualize the connection between the sliding planes and the complete gears, Fig. 5(b) shows two worm gears in mesh with each other. The angles ϕ_1 and ϕ_2 here represent the respective pitch angles of the two worms, and $\phi_2 - \phi_1$ is the angle between the two worm shafts. It is evident that the sliding planes of Fig. 5(a) are a schematic and analogous representation of the system of Fig. 5(b). Our immediate aim is to find the relations between the forces P_1 and P_2, as a function of the angles ϕ_1 and ϕ_2 and of μ.

Consider two sliding planes, whose initial positions are shown by the solid lines of Fig. 6. If plane 1 is displaced by p_1 in the positive direction, then the resulting displacement of plane 2 will be p_2 in the negative direction, as shown by the dotted lines. Applying the law of sines to the small triangle, we obtain

$$-\frac{p_1}{p_2} = \frac{\sin \phi_2}{\sin \phi_1} \tag{1}$$

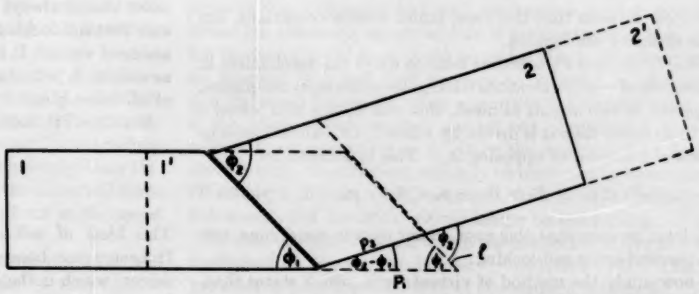

Fig. 6 Movement between sliding planes

where the minus sign takes care of the fact that p_1 and p_2 are always of opposite sign. Similarly, we obtain

$$l = p_1 \cdot \frac{\sin(\phi_2 - \phi_1)}{\sin \phi_2} \quad \text{if} \quad p_1 > 0 \tag{2a}$$

$$l = -p_1 \cdot \frac{\sin(\phi_2 - \phi_1)}{\sin \phi_2} \quad \text{if} \quad p_1 < 0 \tag{2b}$$

where l is the sliding distance. In the following discussion, it will be assumed that

$$\phi_2 > \phi_1 \tag{3}$$

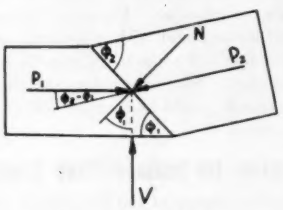

Fig. 7 Forces acting on sliding planes

This is certainly no restriction of the theory, since, if $\phi_2 < \phi_1$, we need only interchange the indexes in the various equations.

The various forces acting on the planes are shown in Fig. 7. V is the vertical reaction on plane 1. (In the case of a gear drive, this represents the axial thrust.) N is the normal force between the two planes. The friction force μN (not shown) is perpendicular to N. Since the forces acting on either one or on both planes are in equilibrium, we can write, for the components in the P_2-direction of all forces acting on both planes from the outside

$$P_2 = P_1 \cos(\phi_2 - \phi_1) + V \sin(\phi_2 - \phi_1) \tag{4}$$

Similarly, for the components in the N-direction of all forces acting on plane 1 alone, we write

$$N = P_1 \sin \phi_1 + V \cos \phi_1 \tag{5}$$

Before proceeding with our analysis, we must now distinguish between three different possible cases:

Case I: P_1 tends to drive the mechanism against P_2, which is denoted mathematically as

$$P_1 > 0 \qquad P_2 > 0 \qquad p_1 > 0 \qquad p_2 < 0$$

This is a symbolic representation only, since possibly $p_1 = 0$, but the tendency is to make $p_1 > 0$. It will later on be seen that Case I represents ordinary driving without any self-locking.

Case II: P_2 tends to drive the mechanism against P_1. (P_2 wants to become the driver.) This is denoted by

$$P_1 > 0 \qquad P_2 > 0 \qquad p_1 < 0 \qquad p_2 > 0$$

It will later be seen that this case, under certain conditions, can lead to ordinary self-locking.

Case III: P_1 and P_2 together tend to drive the mechanism in the direction of $-p_1$, against the friction force between the planes. (As applied to two worms in mesh, this case means that wheel 2 tends to go faster than it is driven by wheel 1; i.e., wheel 2 tries to help wheel 1 instead of opposing it.) This is denoted by

$$P_1 < 0 \qquad P_2 > 0 \qquad p_1 < 0 \qquad p_2 > 0$$

It will later be seen that this case, under certain conditions, can lead to second-order self-locking.

We now apply the method of virtual work, which states that, for a small displacement, the algebraic sum of the work done at the input and at the output must equal the energy dissipated by friction. In other words,

$$P_1 p_1 + P_2 p_2 = \mu N l \tag{6}$$

Considering Case I, for example, the input work is $P_1 p_1$ while the output work is $P_2 p_2$. Taking into account the signs of these four quantities, as specified in the foregoing for Case I, we find that the output work $P_2 p_2$ is negative. (This means that, whereas the input force P_1 does work, the output force P_2 has work done on it.) The physical meaning of equation (6) thus is that the input work minus the output work equals the friction loss. Similar explanations hold for the other two cases. For Case II, $P_2 p_2$ becomes the input work, and $P_1 p_1$ the output work. For Case III, both $P_1 p_1$ and $P_2 p_2$ are positive, which means that both forces perform work together against the friction force.

Combining equation (6) with those previously found, we obtain (see Appendix) the following three relations:

For Case I:

$$P_1 = P_2 \cdot \frac{\sin \phi_1 + \mu \cos \phi_1}{\sin \phi_2 + \mu \cos \phi_2} \quad \begin{cases} P_1 > 0 \\ P_2 > 0 \\ p_1 > 0 \\ p_2 < 0 \end{cases} \tag{7a}$$

For Case II:

$$P_2 = P_1 \cdot \frac{\sin \phi_2 - \mu \cos \phi_2}{\sin \phi_1 - \mu \cos \phi_1} \quad \begin{cases} P_1 > 0 \\ P_2 > 0 \\ p_1 < 0 \\ p_2 > 0 \end{cases} \tag{7b}$$

For Case III:

$$P_1 = P_2 \cdot \frac{\sin \phi_1 - \mu \cos \phi_1}{\sin \phi_2 - \mu \cos \phi_2} \quad \begin{cases} P_1 < 0 \\ P_2 > 0 \\ p_1 < 0 \\ p_2 > 0 \end{cases} \tag{7c}$$

5 Conditions for Self-Locking

The three equations (7) can now be examined to see under what conditions self-locking can occur. The mathematical condition for self-locking is that the driving force needed to overcome the driven force becomes infinitely large. This means that the denominator in equations (7) must become zero.

It is evident that, for Case I, self-locking cannot take place. For Case II, self-locking will occur as soon as $\tan \phi_1 \leqslant \mu$, or when

$$S_1 = \frac{\mu}{\tan \phi_1} \geqslant 1 \tag{8}$$

Here, S_1 represents a "safety factor," which, if self-locking is desired, should always be kept somewhat greater than one, to make sure that self-locking is maintained even if μ should fall below the assumed value. It is evident that equation (7b) becomes invalid as soon as $S_1 > 1$, since the drive is then locked, so that no motion at all takes place.

For Case III, self-locking will occur as soon as

$$S_2 = \frac{\mu}{\tan \phi_2} \geqslant 1 \tag{9}$$

This kind of self-locking is called second-order self-locking. It occurs not because the driven wheel wants to become the driver (which is the cause of ordinary self-locking possible under Case II), but because the driven wheel wants to help the driver.

As before, S_2 represents the safety factor for maintaining second-order self-locking. Also, as before, equation (7*c*) becomes invalid as soon as $S_2 > 1$.

Because of the assumption expressed by equation (3), S_1 will always be larger than S_2. Thus, as μ is increased, we will first reach a condition of ordinary self-locking, and then of second-order self-locking. It is thus impossible to have second-order self-locking without having at the same time also ordinary self-locking. (This explains why we have written both equations (7*b*) and (7*c*), which are actually identical. The appearance of second-order self-locking cannot be predicted from equation (7*b*), since that equation becomes invalid as soon as $S_1 > 1$. As we have seen, second-order self-locking does not occur until $S_2 = 1$, at which time we already have $S_1 > 1$.)

It should be noted here that the μ referred to until now and in the discussion to follow is the "active" or "virtual" coefficient of friction. In the case where the threads of the worm gear have parallel sides (as in a square thread), this virtual coefficient of friction is identical with the actual or "true" coefficient of friction. However, where the threads are inclined (as with Acme threads or V-threads), the virtual coefficient is given by

$$\mu_{\text{virtual}} = \frac{\mu_{\text{true}}}{\cos \theta_n} \tag{10}$$

where θ_n is the pressure angle, or the semiangle of the thread profile measured on a normal section perpendicular to the helix. (For a standard V-thread, for example, this angle is about 30 deg, while for an Acme thread it is about $14^1/_2$ deg.)

The concept of second-order self-locking, being an entirely new concept, may be somewhat difficult to visualize. Therefore, it may not be out of place to conclude this section with a hypothetical example which will help clarify the difference between the three cases, and between the two different types of self-locking.

Consider a drive with (to simplify the argument) a transmission ratio of unity. Assume that wheel 1 is the driver. If the torque on wheel 2 opposes the motion of wheel 1, and is smaller than the torque driving wheel 1, then we have Case I. If, now, the torque on wheel 2 is reversed so that wheel 2 tends to go faster than it is being driven by wheel 1; i.e., wheel 2 tries to help wheel 1, then we have Case III, and three different conditions are possible:

1 If the drive is designed for $S_1 < 1$, then there is no chance at all for self-locking, and the speed of the drive (or the input torque) will merely adjust itself until the total power input of the two torques equals the power dissipated by friction inside the drive.

2 If the drive is designed for $S_1 > 1$ but $S_2 < 1$ (ordinary self-locking) then, as the torque on wheel 2 is reversed, *the drive will not lock*, since the wheel 2 is not opposing wheel 1, but is only trying to help it. Because of the ordinary self-locking, however, this "helping effort" is wasted; i.e., the torque acting on wheel 1 will turn the drive at the speed that it wants to, and not at the speed that torque 2 wants to. (Torque 2, rather than helping, actually interferes by increasing the friction between the tooth surfaces.) As a practical example of this, consider an automobile jacked up on a screw jack. As long as torque 1 is zero, or acts to raise the car but is smaller than the opposing torque 2, we have Case II, and, because of the ordinary self-locking, the jack will not turn. If the jack handle is now turned so as to lower the car, then torque 1 acts downward, and the car (torque 2) tries to help torque 1 by also pushing downward. This is obviously Case III. Yet, since there is only ordinary self-locking, the drive will turn, but at the speed the jack handle wants to, and not at the speed the car wants to.

3 If $S_2 > 1$ (second-order self-locking), then the drive will lock completely as soon as torque 2 is reversed so that wheel 2 tries to help wheel 1. Thus, if a screw jack were built with second-order self-locking, it would clearly be impossible to lower the load. It is obvious, therefore, that second-order self-locking must never be used where it is desired to raise and lower loads.

6 Efficiencies

Having found the conditions under which self-locking takes place, our next step is to find the efficiencies for the various cases.

As long as P_1 is the driving force, and P_2 opposes P_1, we have Case I, and the efficiency can be expressed as

$$\eta = \left| \frac{P_2 p_2}{P_1 p_1} \right| \tag{11}$$

where the absolute value is used, since p_1 and p_2 are of opposite sign. Substituting equations (7*a*) and (1) into (11), we obtain

$$\eta = \frac{1 + \mu/\tan \phi_2}{1 + \mu/\tan \phi_1} = \frac{1 + S_2}{1 + S_1} \qquad \begin{cases} P_1 > 0 \\ P_2 > 0 \\ p_1 > 0 \\ p_2 < 0 \end{cases} \tag{12}$$

This shows that, to increase the efficiency, S_2 should be increased, and S_1 should be decreased. To maintain self-locking, S_1 must of course be kept greater than one. On the other hand, if second-order self-locking is not wanted, then S_2 must be kept smaller than one.

Assuming ϕ_2 and ϕ_1 to be fairly small (smaller than about 20 deg), we can write $\tan \phi \approx \phi$, so that the efficiency can be expressed as

$$\eta = 1 - \frac{S_1/(1 + S_1)}{1 + \dfrac{1}{S_1} \cdot \dfrac{\mu}{(\phi_2 - \phi_1)}} \qquad \begin{cases} P_1 > 0 \\ P_2 > 0 \\ p_1 > 0 \\ p_2 < 0 \end{cases} \tag{12a}$$

where ϕ_1 and ϕ_2 are the respective pitch angles in radians.

This formula shows that, as long as the drive is still in the design stage, once the safety factor S_1 for self-locking has been decided upon, the efficiency can be increased by increasing the factor $\mu/(\phi_2 - \phi_1)$. This is done either by decreasing the difference between the pitch angles, or by increasing the friction coefficient μ. It may seem strange at first that an increase in friction will increase the efficiency. The explanation, however, may be visualized by means of the following vague analogy: If a locomotive is traveling up an inclined track, then an increase in the friction between wheels and the rails will cause less slipping, and therefore an increase in the driving efficiency. As $(\phi_2 - \phi_1)$ is decreased, the sliding velocity also decreases, as shown by equation (2). Using a higher value of μ permits us to design the gear with a larger ϕ_1 and hence a smaller $(\phi_2 - \phi_1)$, at the same time maintaining S_1 constant at the value desired.

This does not mean that we can increase the efficiency by throwing sand into our transmission. On the contrary, once the drive has been designed and built, an increase in friction will decrease the efficiency, as can be seen if we substitute $\phi_1/(\phi_2 - \phi_1)$ for the factor $\mu/S_1(\phi_2 - \phi_1)$ in equation (12*a*). In other words, an increase in μ will only produce an increase in efficiency if μ is increased before the other quantities are decided upon, and if the whole design is then carried out accordingly, so as to utilize this higher value of μ. Once the design is fixed and the drive is built, the efficiency can only be increased by decreasing μ. Of course, if μ is decreased too much, then S_1 will eventually fall below one, and the drive will no longer be self-locking.

It must again be stressed that μ represents the active or virtual coefficient of friction, as defined by equation (10). This fact provides us with the possibility of increasing μ artificially. Thus, to get a high μ for the sake of higher efficiency, we can increase

the pressure angle of the thread. In addition, of course, choice of materials, surface finish, and lubrication should be such as to make μ as large as possible. It is even possible to increase μ by proper chemical treatment of the contact surfaces with acids.

We now consider the case where P_2 is the driving force, and P_1 opposes P_2 (Case II). If $S_1 \geq 1$, we have self-locking, so that the efficiency has no meaning. If $S_1 < 1$, the drive will turn, and the efficiency is now

$$\eta = \left|\frac{P_1 p_1}{P_2 p_2}\right| \tag{13}$$

which, after substituting equations (7*b*) and (1), becomes

$$\eta = \frac{1 - \mu/\tan \phi_1}{1 - \mu/\tan \phi_2} = \frac{1 - S_1}{1 - S_2} \quad \begin{cases} P_1 > 0 \\ P_2 > 0 \\ p_1 < 0 \\ p_2 > 0 \end{cases} \tag{14}$$

Finally, we consider Case III, where both P_1 and P_2 drive in the same direction against the friction between the sliding surfaces. Again, if $S_2 \geq 1$, we have self-locking, so that the efficiency has no meaning. On the other hand, if $S_2 < 1$, the transmission will turn, but again the efficiency has no physical meaning here, since there is no output work. (Both forces do input work, against the friction.) We can, however, calculate the relation between the forces P_1 and P_2. We thus define the *force ratio* η^* as

$$\eta^* = \frac{P_2}{P_1} \cdot \left|\frac{p_2}{p_1}\right| \tag{15}$$

which, after substituting equations (7*c*) and (1), becomes

$$\eta^* = \frac{1 - S_2}{1 - S_1} \quad \text{where} \quad S_2 < 1 \quad \text{and} \quad \begin{cases} P_1 < 0 \\ P_2 > 0 \\ p_1 < 0 \\ p_2 > 0 \end{cases} \tag{16}$$

It is clear that, for a drive with ordinary self-locking, η^* may assume any negative value, and can even be larger than one.

We will now proceed to apply the theory developed so far to a number of practical cases, including the calculation of some numerical examples.

7 Ordinary Worm and Worm-Wheel Drive

Since the assumptions made at the beginning of this article were quite general, we can apply the theory to specific cases. Thus, if we assume $(\phi_2 - \phi_1) = 90$ deg, we have the shafts at 90 deg to each other, and the case represents an ordinary worm and worm wheel, common inclined plane, or common screw. Since here $\tan \phi_1 = -1/\tan \phi_2$ equations (12), (14), and (16) become, respectively

$$\eta_{90°} = \frac{1 - \mu \tan \phi_1}{1 + \mu/\tan \phi_1} = \frac{1 - \mu^2/S_1}{1 + S_1} \quad \text{(for Case I)} \tag{17}$$

$$\eta_{90°} = \frac{1 - \mu/\tan \phi_1}{1 + \mu \tan \phi_1} = \frac{1 - S_1}{1 + \mu^2/S_1} \quad \text{(for Case II)} \tag{18}$$

$$\eta_{90°} = \frac{1 + \mu \tan \phi_1}{1 - \mu/\tan \phi_1} = \frac{1 + \mu^2/S_1}{1 - S_1} \quad \text{(for Case III)} \tag{19}$$

where ϕ_1 is the pitch angle of the worm. As is to be expected, equation (17) is identical to the well-known equation for the efficiency of a square thread. For an Acme or V-thread, equation (17) also applies, but we must use the virtual friction coefficient, as given by equation (10). For self-locking, $\mu \geq \tan \phi_1$, which results in an efficiency $\eta_{90°}$ of less than 50 per cent, a fact known and accepted for a long time.

8 Worm Drive With Ordinary Self-Locking

Assume that the safety factor to obtain self-locking is to be $S_1 = 1.20$, and that the coefficient of friction is $\mu = 0.16$ (a reasonable value for lubricated steel worms). For a conventional worm drive, the efficiency, according to equation (17), will then be $\eta_{90°} = 44$ per cent.

Designing a Twinworm drive using the same S_1 and μ as in the foregoing, we obtain from equation (8) a value of $\tan \phi_1 = \mu/S_1 = 0.133$, so that $\phi_1 = 7.6$ deg. Choosing $(\phi_2 - \phi_1) = 2$ deg, we get $\phi_2 = 9.6$ deg, so that, from equation (9), $S_2 = 0.95$. These values substituted into equation (12) or (12*a*) show an efficiency of $\eta = 89$ per cent, or twice that of the conventional drive.

It should be noted that the choice of $(\phi_2 - \phi_1) = 2$ deg was quite arbitrary. By using a smaller value, an even larger efficiency could be obtained. The minimum practical value of $(\phi_2 - \phi_1)$ is probably fixed by manufacturing considerations, such as tolerances, and pitch angles that can be conveniently cut on the available equipment. Of course, if $(\phi_2 - \phi_1)$ is made too small, then S_2 will become greater than one, and we will get second-order self-locking. This fact provides a limit on the smallest value of $(\phi_2 - \phi_1)$ that can be used in cases where second-order self-locking is not desired.

9 Drive Requiring Same Power to Raise or to Lower Load

Wherever a load is to be raised and lowered, a self-locking device is usually necessary. In some cases, the load is not balanced by a counterweight at all (automobile jack, hoists, and so forth); in other cases, it is only partially counterbalanced (elevator).

With a conventional worm drive, the power required to raise the load is much larger than that required to lower it. The motor or power unit used in the particular application must, of course, be chosen according to the power required to raise the load. Using the Twinworm drive principle, it is possible to design a drive such that the same amount of power will be required for raising or for lowering the load. The necessary size of the motor or power unit will then be at a minimum, and, in any case, will be much smaller than with a conventional worm drive.

While the load is being raised, we have Case I, and the efficiency η is given by equation (12). While the load is being lowered, we have Case III (since the load is trying to help the drive), and the force ratio η^* is given by equation (16). We assume that the load consists only of deadweight, but does not include any frictional resistance outside of that which exists within the worm drive itself. In that case, the magnitude of the load remains the same, both for raising and for lowering. Therefore, to get the same driving power, both for the opposing and for the collaborating driven load, we must set $\eta = -\eta^*$. Substituting the relations (12) and (16) into this condition (and assuming that $\tan \phi \approx \phi$), we obtain the condition

$$\mu = \sqrt{\phi_1 \cdot \phi_2} \tag{20}$$

from which follows

$$1/S_2 = S_1 \tag{20a}$$

This means that S_1, the safety factor for having ordinary self-locking, must equal $1/S_2$, the safety factor for *not* having second-order self-locking. (If there were second-order self-locking, it would be impossible to lower the load altogether.)

Substituting condition (20*a*) into equation (12), we find that

$$\eta = -\eta^* = \frac{1}{S_1} = S_2 = \sqrt{\frac{S_2}{S_1}} \approx \sqrt{\frac{\phi_1}{\phi_2}} \tag{21}$$

Applying this to a numerical example, we again use $S_1 = 1.2$ and $\mu = 0.16$. The pitch angles of the two worms are then $\phi_1 =$ arc tan $\mu/S_1 = 7.6$ deg, and $\phi_2 =$ arc tan $\mu/S_2 =$ arc tan $\mu \cdot S_1 = 10.9$ deg, resulting in an efficiency of $\eta = 1/S_1 = 83$ per cent, as compared to $\eta_{90°} = 44$ per cent obtainable with a conventional worm drive using the same values of μ and S_1. This means that, using the Twinworm drive, the motor or power unit need only be of about half the load capacity.

10 Drive With Minimum Power Consumption for Raising and Lowering Load

Sometimes we are interested in raising and lowering a load with minimum power consumption for one complete cycle. The power required for raising the load will then not be equal anymore to that required to lower it, and the necessary size of the power unit will be larger than in the previous case. The over-all power consumption per cycle will be lower, however, because in the previous case considerable power is wasted in lowering the load.

Assuming that the load W must be raised and lowered through a distance h, we find that the energy E necessary for one cycle is equal to

$$E = \frac{Wh}{\eta} - \frac{Wh}{\eta^*} = Wh\left(\frac{1}{\eta} - \frac{1}{\eta^*}\right) = \frac{2Wh}{\eta_m} \qquad (22)$$

where the apparent mean efficiency η_m is defined by

$$\frac{1}{\eta_m} = \frac{1}{2}\left(\frac{1}{\eta} - \frac{1}{\eta^*}\right) \qquad (23)$$

Substituting the values of η and η^* as expressed by equations (12) and (16), we obtain

$$\eta_m = \frac{1 - S_2^2}{S_1 - S_2} < 2 \qquad (23a)$$

where $S_1 > 1$ and $S_2 < 1$, since we have ordinary self-locking.

In order to obtain minimum power consumption per cycle, we want η_m to be maximum. Setting the derivative $d\eta_m/dS_2$ equal to zero, this leads to the requirement

$$(S_2)_0 = S_1 - \sqrt{S_1^2 - 1} \qquad (24)$$

whereupon the apparent mean efficiency becomes

$$(\eta_m)_0 = 2(S_2)_0 \qquad (25)$$

Applying this to a numerical example, and again using $S_1 = 1.2$ and $\mu = 0.16$, we have, as before, $\phi_1 = 7.6$ deg. From equation (24), we find $(S_2)_0 = 0.54$, so that $\phi_2 =$ arc tan $\mu/S_2 = 16.5$ deg. The power consumption per cycle thus becomes, according to equations (22) and (25), equal to $E = Wh/(S_2)_0 = 1.85\ Wh$.

In order to afford a comparison of power consumption per cycle, we have computed the mean efficiency for the example of section 9 and also for the conventional worm drive.

In order to compare the required size of the power unit for the different examples, we calculate the fraction $P_1p_1 = P_2p_2/\eta$ where, for η, we use either the efficiency η, equation (12), or the force ratio $= \eta^*$, equation (16), *whichever is smaller*.

To facilitate comparison, the results are summarized in Table 1, which should be self-explanatory. The final choice of drive would be made according to what was more important—minimum size of power unit or minimum power consumption.

Table 1

	Required size of power unit	Power consumption per cycle
Ordinary worm drive	$2.27 \times P_2p_2$	$2.44 \times Wh$
Twinworm designed for minimum power-unit size (equal force to raise and to lower load)	$1.20 \times P_2p_2$	$2.40 \times Wh$
Twinworm designed for minimum power consumption	$1.43 \times P_2p_2$	$1.85 \times Wh$

11 Utilization of Worm Friction for Braking Purposes

We have seen that, in Case III, both forces P_1 and P_2 act in the same direction against the friction force between the two worms. This friction force could therefore be utilized to perform a useful braking action. For example, it may be desirable to have a braking action the moment the load begins to help the drive and tries to raise its speed. We assume that a braking torque n times the driving torque of the load is desired. This means that, the braking torque being equal to $P_1p_1 + P_2p_2$, we want $P_1p_1 + P_2 + p_2 = nP_2p_2$. From this follows that $-P_2p_2/P_1p_1 = 1/(1-n)$. Equating equations (15) and (16) and substituting we obtain

$$\tan \phi_2 = \frac{\mu}{1 - \left(\dfrac{S_1 - 1}{n - 1}\right)} \qquad (26)$$

As a numerical example, consider a water pump driven by a nonsynchronous motor. If the pump load should change direction, so that the pump itself wants to drive the motor (pump wants to run faster than it is being driven), then we want a braking torque equal to 150 per cent of the pump's driving torque applied within the transmission. (This means that the motor would then have to overcome a positive torque which is only 50 per cent of the pump's driving torque.)

Assuming $S_1 = 1.1$ and $\mu = 0.16$, and substituting $n = 1.5$ into equation (26), we obtain $\phi_1 =$ arc tan $0.145 = 8.2$ deg, and $\phi_2 =$ arc tan $0.200 = 11.3$ deg.

According to equation (12), the efficiency of this drive, when working under ordinary conditions (opposing load), will be 86 per cent. It should be noted that the efficiency will increase as n is increased, and $n = \infty$ signifies total second-order self-locking. The braking action produced in this example might therefore be visualized as constituting "partial" second-order self-locking. While the drive is not locked, the tendency toward second-order self-locking produces the desired braking force.

12 Design Considerations

The one disadvantage of the Twinworm drive seems to be that the angle between the two worm shafts cannot be made any arbitrary value, but is fixed by the design formulas, according to the specific requirements of the drive. The shafts have to be almost, but not completely parallel, as compared to a 90-deg angle for conventional worm drives.

Obtaining such small shaft angles should not be difficult. In cases where the final input and output shafts have to be absolutely parallel, a flexible drive could be used to connect the worm drive to the rest of the system. Since the angle required is very small and, furthermore, since it remains constant, such a drive would be very simple to design. Bevel gears can also be used, as shown in the application illustrated in Fig. 3. Again, since the required angle is very small, the bevel gear teeth would be almost straight and would thus be easy to manufacture.

The transmission ratio of the Twinworm drive is equal to the ratio of the number of threads on the driving and the driven worms. The transmission ratio can thus be made any reasonable value, as already stated previously. Since, however, the pitch angles of the worms are fixed ahead of time according to other considerations, the number of threads on a worm can only be in-

creased by increasing the worm diameter proportionately. Thus, the transmission ratio varies approximately as the inverse ratio of worm diameters. This fact imposes the only practical limitation on the maximum speed ratio obtainable with a Twinworm drive, since, just as with a pair of ordinary spur gears, extremely high ratios would require one gear to be extremely large in diameter.

The worms of the Twinworm drive can be cut on a lathe, or even on automatic screw machines, the same as ordinary screw threads.

The load-bearing capacity of the Twinworm drive is higher than that of ordinary worm drives, since their high efficiency results in very little heating of the threads. For the same reason, wear will be low. A second factor making for little wear is the fact that the sliding velocity between the teeth is very low, being only a small fraction of the peripheral velocity of the worm, as compared to conventional worm drives where these two velocities are about equal.

In certain applications, especially those demanding second-order self-locking, it may be desirable to connect the output worm to a friction coupling in order to dissipate the kinetic energy of the system when the drive is suddenly locked. This is illustrated in Fig. 3, the friction coupling there being the left extension of the upper worm. Another method of reducing the contact forces during locking consists of connecting the output worm through a flexible torsion spring or shaft. This increases the elastic energy capacity of the system, so that the kinetic energy can be more easily absorbed without producing excessive contact forces. These methods, however, are not generally necessary, but are only called for in special cases.

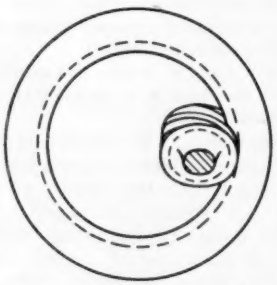

Fig. 8 Internal Twinworm drive

13 Other Forms of Twinworm Drive

The theoretical principles of the Twinworm drive can also be applied to an internal worm drive, as shown in Fig. 8. In that case, of course, the transmission ratio must be other than one. The inside worm being barrel-shaped, as shown in the figure, a greater amount of tooth surface is in contact, so that the load-carrying capacity of the drive is increased.

Similarly, a type of bevel gear could be designed according to Twinworm principles (Fig. 9) so that self-locking with high efficiency would be obtained. Here, again, the larger amount of contact surface would make for a greater load-carrying capacity.

In cases where rotary motion has to be changed to linear motion, a worm could be used driving a type of rack whose teeth represent inclined planes. This is illustrated in Fig. 10. If the pitch angles of worm and rack are calculated according to the design formulas, then the drive will be self-locking with high efficiency. Such a drive might, for example, be used in the automatic or manual raising of automobile or train windows.

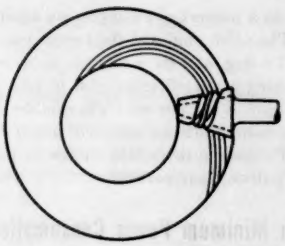

Fig. 9 Bevel Twinworm drive

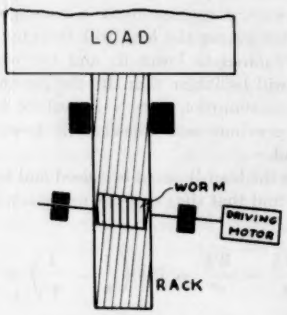

Fig. 10 Twinworm principles applied to worm-rack drive

Finally, where we wish to transmit only linear motion, we could use an inclined-plane transmission, as shown in Fig. 5(*a*), instead of worms. Again, the respective angles of the inclined planes would have to be computed according to the principles enumerated if self-locking with high efficiency is to be obtained. Possible applications include automatic closing of doors in buses or trains, and so forth. Since the drive is self-locking, no air need be applied constantly to the power cylinder to keep the door closed.

In conclusion, let it be stated that, as time goes on, numerous new applications of the Twinworm drive will, undoubtedly, be found. The Twinworm drive represents a powerful new machine element in the hands of the ingenious machine designer.

APPENDIX

Multiplying equation (4) by $\cos \phi_1$, and multiplying equation (5) by $\sin (\phi_2 - \phi_1)$, subtracting the two products, and then multiplying the result by μ, we get

$$\mu P_2 \cos \phi_1 - \mu N \sin (\phi_2 - \phi_1) = \mu P_1 \cos \phi_2 \qquad (27)$$

Dividing equation (6) by p_1 we obtain

$$-P_2 \frac{p_2}{p_1} + \mu N \frac{l}{p_1} = P_1 \qquad (6a)$$

We now substitute equations (1) and (2*a* or *b*) into (6*a*). For Case I, $p_1 > 0$, and we must therefore use equation (2*a*), whereas, for Cases II and III, equation (2*b*) applies. We obtain

$$P_2 \sin \phi_1 \stackrel{+}{=} \mu N \sin (\phi_2 - \phi_1) = P_1 \sin \phi_2 \qquad (28)$$

where the three different signs in front of the μN-term refer to the three different cases, respectively. Adding or subtracting equations (27) and (28), we have

$P_2 (\sin \phi_1 \stackrel{+}{=} \mu \cos \phi_1) = P_1 (\sin \phi_2 \stackrel{+}{=} \mu \cos \phi_2)$ from which follow the three equations (7).

DISCUSSION

J. D. Howell[2]

The authors have disclosed a very promising and useful new mechanism. A word of caution, however, seems in order for the designer who intends to use it. The device must be designed on the basis of energy absorption and heat dissipation. For instance, in the lift mechanism described where equal torque is to be used in raising or in lowering the load, both the input energy and the potential energy given up by the load must be converted into heat at the contact point of the two worms when lowering the load. This is, it is true, a moving point, but temperatures should be kept low enough to prevent surface damage under the high loads present and provision must be made for carrying away the heat produced if operation for any length of time is expected.

W. L. Starkey[3]

The authors deserve sincere congratulations for the conception and development of the Twinworm drive, and for their excellent paper on this very novel machine element. I have carefully examined the analysis of this new gear-configuration and find it to be accurate. It may be suggested, however, that it would be helpful to readers attempting to gain an intuitive understanding of the basic principles involved in this Twinworm drive, if additional schematic models of the contacting surfaces of the mating gears were presented in such a way that the relationship of the frictional forces and the resulting permissible motions were more clearly described.

Considering the possible applications of this device, it seems that its primary unique feature is its ability to be so constructed that it can transmit torque and angular motion in one direction through the drive at high efficiency with a self-locking feature which prohibits reverse transmission in either direction of rotation.

The functions of some configurations of this mechanism, especially where high magnitudes of torques are involved and where the dual self-locking feature is not required, might better be achieved by a combination of an ordinary spur or helical gear pair, together with a no-back-lash, self-locking clutch mechanism.

Although, unquestionably, this new device will find many useful applications, designers should be cautioned that for some configurations, especially where cost, weight, or space requirements would dictate small size, it is probable that excessively high Hertz-type contact stresses may be developed at the gear teeth, and excessively high axial thrust forces might be produced, either of which could lead to premature mechanical failure. Such excessive loads would tend to cause pitting or wear of the tooth surfaces, bearing failure, shaft failure, or gear-wheel web failure. On the other hand, for small power-transmission or where size is not a factor, this device could undoubtedly be designed to last many cycles of useful life.

The authors are particularly deserving of commendation for this contribution to knowledge. They have taken a simple, widely used gear configuration, and by introducing a clever modification, have produced what is essentially a new device having unique capabilities.

[2] Development Engineer, Wallace & Tiernan Inc., Belleville, N. J.
[3] Professor, The Ohio State University, Columbus, Ohio. Mem. ASME.

Authors' Closure

Mr. Howell's comment about heat dissipation is, in general, correct. However, this problem exists with all worm drives and, wherever the heat to be dissipated is excessive, the gears are usually immersed in an oil bath in order to carry the heat away. The Twinworm drive is, in this respect, never worse, but usually much better, than conventional worm drives. This can be seen from Table 1 of the paper, where the column "Power consumption per cycle" also represents the heat that must be dissipated per cycle, for the case where loads are to be raised and lowered. It will be seen from the table that, from the standpoint of heat to be dissipated, the Twinworm designed for minimum power-unit size (equal force to raise and to lower load) is hardly any better than a conventional worm drive. However, if the Twinworm is designed for minimum power consumption, then the heat to be dissipated is appreciably less.

It should also be stressed that this problem of heat dissipation exists only where loads must be alternately raised and lowered continuously. In all other applications where the Twinworm is used to provide ordinary self-locking (as, for example, in the computing mechanism described in the paper), there is hardly any heat to be dissipated because of the Twinworm's high efficiency. In contrast, a conventional worm drive used in such applications would have an efficiency of less than 50 per cent, which means that over 50 per cent of the power transmitted would have to be dissipated in the form of heat.

The authors wish to thank Professor Starkey for examining and verifying the correctness of the Twinworm analysis. We agree that a more schematic explanation of the Twinworm drive is in order and refer the reader to the article, "For Self-Locking at High Efficiency . . . the Twinworm Gear," by Nicholas Chironis, published in the January 18, 1960, issue of *Product Engineering*. In that article, an attempt is made to explain how the Twinworm drive works by means of schematic models of the contacting surfaces.

Concerning the question of the axial thrust forces produced in the Twinworm drive, these are no worse than in conventional worm drives and, in either case, simply are proportional to the cotangent of the pitch angle ϕ, if friction is neglected. Taking the friction into account, the ratio of end thrust to applied force equals $1/(\phi + \mu)$.

Contact stresses are, of course, a problem, but again, this problem is common to all worm drives. The contact between the Twinworm surfaces is, strictly speaking, point contact. In practice, however, the contact sufficiently approaches line contact (i.e., the Hertzian ellipsoid of contact has a large radius), so that the contact stresses are not too large. To reduce these stresses even further, it is possible to make one of the two worms (usually the driven one) in hyperboloid (hour-glass) shape. This increases the number of threads in contact and thus reduces the contact stresses. Such a hyperboloid worm could easily be manufactured by means of hobbing, using a hob having the shape of an ordinary cylindrical (the driving) worm. (The hobbing should preferably be carried out at high speed, because of the low sliding velocity between the Twinworm surfaces.)

Other methods of increasing the contact surfaces and thus reducing the contact stresses are illustrated in Figs. 8, 9, and 10 of the paper.

Determination of Cutter Trajectories for Contoured Turbine Buckets[1]

R. G. DeBIASE
Engineer, General Engineering Laboratory, General Electric Company, Schenectady, N. Y.

The advent of numerically controlled machine-tool systems introduces the serious problem of suitably employing them for part fabrication. To numerically contour the complex surface of a large turbine bucket with this type of machining system, it is necessary to determine the geometrical constraints on the motion of the cutter, which will sweep out the desired part surface as an envelope of the cutter surface. A definition of the turbine-bucket surface is given in terms of unequally spaced cross sections along the length of the part, and an interpolating procedure is employed to define the entire surface with properly faired transitions between the specified cross sections. The procedures outlined in this paper have been used to program an IBM 704 computer for the preparation of digital control tapes, which instruct the motions of the machining system.

THE MATHEMATICAL AND PHYSICAL considerations necessary to the automatic fabrication of contoured turbine buckets on a numerically controlled machine-tool system divide naturally into four distinct categories: (*a*) The definition of the part surface by the general-purpose computer, (*b*) the solution of the geometrical problem relating the cutter to the bucket surface, (*c*) the determination of the cutter trajectories and motion programs which generate the desired surface as an evolute of the cutter surface, and (*d*) satisfying the compatibility requirements of the digital components that constitute the machine-tool system. Although item (*d*) is necessary to the realization of a workable system, it is peculiar to the system studied and will not be discussed further. The first three categories demonstrate more generally applicable techniques and will constitute the subject matter of this paper.

In a companion paper "Automatic Milling of Steam-Turbine Buckets," R. H. Wilke and A. Rubio[2] cover the utilitarian aspects of the work presented and show a turbine bucket that was fabricated by using the techniques described in this paper

Constraints Imposed by the Machine Tool

Fig. 1 is an attempt to show pictorially an inclined toroidal cutter in juxtaposition to the surface of a milled turbine bucket. Two basic Cartesian reference axes are illustrated. An XYZ system serves as the reference axes for part-surface description, and a UVW system placed at the cutter center describes the cutter surface. The operation of the machine tool is such that the part is indexed through 360 deg in angular increments about the Y axis, and the cutter center is constrained to lie in the XY plane. Only two motion channels are controlled at any instant of time, although a channel-sharing feature is provided. Either the XY axes are under servo control while the rotation (β axis) is held fixed, or the $X\beta$ axes are controlled while Y motion is frozen. In this manner a three-dimensional complex surface can be generated by making a longitudinal pass with the cutter while the index angle is held fixed; then the index angle is advanced through an increment of a few degrees, and a return pass is effected. The process is continued until the part has been indexed through a complete rotation.

The Turbine-Bucket Surface

An engineering description of a turbine bucket is set forth as a series of cross sections of the desired bucket at intervals along the Y axis parallel to the XZ plane, and a requirement that the intervening surface provide a "properly faired" transition between the specified sections. A typical cross section might appear as the solid-line curve of Fig. 2. To realize the surface-transition requirement it is necessary that a well-defined interpolation procedure be employed to produce consistent results. Since the machining system is basically designed to operate in a cylindrical co-ordinate system, a logical interpolation procedure should employ a set of radial planes to define the complete surface; however, Fig. 2 shows that the character of the contour is such that multiple-valued R-versus-β functions are encountered, thereby making the resultant data unusable for interpolation. This difficulty was surmounted by developing an envelope surface having

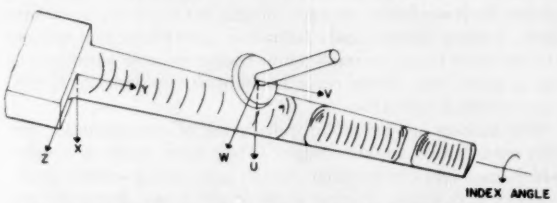

Fig. 1 Isometric view of cutter in relation to bucket surface

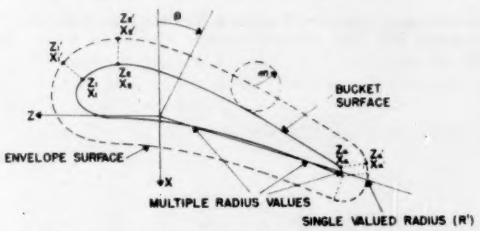

Fig. 2 Generation of envelope surface for interpolation

[1] When this paper was written the author included information and expressed opinions believed to be correct and reliable. Because of the constant advance of technical knowledge, and widely differing conditions of specific application, and the possibility of misapplication, any application of the contents of this paper must be at the sole discretion and responsibility of the user.

[2] ASME Paper No. 59—A-98, *Mechanical Engineering* vol. 82, January, 1960, pp. 44–47.

Contributed by the Machine Design Division and presented at the Annual Meeting, Atlantic City, N. J., November 29–December 4, 1959, of THE AMERICAN SOCIETY OF MECHANICAL ENGINEERS.

NOTE: Statements and opinions advanced in papers are to be understood as individual expressions of their authors and not those of the Society. Manuscript received at ASME Headquarters, July 17, 1959. Paper No. 59—A-111.

a point-to-point correspondence with the bucket surface, but having the desirable property that the R'-versus-β description of each cross section is a single-valued function. The envelope surface is generated by rolling a coin of sufficiently large radius around the periphery of each section, marking the path of the coin's center, and then interpolating the envelope along the length of the bucket in each radial plane. This envelope surface is now the interpolating surface that allows a definition of points on the actual bucket surface between the specified cross sections. A point on the bucket surface is determined by erecting a perpendicular to the envelope surface in a plane parallel to the XZ plane, and then marking off the coin radius m.

The Toroidal-Cutter Surface

For the purpose of providing mechanical clearance, the toroidal cutter was inclined at an angle α to the YZ plane. Details of the cutter surface are illustrated in Fig. 3. A description of the cutter surface in the intermediate U', V', W' reference frame in terms of γ, λ parameters is

$$\left.\begin{aligned} U' &= (b + a\cos\gamma)\cos\lambda \\ V' &= a\sin\gamma \\ W' &= (b + a\cos\gamma)\sin\lambda \end{aligned}\right\} \quad (1)$$

Equations (1) can be converted to the desired U, V, W axes by using the matrix transformation

$$\begin{bmatrix} U \\ V \\ W \end{bmatrix} = \begin{bmatrix} \cos\alpha & -\sin\alpha & 0 \\ \sin\alpha & \cos\alpha & 0 \\ 0 & 0 & 1 \end{bmatrix} \begin{bmatrix} U' \\ V' \\ W' \end{bmatrix} \quad (2)$$

With the result

$$\left.\begin{aligned} U &= (b + a\cos\gamma)\cos\lambda\cos\alpha - a\sin\gamma\sin\alpha \\ V &= (b + a\cos\gamma)\cos\lambda\sin\alpha + a\sin\gamma\cos\alpha \\ W &= (b + a\cos\gamma)\sin\lambda \end{aligned}\right\} \quad (3)$$

The effective cutting surface lies in the range

$$-\frac{\pi}{2} \leqq \gamma \leqq \frac{\pi}{2}, \quad \text{and} \quad -\frac{\pi}{2} \leqq \lambda \leqq \frac{\pi}{2}$$

An assignment of a value for γ and a value for λ in their appropriate ranges defines a point in the UVW space that is on the cutter surface. In the XYZ system the cutter surface can be expressed as

$$\left.\begin{aligned} X &= X \text{ cutter center} + U(\gamma, \lambda) \\ Y &= Y \text{ cutter center} + V(\gamma, \lambda) \\ Z &= W(\gamma, \lambda) \end{aligned}\right\} \quad (4)$$

It is to be noted that at this point a numerical definition of the entire bucket surface can be determined from the construction of the interpolating envelope surface, and the cutter surface is specified analytically by equations (3) and (4).

Determination of the Cutter-Center Trajectories

Having established an appropriate description of the bucket surface and the cutter surface, the object is to determine at every specified section the values for X cutter center and Y cutter center that cause an osculation of the cutter and part surfaces. This same determination must be carried out for all of the possible indexed positions of the bucket.

The procedure for effecting a solution to the problem of locating the cutter center will be described as two steps. First, a gross approximation will be obtained by employing a specific curve on the cutter surface projected onto a generic jj cross-section plane [see Fig. 4(a)]. This curve will be called an extremum curve.

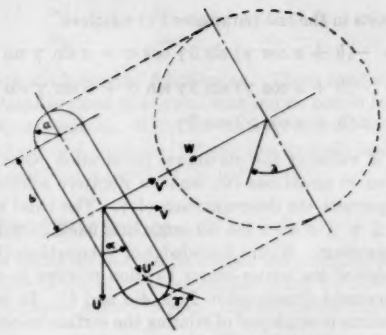

Fig. 3 Toroidal cutter details

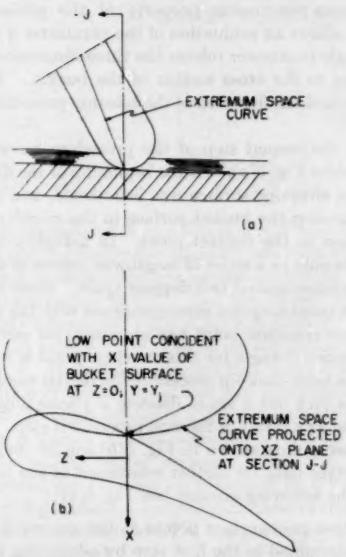

Fig. 4 Initial cutter placement relative to bucket surface

Then, having determined the first approximation point, the surface of the part will be developed in an approximate manner by a "least-squares" procedure, and the analytically defined cutter will be developed as a bivariate Taylor series. It should be noted that these surface determinations are only required to be valid in the near vicinity of this first approximation point and are discussed in more detail in the Appendix.

To examine the procedure for determining the first approximation in more detail, consider Fig. 4(b). As a mathematical abstraction, the projected extremum curve is placed in coincidence with the blade surface as shown. This relationship causes the cutter to undercut the workpiece either on the positive Z side or the negative Z side of the rotation axis. A decision is made by the general purpose computer to determine where the workpiece undercut occurs, by evaluating the X values of the part surface at $Z = \pm 0.05$ in. When the decision is made, the Z value is sequentially advanced in 0.05-in. increments, and at each Z value a number $X_{\text{part}} - X_{\text{cutter}}$ is evaluated. Differencing the sequentially determined $X_{\text{part}} - X_{\text{cutter}}$ numbers allows a determination of the maximum penetration point, because at this point the difference $(X_{\text{part}} - X_{\text{cutter}})_n - (X_{\text{part}} - X_{\text{cutter}})_{n+1}$ will change sign.

Analytically the extremum space curve on the cutter surface is defined by the equation

$$\lambda = 3\gamma + \frac{\pi}{2} \quad (5)$$

which results in the one-parameter (γ) relations,

$$\left.\begin{aligned} U &= -(b + a\cos\gamma)\sin 3\gamma\cos\alpha - a\sin\gamma\sin\alpha \\ V &= -(b + a\cos\gamma)\sin 3\gamma\sin\alpha + a\sin\gamma\cos\alpha \\ W &= \pm(b + a\cos\gamma)\cos 3\gamma \end{aligned}\right\} \quad (6)$$

Now the Z value of the maximum penetration point is the W value given in equations (6), and an iterative solution of this equation permits the determination of γ. The valid range of γ is $-\pi/6 \leqq \gamma \leqq 0$ since the tilt angle α is fixed at $\pi/6$ for this machining system. With a knowledge of γ, equations (6) provide a knowledge of the cutter-center location relative to the initial cutter placement illustrated in Figs. 4(a and b). In brief terms the mechanism is employed of relating the surface co-ordinates γ, λ by equation (5), which defines an explicit curve on the cutter. The maximum-penetration property of the projection of this space curve allows an evaluation of the parameter γ at the point, and this single parameter relates the three-dimensional character of the cutter to the cross section of the bucket. The first approximation and the first step of the solution procedure is thereby realized.

To make the second step of the procedure more readily apparent, consider Fig. 5(a). At the beginning of the discussion the interpolating envelope surface was introduced, and it is now employed to develop the bucket surface in the vicinity of the first approximation to the contact point. In actuality the envelope surface exists only as a series of lengthwise curves in a discrete set of radial β planes spaced two degrees apart. Since the envelope surface has a point-to-point correspondence with the part surface, the first approximation point has an associated envelope point, and the included β angle for this envelope point is readily determined. By a table-look-up procedure the digital computer can be instructed to pick out a set of discrete β planes adjacent to the β plane found as a result of the first procedural step. The grid of bucket-surface points shown in Fig. 5(b) can be found from the envelope-surface data for further refinement of the contact-point location in the following manner [see Fig. 5(b)]:

1 The three-part surface points at the generic $Y = Y_j$ section were determined in the first step by advancing the Z value by increments of 0.05 in. and calculating sequentially the corresponding X values for the given cross section.

2 The additional six points at $Y = Y_j + 0.1$ and at $Y = Y_j - 0.1$ are obtained by using the envelope data in the adjacent, discrete β planes to interpolate 0.1 in. above and below the specified cross section, and then projecting these six envelope points back to the part surface.

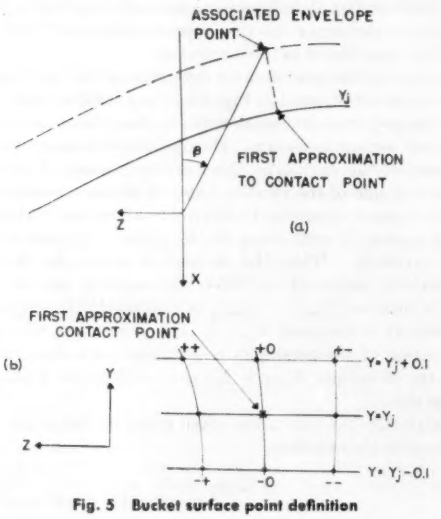

Fig. 5 Bucket surface point definition

A further discussion of the analytical details employed to develop the part surface in the vicinity of the gross contact point is given in the Appendix. The point to be emphasized is that a development of the area of the bucket surface in which the true point of contact lies can be established numerically and can be used to refine the location of the cutter-center point to mate the surfaces properly.

In the Appendix an expression for the bucket surface is developed in the vicinity of the contact or first-approximation point. The form of this expression is

$$X_B(Y_0 + \Delta Y, Z_0 + \Delta Z) = X_B|_{Y_0,Z_0} + a_1\Delta Y + a_2\Delta Y^2 + a_3\Delta Y\Delta Z + a_4\Delta Z + a_5\Delta Z^2 \quad (7)$$

Referring again to the Appendix the equation describing the cutter surface in the vicinity of the point of contact follows

$$X_C(Y_0 + \Delta Y, Z_0 + \Delta Z) = X_C|_{Y_0,Z_0} + b_1\Delta Y + b_2\Delta Y^2 + b_3\Delta Y\Delta Z + b_4\Delta Z + b_5\Delta Z^2 \quad (8)$$

Physically, a review of Figs. 4(a and b) indicates that the initial placement of the cutter must be modified to mate the bucket and cutter developments of (7) and (8). Here the previously determined γ value serves to determine a V value from equations (6), which is exactly the Y displacement of the cutter center from the section jj that does in fact properly relate the surfaces. A situation now exists in which, due to the initial placement shown in Fig. 4(b), an undercut condition is assured, and the region including the point of maximum undercut is described by equations (7) and (8). Forming

$$X_c - X_b = X_c|_{Y_0,Z_0} - X_b|_{Y_0,Z_0} + (b_1 - a_1)\Delta Y + (b_2 - a_2)\Delta Y^2 + (b_3 - a_3)\Delta Y\Delta Z + (b_4 - a_4)\Delta Z + (b_5 - a_5)\Delta Z^2 \quad (9)$$

and then determining the point of maximum penetration by differentiating (9) partially with respect to ΔY and ΔZ below

$$\frac{\partial(X_c - X_b)}{\partial\Delta Y} = 0, \quad \frac{\partial(X_c - X_b)}{\partial\Delta Z} = 0 \quad (10)$$

Equations (10) permit an evaluation of a set of values for ΔY and ΔZ, which when reinserted into (9) gives the maximum penetration of the cutter into the workpiece. When the cutter is withdrawn from its initial placement by the amount of the maximum penetration determined, a refined set of values for $X_{\text{cutter center}}$ and $Y_{\text{cutter center}}$ is obtained.

When it is recalled that all of the sections coupled with all of the possible index angles require a determination of this information, one can see that a very extensive set of calculations must be performed by the general-purpose computer to generate a control tape.

An unconnected set of $X_{\text{cutter center}}$, $Y_{\text{cutter center}}$ point determinations has been obtained up to now. It is therefore necessary to discuss the manner of connecting or interpolating these data so that the machining system does in fact produce a part surface that is properly faired and meets or exceeds the requirements of the engineering and manufacturing groups.

A moment's digression will serve to clarify the reason for the interpolation procedure finally chosen. The machine-tool system is composed of three parts—a general-purpose computer, a machine-tool director, and the actual machine tool. The director employed for interpolation solves the finite-difference equations which generate parabolic motion in each machine axis, and thus due to the nature of the director a parabolic interpolating scheme was used. In particular consider the set of $X_{\text{cutter center}}$, $Y_{\text{cutter center}}$ values associated with a single cutter pass along the bucket. The chord line joining the points adjacent to a particular point is

used to define the slope at the particular point. In traversing the path along the bucket from one point with a given slope to the next point also having a specified slope, one finds that a single parabola does not suffice because too many conditions are imposed. A final and acceptable version of the many possible interpolating techniques was to use two connecting parabolas with continuous slopes and ordinates at their junction to satisfy the ordinates and chord-determined slopes along the cutter trajectory.

Conclusions

The techniques discussed are quite general in nature and can be employed for the contouring of many three-dimensional surfaces. It is to be noted that although the discussion was pointed toward the fabrication of contoured turbine buckets the technique need not be restricted to these parts. It is quite apparent that the only restrictions on the class of surfaces that can be cut are imposed by the cutter radii and the machine interferences.

A digital control tape can be generated on the IBM 704 computer with the program developed from these methods, within 25 to 45 minutes after insertion of the required engineering data. The time interval varies with the complexity of the bucket. This relatively rapid preparation of new control tapes provides a high degree of flexibility in the utilization of the machining system. The machining tapes produced parts with the desired surface contour, and within the prescribed tolerances.

Acknowledgment

The author is indebted to A. Rubio and to R. H. Wilke for many helpful suggestions during the course of the project. Mrs. J. K. Dunham and Mrs. M. S. Dyrkacz provided the competent IBM 704 programming assistance required.

APPENDIX

The Turbine-Bucket Surface

From the data used to obtain the first approximation, the gross contact point and its two adjacent Y_j points at $\Delta Z = \pm 0.05$ in. are obtained. The envelope-surface interpolating procedure gives three bucket-surface points at $Y_j + 0.1$ in. and three points at $Y_j - 0.1$ in. [see Fig. 5(*b*)]. An appropriate description of the part surface can be written in the vicinity of the point of contact as

$$X_B(Y_0 + \Delta Y, Z_0 + \Delta Z) = X_B|_{Y_0,Z_0} + a_1\Delta Y + a_2\Delta Y^2 + a_3\Delta Y\Delta Z + a_4\Delta Z + a_5\Delta Z^2 \quad (11)$$

Since the data on the Y_j section is the best information available, it is assumed that the approximate surface (11) passes exactly through the three points in the *jj* plane. From the X values and the locations of these three points, the coefficients $X_B|_{Y_0,Z_0}$, a_4, and a_5 are readily evaluated. The six additional off-section points can be used to determine the remaining approximating coefficients a_1, a_2, and a_3 by a "least-squares" procedure. At each of the six off-section points the difference between the known surface value and the form (11), with appropriate insertions of the ΔY and ΔZ values is found. All six of these differences are squared and the results summed. By partially differentiating this sum of squares ϵ_T with respect to the unknown parameters a_1, a_2, and a_3, three equations

$$\frac{\partial \epsilon_T}{\partial a_1} = 0, \quad \frac{\partial \epsilon_T}{\partial a_2} = 0, \quad \frac{\partial \epsilon_T}{\partial a_3} = 0 \quad (12)$$

result, which minimize the function ϵ_T. There results a set of three equations in three unknowns that can be solved for the coefficients a_1, a_2, and a_3. With the six approximate surface coefficients determined, equation (11) provides an analytical description of the region of interest on the part surface.

The Toroidal-Cutter Surface

Since the cutter surface can be defined analytically, its surface in the vicinity of the first approximation point Y_0, Z_0 will be developed in a Taylor series. In form, this approximating surface is

$$X_c(Y_0 + \Delta Y, Z_0 + \Delta Z) = X_c|_{Y_0,Z_0} + b_1\Delta Y + b_2\Delta Y^2 + b_3\Delta Y\Delta Z + b_4\Delta Z + b_5\Delta Z^2 \quad (13)$$

where

$$b_1 = \left.\frac{\partial X}{\partial Y}\right|_{Y_0,Z_0} \qquad b_2 = \frac{1}{2!}\left.\frac{\partial^2 X}{\partial Y^2}\right|_{Y_0,Z_0} \qquad b_3 = \left.\frac{\partial^2 X}{\partial Y \partial Z}\right|_{Y_0,Z_0}$$

$$b_4 = \left.\frac{\partial X}{\partial Y}\right|_{Y_0,Z_0} \qquad b_5 = \frac{1}{2!}\left.\frac{\partial^2 X}{\partial Z^2}\right|_{Y_0,Z_0}$$

Although an expression for X as a function of Y and Z is desired, equations (3) which describe the cutter surface from cutter-center co-ordinates are entirely adequate for the evaluation of the partial derivatives required in (13); and the Taylor expansion is then completely determined when $X_c|_{Y_0,Z_0}$ is known.

Equations (3) express U, V, and W as a function of the two parameters γ, λ. It should be recalled that γ was obtained from the last equation of the set (6) at the first approximation point. But Equation (5) which relates γ and λ can be used to evaluate the λ when γ is known. This particular γ, λ pair defines the contact point on the cutter surface. Thus the partial derivatives required for (13) can be evaluated in UVW space in terms of the γ, λ parameters, and the numerical evaluation of the partial derivatives is obtained when the particular γ, λ contact point values are inserted.

Since the required partial differentiations of equations (3) are tedious and quite straightforward, only a listing of the desired answers will be given. In particular if $K_1 = \cos\alpha$ and $K_2 = -\sin\alpha$

$$\frac{\partial X}{\partial Y} = \frac{-K_1 \sin\gamma + K_2 \cos\gamma \cos\lambda}{K_2 \sin\gamma + K_1 \cos\gamma \cos\lambda} \quad (14)$$

$$\frac{\partial X}{\partial Z} = \frac{-\cos\gamma \sin\lambda}{K_2 \sin\gamma + K_1 \cos\gamma \cos\lambda} \quad (15)$$

and letting $D = (K_2 \sin\gamma + K_1 \cos\gamma \cos\lambda)^2$ the expressions for the second partial derivatives are

$$\frac{\partial^2 X}{\partial Y^2} = -\frac{1}{D}\,\frac{(b + a\cos\gamma)\cos^2\lambda + a\sin^2\gamma \sin^2\lambda \cos\gamma}{(b + a\cos\gamma)(K_2 a \sin\gamma + K_1 a \cos\gamma \cos\lambda)} \quad (16)$$

$$\frac{\partial^2 X}{\partial Z^2} = -\frac{1}{D}\,\frac{K_2^2 (b + a\cos\gamma)\sin^2\lambda + (K_2 a \sin\gamma \cos\lambda + K_1 a \cos\gamma)(K_2 \sin\gamma \cos\gamma \cos\lambda + K_1 \cos^2\gamma)}{(b + a\cos\gamma)(K_2 a \sin\gamma + K_1 a \cos\gamma \cos\lambda)} \quad (17)$$

$$\frac{\partial^2 X}{\partial Y \partial Z} = \frac{1}{D}\,\frac{K_2 \sin\lambda \cos\lambda (b + a\cos\gamma) - (K_2 \sin\gamma \cos\gamma \cos\lambda + K_1 \cos^2\gamma)(a \sin\gamma \sin\lambda)}{(b + a\cos\gamma)(K_2 a \sin\gamma + K_1 a \cos\gamma \cos\lambda)} \quad (18)$$

Inserting the appropriate γ, λ values associated with the first approximation point allows the calculation of the required b_1, b_2, b_3, b_4, and b_5 coefficients.

DISCUSSION

W. W. Kuyper[3]

These papers[4] describe a significant step both in the art of manufacturing steam turbine buckets and of building numerically controlled machine tools. The work of the authors is a further growth beyond the recent developments in skin mills and spar mills, and other contouring machines. It will, in turn, show the way for other applications of computers and numerical controls to the machining of metals.

The geometry of turbine buckets with the necessary taper, twist, and reinforcing pads for tie-wires, tends to be complex. This geometry, added to the accuracy required, leads to an analytical and computer programming problem of major proportions. Its satisfactory solution is gratifying indeed. The fact that the inherent high accuracy and effectiveness of the system appears to be achieved is a credit to all concerned in this effort.

It is difficult to escape the impression that numerically controlled machining has now come of age. The period of rapid and awkward growth is largely behind; the period of maturity, of full development in many directions, and of major usefulness, is ahead.

George Yaremkevych[5]

The purpose of the paper presented is to illustrate the method of preparing numerical controls for cutting a turbine bucket with a toroidally shaped cutter. The toroidal cutter has to osculate the bucket in at least second degree. Therefore, the center of the cutter has to be led along a specific line whose co-ordinates have to be evaluated for subsequent transfer to a tape.

The surface to be cut is not defined by a mathematical equation, merely thought of as consisting of small overlapping areas with borders sufficiently apart or as a total of thin cross sections. The equations of cutter surface given in the paper are easily verified by Fig. 6.

The author introduces into his consideration a specific curve which he calls "extremum curve" with an equation $\lambda = 3(\gamma - \pi/2)$. This particular "embankment curve" was chosen out of all possible curves on the toroidal surface because it meets some other specific demands arising during the designing process. It is an algebraic curve which winds itself 3 times around the surface touching in one point the surface of the bucket. The theory of the curve is rather complicated and leads to the following expressions of its curvature at current point:

$$\rho^2 = R^3/P^2$$

where

$$R = a^2 + 9\Lambda^2$$

and

$$P^2 = a^4(1 + 36\sin^2\gamma) + 18\,a^3\Lambda\cos\gamma + 9a^2\Lambda^2(1 + 9\cos^2\gamma + 36\sin^2\gamma) - 81a\Lambda^3\cos\gamma + 729\,\Lambda^4$$

with

$$\Lambda = C + a\cos\gamma$$

This radius of curvature is certainly not the largest one possible at the point given, the main normal to the skew curve being not coincident with the normal of the surface.

The author now proceeds to more detailed computations of the path of the center of the cutter. He replaces the surface of the cutter by an osculating surface of the second degree

$$\frac{\xi^2}{R_1} + \frac{\zeta^2}{R_2} + 2a_1\xi\zeta + 2a_2\xi\eta + a_3\zeta + 2\eta = 0$$

and seeks for an osculating second degree surface (an ellipsoid or paraboloid) for the bucket surface. From a grid of points on this surface (which are not expressed analytically, but tabulated, I presume) a powerful computing machine is able to get the necessary data in short time. The cutter has to be placed so that the osculating ellipsoid matches the computed one in the current point as close as possible. The co-ordinates of the center of the cutter will be established from point to point after the computer evaluated the coefficients a_1, a_2, a_3, by solving the equations mentioned in the appendix to the subject paper. Those equations are by no means short ones, but are facilitated somewhat by the relationship between γ and λ mentioned. All equations have to be restricted, of course, to the areas forthcoming in the cutting process.

I consider the paper presented as a very valuable, fine and rare specimen of application of differential geometry of curved surfaces to engineering, and I hope it will be of help to many designers faced with similar problems.

[3] Engineering Manager, Turbine Division, General Electric Company, Schenectady, N. Y. Mem. ASME.

[4] This discussion refers to this paper and also the paper by R. H. Wilke and D. Rubio, "Automatic Milling of Steam-Turbine Buckets."

[5] The Warner & Swasey Company, Cleveland, Ohio.

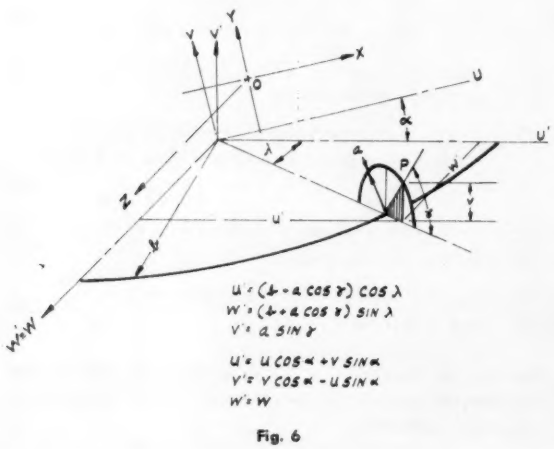

Fig. 6

Author's Closure

The author appreciates Mr. Kuyper's comments on the work described in both papers.

The discussion by Mr. Yaremkevych brings out the salient points of the method and thus serves as a good précis of the paper. A comment on the selection of the space curve described by the constraint relation $\lambda = 3(\gamma - \pi/2)$ is necessary. It is possible to describe particular curves on the surface of the toroidal cutter, that are extremum in some sense (i.e., the locus of lowest points on the cutter relative to the YZ-plane of Fig. 1, or the locus of points defined by a tangent cylinder with elements parallel to the Y-axis, etc.). In the evolution of the method these "extremum" curves were considered, but due to the nature of the parts to be machined, no great advantage could be attributed to any single curve. The $\lambda = 3(\gamma - \pi/2)$ curve had the desirable advantages that: 1 It is a curve that is almost centered in the effective cutting region; 2 computationally, it is far simpler to use than the equations describing the curves mentioned in the parenthetical remark; and 3 no additional error is introduced by its use because of the subsequent Taylor series refinement.

Mathematically speaking the curve is extremum in no sense, although the word extremum was used to convey the idea of an outside curve. As Mr. Yaremkevych points out, the words "embankment curve" might be more descriptive.

An Analysis of Factors Used for Strength Rating Helical Gears

E. J. WELLAUER
Director, Research and Development, The Falk Corporation, Milwaukee, Wis. Mem. ASME

This paper discusses the factors used to rate the strength of helical-gear teeth by means of the fundamental tooth-strength formula developed by the American Gear Manufacturers Association's Gear Rating Committee. The new approach combines different concepts of geometry factors, an improved evaluation of dynamic loads, rational allowable stresses, and risk or reliability considered as a statistical probability. In addition, the inclusion of the effect of operating error and load-distributing tooth flexibility provides the gear engineer with a more accurate means for helical-gear strength rating.

AGMA Fundamental Stress Formula

THE basic equation for the bending stress in a gear tooth is

$$s_t = \frac{W_t K_0}{K_v} \frac{P_d}{F} \frac{K_s K_m}{J} \tag{1}$$

The relation of calculated stress to allowable stress is

$$s_t \leqq \frac{s_a K_L}{K_T K_R} \tag{2}$$

The terms in equation (1) are divided into three groups, the first of which concerns the load, the second the tooth size, and the third the stress distribution. The derivation of the formulas and the terms applied to helical gears are given in the Appendix.

The factors are:

s_t = calculated tensile stress at root of tooth, psi

Load:
- W_t = transmitted tangential load at operating pitch diameter, lb
- K_0 = overload factor
- K_v = dynamic factor

Tooth size:
- P_d = transverse diametral pitch
- F = net face width, in.

Stress distribution:
- K_s = size factor
- K_m = load-distribution factor
- J = geometry factor

Allowable stress:
- s_a = allowable stress for material and heat-treatment, psi
- K_L = life factor
- K_T = temperature factor
- K_R = factor of safety

Factors Associated With Load

Transmitted Load W_t. The transmitted load is calculated directly from the power transmitted by the gear set. These loads cannot always be evaluated accurately. When the transmitted load is not uniform, consideration should be given not only to the peak load and its anticipated number of cycles, but also to intermediate loads and their number of cycles. The magnitude and to some extent the frequency of application of overloads are measured by the overload factor K_0.

Overload Factor K_0. The overload factor makes allowances for the roughness or smoothness of operation of both the driving and driven apparatus. In determining the overload factor, consideration should be given to the fact that many drives transmit momentary overload torques appreciably greater than those determined by the nameplate ratings of either the prime mover or the driven apparatus. Inertia loading and acceleration forces also must be evaluated. In the absence of specific overload factors, the values in Table 1 may be used.

The character of typical commercial drive combinations is shown in Table 2.

Table 1 Overload factors, K_0

	Character of load on driven machine		
Power source	Uniform	Moderate shock	Heavy shock
Uniform	1.00	1.25	1.75
Light shock	1.25	1.50	2.00
Medium shock	1.50	1.75	2.25

Table 2 Typical drive combinations

Typical examples of power-source character		
Uniform	Moderate shock	Heavy shock
Electric-motor turbine	Multicylinder internal-combustion engine	Single-cylinder internal-combustion engine

Typical example of load character		
Uniform	Moderate shock	Heavy shock
Centrifugal blower	Lobe-type blower	Ore crushers
Pure liquid agitator	Liquid and solid agitator	Single-cylinder compressor
Belt conveyer (uniform feed)	Belt conveyer (nonuniform feed)	Reciprocating conveyer

When sufficient reliable field experience is obtained for certain gears having similar combinations of mounting and production accuracy, it is possible to develop "service factors" which can replace the overload factor, and partially compensate for the factor of safety and life factor. Service factors are widely used in AGMA Standards [1, 2][1] and these can be used as guides. If a specific service factor is used in place of the overload factor K_0, use a value of 1.0 for both K_R and K_L.

Dynamic Factor K_v. The dynamic factor depends on:

1 Effect of tooth spacing and profile errors.
2 Effect of pitch line speed and rpm.
3 Inertia and stiffness of all rotating elements.
4 Transmitted loads per inch of face.
5 Tooth stiffness.

Contributed by the Machine Design Division and presented at the Annual Meeting, Atlantic City, N. J., November 29–December 4, 1959, of THE AMERICAN SOCIETY OF MECHANICAL ENGINEERS.
NOTE: Statements and opinions advanced in papers are to be understood as individual expressions of their authors and not those of the Society. Manuscript received at ASME Headquarters, August 13, 1959. Paper No. 59—A-121.

[1] Numbers in brackets designate References at end of paper.

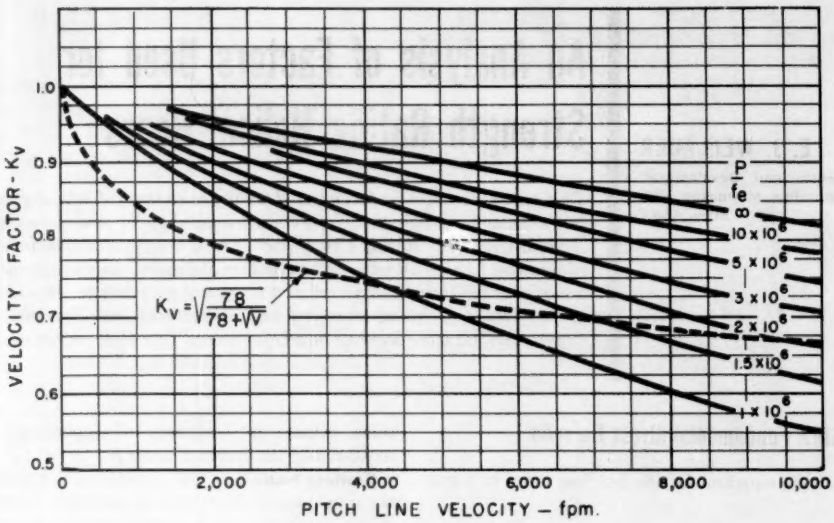

Fig. 1 Helical-gear velocity factors

A complex procedure is required to evaluate accurately the effect of dynamic loadings caused by tooth error and elastic flexibility. The dynamic factors, as determined by recent tests of Niemann and Rettig [3], Attia [4], and Harris [5], seemingly show that the dynamic-load increment increases linearly with the velocity unless resonant conditions occur but becomes a lesser percentage of the transmitted load as the load increases. The effect of the variation in tooth deflection as determined by changes in contact length or number of teeth in contact can be as important as the dynamic increment caused by the errors conventionally found in commercial gearing. It is for this reason that the design of uniform contact conditions needs attention and explains why spur gears with their 1 to 2 tooth-contact variation usually develop higher dynamic stresses than helical gears in which only a minor contact variation normally exists. An empirical relation (developed from the spur-gear tests of Niemann and Rettig [3]) for helical gears having less than 10 per cent contact-length variation from the average is plotted in Fig. 1. Its value is

$$K_v = \frac{1}{1 + \left(0.225 \times 10^{-4} + 60\,\frac{f_e}{P}\right) v} \qquad (3)$$

where

f_e = base pitch spacing error, in.
P = tangential load per inch of face, lb/in.
v = pitch line velocity, fpm

If tooth flexibility, accuracy, and loading cannot be estimated accurately, use of the following velocity factor has been found satisfactory and presumes the gears have been manufactured by suitable techniques for the particular operating speeds:

$$K_v = \left(\frac{78}{78 + \sqrt{v}}\right)^{1/2} \qquad (4)$$

Factors Associated With Tooth Size

The factors concerned with tooth size are the diametral pitch and the face width. These are measurable factors but it should not be construed that the strength capacity is directly proportionate.

Factors Associated With Stress Distribution

The stress-distribution factors require the utmost understanding to evaluate their magnitude properly.

Size Factor K_s. The size factor depends primarily upon:

1 Tooth pitch.
2 Diameter of parts.
3 Ratio of tooth size to diameter of part.
4 Face width.
5 Dimensions of maximum stress pattern and gradient of stress therein.
6 Ratio of case-hardened depth to tooth thickness.
7 Hardenability and heat-treatment of materials.

That a size factor exists in the performance of materials seems evident from numerous service experiences. Horger [6], Lundberg and Palmgren [7], and WADC [8] seem to consider a size effect as a reflection of the increasing statistical possibilities of a weak spot being encountered as the size of the part or the stressed area becomes larger. Uzhiz [9] reports that the stress gradient across the sensitive outer layer is important.

It is the author's opinion that the size factor may be taken as unity for most helical gears, provided that a proper choice of steel composition and heat-treatment procedures is made. When coarse-pitch, case-hardened teeth are used, it might be desirable to derate to reflect the lesser strengthening effect of the surface compressive stresses developed by the case. With K_s equal to unity for a 10-diametral pitch gear, a K_s of 1.25 might be suitable for a 1-diametral pitch case-hardened tooth.

Load Distribution Factor K_m. The evaluation of this factor is one of the newer contributions to gear rating. The load distribution factor K_m depends upon:

1 Misalignment of axes of rotation.
2 Alignment errors due to tooth inaccuracies.
3 Elastic deflections of shafts, bearings, and blanks.

The foregoing errors can combine so that less than the full face-width contacts with the mating element or full contact but non-uniform loading can result. For large lead deviations corrections are sometimes made by tapering the teeth so that a more uniform contact condition is secured under load. The deflections of the teeth themselves compensate for misalignment by a calculable amount:

With

$$F_m = \left(\frac{2W_t}{eG}\right)^{1/2} \tag{5}$$

where

F_m = maximum theoretical face width which would contact with load varying from zero at one side of face to a maximum at other side
e = lead deviation between mating teeth, in/in.
G = stiffness constant, lb/in. lead deviation/in. of face

then for

$$F_m < F; \quad K_m = \frac{2F}{F_m} \tag{6}$$

$$F_m > F; \quad K_m = \frac{F_m}{F_m - (F/2)} \tag{7}$$

For spur gears, the stiffness constant G was found by Weber [10] and Niemann and Rettig [3] to vary from 1.6×10^6 at tip contact to 2.41×10^6 at the rolling point. Van Zandt [11] suggests a design value of 1.18×10^6. Dudley [12] reports variations of G from 0.5×10^6 to 2×10^6.

The mesh stiffness of helical gears does not undergo the drastic change which occurs with spur gears. For helical gears the tangential load to just make 100 per cent contact across a face width F_m is

$$W_t = \frac{G}{2} eF_m^2 \frac{Z}{2p_b} K \tag{8}$$

where

G = stiffness constant (suggest 1.2×10^6)
e = total lead deviation, in/in.
Z = total length of line of action in plane of rotation, in.
p_b = base pitch, in.
K = inclination factor compensating tooth stiffness for helix angle, based upon Trobojevic [13]

Using this formula, the load-distribution factor K_m for helicals can be determined by Fig. 2. There is reason to believe that, when the tooth can be considered as a plate, the K_m-values for lower face to tooth-height ratios will be as indicated in Fig. 2(*b*).

The amount of lead deviation represents the combined effect of helix error of the pinion, helix error of the gear, and the misalignment of the pinion and gear axes under load. F_m should generally exceed F.

Cognizance should be had of the fact that the operating alignment errors are not always easily evaluated. As a guide, the K_m-values in Table 3 have been found typical for commercial gears covered by Fig. 2.

In the manufacture of wide-face helical gears, the errors per inch of face across the face width are in some areas partially compensated so that a wavelike error rather than a uniformly increasing error is present. A stiffness calculation then becomes too involved for a practical solution. Under these circumstances, special design procedures involving bending and torsional deflection are used and correlated with appropriate manufacturing techniques. For this type of gear, the K_m-values in Table 4 may be used.

Table 3 Typical K_m-values

Condition	K_m
Accurate mountings, low bearing clearances, minimum elastic deflection, precision gears	1.1–1.4
Less rigid mountings, less accurate gears, contact across full face	1.5–1.8
Accuracy and mounting such that less than full face contacts	Over 2 to over 4

Table 4 Guide to load-distribution factor K_m for wide-face helical gears

Ratio of F/d	Tooth contact	Load-distribution factor, K_m
1.0 or less	95% face-width contact obtained at 1/3 torque	1.4 at 1/3 torque
	95% face-width contact obtained at full torque	1.1 at full torque
	75% face-width contact obtained at 1/3 torque	1.8 at 1/3 torque
	95% face-width contact obtained at full torque	1.3 at full torque
	35% face-width contact obtained at 1/3 torque	2.5 at 1/3 torque
	95% face-width contact obtained at full torque	1.9 at full torque
	20% face-width contact obtained at 1/3 torque	4.0 at 1/3 torque
	75% face-width contact obtained at full torque	2.5 at full torque
	Teeth are crowned	
	35% face-width contact at 1/3 torque	2.5 at 1/3 torque
	85% face-width contact at full torque	1.7 at full torque
Over 1 less than 2	Calculated combined twist and bending of pinion not over 0.001 in. over entire face	
	Pinion not over 250 Bhn hardness	
	75% contact obtained at 1/3 torque	2.0 at 1/3 torque
	95% contact obtained at full torque	1.4 at full torque
	Calculated combined twist and bending of pinion not over 0.0007 in. over entire face	
	Pinion not over 350 Bhn hardness	
	75% contact obtained at 1/3 torque	2.0 at 1/3 torque
	95% contact obtained at full torque	1.4 at full torque
	30% contact obtained at 1/3 torque	4.0 at 1/3 torque
	75% contact obtained at full torque	3.0 at full torque
	Twist and bending exceeds 0.001 in. over entire face	Calculate effects of deflection and either adjust helix angle to compensate for deflection or increase K_m to allow for both misalignment errors and deflection

Geometry Factor J. The geometry factor evaluates for stress-computing purposes the shape of the tooth, the position at which the load is applied, the stress concentration and correction effects, and the sharing of load along the contact lines.

For many years tooth-stress calculations were largely based upon the Lewis' parabolic beam and other modified cantilever-beam analyses. With the helical type of contact, the theory of plates is more suited for certain conditions and has been reported by MacGregor [14] and Marin and Shenk [15]. Wellauer and Seireg [16] present this approach based upon theoretical analysis and experimental verification.

Different load conditions cause the maximum stress to be located at certain positions across the face of the gear tooth. For

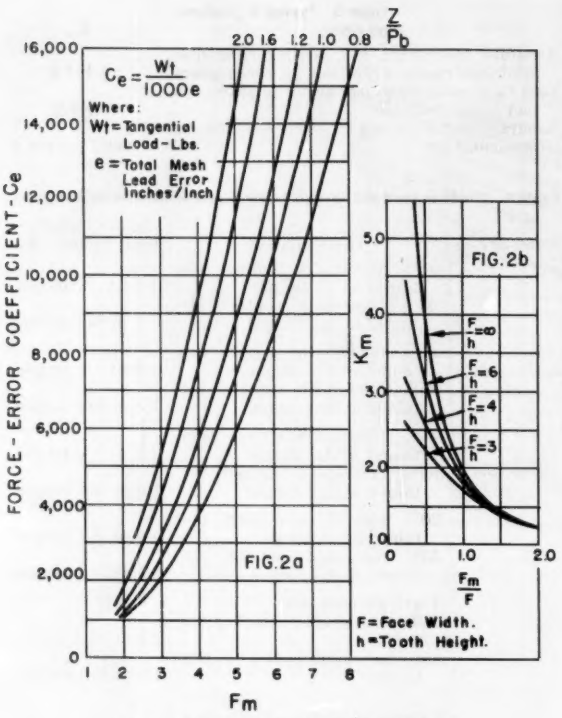

Fig. 2 Helical-gear load-distribution factors

example, in Fig. 3 are shown three different contact and bending-moment conditions for helical gears.

For specific cases, any one of these three contact conditions might be the worst loading condition for the derivation of a tooth-form factor. For example, a helical-gear tooth with low axial overlap might be considered as a beam loaded obliquely from the edge of the face to the tip of the tooth, as in Fig. 3(*a*). A wider face width with properly relieved ends might change the system to an elastic plate having oblique loading and double buttressing to augment the load capacity as in Fig. 3(*b*). The normal worst loading condition using the tooth as a cantilever plate with an oblique line of loading is shown in Fig. 3(*c*). Other variations of contact conditions or load distribution across the contact line might have to be considered.

The geometry factor also includes other geometric terms and, in the development and use of a particular formula, the various functions of the angles may be included in the geometry factor for simplicity of computation. It is for this reason that considerable care should be taken in using the geometry-factor terms from various standards or rating formulas to be sure that they include all the factors necessary for the stress calculation. For example, the helical geometry factor includes the term $\cos \psi$ to permit the transverse diametral pitch rather than the normal diametral pitch to be used in the stress and power formula.

For helical gears, a suggested geometry factor is

$$J = \frac{Y_c \cos^2 \psi}{K_f m_N} \tag{9}$$

where

Y_c = form factor for one normal diametral pitch taken at most critical loading

K_f = stress correction factor which depends on:

1 Effective stress concentration
2 Location of load.
3 Plasticity effects.
4 Residual-stress effects
5 Materials-composition effects.
6 Surface finish:
  (*a*) Resulting from gear production.
  (*b*) Resulting from service.
7 Hertz stress effects.
8 Size effect.
9 End of tooth effects.
10 Notch sensitivity.

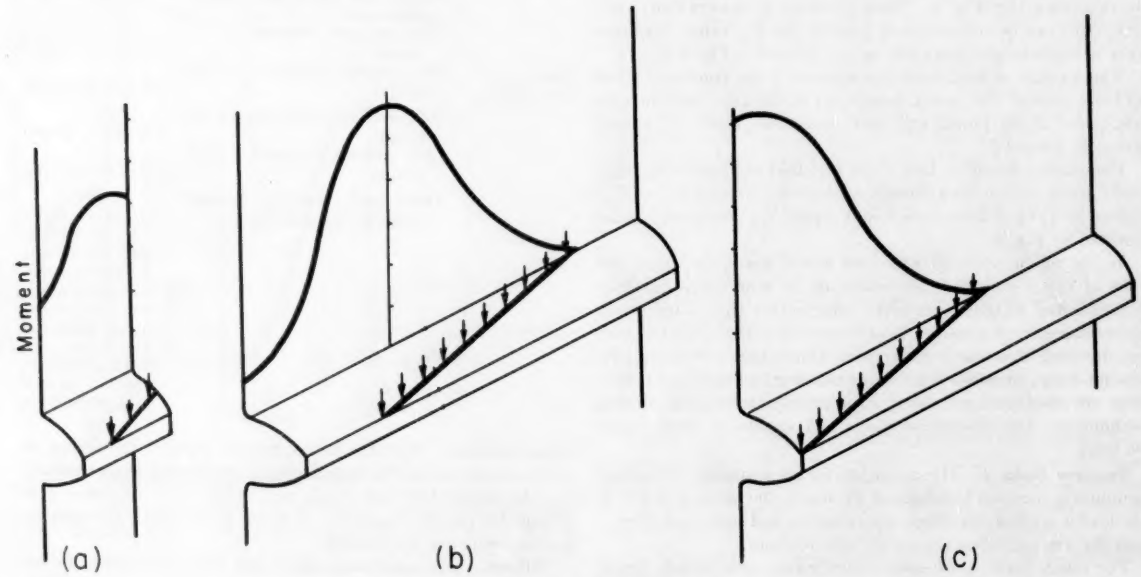

Fig. 3 Helical-gear contact conditions and bending moment

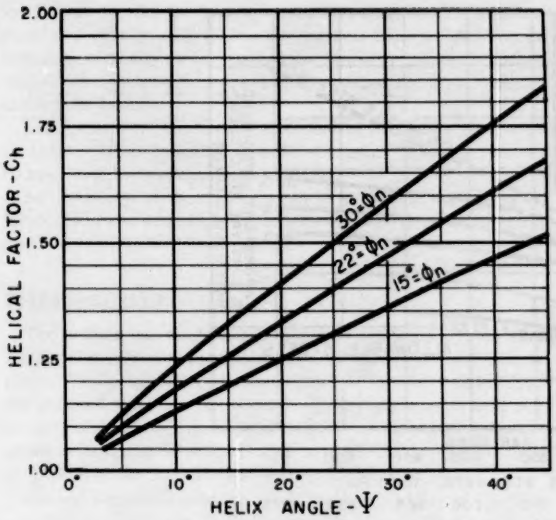

Fig. 4 Helical factor

m_N = load-sharing factor, composed of:

1 Profile contact ratio.
2 Face-contact ratio.
3 Crowning effect.
4 Strengthening effect of unloaded ends.
5 Intensity of loading along the contact line.

ψ = helix angle

For loading conditions as in Fig. 3(*c*), the form factor is

$$Y_c = \frac{1}{\frac{\cos \phi_{LN}}{\cos \phi_n}\left(\frac{1.5}{XC_h} - \frac{\tan \phi_{LN}}{t_w}\right)} \tag{10}$$

where

values for the helical factor C_h are in Fig. 4

C_h = ratio of root bending moment produced by tip loading to root bending moment produced by same intensity of loading applied along oblique helical contact line

ϕ_n = normal pressure angle

ϕ_{LN} = angle of load application at tip

t_w = tooth thickness at section of critical loading

X = $t_w^2/4h$ (conventional value obtained from the Lewis layout)

The advantage of equation (10) is that it can make use of the widely published data on form factors developed for spur-gear tip loading normally used in the Lewis type formula. Important gear applications requiring very accurate results should be computed individually.

The stress-correction factors normally used are based upon photoelastic studies and unfortunately are mainly useful for the spur-gear type of loading. The values used for helical gears must reflect the special condition of the oblique line of contact. The tip-loading results of Dolan and Broghamer [17] seem reasonable to accept since the location of the maximum bending moment occurs beneath the upper portion of the oblique contact line. For narrower faced gears which can be considered as a beam having the equivalent load nearer the root, an increased K_f-factor might be necessary.

Emphasis is placed upon the necessity of correcting stress-concentration effects by the notch-sensitivity properties of the material. This phenomenon is clearly reflected in gear performance and can be as much as 25 per cent in increased capacity for annealed gears. The data of Sines and Waisman [18] have been used successfully.

It must be recognized that the stress-concentration factor varies from one at a few number of cycles to a maximum at approximately 10^8 cycles. The data supplied by Finch [19] have been used successfully for gears.

The load-sharing factor m_N as applied to helical gears can be considered as a measure of the maximum load intensity along the lines of oblique contact.

The average length of contact for helical gears is

$$L_{AVE} = \frac{0.95ZF}{p_N} \tag{11}$$

If the load is divided evenly along the lines of contact, m_N can be considered as

$$m_N = \frac{p_N}{0.95Z}$$

where Z = length of line of action in plane of rotation, in.

Various calculations to estimate load sharing have been made to compensate for the Hertz contact deflection, and the like. Fig. 5 shows a typical case which indicates that both the pinion and gear deflection can affect the results importantly and, hence, individual analysis is required for accurate computation. It is expected that m_N varies between the values $p_N/0.80Z$ to $p_N/0.95Z$.

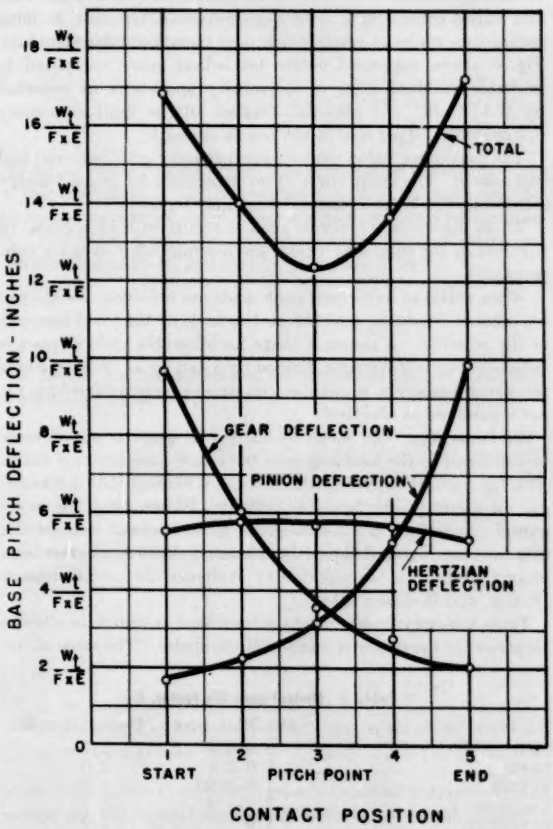

Fig. 5 Base pitch deflection during various phases of contact

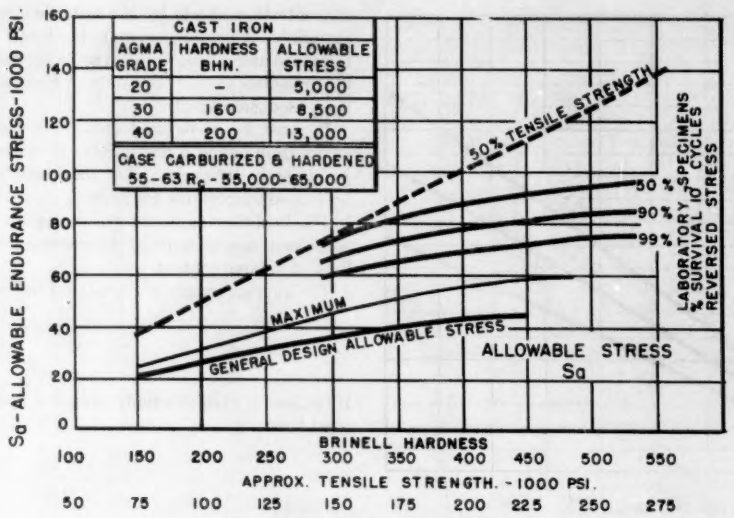
CAST IRON
AGMA GRADE | HARDNESS BHN. | ALLOWABLE STRESS
20 | – | 5,000
30 | 160 | 8,500
40 | 200 | 13,000
CASE CARBURIZED & HARDENED
55–63 Rc - 55,000–65,000
50% TENSILE STRENGTH
50 %
90 %
99 %
LABORATORY SPECIMENS % SURVIVAL 10^7 CYCLES REVERSED STRESS
MAXIMUM
GENERAL DESIGN ALLOWABLE STRESS
ALLOWABLE STRESS Sa
Sa - ALLOWABLE ENDURANCE STRESS - 1000 PSI.
BRINELL HARDNESS
100 150 200 250 300 350 400 450 500 550
APPROX. TENSILE STRENGTH. - 1000 PSI.
50 75 100 125 150 175 200 225 250 275
0 20 40 60 80 100 120 140 160

Fig. 6 Helical-gear allowable stresses

Factors Associated With Allowable Stress

The calculated stress cannot exceed an allowable stress modified for the operating temperature, the factor of safety, and the number of cycles of load application.

Allowable Stress s_a. The allowable stress for 10,000,000 cycles of load application is usually best determined by field experience and varies considerably with heat-treatment methods, forming techniques, material composition, and metallographic structure. Fig. 6 shows suggested values for helical gears, compared to probable survival rates of laboratory specimens as reported by WADC [8], and also the flexural fatigue limit commonly designated as 50 per cent of the tensile strength.

The maximum value requires exceptionally good material and processing. The lower curve is recommended for general design purposes, even lower values are sometimes required.

When the stress is reversed such as occurs with idler gears, 70 per cent of the suggested values are recommended as being conservative.

When static or infrequent peak loads are involved, the allowable stresses might be selected on the basis of the yield strength of the material. A common range for allowable yield stresses is between the yield strength divided by 3 and by 4. When yield is the governing stress, sometimes the stress-concentration factor is not considered as effective.

Life Factor K_L. The stress developed in gears is not directly proportional to the load and even the stress concentration varies with the number of cycles; therefore, it is evident that determining an accurate life factor is difficult. When long life is required, consideration must be given to the normal wear of the gear and bearings and the effect this might have on contact conditions. Life data are reported by Wellauer [20] and Coleman, Dudley, and Wellauer [21].

Table 5 shows values which have been used to adjust the allowable stress for the required number of life cycles. The slope of the curve in the finite region will vary with the material, hardness, and heat-treatment, the lower values being applicable to the lower hardnesses.

Table 5 Helical-gear life factor, K_L

No. of cycles	450 Bhn max	Case-carburized
1000	3.0–4.0	2.7
10000	2.0–2.6	2.0
100000	1.6–1.80	1.5
1 million	1.1–1.4	1.1
10 million	1.0	1.0
100 million	1.0–0.9	1.0–0.9

When a gear set is to be operated at varying loads and number of cycles, the author's experience seems to indicate that the loadings beneath the endurance limit do not contribute to a decreased life. The exact point at which accumulative fatigue damage to gears occurs is not yet well established.

Factor of Safety K_R. An increasing awareness of the spread or scatter of material properties and the similar performance of actual machine elements subjected to fatigue stress have brought about a wider scope of meaning to the term "factor of safety." The old concept of factor of safety to guard against any possible failure, or to cover ignorance, must accommodate modern notions regarding risk or reliability as related to percentages of failure. Wellauer [22] indicated a rational basis upon which to select a factor of safety. The values in Table 6 seem reasonable. Failure in this table does not mean immediate fracture by the applied load, but rather a shorter life than expected.

Table 6 Helical-gear factor of safety, K_R

Requirements of application	Factor of safety
High reliability	1.50–3.00
Fewer than 1 failure in 100	1.00–1.25
Fewer than 1 failure in 3	0.70–0.80

Temperature Factor K_T. Temperature can affect helical-gear capacity by its tempering effect on the material, lowering of the properties, and by distorting the blank or teeth. For most helical gears, no correction is required if the blank temperature does not exceed 250 F, and K_T is then used as 1. Case-carburized gears operating above 160 F might require a correction. If accurate data are not available, the following correction used for bevel gears might be satisfactory:

$$K_T = \frac{460 + T_F}{620} \qquad (12)$$

where T_F = peak operating temperature of oil, deg F.

Conclusions

This paper indicates the complex selection of factors required to evaluate the strength of helical-gear teeth accurately. Some of

the factors are not evaluated accurately, some are even understood imperfectly. Therefore, the engineer must judge his computations critically on the basis of the validity of the assumptions used for operating accuracy, allowable stresses, dynamic loadings, and similar factors.

The factors and coefficients discussed in this paper are known to directly affect helical-gear-tooth strength. These factors can be simplified to develop design formulas.

An awareness of these factors can be employed usefully to interpret field and laboratory experiences as well as to lead to more precise evaluations of the variable.

Acknowledgments

The author has made use of data accumulated by the Gear Rating Committee of the American Gear Manufacturers Association. Thanks are offered to the committee members and AGMA for permission to use these data. Many statements and suggested values for factors are the personal opinion or contribution of the author, and these should not be construed as officially those of AGMA or the AGMA Gear Rating Committee.

Special acknowledgment is made to Darle Dudley of the General Electric Company, Wells Coleman of Gleason Works, and also to Q. Hein and Ali Seireg of The Falk Corporation for their help and contributions.

References

1 AGMA Standard No. 151.01, "Application Classification for Enclosed Speed Reducers," American Gear Manufacturers Association, Washington, D. C., 1957.

2 AGMA Standard No. 150.01, "Application Classification for Gearmotors," American Gear Manufacturers Association, Washington, D. C., 1953.

3 G. Niemann and H. Rettig, "Dynamic Gear Tooth Loads, Part 1 and 2," *Zeitschrift des Vereines Deutscher Ingenieure*, vol. 99, 1957, pp. 89–96 and 131–137.

4 A. Y. Attia, "Dynamic Loading of Spur Gear Teeth," TRANS. ASME, series B, JOURNAL OF ENGINEERING FOR INDUSTRY, vol. 81, 1959, pp. 1–9.

5 S. L. Harris, "The Dynamic Loads in the Teeth of Spur Gears," *Proceedings of The Institution of Mechanical Engineers*, vol. 172, 1958, pp. 87–100.

6 O. J. Horger, T. J. Dolan and B. J. Lazan, "Fatigue" (three papers presented at National Metal Congress, 1953), American Society for Metals, Cleveland, Ohio, 1954.

7 G. Lundberg and A. Palmgren, "Dynamic Capacity of Rolling Bearings," *Acta Polytechnica*, vol. 1, No. 3, 1947, (also IVA, Handlingar No. 196).

8 Wright Air Development Center, Technical Report 54-531, Supplement 1, WADC, October, 1955.

9 G. V. Uzhiz, "Mechanical Aspect of Size Effect on Fatigue of Metals," International Conference on Fatigue of Metals, 1956, London, England, The Institution of Mechanical Engineers, Paper No. 17, 1956.

10 C. Weber and K. Banaschek, "Form and Profile of Spur and Helical Gears," VDMA, *Fachgemeinschaft Getriebe und Antriebselemente, Schriftenreihe Antriebstechnik*, heft 11, F. Vieweg and Sohn, Braunschweig, Germany, 1953.

11 R. P. Van Zandt, "Proposed Practice for the Strength of Spur Gears," AGMA, October, 1951.

12 D. W. Dudley, "Practical Gear Design," McGraw-Hill Book Company, Inc., New York, N. Y., 1954.

13 M. D. Trobojevic, "Load Distribution on Helical Gear Teeth," *The Engineer*, vol. 204, 1957, pp. 187-190 and 222–224.

14 C. W. MacGregor, "Deflection of a Long Helical Gear Tooth," *Mechanical Engineering*, vol. 59, 1935, pp. 225–227.

15 J. Marin and R. H. Shenk, "Stresses and Deflections in Eccentrically Loaded Gear Teeth," ASME Paper No. 54—A-79, 1954 (unpublished).

16 E. J. Wellauer and A. Seireg, "The Bending Stress of Gear Teeth," published in this issue, pp. 213–222.

17 T. J. Dolan and E. L. Broghamer, "A Photoelastic Study of Stresses in Gear Tooth Fillets," University of Illinois, Engineering Experiment Station, Bulletin No. 335, 1942.

18 G. Sines and J. L. Waisman, "Metal Fatigue," McGraw-Hill Book Company, Inc., New York, N. Y., 1959, p. 303.

19 W. G. Finch, "A Study of Fatigue of Steels in the Finite Region of the *S-N* Curve," *Proceedings, ASTM*, vol. 52, 1952, pp. 759–778.

20 E. J. Wellauer, "Strength-Stress Life of Helical Gear Teeth," *Proceedings of the Society for Experimental Stress Analysis*, vol. 10, No. 2, 1953, pp. 37–52.

21 W. Coleman, D. W. Dudley and E. J. Wellauer, "Fatigue Strength Characteristics of Gear Teeth," a Symposium, AGMA, June, 1954.

22 E. J. Wellauer, "What Do Calculated Gear Stresses Mean?" *SAE Transactions*, vol. 65, 1957, pp. 392–402.

APPENDIX

Simplified Derivation of Strength Formula for Helical-Gear Teeth

In a beam or plate the maximum stress is computed as follows:

$$s = \frac{6m}{t^2}$$

where

m = moment lb-in. per in. of width

t = thickness at section of maximum stress

For a spur gear—(0-deg helical angle)

$$m = \frac{W_t h}{F}$$

where

W_t = transmitted tangential load force

F = face width

h = moment arm

or

$$s = \frac{W_t 6h}{Ft^2}$$

The term $t^2/6h$ can be expanded to a form factor (designated Y). In this derivation it will be combined with other geometrically dependent parameters and called a geometry factor (designated J). Form factors and geometry factors are conventionally determined for unity P_d and for any particular pitch:

$$s = \frac{W_t P_d}{FJ}$$

In helical gearing, instead of the tangential load W_t, the load in normal plane is used.

$$W_n = \frac{W_t}{\cos \psi}$$

where W_n = tangential load in the normal plane.

Instead of the load being distributed along the line of contact equal to net face width F, it is distributed along a minimum length of contact:

$$L_{\min} = \frac{0.95FZ}{p_N}$$

where

$L_{\min}$ = minimum contact length

Z = length of line of action in plane of rotation

p_N = normal base pitch

The form factor Y_c for helical gears is based on the normal tooth section for the virtual number of teeth at a normal diametral pitch of unity:

$$W_n = \frac{W_t}{\cos \psi} = \frac{s_t\, 0.95FZ\, Y_c}{K_f p_N P_{nd}}$$

where

s_t = calculated stress, psi
K_f = stress concentration factor
P_{nd} = normal diametral pitch
m_N = load sharing ratio
$m_N = p_N/0.95Z$
$P_{nd} = P_d/\cos \psi$
P_d = transverse diametral pitch
J = geometry factor

$$J = \frac{Y_c \cos^2 \psi}{K_f m_N}$$

$$W_t = \frac{s_t F Y_c \cos^2 \psi}{m_N K_f P_d}$$

$$W_t = \frac{s_t F J}{P_d}$$

Rearranging terms and adding the modifying terms developed by the AGMA Gear Rating Committee results in the final equation:

$$s_t = \frac{W_t K_0}{K_v} \frac{P_d}{F} \frac{K_s K_m}{J}$$

DISCUSSION

J. K. Morris[2]

This paper is a very excellent presentation of the many factors involved in determining the strength of helical gear teeth. Tremendous quantities of data have been considered, analyzed, and studied as a background for this paper. The author has ably pointed up the problem and in most cases offered the designer a workable solution with recommendations for the application of generally suitable factors. The suggested reliability numbers related to factor of safety are helpful and courageous.

All the factors mentioned have their impact on the prophesying and predicting of gear life and reliability, but necessarily must be integrated with additional factors before the final gear selection can be determined.

In agreement with the author, I must also emphasize that considerably more data must be obtained and carefully analyzed before final values can be placed on each of the factors. Funds are needed but have not been available for engineers to thoroughly research and analyze this subject. However with the advance of technology and the availability of high-speed computers, more thorough investigations can be made into the many variables affecting gear mesh dynamics and geometry. The gear mesh regime as pointed out by the author is not fully understood and catalogued.

The mechanical engineer who is not a trained gear specialist is advised to carefully consider the author's statements in this paper. These statements necessarily had to be brief, but they encompass large amounts of experience, calculation, and investigation of gear engineering principles.

[2] Manager of Engineering, Western Gear Corporation, Lynwood, Calif. Mem. ASME.

Mr. Wellauer has been working with this problem for many years and has recently been co-ordinating the activities of the AGMA Gear Rating Committee. He has been careful to definitely state those areas which are based on experience and those which are based on opinion. For this frankness, he should be commended highly.

This paper as presented is another useful tool to the gear engineer, while pointing out direction for further investigations and analytical work in the field of strength rating of helical gears.

W. P. Welch[3]

The paper is a thorough and able presentation of the factors affecting the strength of helical gears. The following comments are based on the writer's experience with wide-face high-power high-speed helical gears.

Dynamic effects *per se* are not of great importance in accurately cut high-speed helical gears, as contrasted with subtle thermal effects and distortions due to centrifugal forces, these being of more importance by an order of magnitude. For these reasons, we would not apply the velocity factors of Fig. 1 to this class of gearing. Instead we would use a factor of 1.0.

Table 4, a guide to load-distribution factors for wide-face helica gears, is a very fine contribution and should provide a good basis for the development of standards for tooth marking. The fact that K_m is shown higher for partial loads of one third torque emphasizes two factors:

(a) Heavily loaded gears should always be marked at partial loads to assure good alignment and tooth geometry.

(b) Good marking at full power does not assure good alignment for heavily loaded gears, and, conversely, misalignment is relatively more serious in lightly loaded gears than in heavily loaded gears, provided both gear sets are designed with the same nominal factor of safety.

The helical gear load distribution factors of Fig. 2 are very useful but should be extended to at least $C_c = 100{,}000$ to be applicable to wide-faced helical gears.

The helical factors (or "diagonal loading factors") of Fig. 4 should always be applied when an accurate calculation of tooth stress in a helical gear is to be made. These factors should not be based on the worst case of loading, Fig. 3(c), for wide-faced gears, since the greater flexibility of the tooth ends does not allow the load to be uniform to the tip end of the contact line as portrayed in Fig. 3(c). In this connection, we would like the author's comments on what consists of "properly relieved ends," as referenced on the top line of page 208, since a good theoretical case can be made for not relieving the tooth ends, if one considers the enhanced flexibility of the end of the tooth in contrast to that of an infinitely long tooth.

Author's Closure

The author wishes to thank those who so kindly offered verbal and written discussions.

To Mr. Welch's statement that Fig. 2 should be extended to $C_c = 100{,}000$, the author agrees. Data someday should be available to extend the curve to these higher values.

By "properly relieved ends" is meant a relief of load either by dimensional modifications or inherent flexibility controlled by design.

[3] Manager, Gearing Section, Marine Products Engineering, Westinghouse Electric Corporation, Lester, Pa. Mem. ASME.

Bending Strength of Gear Teeth by Cantilever-Plate Theory

E. J. WELLAUER
Director, Research and Development, The Falk Corporation, Milwaukee, Wis. Mem. ASME

A. SEIREG
Advisory Engineer, Research and Development, The Falk Corporation, Milwaukee, Wis.

This paper presents a study of the bending strength of gear teeth based on a cantilever-plate approach. A semiempirical solution is given for the finite cantilever plate under transverse loads at any location on its surface. The solution which is based on the principle of superposition and a proposed moment-image method showed good agreement with results from strain-gage investigations on cantilever plates simulating the gear tooth. The effects of the position of the line load and the variation of load intensity on the stress distribution at the root are discussed.

THE WELL-KNOWN LEWIS FORMULA for gear teeth [1][1] arrives at the fillet stress from a consideration of the bending of the tooth as a cantilever beam. Lewis assumed that the critical section of the tooth-shaped beam can be determined by the point of tangency of this beam with a hypothetical constant-stress beam represented by a parabola plotted on the center line of the tooth with its vertex on the load line.

With the development of the photoelastic technique, the Lewis approach was found to be in error. This was expected because of its violation of Saint Venant's principle which indicates that the elementary beam theory can only be applied for sections of the beam at distances from both the load and the support which are large in comparison to the depth of the beam. Both the magnitude and the location of the maximum stress as suggested by Lewis were found to be inaccurate, and several empirical methods were introduced for calculating a maximum stress in agreement with the photoelastic findings. Some of the earlier methods (Black [2], Dolan and Broghamer [3], and others) retained the classical Lewis construction and provided modifications on it; while the most recent ones disregarded completely the Lewis approach (Heywood [4], Jacobson [5], Glaubitz [6], Kelley and Pedersen [7]).

Most of the available data on tooth strength are based on experiments with thin models having the load applied normal to the tooth curvature and parallel to the edge. In other words, they are based on the assumption of uniform bending-moment distribution at the root. However, it is well known that the tooth face in practice is usually of considerable length and that the conditions of loading are such that nonuniform bending-moment distribution is expected at the tooth root. The cantilever-beam approach is, therefore, no longer justified for these cases.

In the following work, a cantilever-plate approach to the gear-strength problem will be considered. The approach is general in nature and can be applied to spur, helical, bevel, or worm gears. The answer is formulated so that it can take advantage of the accumulated experimental knowledge on fillet stresses.

The Cantilever Plate

The treatment of the gear tooth as a cantilever plate was first published by MacGregor [8] who applied the theory of elasticity to obtain an exact solution for the deflection along the free edge and the moments at the clamped edge for a thin plate with infinite length loaded by a force acting perpendicularly to the plane of the plate and concentrated in a single point on the outer edge. Because of the complicated Fourier integrals representing the deflection of the plate, the calculation of the deflections and moments were obtained only at the critical points.

Holl [9] used the method of finite differences to obtain an approximate solution for the moments and deflections in a cantilever plate of finite length. By choosing the length of the plate equal to four times its width, the difficult boundary conditions at the free corners were considered in the solution. The plate was divided into square nets of width equal to half the width of the plate and 41 differential equations were solved simultaneously to obtain approximate values of the bending moments at all points of the plate surface.

Jaramillo [10] obtained exact solutions in terms of improper integrals for the deflections and moments due to a transverse concentrated load acting at any arbitrary point of an infinitely long plate (see Appendix). The solution gave the same value as obtained by MacGregor for the case of edge loading. For any position of the load, the value of the maximum bending moment at the fixed edge was found to be independent of the absolute width of the plate or the absolute normal distance between the load and the fixed edge, and was only dependent on their relative value.

In all previous attempts, solutions were obtained for thin cantilever plates loaded by a transverse load acting in the middle section of the plate. However, in gear problems, the loading can be expected on any point of the tooth surface, including the very difficult corner point. A mathematical solution of the moment distribution along the fixed edge of a cantilever plate with finite length, loaded at points away from the central plane is not available and would be a very difficult undertaking in the theory of elasticity.

An experimental evaluation of this problem was attempted by Vartak [11] on steel plates with dimensions (96 × 24 × 0.13 in.) and (36 × 6 × 0.13 in.). The strains at the fixed edge in the direction of the overhung load were measured by electric strain gages. The first plate yielded large deflections (in the order of $3^1/_2$ times the thickness). Therefore only the results from the second plate (where the maximum deflection was about $^1/_2$ the thickness) are of interest here.

In this work a semiempirical solution is given for the cantilever-plate problem under transverse loads on any location on the plate surface. This solution, which is based on the work of MacGregor, Holl, and Jaramillo, was found to be in general agreement with the experimental data of Vartak on thin plates and the tests performed at The Falk Corporation on a thick plate whose thickness is in the same order as its width.

[1] Numbers in brackets designate References at end of paper.

Contributed by the Machine Design Division and presented at the Annual Meeting, Atlantic City, N. J., November 29–December 4, 1959, of THE AMERICAN SOCIETY OF MECHANICAL ENGINEERS.

NOTE: Statements and opinions advanced in papers are to be understood as individual expressions of their authors and not those of the Society. Manuscript received at ASME Headquarters, June 24, 1959. Paper No. 59—A-50.

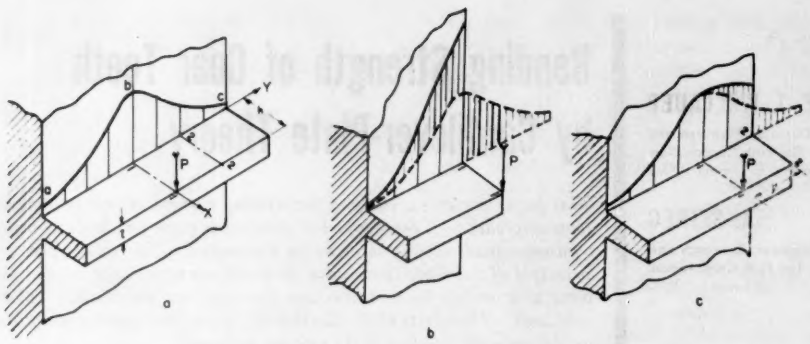

Fig. 1 The moment-image method

The Semiempirical Solution

Considering a plate of infinite length, Fig. 1(*a*), with width h and thickness t, the bending-moment distribution at the fixed edge is known for any transverse load in the plane 1-1. Taking the edge load P as an example, the moment distribution at the fixed edge will be as shown by the curve *abc*.

Now assuming that the plate is cut along the central plane 1-1 and that the load is now applied at the corner of the left-hand portion of the plate. Therefore the moment distribution at its fixed edge has to be changed to accommodate for the fixation moment which was carried by the right-hand part of the plate. By assuming that this extra moment is superimposed on the original part of the moment diagram *ab* as the exact image of the nonexisting part (*bc* in this case), therefore the moment distribution due to a corner load can be easily obtained, Fig. 1(*b*). This procedure of moment images can be used to obtain the moment distribution when the load P is at any finite distance y from the corner of the plate as shown in Fig. 1(*c*).

Although this approach may disturb the orthodox mathematician, the experimental agreement makes it a very simple empirical solution which can be used with enough accuracy for practical engineering purposes.

Knowing that the cantilever-plate problem is a linear problem where superposition can be applied, the moment distribution at the fixed edge due to any type of transverse loading on a finite length of the plate can be readily obtained.

Examples. The case of a load uniformly distributed along the free edge of a finite plate is first considered as a check to the validity of the method. By assuming that the plate, Fig. 2, extends infinitely on both sides of the finite load line *ab*, dividing the load into small increments and applying superposition and the moment-image method, a uniform moment distribution is obtained as expected at the clamped edge of the finite plate, whose length is equal to *ab*.

Several examples which can be of use in gear design are calculated and shown in Figs. 7(*a*) to 10(*a*).

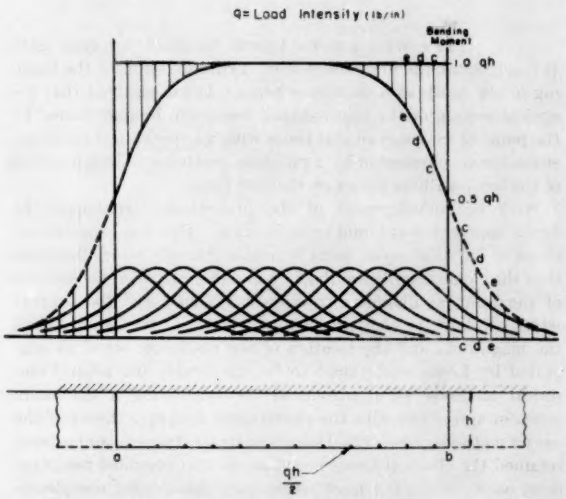

Fig. 2 Moment distribution at the clamped edge of a cantilever plate with uniform loading on the free edge

Tests

An experimental investigation of the problem was performed. Two test models cut from solid pieces of steel were used in the investigation. The first, Fig. 3, represents a thick cantilever plate whose dimensions are $12 \times 2^1/_4 \times 2$ in. with a $^1/_8$-in. fillet at the fixed edge. The second, Fig. 4, represents a rack tooth with 22-deg pressure angle cut in the steel block in such a manner that the loaded surface is horizontal, therefore avoiding the problem of loading and supporting the model.

Rectangular rosettes were used to measure the strain and were formed of individual electric-resistance strain gages with $^1/_8$-in. active length. The rosettes were placed 2 in. apart along the root

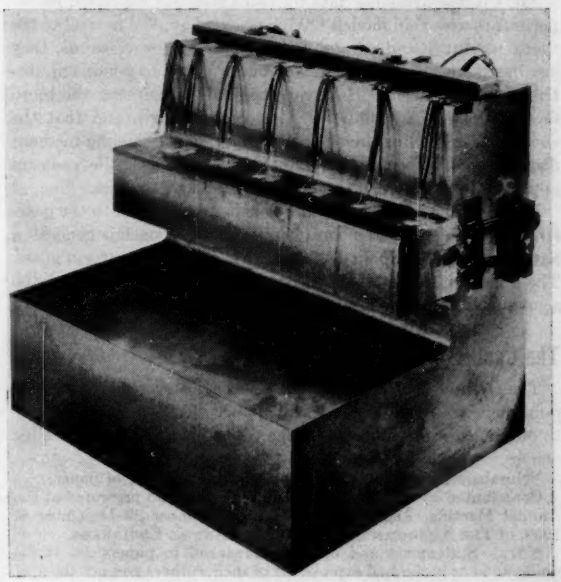

Fig. 3 Thick cantilever plate

of the cantilevers on the flat surface at the junction with the fillet.

The Loading Device. The test models were loaded in a 25-ton Olsen Machine. The point loads were applied with a steel ball, $^1/_2$ in. in diameter. A special device, Fig. 5, was designed in order to insure uniform load distribution for the case of line loads. This device was made of built-up blocks supported on pins. A copper wire $^1/_8$ in. in diameter was placed on the test model underneath the loading blocks to define the position of the load line and to accommodate for any localized deflection or high points. This arrangement was found to insure uniform distribution within ±5 per cent on a 12-in. line.

Procedure and Results. Point loads were applied at several points along the free edge of the first model including the corner point. The test results are shown in Fig. 6. Line loads were also applied at inclination angles of 10, 20, and 90 deg from the free edge of the plate with the load line ending at the corner and near the center of the plate in each case.

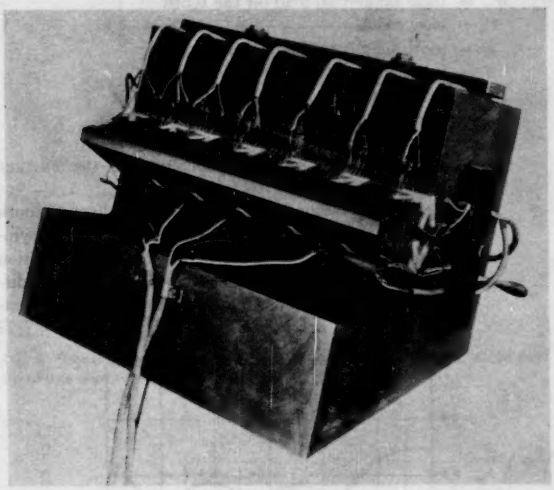

Fig. 4 Tooth-shaped plate

The tooth-shaped plate was loaded at different positions on its surface with uniform line loads varying from 1 to 12 in. in length and with inclination angles from 0 to 90 deg.

In plotting the test results, the moments M_x were considered in all cases to be proportional to the strain e_x measured in the direction perpendicular to the fixed edge. Under the loading conditions given in Figs. 7, 8, and 9 the results were plotted in terms of an inclination factor C which is defined by the ratio of the strain reading e_x under a particular type of loading to the corresponding value under a condition of full line load at the free edge, provided that the load intensity is kept constant. For the loading conditions shown in Fig. 10, the results were plotted in such a manner as to illustrate the effect of the length and position of contact line on the moment distribution at the root due to a total load P applied at the tip of the tooth. The given moment relationships were obtained from the strain readings e_x in each case as compared to the corresponding e_x due to a full-load line at the tip under the same total load.

In converting the strain readings into moments for all the reported conditions, it was assumed that $M_y = \mu M_x$ at all points from which

$$\sigma_y = \mu\sigma_x$$

and

$$e_x = \frac{(1 - \mu^2)\sigma_x}{E}$$

$$= \frac{6(1 - \mu^2)}{Et^2} M_x$$

where

M_x, M_y = moment per unit length in the x and y-directions
σ_x, σ_y = stresses in the x and y-directions
e_x = strain in the x-direction
μ = Poisson's ratio
E = modulus of elasticity
t = plate thickness at the considered section

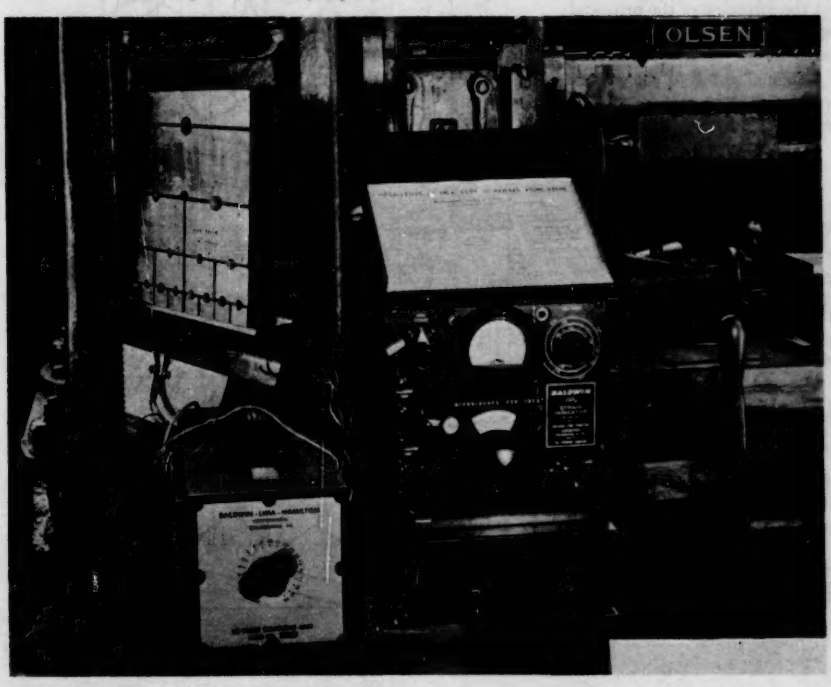

Fig. 5 Test setup

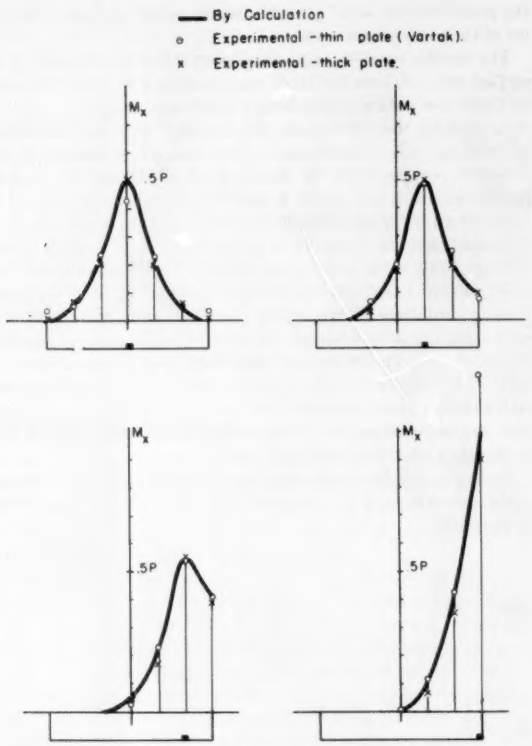

Fig. 6 Moment distribution at the fixed edge due to a concentrated load P at different points of the free edge

The principal stresses and their inclination to the fixed edge were calculated from the strain measurements. It was noticed at the point of maximum strain that the direction of the principal stress is between 0 and 15 deg from the normal to the fixed edge for the loading conditions considered in the test. It was also found that the magnitude of the principal stress at all critical points is 10 to 20 per cent higher than the value of Ee_x or, in other words, it is from 0 to 10 per cent higher than the value of σ_x defined by

$$\sigma_x = \frac{6M_x}{t^2} = \frac{Ee_x}{(1 - \mu^2)}$$

Effect of Nonuniformity of Load Distribution

The bending-moment distribution at the root of a gear tooth can be easily obtained by using the suggested method if the load distribution on the contact line is known beforehand. It is well known that the load distribution is generally nonuniform over the faces of two gears in mesh due to the machining and assembling errors and the elasticity of the gears and their mountings. Several investigations have been conducted to predict the load distribution in both spur and helical gears (Niemann [12], Van Zandt [13], Mönch and Roy [14], Trbojevic [15], and others) and this phase of the gear problem will not be included in this paper.

However, in order to demonstrate the effect of the variable load intensity on the bending distribution at the tooth root, some hypothetical cases are assumed to represent extreme conditions of maldistribution in both spur and helical gears. These cases are shown in Figs. 11 and 12.

The Spur-Gear Tooth

It can be easily seen that the cantilever-beam approach can only be applied to spur gears if the load distribution along the total face width is known to be uniform. A general equation for the maximum bending stress in a spur tooth under a condition of tip loading can be written as

$$S_b = K_m \frac{W_n}{F} \frac{6h}{t^2} K_f$$

or in the familiar form

$$S_b = K_m \frac{W_t}{F} \frac{P_d}{Y}$$

where

W_n = total normal load on the tooth
W_t = total tangential load on the tooth
F = face width
h = tooth height to the critical section
t = tooth thickness at the critical section
P_d = diametral pitch
K_f = stress-concentration factor
K_m = moment-distribution factor
= ratio between maximum moment and the average moment over the total face width
Y = a geometry factor which combines the effect of tooth form, the stress concentration, and the nonsymmetrical stress distribution at the critical section due to the pressure angle—this factor has been discussed extensively in the literature and several empirical formulas are available, [2] to [7], [16], [17]

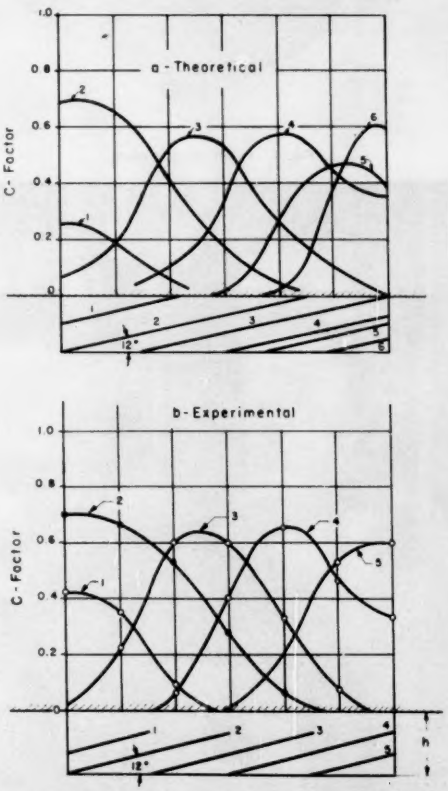

Fig. 7 Moment distribution at the fixed edge for different positions of load line with 12-deg inclination angle

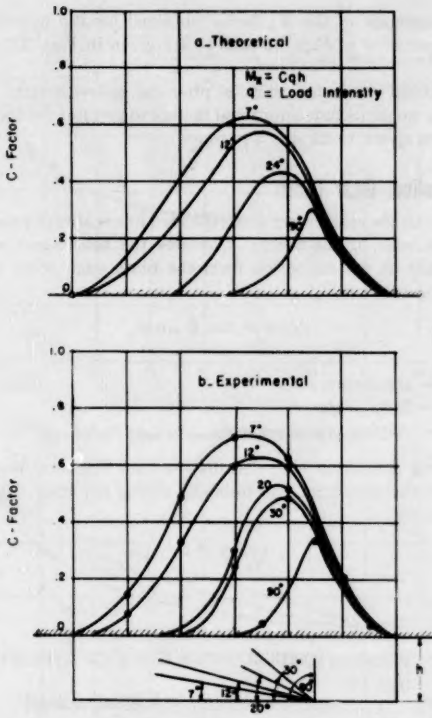

Fig. 8 Effect of inclination angle on the moment distribution at the root (load line away from the corner)

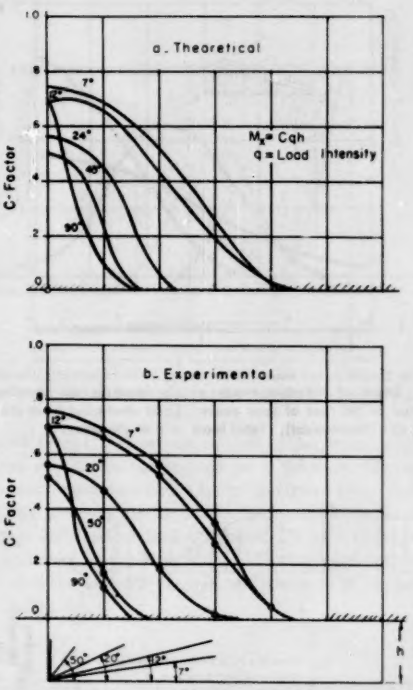

Fig. 9 Effect of inclination angle on the moment distribution at the root (load line starting at the corner)

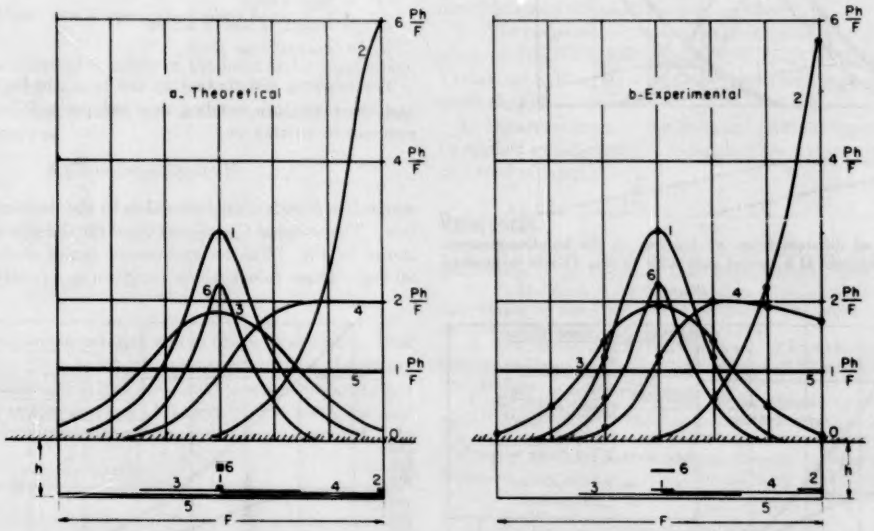

Fig. 10 Effect of different types of tip loading on bending distribution at the root of spur gears; total load = P in all cases. Load uniformly distributed.

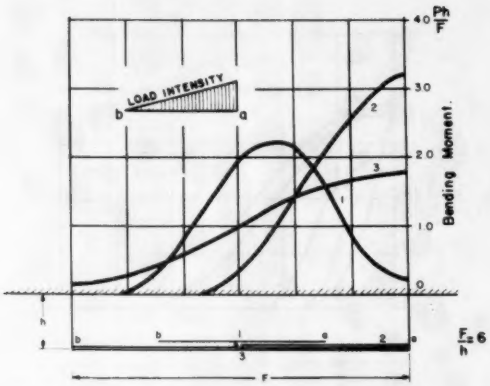

Fig. 11 Effect of different types of tip loading on bending-moment distribution at the root of spur gears. Load changing from maximum at *a* to zero at *b* (theoretical). Total load = *P* in all cases.

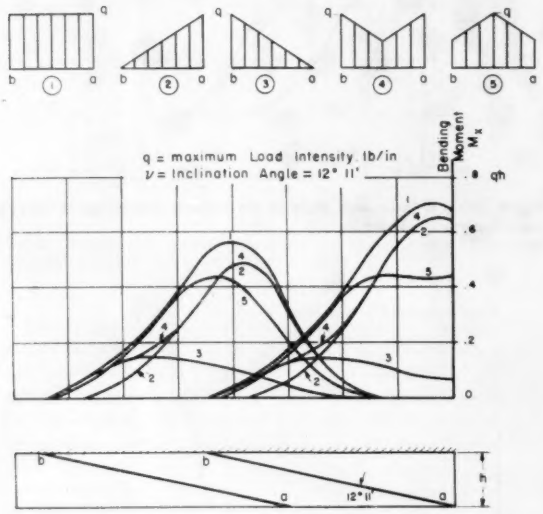

Fig. 12 Effect of different types of loading on the bending-moment distribution at the root of a helical gear with 12-deg 11-min inclination angle

Some examples of the K_m factor obtained for the hypothetical load conditions of Figs. 10 and 11 are given in Figs. 13(*a*) and 13(*b*).

It should be noted that a practical gear-strength rating formula would include additional factors to account for the effect of errors, speed, tooth size, and so on.

The Helical-Gear Tooth

While in the case of spur gears the load line is always parallel to the free edge of the tooth; it crosses the helical-gear surface diagonally at an inclination from the tooth edge given by the following relationship

$$\tan \nu = \tan \psi \sin \phi_n$$

where

ν = inclination angle
ψ = helix angle
ϕ_n = normal pressure angle

Assuming a uniform load distribution over the total length of contact, the maximum load intensity during one mesh cycle can be given by

$$q_n = \frac{W_n}{L_m}$$

where

W_n = total transmitted normal load
L_m = minimum length of contact during the mesh cycle
$= \dfrac{0.95\,FZ}{p_N}$ approximately for well-designed gears
$= Fm_N$

m_N = load-sharing factor $= \dfrac{0.95\,Z}{p_N}$

F = face width
Z = length of line of action
p_N = normal base pitch

The bending distribution at the root can be easily obtained and the maximum bending moment per unit length along the root can be written as

$$M \text{ (maximum)} = Cq_nh$$

where C is a reduction factor due to the inclination of the load line. The value of C was calculated for the critical load position shown in Fig. 14(*a*) for inclination angles changing from 0 to 90 deg. These values which are given as a function of the angle

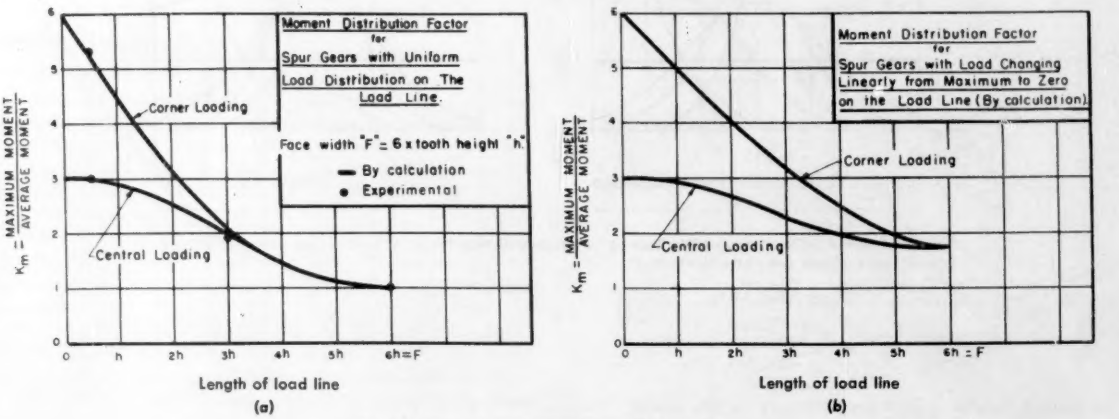
Moment Distribution Factor for Spur Gears with Uniform Load Distribution on The Load Line.
Face width "F" = 6 x tooth height "h"
By calculation
Experimental
Corner Loading
Central Loading
Km = MAXIMUM MOMENT / AVERAGE MOMENT
0 h 2h 3h 4h 5h 6h=F
Length of load line
(a)
Moment Distribution Factor for Spur Gears with Load Changing Linearly from Maximum to Zero on the Load Line (By calculation)
Corner Loading
Central Loading
Km = MAXIMUM MOMENT / AVERAGE MOMENT
0 h 2h 3h 4h 5h 6h = F
Length of load line
(b)

Fig. 13 Moment-distribution factors for spur gears

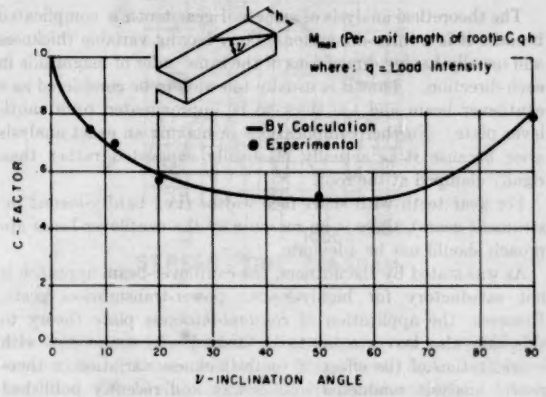

Fig. 14(a) Line of contact inclination factor C

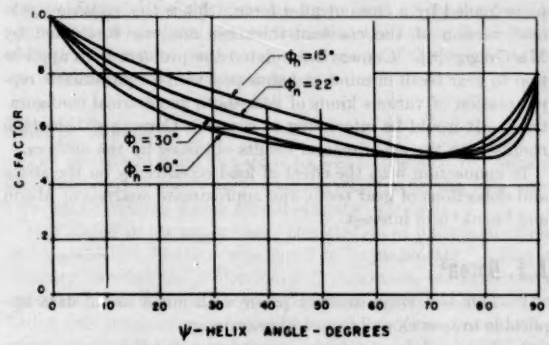

Fig. 14(b) Line of contact inclination factor C

ν in the figure are plotted in terms of the helix and normal pressure angles in Fig. 14(*b*).

The maximum bending stress due to the transmitted load can, therefore, be written as

$$S_b = Cq_n h/Z_e$$

where Z_e is an equivalent modulus in bending for the critical tooth section per unit length, or in the familiar form

$$S_b = C\frac{W_t}{Fm_N}\frac{P_d}{Y\cos^2\psi}$$

where Y is a geometry factor obtained in the normal plane. This factor which is the same as for spur gears accounts for the effects of the tooth form, the pressure angle, and the stress concentration at the root. Dynamic factors, size factors, and so forth, are also used for practical rating of helical gears.

The Wildhaber-Novikov Gearing

The cantilever-plate approach is particularly useful in analyzing strength of gears employing unusual or extreme conditions of loading as in the Wildhaber-Novikov gearing. This gearing system which is being widely introduced in the USSR at the present time was developed independently by E. Wildhaber in 1923 [18] and Novikov in 1954 [19]. In this type of gearing, the load line crosses the tooth surface at a 90-deg inclination to the free edge at any phase of the engagement.

The tooth was treated as a cantilever beam in the Russian literature [20]. In other words, the maximum bending moment at the root was considered to be directly proportional to the moment

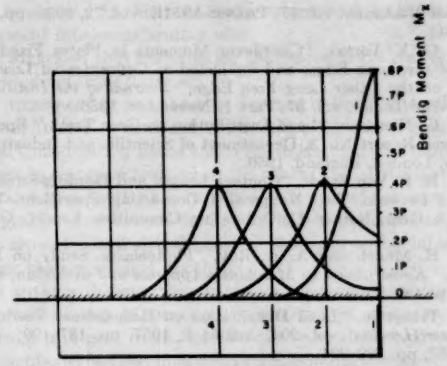

Fig. 15 Bending-moment distribution at the root for different positions of load line with 90-deg inclination angle (Wildhaber-Novikov gearing)

arm (or tooth height). However, in view of the previous analysis, the problem can be better treated as a thick cantilever plate where the load line is perpendicular to the free edge. The maximum bending moment at the fixed edge would be a function of the load only and independent of the tooth height provided that it does not exceed $^1/_3$ the face width. Examples of the moment distribution at the root due to different positions of the load line are given in Fig. 15.

Conclusion

1 A cantilever-plate approach is necessary for rational evaluation of the bending strength of gear teeth with face width considerably larger than the height. This approach which was applied to spur, helical, and Wildhaber-Novikov gearing is also applicable to bevel and worm gears when the load position and distribution on the tooth surface are known.

2 The proposed semiempirical solution of the finite cantilever-plate problem checked closely with the experimental data of Vartak on a thin plate and the performed tests on thick and tooth-shaped plates.

3 Superposition and the proposed moment-image method can be applied satisfactorily in finite cantilever-plate problems under any type of lateral loads.

References

1 W. Lewis, "Investigation of the Strength of Gear Teeth," *Proceedings of the Engineers Club (Philadelphia)*, 1893.

2 P. H. Black, "An Investigation of Relative Stresses in Solid Spur Gears by the Photoelastic Method," University of Illinois Experiment Station, Bulletin No. 228, 1936.

3 T. J. Dolan and E. I. Broghamer, "A Photoelastic Study of the Stresses in Gear-Tooth Fillet," University of Illinois Experiment Station, Bulletin No. 335, 1942.

4 R. B. Heywood, "Tensile Fillet Stresses in Loaded Projections," *Proceedings of The Institution of Mechanical Engineers*, vol. 159, 1948, pp. 384–391.

5 M. A. Jacobson, "Bending Stresses in Spur-Gear Teeth—Proposed New Design Factors Based on a Photoelastic Investigation," *Proceedings of The Institution of Mechanical Engineers*, vol. 169, 1955, pp. 587–609.

6 H. Glaubitz, "The Root-Strength of Straight-Toothed Steel Spur Gears," Sponsored Research Report No. 23, Department of Scientific and Industrial Research, London, England, 1950.

7 B. W. Kelley and R. Pedersen, "The Beam Strength of Modern Gear-Tooth Design," SAE Earth-Moving Conference, Peoria, Ill., March, 1957.

8 C. W. MacGregor, "Deflection of a Long Helical Gear Tooth," *Mechanical Engineering*, vol. 57, 1935, pp. 225–227.

9 D. L. Holl, "Cantilever Plate With Concentrated Edge Load," *Journal of Applied Mechanics*, vol. 4, Trans. ASME, vol. 59, 1937, pp. A-8-10.

10 T. J. Jaramillo, "Deflections and Moments Due to a Concentrated Load on a Cantilever Plate of Infinite Length," *Journal of*

Applied Mechanics, vol. 17, TRANS. ASME, vol. 72, 1950, pp. 67–72, 342–343.

11 G. V. Vartak, "Cantilever Moments in Plates Fixed Along One of the Long Edges and Subjected to Concentrated Loads at a Point on the Other Long Free Edge," *Journal of the Institution of Engineers* (India), vol. 37, Part 1, November, 1956.

12 G. Niemann, "Load Distribution on Gear Teeth," Sponsored Research Report No. 3, Department of Scientific and Industrial Research, London, England, 1950.

13 R. P. Van Zandt, "Contact Length and Bending-Stress Conditions Between Two Nonparallel Contacting Spur-Gear Teeth," AGMA Gear Rating Co-Ordinating Committee Report, October, 1951.

14 E. Mönch and A. K. Roy, "Photoelastic Study on Helical Gears," *Konstruktion in Maschinen-Apparate-und Gerätebau*, vol. 11, 1957, p. 429.

15 Trbojevic, "Load Distribution on Helical-Gear Teeth," *The Engineer* (*London*), vol. 204, August 9, 1957, pp. 187–190; August 16, 1957, pp. 222–224.

16 W. J. Rudinsky, "Effective Coefficient of Stress Concentration at the Root of Gear Teeth," *Vestnik Machinostrojenya*, vol. 37, 1957.

17 L. Kotiuk, "Calculation of Teeth Strength in Bending," *Vestnik Machinostrojenya*, no. 5, 1953.

18 E. Wildhaber, "Helical Gearing," United States Patent Office No. 1,601,750, October 5, 1926.

19 R. W. Fediakian and W. A. Tschechonow, "Gear Transmission With Novikov System," *Vestnik Machinostrojenya*, no. 4, 1958.

20 R. W. Fediakian and W. A. Tschechonow, "Calculations for Novikov Gearing," *Vestnik Machinostrojenya*, no. 5, 1958, pp. 11–19.

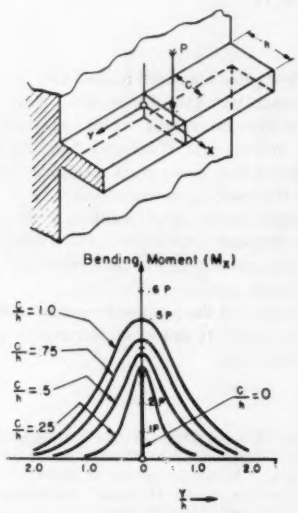

Fig. 16 Bending-moment distribution for a cantilever plate with infinite length (Jaramillo)

APPENDIX

Jaramillo's solution for the moments at the fixed edge of an infinite cantilever plate due to a concentrated load acting on an arbitrary point on its surface is given in Fig. 16.

DISCUSSION

C. W. Bert[2]

The authors are to be commended for their worth-while experimental work and for their correlation of cantilever-plate theory as applied to long gear teeth. This work is another step forward in the important problem of the analysis of stresses and deflections of gear teeth of practical configuration and dimensions.

[2] Department of Engineering Mechanics, The Ohio State University, Columbus, Ohio. Assoc. Mem. ASME.

The theoretical analysis of an actual gear tooth is complicated because it is a three-dimensional body having variable thickness and usually having dimensions of the same order of magnitude in each direction. Thus it is usually too wide to be considered as a cantilever beam and too thick to be approximated by a cantilever plate. Further complications in making an exact analysis arise because it is actually elastically supported rather than rigidly clamped at the root.

For gear teeth with short face widths (i.e., lightly-loaded instrument gears), there is no reason why the cantilever-beam approach should not be adequate.

As was stated by the authors, the cantilever-beam approach is not satisfactory for highly-loaded power-transmission gears. However, the application of *constant-thickness* plate theory to this case also leaves a lot to be desired. In connection with consideration of the effect of tooth-thickness variation, a theoretical analysis conducted by Conway and recently published in Germany (but written in English) is of considerable interest.[3] He considered an infinitely long, variable-thickness, cantilever plate loaded by a concentrated force; this is the variable-thickness version of the constant-thickness analysis conducted by MacGregor [8]. Conway formulated the problem with application to gear teeth in mind and thus provided for parametric representation of various kinds of gear-tooth geometrical configurations. It would be interesting to compare Conway's theoretical results with the experimental results obtained by the authors.

In connection with the effect of load eccentricity on the stress and deflections of gear teeth, the approximate analysis of Marin and Shenk[4] is of interest.

J. F. Boron[5]

1 This is a very excellent paper with much useful data applicable to spur as well as helical gear design.

2 The tooth bending stress formula presented for helical gear design is similar to that proposed and used by Westinghouse in that the bending stress is calculated as a tip loaded cantilever plate, as per Lewis equation, then multiplied by the contact inclination factor (or what we call the diagonal loading factor).

3 The value of the contact inclination factor presented is slightly higher than that used by Westinghouse. See comparison for a 15-deg pressure angle tooth.

Helix angle	Falk factor	Westinghouse factor	Per cent difference
0	1.0	1.0	0
10	0.89	0.86	3.5
20	0.81	0.75	8.0
30	0.75	0.66	13.5
45	0.66	0.54	22.1

The main reason for the difference in the Falk factor is based on the worst load position, or tooth end loading shown in Fig. 14(*a*), while the Westinghouse factor is based on mid-tooth loading. A comparison of these loadings is seen in Fig. 12. The assumption of end tooth loading for accurate helical gears is unduly pessimistic since the tooth ends are more flexible than their centers.

4 Fig. 12 which compares the tooth root bending moment with several types of loadings would be more useful if the various cases were based on equal total tooth loads rather than equal peak loads as done for the spur tooth loading in Fig. 10.

5 To show that the static tooth load analyses, both theoretical

[3] H. D. Conway, "The Flexure of Infinite Rectangular Plates of Varying Thickness," *Ingenieur-Archiv*, vol. 26, 1958, pp. 143–145.

[4] Joseph Marin and R. H. Shenk, "Stresses and Deflections in Eccentrically Loaded Gear Teeth," ASME Paper No. 54—A-79.

[5] Design Engineer, Westinghouse Electric Corporation, Philadelphia, Pa.

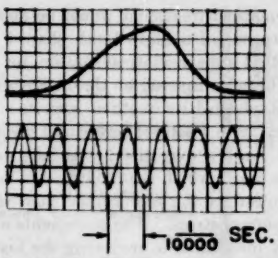

STRESS - TIME DIAGRAM

Fig. 17

and experimental, as described in this paper are acceptable for comparison of stresses and strains in gear teeth under high-speed operation, Fig. 17 shows an oscilloscope signal representing strain of a loaded pinion tooth under high-speed operation as a function of time. This photograph has been taken during high-speed operation of our laboratory high-speed gear test. Note the smooth approach and recession of the strain diagram during the instant of mesh. Also note the asymmetrical shape of the signal due to the inclined load on the pinion tooth.

Allan H. Candee[6]

The writer will point out what he sees in the new and helpful idea presented in this paper, and its relation to the idea contributed by Wilfred Lewis almost seventy years ago.

It is stated in the paper that "the location of maximum stress as suggested by Lewis. . .was found to be inaccurate." This is contrary to what the writer found in measurements made on a considerable number of photoelastic stress patterns obtained by Dolan and Broghamer, in which the position of maximum stress came surprisingly close to the point of tangency of the Lewis parabola with the fillet curve in the gear-tooth outline.

Furthermore, in the publication entitled "Coordinated Rating for the Strength of Gear Teeth," a Symposium sponsored by the American Gear Manufacturers Association Gear Rating Coordinating Committee, E. J. Wellauer, Chairman, 1956, it is shown that the geometry factor Y which appears in equations of the present paper is based upon the position of maximum stress as determined graphically by the method described by Lewis in 1892.

Also, the following line appears on page 209 of the accompanying Paper No. 59—A-121, by E. J. Wellauer (pp. 205–212, this issue): "$X = l_w^2/4h$ (conventional value obtained from the Lewis layout)"

What Lewis did was to provide a practical method of determining the point of maximum stress in the *profile* of a gear tooth. Later, the photoelastic method of showing stress patterns was developed, and that method enables us to determine the ratio of maximum stress to the value estimated by assuming linear variation of stress from a neutral axis of flexure outward to the surface of the tooth. The ratio is usually termed a *stress concentration factor;* and Dolan and Broghamer provided the most extensive information so far about such factors for the cross sections of gear teeth.

The present paper gives us what seems to be a very practical way to determine the stress variation and the position of maximum stress along the *length* of a straight gear tooth, when the load is concentrated at a point and also when it is applied on lines of contact of various lengths and at various inclinations and positions.

In the reported experimental investigation the values measured were of *strain*. The gear designer customarily uses *stress* in his estimates; and stress is considered to be directly proportional to strain. It therefore seems unnecessary to bring bending moment into consideration also.

It is suggested that the term for the values in the charts could be *longitudinal stress factor*.

The treatment in the paper is directed entirely to teeth that are straight and of constant cross section for end to end. Additional consideration seems called for in the case of a tooth that increases in size from one end to the other (as in a straight bevel gear), and to a tooth that in addition is curved (as in a spiral bevel gear). And even a tooth of a helical pinion, that wraps partly around a cylindrical base, would seem to be inherently stronger than a straight tooth.

The authors deserve the thanks of gear engineers for their very practical way of treating the question of stress variation lengthwise of a gear tooth, and for the values obtained in their experiments, to be used in estimating maximum stress.

T. R. Rideout[7]

This paper is a notable contribution to the art of gear design. The method devised by the authors for determining moments by the superimposition of moment images is an excellent example of engineering analysis, the empirical result replacing an otherwise impractical solution.

The data and curves point the way to a solution to the problem of the effect of mal-distribution of load across the face. This will eliminate much of the confusion resulting from proposed methods and eliminate the present arbitrary face widths reduction factor. Of particular value is the fact that values can be established directly from the curves on the basis of the known accuracy of the gears and their alignment and from an estimate of the deflections involved.

As stated, the maximum moment at the fixed edge is independent of the position of the load, but is that moment constant for any point between the load and the fixed edge? The question is prompted by the photographs which seemed to show a rosette position well above the fillet or fixed edge. It is assumed that, if the position is as shown, the authors have some means of correcting the moment for the true value of h.

In applying the moment-distribution factor to the case of spur gears, the question arises as to whether it is truly applicable, as determined, since the increase in the moment, due to the fact that the gear tooth is a short cantilever, is already taken care of by the stress concentration factor K_f, if and when the latter is determined photoelastically. It would seem as though the applicable case of M factors would be only those covering the effect of mal-distribution such as Fig. 10, and that the factor would have to be corrected in some way to avoid doubling the moment increase factor.

On the basis of Case 2 in Fig. 10 and the analysis as described for the moment-image method in Fig. 1, it is difficult to see why, in the case of loading such as 4 and 5, there was not an upturn in each of the curves for the condition at the edge of the face. In other words, can the moment be constant at the edges for a beam of finite length if that moment is determined by superimposing the moment image for an imaginary continuation of the face?

It is unfortunate that deflection readings were not taken along the free edge of the cantilever. The results would be interesting and might throw considerable light on the question of load distribution with particular respect to helical gears. It is believed that the load distribution between teeth in helical gears will have more effect on the bending moments than that of diagonal loading and only can be ignored in the case of wide face gears with a high face contact ratio.

The existing formula assumes, as do the authors, that the load

[6] Rochester, N. Y. Fellow ASME.

[7] Consulting Engineer, Portchester, N. Y. Mem. ASME.

per inch of contact length is uniform for all of the teeth in contact. This is highly questionable as is the unqualified use of the "critical" load position (Fig. 14*a*) for all cases.

The paper is not clear in that the C factor appears to cover only the case of diagonal loading. Is it intended to apply also the same K_m moment distribution factor as established for spur gears? Certainly there are as many helical gears with maldistribution of loading across the face as there are spur gears if one discounts the case of high speed, fine pitch, wide-faced gears such as used in marine propulsion drives.

It is hoped that the authors will appreciate that the foregoing are questions of application rather than of the method and that those questions are prompted by a belief that considerably more work of this nature has to be done before a satisfactory means of determining the breaking strength of gear teeth is evolved. To repeat, this work is a notable contribution to that end.

Authors' Closure

The comments of the discussers are very much appreciated. The Westinghouse stress-time diagram (Fig. 17) is of particular interest since it provides some backing to the application of the theory to an actual gear tooth under high-speed operation. The work presented in this paper is based on a simplified analogy and it is well recognized that the actual gear problem involves many complex conditions which were deliberately avoided in this investigation. Mr. Bert is to be thanked for pointing out the paper by H. Conway which would be valuable in future refinement of the proposed method especially with regard to deflections and load distribution on the contact line. Conway's paper, however, deals only with central loading on an infinite plate and more elaborate mathematical treatment would be necessary for loads at or near the corner of a finite tooth shaped plate. It is of interest to note that a mathematical solution for the finite cantilever plate has been completed at the University of Wisconsin based on the Rayleigh-Ritz method and the findings are in general agreement with Falk's experimental results.[8]

Mr. Candee's concern over the Lewis form factor is beyond the scope of this paper which is primarily dealing with moment or stress distribution at the root rather than the location and value of the maximum stress. The statements on the Lewis approach were only mentioned in reviewing the historical development of gear strength studies and were based on the findings in references [4, 5, 6, and 7]. However, the Lewis construction is widely used and would be acceptable for conventional gears as long as a stress correction factor is used in conjunction with it.

Mr. Rideout's questions are to be answered in the following:

1 As mentioned in the paper, for long cantilever plates, the maximum moment in a cantilever plate is independent of the absolute position of the load or the absolute width of the plate and is only dependent on their relative value.

2 The strain values on which the moment distribution is based were measured away from the region of stress concentration. The summation of the moment checked very closely with the moment of the load about the considered plane.

3 Cases 4 and 5 of Fig. 10 were obtained both experimentally and by the moment image method. The results checked closely as shown in the paper.

4 The deflection measurements would have been quite difficult in models of the size considered in the investigation

[8] MSc thesis, September, 1959, by R. Little, Department of Engineering Mechanics, University of Wisconsin

Rocket Motor Gear Tooth Analysis (Hertzian Contact Stresses and Times)[1]

ERNEST K. GATCOMBE
ROY W. PROWELL
Professors, U. S. Naval Postgraduate School, Monterey, Calif. Mem. ASME

In this paper a rocket motor turbine-pump reduction gear system is analyzed in regard to Hertzian gear tooth contact stresses and times of contact. It is found that the Hertzian contact stresses vary from approximately 100,000 psi to 200,000 psi. The times of contact vary from three to eight microsec. Some observations regarding the correlation between contact times and gear failures are made. It is indicated that it may be possible to establish design limitations on the contact times to insure satisfactory gear operation. Sample calculations for evaluating each of the typical quantities found in the tables are included.

In the rocket motor to be considered, the liquid oxygen (LOX) and fuel pumps are gear driven off the main turbine shaft through sets of reduction gears as is shown in Fig. 1.

The turbine shaft reaches full speed and full load in 1 sec from start-up. From the data given we have based our calculations on steady-state conditions of 27,000 rpm and 4000 hp. Necessary information for consideration of the accelerating period was not supplied. The analysis pertains to a set of gears found to be most satisfactorily designed, thus a knowledge of the contact stresses and times of contact are pertinent.

We will show how these stresses are determined, tabulate their values, and draw certain conclusions and comparisons with those of other researchers.

Statement of Problem

The problem is that of determining the Hertzian gear-tooth contact stresses and duration of contact for each of five phases of contact for each gear set; namely, the pinion and LOX pump gear, the pinion and idler gear for the fuel pump system, and the idler and gear of the fuel pump reduction gear system.

Data

The following data were supplied by Aero-Jet General Corporation and Western Gear Corporation. The turbine shaft reaches a speed of 27,000 rpm in 1 sec from start-up. It delivers 4000 hp at the 27,000 rpm.

Pinion	LOX Gear	Idler	Fuel Gear
PD = 2.500 in.	PD = 7.9167 in.	PD = 6.0833 in.	PD = 7.1667 in
N = 30	N = 95	N = 73	N = 86
ϕ = 25°	ϕ = 25°	ϕ = 25°	ϕ = 25°
P = 12	P = 12	P = 12	P = 12
a = 0.092 in	a = 0.068 in.	a = 0.068 in.	a = 0.092 in.
F = 1.50 in.	F = 1.50 in.	F = 1.50 in.	F = 1.50 in.
hp = 4000	hp = 2210	hp = 1800	hp = 1800
rpm = 27000	rpm = 8520	rpm = 11100	rpm = 9420
SAE 4620	SAE 4620	SAE 4620	SAE 4620
$(R_c)_s$ = 60 min	$(R_c)_s$ = 60 min	$(R_c)_s$ = 60 min	$(R_c)_s$ = 60 min
$(R_c)_c$ = 30 min	$(R_c)_c$ = 30 min	$(R_c)_c$ = 30 min	$(R_c)_c$ = 30 min

Lubricating oil is MIL-L 7808.
Average temperature of gear box is 150 to 200 F.

Remarks

The Hertzian contact stress in gears is one indicator of the permissible load which a given set of teeth may carry safely. It is a factor used in determining score loads, pitting loads, and so on. Of course there are other factors of great importance, such as surface treatment, the lubricant used, the temperature involved, sliding velocity, and the like, but the contact stress serves as a definite indicator of permissible loads to be transmitted.

The Hertzian contact times are now becoming of importance also, since it has been observed that these contact times are of

[1] Sponsored in part by ONR.
Contributed by the Machine Design Division and presented at the Annual Meeting, Atlantic City, N. J. November 29–December 4, 1959, of The American Society of Mechanical Engineers.
Note: Statements and opinions advanced in papers are to be understood as individual expressions of their authors and not those of the Society. Manuscript received at ASME Headquarters, August 11, 1959. Paper No. 59—A-256.

Nomenclature

a = addendum, in.
b = half width of band of contact, in.
C = center distance, in.
d = distance from pitch point along pinion surface, in.
E = modulus of elasticity, psi
F = face width, in.
$(H_t)_p$ = contact time of pinion, microsec
$(H_t)_g$ = contact time of gear, microsec
$(H_t)_L$ = maximum contact time of lubricant, microsec
hp = horsepower
M_t = transmitted torque, lb in.
N = number of teeth
$\bar{N}$ = contact ratio
n = number of pairs of teeth in contact
P = diametral pitch
PD = pitch diameter, in.
p_b = base pitch, in.
p_c = circular pitch, in.
q_0 = maximum contact pressure between teeth, psi
R = pitch radius of gear, in.
r = pitch radius of pinion, in.
R_o = outside radius of gear, in.
r_o = outside radius of pinion, in.
R_b = base radius of gear, in.
r_b = base radius of pinion, in.
$(R_c)_s$ = Rockwell hardness of surface
$(R_c)_c$ = Rockwell hardness of core
rpm = revolutions per minute
W = transmitted load normal to tooth profile, lb
Z = length of action, in.
ρ = radius of curvature of tooth profile, in.
ϕ = pressure angle, deg
ω = angular velocity, radians/sec
ψ_p = angle shown on Fig. 2, deg
ψ_g = angle shown on Fig. 2, deg

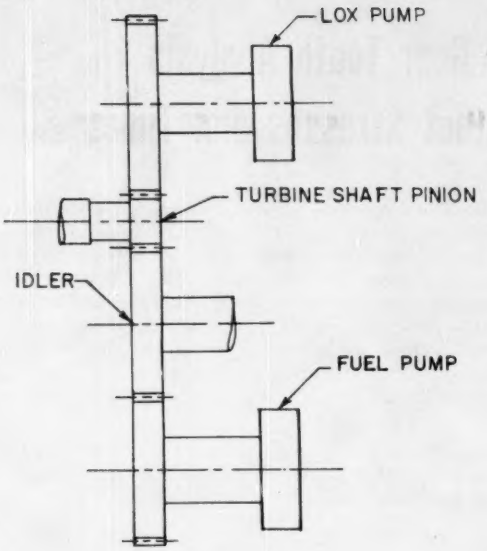

Fig. 1 Arrangement of gears

the same order of magnitude as the relaxation times of the lubricants. It has been observed also, that these thin oil films, such as are found in gear-tooth mating, exhibit peculiar physical properties when loaded with extreme suddenness. These films are believed to act as elastic or plastic solids under these conditions, providing great protection for the tooth surfaces. It is for these reasons that an analysis of these stresses and contact times may be of value.

Definition of Hertzian Contact Stresses and Times

Hertz, the German physicist, derived the equations of elasticity by means of which the contact stresses between elastic bodies could be predicted[1].[2] For a pair of spur gears making contact the elastically deformed area of contact is a rectangle. The maximum contact stress at the middle of this rectangle depends upon the load, the principal radii of curvature, the moduli of elasticity of the materials, Poisson's ratio, and face width.

The Hertzian duration of contact could be defined in any one of several ways. It could be defined as the time that a given *patch* of the lubricant is entrapped between the surfaces of the contacting teeth for any given phase of contact. The patch could have any one of several areas. It could correspond to areas of molecular dimensions, line dimensions, full width of the band of contact dimensions, or the half-width of the band of contact dimensions. In this paper, we have used a *patch* whose area corresponds to the half-width of the band of contact multiplied by the face width of the gears. Thus the contact time for any particular phase of contact is defined as the time that this *patch* of lubricant is entrapped between the surfaces of the gear teeth.

Method of Solution

The contact stresses, for any given phase of contact, will be found by simply substituting proper values of the several variables involved into the appropriate equations for the stresses. These equations will be listed under Equations Used. Likewise, the equations for the Hertzian contact times will be listed under Equations Used.

[2] Numbers in brackets designate References at the end of the paper.

Equations Used

Five phases of contact of any particular pair of teeth are found to be of prime interest, namely, 1 the first or initial phase of contact *i;* 2 the phase where one pair of teeth begins to carry all the load *c;* 3 the pitch point phase *P;* 4 the phase where two teeth again share the load *d;* 5 the last phase of contact *e.* The following is a list of the important equations used:

$$M_t = \frac{63030 \times \text{hp}}{\text{rpm}} \tag{1}$$

$$W = \frac{M_t}{\text{Base radius}} \tag{2}$$

$$\omega = \frac{\text{rpm} \times 2\pi}{60} \tag{3}$$

$$\bar{N} = \frac{\bar{ie}}{p_b} = \frac{Z}{p_b} \tag{4}$$

Radii of Curvature (Fig. 2)

Point i

$$(\rho_p)_i = C \sin \phi - R_o \sin \psi_g \tag{5}$$
$$(\rho_g)_i = R_o \sin \psi_g$$

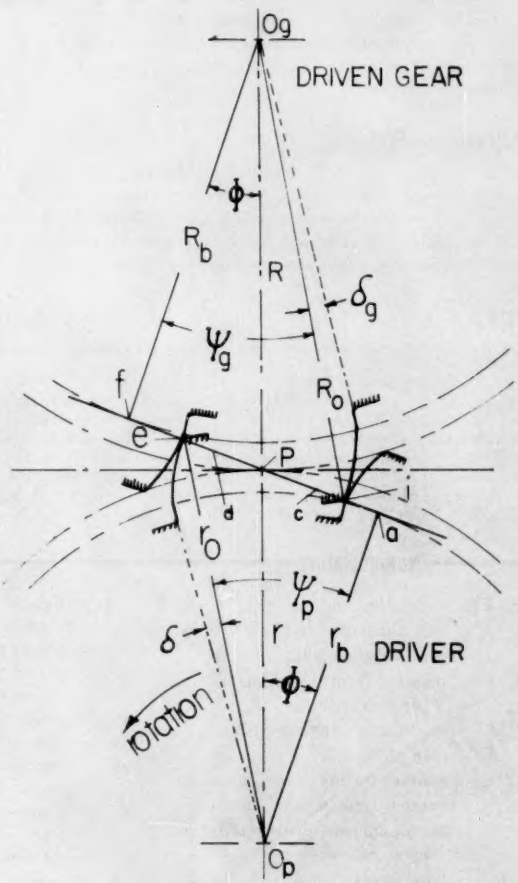

Fig. 2 Spur gear geometry

Point c $(\rho_p)_c = r_o \sin \psi_p - p_b$ (6)
$(\rho_g)_c = C \sin \phi - r_o \sin \psi_p + p_b$

Point P $(\rho_p)_P = r \sin \phi$ (7)
$(\rho_g)_P = R \sin \phi$

Point d $(\rho_p)_d = C \sin \phi - R_o \sin \psi_g + p_b$ (8)
$(\rho_g)_d = R_o \sin \psi_g - p_b$

Point e $(\rho_p)_e = r_o \sin \psi_p$ (9)
$(\rho_g)_e = C \sin \phi - r_o \sin \psi_p$

The maximum Hertzian contact stress q_0 [1] is given by

$$q_0 = 0.418 \left[\frac{WE\,(\rho_p + \rho_g)}{nF(\rho_p \rho_g)} \right]^{1/2} \tag{10}$$

In this equation and in equation (11) a simplifying assumption is made that the load is equally distributed between the two pairs of teeth in contact.

The half-width of the band of contact for any particular phase is given by

$$b = 0.635 \left(\frac{W}{nF\,q_0} \right) \tag{11}$$

The pinion velocity at the contact point perpendicular to the line of action is given by $\rho_p \omega_p$ and that of the gear is given by $\rho_g \omega_g$. The velocity of sliding at the point of contact of the pinion with respect to the gear is given by $\rho_p \omega_p - \rho_g \omega_g$. The numerical values of the products $\rho_p \omega_p$ and $\rho_g \omega_g$ are such that the result is negative for the period of approach and positive for the period of recess. This indicates a change in the direction of the velocity of sliding at the pitch point.

The Hertzian Contact Times

For the pinion $(H_t)_p = \dfrac{b}{\rho_p \omega_p}$ (12)

For the gear $(H_t)_g = \dfrac{b}{\rho_g \omega_g}$ (13)

For the lubricant $(H_t)_L$ is the smaller of the results of equations (12) or (13).

Distance From Pitch Point

It is found convenient to plot several of the variables involved against the distance from the pitch point to any point of contact measured on the surface of the pinion. An expression for this distance d is

$$d = \frac{1}{2r_b} (\rho^2 - \rho_P{}^2)_p \tag{14}$$

where ρ = radius of curvature of the pinion at the point considered, and ρ_P = radius of curvature of the pinion at the pitch point.

Results

The results of the analysis are tabulated in Tables 2, 3, and 4. Table 1 gives the system data. A sample calculation of each of the pertinent quantities in these tables is given in the Appendix.

Table 2 indicates that when the pinion and LOX pump gear mate at the initial phase of contact (i) the radius of curvature of the pinion will be 0.373 in. That of the gear is 1.828 in. The number of pairs of teeth in contact (n) is 2 for this phase. The maximum contact stress is 161,000 psi. The half-width of the band of contact is 0.00599 in. The sliding velocity is −580 in. per sec. The Hertzian contact time for the lubricant is 0.00000368 sec. The distance from the pitch point to this initial point of contact, measured along the surface of the pinion tooth, is −0.062 in. Further, Table 2 gives these values for each of the other four phases of contact. It will be seen that the maximum contact stress of those found in Table 2 is 206,000 psi. This comes at

Table 1 Gear data

	Symbol	Turbine Shaft Pinion	Lox Pump Gear	Turbine Shaft Pinion	Idler Gear	Fuel Pump Gear
Diametral Pitch	P	12	12	12	12	12
Center Distances, inches	C	← 5.2083 →		← 4.2917 →	← 6.6250 →	
Pressure Angle, degrees	ϕ	25	25	25	25	25
Face Width, inches	F	1.5	1.5	1.5	1.5	1.5
Circular Pitch, inches	p_c	0.2618	0.2618	0.2618	0.2618	0.2618
Base Pitch, inches	p_b	0.2373	0.2373	0.2373	0.2373	0.2373
Addendum, inches	a_p | a_g	0.092	0.068	0.092	0.068	0.092
Contact Ratio	$\overline{m}$	← 1.46 →		← 1.45 →	← 1.52 →	
Transmitted Load, pounds	W	4540	4540	3710	3710	3710
Number of Teeth	N_p | N_g	30	95	30	73	86
Pitch Radius, inches	r | R	1.2500	3.9583	1.2500	3.0417	3.5834
Outside Radius, inches	r_o | R_o	1.3420	4.0263	1.3420	3.1097	3.6754
Base Radius, inches	r_b | R_b	1.1329	3.5874	1.1329	2.7567	3.2474
Angle ψ, degrees	ψ_p | ψ_g	32°25'	27°00'	32°25'	27°34'	27°56'
Angular Velocity, radians/second	ω_p | ω_g	2826	892	2826	1162	986

phase (*c*) at that instant when the load is now carried by one pair of teeth. The shortest Hertzian contact time is 3.66 microsec at phase *e*.

Table 3 lists these various quantities for the pinion and idler combination. We note here that the greatest contact stress is 191,000 psi. It also comes at phase (*c*). The shortest contact time comes at phase (*e*) again. It is 3.16 microsec.

Table 4 lists these results for the idler and fuel pump gear system. It indicates a greatest contact stress of 137,000 psi, coming again at point (*c*). The shortest contact time is 4.68 microsec, coming at phase (*i*). The greatest contact stress for the reduction gear system is 206,000 psi, coming at phase (*c*) of the pinion and LOX pump gears. The smallest contact stress is 96,200 psi, coming at phase (*e*) of the idler and fuel pump gear combination.

The greatest lubricant contact time is 7.70 microsec, coming at

Table 2 Analysis of gear operating conditions; turbine shaft pinion and LOX pump gear

Contact Phase	(i)	(c)		(P)	(d)		(e)
Radius of Curvature pinion ρ_p, inches	0.373	0.482		0.528	0.610		0.719
Radius of Curvature gear ρ_g, inches	1.828	1.719		1.673	1.591		1.482
Number of Pairs of Teeth in Contact, n	2	2	1	1	1	2	2
Maximum Hertz Stress q_o, ksi	161	145	206	199	189	134	129
Half Width of Band of Contact b, mils	5.99	6.62	9.35	9.66	10.1	7.13	7.40
Tangential Velocity ($\rho_p\omega_p$) pinion, inches per second	1050	1360		1490	1730		2030
Tangential Velocity ($\rho_g\omega_g$) gear, inches per second	1630	1530		1490	1420		1320
Velocity of Sliding, inches per second	-580	-170		0	310		710
Contact Time, pinion $(H_t)_p$ surface, microseconds	5.68	4.86	6.87	6.46	5.86	4.12	3.66
Contact Time, gear $(H_t)_g$ surface, microseconds	3.68	4.32	6.10	6.46	7.13	5.02	5.63
Maximum Lubricant $(H_t)_L$ Contact Time, microseconds	3.68	4.32	6.10	6.46	5.86	4.12	3.66
Distance from Pitch Point(P) along pinion surface, in.	-0.062	-0.021		0	0.041		0.105

Table 3 Analysis of gear operating conditions; turbine shaft pinion and idler gear

Contact Phase	(i)	(c)		(P)	(d)		(e)
Radius of Curvature pinion ρ_p, inches	0.375	0.482		0.528	0.612		0.719
Radius of Curvature gear ρ_g, inches	1.439	1.332		1.285	1.202		1.094
Number of Pairs of Teeth in Contact, n	2	2	1	1	1	2	2
Maximum Hertz Stress q_o, ksi	148	135	191	186	179	126	122
Half Width of Band of Contact b, mils	5.31	5.80	8.20	8.44	8.78	6.21	6.42
Tangential Velocity ($\rho_p\omega_p$) pinion, inches per second	1060	1360		1490	1730		2030
Tangential Velocity ($\rho_g\omega_g$) gear, inches per second	1670	1550		1490	1400		1270
Velocity of Sliding, inches per second	-610	-190		0	330		760
Contact Time, pinion $(H_t)_p$ surface, microseconds	5.02	4.26	6.02	5.65	5.08	3.59	3.16
Contact Time, gear $(H_t)_g$ surface, microseconds	3.18	3.75	5.30	5.65	6.29	4.45	5.05
Maximum Lubricant $(H_t)_L$ Contact Time, microseconds	3.18	3.75	5.30	5.65	5.08	3.59	3.16
Distance from Pitch Point(d) along pinion surface, in.	-0.061	-0.021		0	0.042		0.105

Table 4 Analysis of gear operating conditions; idler pinion and fuel pump gear

Contact Phase	(1)	(c)		(P)	(d)		(e)
Radius of Curvature pinion ρ_p, inches	1.078	1.202		1.285	1.315		1.439
Radius of Curvature gear ρ_g, inches	1.722	1.598		1.514	1.484		1.361
Number of Pairs of Teeth in Contact, n	2	2	1	1	1	2	2
Maximum Hertz Stress q_o, ksi	98.8	97.1	137	136	136	96.4	96.2
Half Width of Band of Contact b, mils	7.94	8.08	11.4	11.5	11.5	8.14	8.15
Tangential Velocity ($\rho_p \omega_p$) pinion, inches per second	1250	1400		1490	1530		1670
Tangential Velocity ($\rho_g \omega_g$) gear, inches per second	1700	1580		1490	1460		1340
Velocity of Sliding, inches per second	-450	-180		0	70		330
Contact Time, pinion $(H_t)_p$ surface, microseconds	6.34	5.79	8.19	7.70	7.53	5.33	4.87
Contact Time, gear $(H_t)_g$ surface, microseconds	4.68	5.13	7.26	7.70	7.87	5.56	6.08
Maximum Lubricant $(H_t)_L$ Contact Time, microseconds	4.68	5.13	7.26	7.70	7.53	5.33	4.87
Distance from Pitch Point(d) along pinion surface, in.	-0.089	-0.038		0	0.014		0.076

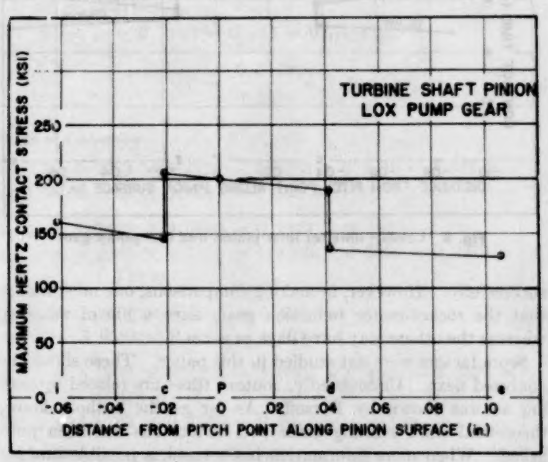

Fig. 3 Contact stress for turbine shaft pinion and LOX pump gear

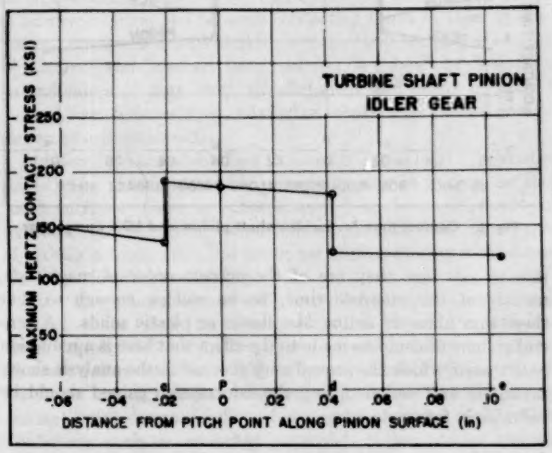

Fig. 4 Contact stress for turbine shaft pinion and idler gear

the pitch point phase of the idler and fuel pump gears. The shortest contact time is 3.16 microsec, coming at phase (*e*) of the pinion and idler gears.

Figs. 3, 4, 5 show the maximum Hertzian contact stresses plotted against the distance from the pitch point to the points of contact of the five phases of contact. Figs. 6, 7, 8 show the contact times plotted against the distance from the pitch point to the points of contact of each of the five phases of contact. In these figures, calculations were made only for each of the five phases shown. In connecting the points on these graphs, straight lines were used for simplicity. These straight lines do not necessarily represent the functional relationship between the co-ordinates for other phases of contact.

Conclusions

It may be concluded that the Hertzian contact stresses fall within the general range of values found for any sets of well designed and proportioned gears. From the point of view of contact stresses alone it would be expected that these gears would perform well as they have been found to do.

From the point of view of contact times we find that these values are relatively high compared with the contact time of one microsec at which Borsoff [3] found that it was difficult to impose loads great enough to cause scoring. It is difficult to predict at present just what effect this might have on the over-all operation of the gears, because not enough is known concerning these contact times and their consequences. But it is probably

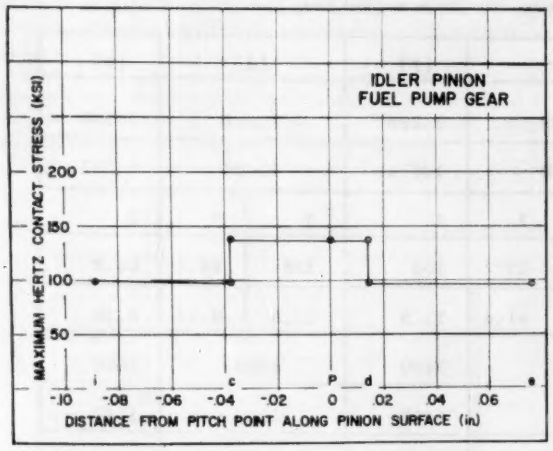

Fig. 5 Contact stress for idler gear and fuel pump gear

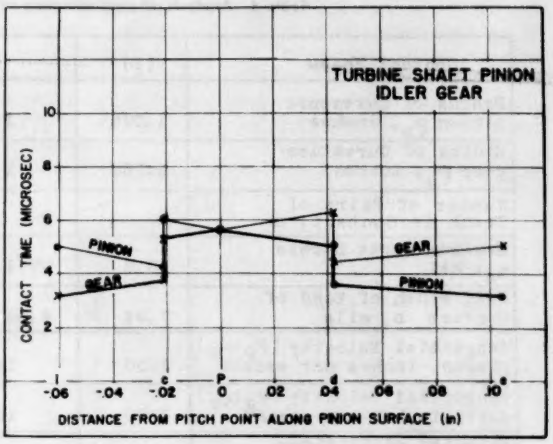

Fig. 7 Contact time for turbine shaft pinion and idler gear

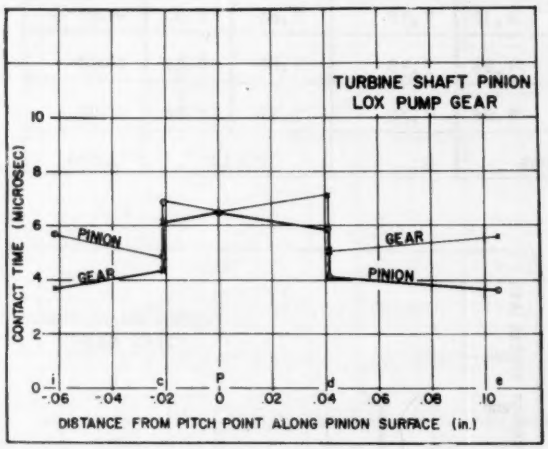

Fig. 6 Contact time for turbine shaft pinion and LOX pump gear

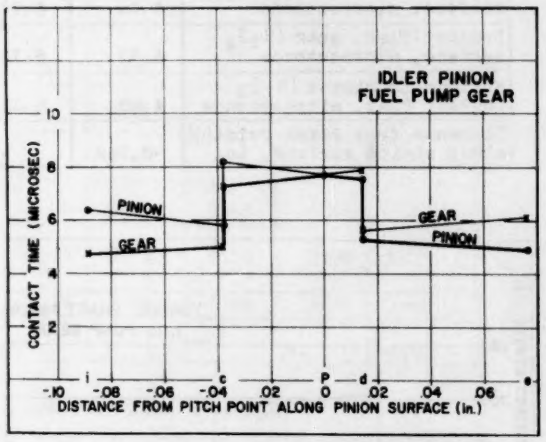

Fig. 8 Contact time for idler pinion and fuel pump gear

safe to say that they are of the correct order of magnitude, namely of the microsec time, to be sudden enough so that these thin films are acting like elastic or plastic solids. A general statement could be made to the effect that here is a reduction gear system which has proved very successful, the analysis shows that it is well designed, and the information gained should be valuable in future designs.

Comparisons

Recently Gatcombe, Hunnicutt, and Kinney [5] presented similar analytical work in which a set of gears used by Borsoff [3] was analyzed. In this work a set of steel gears, having approximately the same hardness as those used by Aero-Jet had contact stresses ranging from 108,900 to 177,500 psi with contact times from 4.7 to 18.6 microsec for a speed of 5000 rpm.

For a speed of 27,000 rpm the contact times of Borsoff's gears would be approximately 0.87 to 3.44 microsec. One observes that these times compare quite closely with those found in the present paper. Borsoff found that it was difficult to impose loads great enough to cause scoring when operating at speeds above 20,000 rpm. It would then appear that a contact time of 4 or 5 microsec is short enough to cause these films to act as elastic or plastic solids rather than viscous fluids.

Both Borsoff's gears and those of Aero-Jet carried their load successfully. However, in making comparisons, one must realize that the rocket-motor reduction gears have a life of minutes, whereas the others may have days or years.

Score factors were not studied in this paper. These should be analyzed next. Undoubtedly, contact times are related to scoring as was shown by Borsoff. As far as the authors know, theoretical work relating these two factors has not been published. When more information is obtained, a possible *ranking* system for the gear materials may be initiated.

The authors would encourage others to carry out similar analyses on gears which have not proved entirely successful, as well as those which have had successful operations. Further studies would then lead to establishment of valuable design limitations.

References

1 S. Timoshenko and J. N. Goodier, "Theory of Elasticity," Engineering Societies Monograph, McGraw-Hill Book Company, Inc., New York, N. Y., second edition, 1951.

2 H. E. Merritt, "Gears," Pitman, London, England, third edition, 1954.

3 V. N. Borsoff, "On the Mechanism of Gear Lubrication," *Journal of Basic Engineering*, series D, TRANS. ASME, vol. 81, 1959, p. 79.

4 D. W. Dudley, "Practical Gear Design," McGraw-Hill Book Company, Inc., New York, N. Y., 1954.

5 E. K. Gatcombe, R. P. Hunnicutt, and G. S. Kinney, "Spur Gear-Hertzian Contact Times," ASLE Preprint No. 59AM 1O-1, 1959.

APPENDIX

Sample calculations are now carried out for evaluating each of the typical quantities found in the tables. These quantities are computed for phase (i) for the pinion and LOX pump gear.

$$M_t = \frac{63030 \times 2200}{8520} = 16{,}300 \text{ lb in.} \quad (1)$$

$$W = \frac{16300}{3.5874} = 4540 \text{ lb} \quad (2)$$

$$\omega_p = \frac{27000 \times 6.28}{60} = 2826 \text{ rad/sec} \quad (3)$$

$$\cos \psi_p = \frac{r_b}{r_o} = \frac{1.1329}{1.3420} = 0.8442$$

$$\psi_p = 32° 25'$$

$$\cos \psi_g = \frac{R_b}{R_o} = \frac{3.5874}{4.0263} = 0.8910$$

$$\psi_g = 27° 00'$$

$$Z = \overline{ie} = \overline{ae} - \overline{ai}$$

$$\overline{ae} = r_o \sin \psi_p = 1.342 \times 0.5360 = 0.7193 \text{ in.}$$

$$\overline{ai} = (\rho_p)_i = 5.2083 \times 0.4226 - 4.0263 \times 0.4540$$

$$\overline{ai} = 0.373 \text{ in.}$$

$$Z = \overline{ie} = 0.7193 - 0.373 = 0.3463 \text{ in.}$$

$$\overline{N} = \frac{0.3463}{0.2373} = 1.46 \quad (4)$$

Radii of Curvature

$$\left.\begin{aligned}(\rho_p)_i &= 5.2083 \times 0.4226 - 4.0263 \times 0.4540 = 0.373 \text{ in.}\\ (\rho_g)_i &= 4.0263 \times 0.4540 = 1.828 \text{ in.}\end{aligned}\right\} \quad (5)$$

$$\left.\begin{aligned}(\rho_p)_e &= 1.3420 \times 0.5360 - 0.2373 = 0.482 \text{ in.}\\ (\rho_g)_e &= 5.2083 \times 0.4226 - 1.3420 \times 0.5360 + 0.2373 = 1.719 \text{ in.}\end{aligned}\right\} \quad (6)$$

$$\left.\begin{aligned}(\rho_p)_P &= 1.2500 \times 0.4226 = 0.528 \text{ in.}\\ (\rho_g)_P &= 3.9583 \times 0.4226 = 1.673 \text{ in.}\end{aligned}\right\} \quad (7)$$

$$\left.\begin{aligned}(\rho_p)_d &= 5.2083 \times 0.4226 - 4.0263 \times 0.4540 + 0.2373 = 0.610 \text{ in.}\\ (\rho_g)_d &= 4.0263 \times 0.4540 - 0.2373 = 1.591 \text{ in.}\end{aligned}\right\} \quad (8)$$

$$\left.\begin{aligned}(\rho_p)_e &= 1.3420 \times 0.5360 = 0.719 \text{ in.}\\ (\rho_g)_e &= 5.2083 \times 0.4226 - 1.3420 \times 0.5360 = 1.482 \text{ in.}\end{aligned}\right\} \quad (9)$$

Hertzian Contact Stress

$$(q_0)_i = 0.418 \left[\frac{4540 \times 30 \times 10^6 (0.373 + 1.828)}{2 \times 1.5 (0.373 \times 1.828)}\right]^{1/2}$$

$$= 161{,}000 \text{ psi} \quad (10)$$

Half-Width of Band of Contact

$$(b)_i = 0.635 \times \frac{4540}{2 \times 1.5 \times 161{,}000} = 0.00599 \text{ in.} \quad (11)$$

Tangential Velocity and Velocity of Sliding

$$\rho_p \omega_p = 0.373 \times 2826 = 1050 \text{ in./sec}$$

$$\rho_g \omega_g = 1.828 \times 892 = 1630 \text{ in./sec}$$

$$\text{Velocity of sliding} = \rho_p \omega_p - \rho_g \omega_g$$

$$= 1050 - 1630 = -580 \text{ in./sec}$$

Hertzian Contact Times

$$\text{For the pinion } (H_t)_i = \frac{0.00599}{0.373 \times 2826} = 5.68 \text{ microsec} \quad (12)$$

$$\text{For the gear } (H_t)_i = \frac{0.00599}{1.828 \times 892} = 3.68 \text{ microsec} \quad (13)$$

For the lubricant $(H_t)_i = 3.68$ microsec

Distance From Pitch Point Along Pinion Surface

$$(d)_i = \frac{1}{2 \times 1.1329} [(0.373)^2 - (0.528)^2] = -0.062 \text{ in.} \quad (14)$$

A negative sign indicates contact on the flank of the tooth; a positive sign indicates contact on the face of the tooth.

DISCUSSION

C. N. Epstein[3]

As it is with all gear rating or qualification factors that have been suggested from time to time, the relationship of Hertzian contact stresses and contact times to the outlook for successful performance of any gear mesh would depend, as Gatcombe and Prowell have noted, on the implementation of similar analyses from many other gear designs which might afford the opportunity of detailed performance study.

Certain basic assumptions in this analysis are acknowledged to be arbitrary. The shape, and hence the area, of the patch of lubricant entrapped between contacting tooth surfaces at any instant, upon which determinations of the "half-width of the band of contact" and "contact time" depend, is subject to distortion by influences of gear tooth misalignment and errors of manufacture, even before a more detailed or coherent theoretical analysis can be contemplated.

Lubricating films which "are believed to act as elastic or plastic solids under these conditions, providing great protection for the tooth surfaces" have in other studies been found to result in hydraulic disintegrating forces following the first developments of pitting in tooth pitch line areas, for gears requiring some duration of performance reliability.

The "five phases of contact" for which contact stresses and contact times have been determined, it should be emphasized, apply for contact ratios between 1.00 and 2.00. Contact ratios less than 1.00 or greater than 2.00 sometimes result or are deliberately designed for, and other "phases of contact" and dynamic affects have to be reckoned with, which render any analysis somewhat incomplete if they are not considered.

Most seriously, we wonder whether the analytical evaluation of particular characteristics of gears for common performance indicators is at all worth while, if applied to gears designed for limited life functions, unless the total time of operation and an integration of all performance cycles are also considered. In the case of gears designed for longer or indefinite periods of operation, where survival through a critical wearing-in period may serve to indicate the suitability of gears of a particular assembly for a much longer period of reliable performance, the analytical ferreting out of common successful performance indicator factors is likely to be more rewarding. This has been the case in the development of various scoring factors—which,

[3] Design Engineer, Rotating Machinery Department, Aerojet-General Corporation, a subsidiary of The General Tire & Rubber Company, Sacramento, Calif.

incidentally are of little use in assessing the capacity of gears designed for limited life performance.

We cannot escape the conclusion that analyses which may only establish approximations of physical effects, subject to an assortment of errors, are of potential value only as implements of differential analysis where many of the elements of a number of gear designs and subsequent product assemblies can be subjected to careful controls during evaluation. In this general connection, we would suggest that analyses of the nature of this Gatcombe-Prowell study be encouraged to include considerations of the effects of manufacturing errors, material displacement characteristics, at least up to elastic limits, and total times and conditions of operation. Under these practices, the evolution of a science of comprehensive analysis of gear design might eventually replace the erratic and somewhat unreliable routines of gear performance analysis which at the present time seem to dominate the field.

J K. Morris[4]

The authors should be complimented for attacking this very difficult problem from an analytical standpoint.

Only little is known and very little has been published regarding the basic dynamics and conditions occurring within the mesh of high-speed gears.

As stated in the paper, the authors' approach endeavors to establish a basis for comparison of data applicable to the lubricant load carrying and load transmitting problem.

Before a complete understanding of the full gear mesh problem can be obtained, considerably more investigation is going to be necessary, for many factors contribute to the conditions at the mesh point of gears mating at high speeds. The gear system analyzed was a successful application; however, many of the other factors involved in this particular mesh have not been considered or mentioned in the paper. To operate gears successfully at high speeds through the mesh point requires determination and selection of many variable factors. The analysis and relationships of all these factors have their impact on successful operation, therefore, each factor must be considered carefully in its relationship to every other analysis less some important factor be overlooked and thereby misdirect the conclusions. The accuracy of the gear, the tooth form and profile, the accuracy of the mountings, the runout and stability characteristics of the bearings, the temperature, the hydrodynamic and aerodynamic characteristics of the "air-oil" mixture in the mesh areas are important factors.

The type of lubricant, the condition of the lubricant, the shape of the gear blank, the characteristics of the gear body and gear rim relative to vibration and natural frequencies, the characteristics of the load being transmitted, and the metallurgical conditions of the gear teeth and gear tooth surfaces, as well as the type of material and surface finishes are but a few of the elements which have impact on the operating characteristics of a high speed gear mesh point.

That these factors exist and must be considered in gear designs, in no way detracts from the value of this most important research and investigation. The work done for this paper, as well as the work done by others in this field, must be highly commended and encouraged. Thorough analytical analysis, combined with the collection of statistical data on this subject, should eventually lead to a more complete and thorough understanding of lubrication of gears and design of gearing, and lubricants. Hidden here are undoubtedly some of the factors affecting the gear mesh action that result in problems plaguing gear users as well as designers, by upsetting calculated results and by disrupting the logical conclusions based on previous experiences.

[4] Manager of Engineering, Western Gear Corporation, Lynwood Calif. Mem. ASME.

Authors' Closure

We agree with Mr. Epstein's general philosophy concerning the value which should be attached to theoretical analyses of gears. We also agree with that of Mr. Morris.

We do wish, however, to stress that, as these theoretical analyses take more and more factors into account, then they are going to become of more and more value to gear designers. As Mr. Morris points out there are many, many factors which we know affect gear tooth operation which are not incorporated in this analysis. But this is just the beginning of a long range program in which more and more of these factors will be treated in the theoretical work.

Such items, mentioned by Mr. Morris, as the conditions of the gear blank, the characteristics of the gear body relative to vibration and deformation effects, the metallurgical conditions of the teeth as well as many other factors mentioned may eventually be treated in detail in such analyses. When it becomes possible to incorporate most of these factors, the time and money saved through the use of theoretical analyses as a guide in gear design will become tremendous.

B. AVITZUR
Former Graduate Student, Department of Mechanical Engineering, University of Michigan, Ann Arbor, Mich.; now Research Engineer, Ford Motor Company, Dearborn, Mich. Assoc. Mem. ASME

C. T. YANG
Associate Professor of Mechanical Engineering, University of Michigan, Ann Arbor, Mich.

Analysis of Power Spinning of Cones

The geometry of the cone, the roller, and the spinning operation are described mathematically. A shear type of deformation is postulated, based on experimental evidence. The displacement, velocity, strain rate, and stress fields are computed for "Mises' material," and hence with Mises' stress-strain rate law. The power consumed in the operation is computed from the strain rate and stress fields. The expression for the power is in a form that can scarcely be solved analytically. A numerical solution is therefore employed and results are presented in graphical forms, where the power and tangential force are plotted for a variety of the process variables. The numerical solution is compared with actual power and force measurement in experimental tests and the agreement is reasonably good.

SPINNING is generally a cold-working process in which a rotating disk of sheet metal is deformed into a cup or cone by applying a localized pressure to the outside of the disk with a simple round-ended wood or metal stick. In common spinning practice the disk is deformed against a pattern having the final shape of the desired product. A very skillful machinist could, however, spin-form a cup or cone with no pattern support at all. In these conventional types of spinning the thickness of the sheet metal is practically unchanged.

In the past few years a new type of spinning called "shear spinning" has been developed. It has also other names, such as "power spinning," "flow-turning," or "roll-forming." Essentially they mean the same operation. In this process the work is done on a machine having the pattern and blank attached to the spindle as usual but the metal is deformed by a roller which is mechanically operated, Fig. 1. Moreover, in this operation the radial distance at any point on the cone remains the same before and after spinning and the thickness is therefore bound to be changed. This process has been widely used in making television picture-tube cones, and the like.

Contributed by the Metal Processing Activity of the Production Engineering Division and presented at the Annual Meeting, Atlantic City, N. J., November 29–December 4, 1959, of THE AMERICAN SOCIETY OF MECHANICAL ENGINEERS.

NOTE: Statements and opinions advanced in papers are to be understood as individual expressions of their authors and not those of the Society. Manuscript received at ASME Headquarters, August 12, 1959. Paper No. 59—A-173.

Previous researchers [1][1] have done some work on the analysis of power, forces, and stresses involved in this problem. But they are all limited to a certain extent. The authors attempted to study the problem in more detail—first with an analytical approach and then the results were checked by experimental tests.

Nature of Deformation of Metal in Process

A sheet-metal blank in power spinning could be deformed by a process of bending, shearing, or a combination of both, Fig. 2. In bending the radial distance of any point at mid-thickness of the cone (point 0 or s in Fig. 2) remains unchanged. The lines AB and CD in Fig. 2 remain straight and normal to the surfaces. Therefore the thickness before and after spinning can be related by the following equation:

$$\text{Thickness } A'B' = \text{thickness } AB \sin \alpha_0$$

In shearing, however, not only points at mid-thickness but any material point has the same radial distance before and after deformation. The straight lines AB and CD in the lower half of Fig. 2 change to $A'B'$ and $C'D'$ but remain parallel to the Z-axis. Besides, $AB = A'B'$ and $CD = C'D'$; thus thickness after deformation = (thickness before deformation) sin α_0.

From the experimental tests described later it was found that the actual deformation pattern is a combination of bending and shearing. However, for the case of small included angles of a spun cone, the deformation is close to pure shear. Also, for the

[1] Numbers in brackets designate References at end of paper.

Nomenclature

$\dot{w}$ = rate of work or energy of deformation per unit volume, in-lb/in.^{3} min
$\dot{W}$ = total energy of deformation
V = volume under roller
$\bar{\sigma}$ = effective stress
$\bar{\dot{\phi}}$ = effective strain rate
R, θ, Z = polar co-ordinate directions of spun cone
$\dot{\epsilon}$ = strain rate
$\dot{\epsilon}_{RR}, \dot{\epsilon}_{\theta\theta}, \dot{\epsilon}_{ZZ}$ = normal strain rates in R, θ, and Z-directions
$\dot{\epsilon}_{R\theta}, \dot{\epsilon}_{\theta Z}, \dot{\epsilon}_{ZR}$ = shear-strain rates
U_R, U_θ, U_Z = velocities in R, θ, and Z-directions
N = rotating speed of the cone, rpm
ϵ_{ij} = strain-deviator tensor
S_{ij} = stress-deviator tensor
$1/\mu$ = modulus of plasticity
$\dot{e}$ = hydrostatic strain rate
$\dot{e}_{ii}$ = summation of three principal strain rates = $\dot{e}_{11} + \dot{e}_{22} + \dot{e}_{33}$
X, Y, Z = rectangular co-ordinate directions of spun cone
k = yield limit in shear = $\sigma_0/\sqrt{3}$
σ_0 = yield limit in tension
$S_{RZ}, S_{Z\theta}, S_{\theta R}$ = deviator shear stresses
$\tau_{RZ}, \tau_{Z\theta}, \tau_{\theta R}$ = total shear stresses
σ_{ij} = total stress tensor
S = hydrostatic stress tensor
δ_{ij} = unit tensor

(continued on next page)

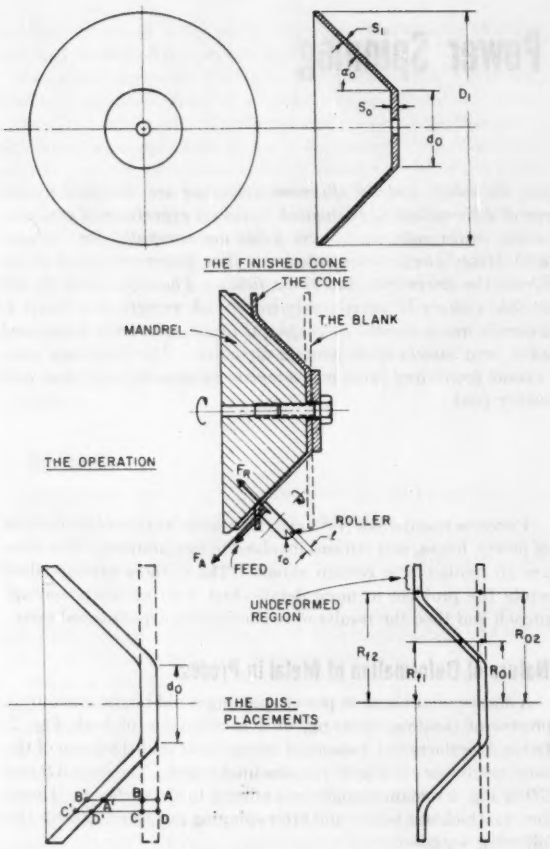

Fig. 1 Cone, mandrel, and operation

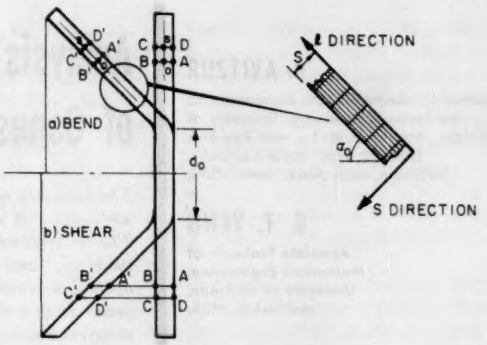

Fig. 2 Shear and bending strains

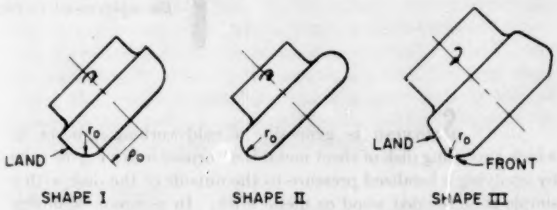

Fig. 3 Different shapes of roller

sake of simplicity the pure shear deformation is assumed in the following analysis.

The Analysis

In the analysis the following assumptions were made:

1 Mises' material is used, which implies that:

(*a*) The material is homogeneous and isotropic.

(*b*) There is no elastic deformation and consequently no volumetric change.

(*c*) There is no strain-hardening.

2 The thickness of the blank is much smaller than the minimum radius of the cone.

3 The metal deforms under the roller in pure shear.

4 The frictional force under the roller is neglected. This is justified, because the relative velocity between the cone and the roller is very small. Also, this was substantiated by a previous publication by Reicher [2] which states that lubricants do not affect the force.

It was observed in the actual process and followed in the analysis that metal deforms instantaneously underneath the roller. The remainder of the cone is strain-free at the instant. From a variety of roller shapes, as shown in Fig. 3, shape I was chosen to be analyzed. The roller is assumed to have its axis parallel to the side of the cone. The choice of the co-ordinate axes XYZ with the origin at O is indicated in Fig. 4. Another set of cylindrical polar co-ordinates (R, θ, Z) with the same origin and Z-axis as in XYZ-co-ordinates was introduced. The assumed shear-strain field is also illustrated in the lower part of Fig. 4. In the analysis the "deformation-energy" theory was used which is indicated as follows:

$$\dot{W} = \int \bar{\sigma} \dot{\bar{\phi}} dV \qquad (1)$$

where

Nomenclature

s = surface area
s_0 = initial thickness of blank
α_0 = 1/2 included angle of cone
n = number of revolutions
r_0 = radius of round-off of roller
x, y, z = co-ordinate directions for roller, z in direction of feed, F; x is direction normal to cone surface; y is normal to xz-plane
F = feed of roller, in. per revolution (ipr)
R_0 = instantaneous radius at which roller touches cone
ρ_0 = radius of torus on roller
T = time passed from starting point
t = tangential force
$\dot{W}_T$ = tangential power
$\dot{W}_F$ = feed power
γ = shear strain
ξ = shear deformation
$\dot{W}^0$ = power consumption to deform cone in experimental tests, assumed equal to $\dot{W}$
T_0 = starting time
$\dot{W}'$ = weighted power = $\dot{W}\sqrt{3}/(\sigma_0 s_0 N)$
t' = weighted tangential force = $t/(s_0\sigma_0)$

$\dot{W}$ = total energy of deformation
V = volume worked underneath roller
$\bar{\sigma}$ = effective stress
$\dot{\bar{\phi}}$ = effective strain rate

$\bar{\sigma}$ will be assumed to be a constant and $\dot{\bar{\phi}}$ is to be derived from the velocity field. V is the product of the contact area between the cone and the roller and the thickness of the cone. The angles and dimensions of the cone and the shape and dimensions of the roller are shown in Figs. 1 and 3, respectively.

Strain Rates. The strain rates in cylindrical polar co-ordinates assume the form [3]:

$$\left.\begin{aligned} \dot{\epsilon}_{RR} &= \frac{\partial U_R}{\partial R};\quad \dot{\epsilon}_{\theta\theta} = \frac{U_R}{R} + \frac{1}{R}\frac{\partial U_\theta}{\partial \theta};\quad \dot{\epsilon}_{ZZ} = \frac{\partial U_Z}{\partial Z} \\ \dot{\epsilon}_{R\theta} &= {}^1/_2\left(\frac{1}{R}\frac{\partial U_R}{\partial \theta} + \frac{\partial U_\theta}{\partial R} - \frac{U_\theta}{R}\right) \\ \dot{\epsilon}_{RZ} &= {}^1/_2\left(\frac{\partial U_R}{\partial Z} + \frac{\partial U_Z}{\partial R}\right) \\ \dot{\epsilon}_{\theta Z} &= {}^1/_2\left(\frac{\partial U_\theta}{\partial Z} + \frac{1}{R}\frac{\partial U_Z}{\partial \theta}\right) \end{aligned}\right\} \quad (2)$$

Where $\dot{\epsilon}_{RR}$, $\dot{\epsilon}_{\theta\theta}$, $\dot{\epsilon}_{ZZ}$, $\dot{\epsilon}_{R\theta}$, $\dot{\epsilon}_{RZ}$, and $\dot{\epsilon}_{\theta Z}$ are the components of the strain-rate tensor field; U_R, U_θ, and U_Z are the components of the velocity-vector field.

To solve our particular deformation field, the velocity field under the roller was computed first.

Because the angular velocity of the spinning cone is constant, one gets the circumferential velocity at any point on the cone as follows:

$$U_\theta = 2\pi RN \quad (3)$$

where

U_θ = circumferential velocity
R = radius of point considered
N = velocity of rotation, rpm

Also, because there is no change in the radius R at any point on the cone during spinning, the radial velocity U_R will be

$$U_R = 0 \quad (4)$$

It is apparent that the cone under the area of contact during deformation takes the shape of the roller. Let the geometry of the roller be described as follows:

$$Z = H(R, \theta, n) \quad (5)$$

Thus

$$dZ = \frac{\partial Z}{\partial R}\,dR + \frac{\partial Z}{\partial \theta}\,d\theta + \frac{\partial Z}{\partial n}\,dn \quad (6)$$

and

$$U_Z = \frac{dZ}{dT} = \frac{\partial Z}{\partial R}\frac{dR}{dT} + \frac{\partial Z}{\partial \theta}\frac{d\theta}{dT} + \frac{\partial Z}{\partial n}\frac{dn}{dT} \quad (7)$$

where

T = time passed from time $T = T_0$ to the instant
n = number of revolutions passed from time $T = T_0$ to the instant
U_Z = velocity component in Z-direction

One now continues to compute the derivatives with respect to time in the following:

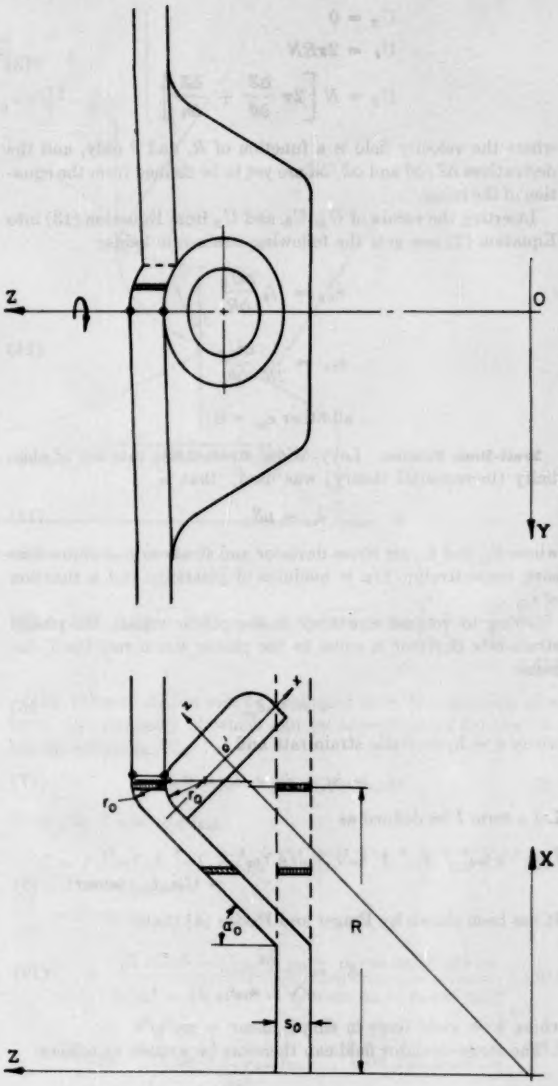

Fig. 4 Deformation in process

$$n = N(T - T_0) \quad (8)$$

$$\frac{dn}{dT} = N \quad (9)$$

$$\frac{d\theta}{dT} = \frac{U_\theta}{R} = 2\pi N \quad (10)$$

$$\frac{dR}{dT} = U_R = 0 \quad (11)$$

Substituting the foregoing derivatives into Equation (7) yields

$$U_Z = \frac{\partial Z}{\partial \theta}\,2\pi N + \frac{\partial Z}{\partial n}\,N = N\left[2\pi\frac{\partial Z}{\partial \theta} + \frac{\partial Z}{\partial n}\right] \quad (12)$$

Therefore the complete velocity field can be summarized as:

$$\left.\begin{aligned} U_R &= 0 \\ U_\theta &= 2\pi RN \\ U_Z &= N\left[2\pi\frac{\partial Z}{\partial\theta} + \frac{\partial Z}{\partial n}\right] \end{aligned}\right\} \quad (13)$$

where the velocity field is a function of R, and θ only, and the derivatives $\partial Z/\partial\theta$ and $\partial Z/\partial n$ are yet to be defined from the equation of the roller.

Inserting the values of U_R, U_θ, and U_Z from Equation (13) into Equation (2) one gets the following strain-rate fields:

$$\left.\begin{aligned} \dot{\epsilon}_{RZ} &= {}^1/_2\frac{\partial U_Z}{\partial R} \\ \dot{\epsilon}_{\theta Z} &= \frac{1}{2R}\frac{\partial U_Z}{\partial\theta} \\ \text{all other } \dot{\epsilon}_{ij} &= 0 \end{aligned}\right\} \quad (14)$$

Stress-Strain Relation. Levy-Mises' stress-strain rate law of plasticity (incremental theory) was used; that is,

$$\dot{\epsilon}_{ij} = \mu S_{ij} \quad (15)$$

where S_{ij} and $\dot{\epsilon}_{ij}$ are stress deviator and strain-rate deviator tensors, respectively; $1/\mu$ is modulus of plasticity and a function of $\dot{\epsilon}_{ij}$.

Owing to volume constancy in the plastic region, the plastic strain-rate deviator is equal to the plastic strain rate itself, because

$$\dot{e} = {}^1/_3\dot{e}_{ii}, \quad (16)$$

where $\dot{e}$ = hydrostatic strain rate and

$$\dot{e}_{ii} = \dot{e}_{11} + \dot{e}_{22} + \dot{e}_{33} = 0 \quad (17)$$

Let a term I be defined as

$$I = {}^1/_3(\dot{\epsilon}_{xx}^2 + \dot{\epsilon}_{yy}^2 + \dot{\epsilon}_{zz}^2) + {}^1/_4(\dot{\gamma}_{xy}^2 + \dot{\gamma}_{yz}^2 + \dot{\gamma}_{zx}^2) = {}^1/_2\dot{\epsilon}_{ij}\dot{\epsilon}_{ij}\,(\text{tensor}) \quad (18)$$

It has been shown by Prager and Hodge [4] that:

$$S_{ij} = \frac{k\dot{\epsilon}_{ij}}{\sqrt{{}^1/_2\dot{\epsilon}_{kl}\dot{\epsilon}_{kl}}} \quad (19)$$

where k = yield limit in simple shear = $\sigma_0/\sqrt{3}$.

The stress-deviator field can therefore be written as follows:

$$\left.\begin{aligned} S_{RZ} = \tau_{RZ} &= \frac{k\dot{\epsilon}_{RZ}}{\sqrt{\dot{\epsilon}_{RZ}^2 + \dot{\epsilon}_{\theta Z}^2}} \\ \text{and} \\ S_{\theta Z} = \tau_{\theta Z} &= \frac{k\dot{\epsilon}_{\theta Z}}{\sqrt{\dot{\epsilon}_{RZ}^2 + \dot{\epsilon}_{\theta Z}^2}} \\ \text{all other} \\ S_{ij} &= 0. \end{aligned}\right\} \quad (20)$$

The Power. Let the rate of work per unit volume = $\dot{w}$

$$\dot{w} = \sigma_{ij}\dot{\epsilon}_{ij} \quad (21)$$

Now

$$\sigma_{ij} = S_{ij} + S\delta_{ij} \quad (22)$$

where

S_{ij} = deviator stress
S = hydrostatic tensor
δ_{ij} = unit tensor, equals 1 when $i = j$
equals 0 when $i \neq j$

Again because of volume constancy, $\dot{\epsilon}_{ii} = 0$, thus

$$\dot{w} = S_{ij}\dot{\epsilon}_{ij} \quad (23)$$

Therefore

$$\dot{w} = S_{ij}S_{ij}\sqrt{{}^1/_2\dot{\epsilon}_{ij}\dot{\epsilon}_{ij}}\left(\frac{1}{k}\right) \quad (24)$$

Now that the yielding condition

$$J_2 = {}^1/_2S_{ij}S_{ij} = k^2, \quad (25)$$

One gets:

$$\dot{w} = 2k\sqrt{{}^1/_2\dot{\epsilon}_{ij}\dot{\epsilon}_{ij}} = \frac{2}{\sqrt{3}}\sigma_0\sqrt{{}^1/_2\dot{\epsilon}_{ij}\dot{\epsilon}_{ij}}$$

$$= \frac{2}{\sqrt{3}}\sigma_0\sqrt{\dot{\epsilon}_{RZ}^2 + \dot{\epsilon}_{\theta Z}^2} = \frac{2}{\sqrt{3}}\sigma_0\sqrt{\left({}^1/_2\frac{\partial U_Z}{\partial R}\right)^2 + \left(\frac{1}{2R}\frac{\partial U_Z}{\partial\theta}\right)^2}$$

$$= \frac{\sigma_0}{\sqrt{3}}\sqrt{\left(\frac{\partial U_Z}{\partial R}\right)^2 + \left(\frac{1}{R}\frac{\partial U_Z}{\partial\theta}\right)^2} \quad (26)$$

The rate of total work done on metal under the contact area, $\dot{W} = \int\dot{w}dV$; that is,

$$\dot{W} = \int_{\text{vol}}\frac{\sigma_0}{\sqrt{3}}\sqrt{\left(\frac{\partial U_Z}{\partial R}\right)^2 + \left(\frac{1}{R}\frac{\partial U_Z}{\partial\theta}\right)^2}\,dV$$

$$= \frac{\sigma_0}{\sqrt{3}}\int_{\substack{\text{surface}\\ \text{area}}}\left[\int_{Z=0}^{Z=s_0}\sqrt{\left(\frac{\partial U_Z}{\partial R}\right)^2 + \left(\frac{1}{R}\frac{\partial U_Z}{\partial\theta}\right)^2}\,dZ\right]ds \quad (27)$$

where ds = infinitesimal surface area ($ds = Rd\,\theta\,dR$).

Because the terms under the square root are independent of Z, one gets

$$\dot{W} = \frac{\sigma_0}{\sqrt{3}}s_0\int_\theta\int_R R\sqrt{\left(\frac{\partial U_Z}{\partial R}\right)^2 + \left(\frac{1}{R}\frac{\partial U_Z}{\partial\theta}\right)^2}\,dR\,d\theta \quad (28)$$

where the integration is to be done along the boundaries of the area of contact between the roller and the cone.

Let $\dot{W}'$ be designated as weighted power and defined as

$$\dot{W}' = \frac{\dot{W}\sqrt{3}}{\sigma_0 s_0 N} \quad (29)$$

or

$$\dot{W}' = \frac{1}{N}\int_\theta\int_R R\sqrt{\left(\frac{\partial U_Z}{\partial R}\right)^2 + \left(\frac{1}{R}\frac{\partial U_Z}{\partial\theta}\right)^2}\,dR\,d\theta \quad (30)$$

Also let

$$\delta = \left[\frac{1}{R}\frac{\partial U_Z}{\partial\theta}\Big/\frac{\partial U_Z}{\partial R}\right]^2 \quad (31)$$

The following equation yields

$$\dot{W}' = \frac{1}{N}\int_\theta\int_R R\sqrt{1+\delta}\left(\frac{\partial U_Z}{\partial R}\right)dR\,d\theta \quad (32)$$

The function of the cylindrical portion of the roller is to smooth out the feed mark, and the work done by it is very small compared with that done by the torus. Thereby the work done by the cylindrical portion of the roller is neglected. The actual and simplified areas of contact are shown in Figs. 5 and 6. Assuming δ is independent of R and θ, one has:

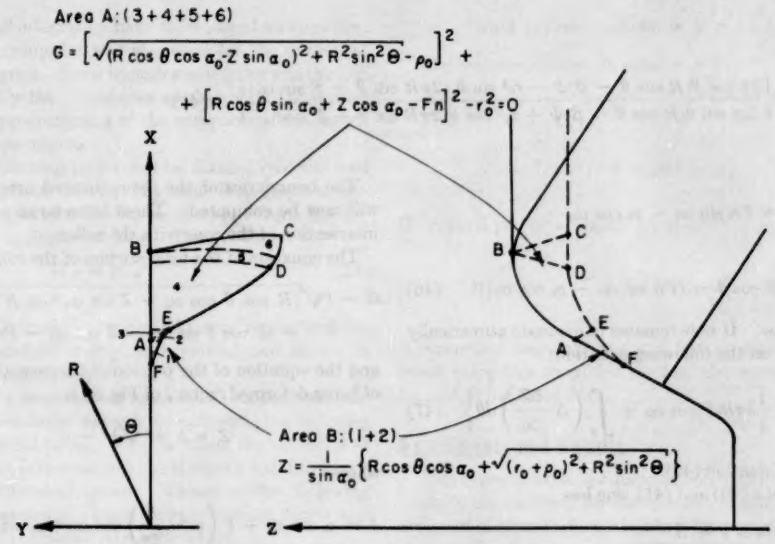

Fig. 5 Area of contact between roller and cone

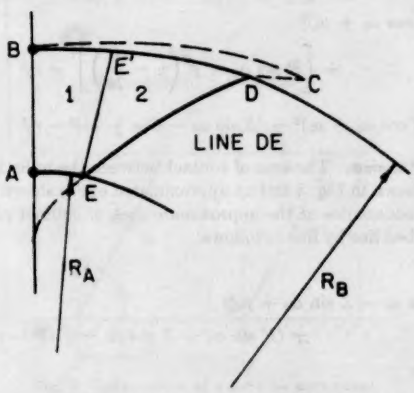

Fig. 6 Approximated area of contact

$$\dot{W}' = \frac{1}{N}\sqrt{1+\delta}\int_\theta\int_R R\left(\frac{\partial U_z}{\partial R}\right)dR\,d\theta \qquad (33)$$

Since $\partial U_z/\partial R$ changes appreciably for slight change of R, R itself can be considered as constant ($R \doteq R_0$). Therefore

$$\dot{W}' = \frac{\sqrt{1+\delta}}{N}R_0\int_\theta\left[|U_z|\begin{matrix}R = \text{upper limit}\\ R = \text{lower limit}\end{matrix}\right]d\theta = \frac{\sqrt{1+\delta}}{N}R_0\int_\theta \Delta U_z\,d\theta \qquad (34)$$

Again since $U_z = N\left[2\pi\frac{\partial Z}{\partial\theta} + \frac{\partial Z}{\partial n}\right]$,

one has

$$\dot{W}' = \sqrt{1+\delta}\,R_0\left\{\int_\theta 2\pi\left(\Delta\frac{\partial Z}{\partial\theta}\right)d\theta + \int_\theta\left(\Delta\frac{\partial Z}{\partial n}\right)d\theta\right\} \qquad (35)$$

Now that

$$\int_\theta\left(\Delta\frac{\partial Z}{\partial\theta}\right)d\theta = \Delta Z = F\cos\alpha_0 \qquad (36)$$

$$\dot{W}' = 2\pi R_0\sqrt{1+\delta}\,F\cos\alpha_0 + \sqrt{1+\delta}\,R_0\int_\theta\left(\Delta\frac{\partial Z}{\partial n}\right)d\theta \qquad (37)$$

The value of $\partial Z/\partial n$ can be evaluated from the equation of a torus, the geometry of which can be approximated by the following equation, Fig. 7:

$$(a - Z)^2 + (b - X)^2 = r_0^2 \qquad (38)$$

From Fig. 7 also one has

$$Z = Fn\cos\alpha_0 + \rho_0\sin\alpha_0 + \sqrt{r_0^2 - (b - R\cos\theta)^2} \qquad (39)$$

$$\frac{\partial Z}{\partial n} = F\cos\alpha_0 + \frac{[R\cos\theta - (Fn\sin\alpha_0 - \rho_0\cos\alpha_0)]F\cos\alpha_0}{\sqrt{r_0^2 - [R\cos\theta - (Fn\sin\alpha_0 - \rho_0\cos\alpha_0)]^2}} \qquad (40)$$

$$\Delta\frac{\partial Z}{\partial n} = \left(\frac{\partial Z}{\partial n}\right)_{R=\text{upper limit}} - \left(\frac{\partial Z}{\partial n}\right)_{R=\text{lower limit}} \qquad (41)$$

Thus the equation $\dot{W}'$ can be evaluated except for the value of δ, the strain ratio, which will be dealt with in the following section.

Evaluation of Strain Ratio. From the approximate equation of the torus, Equation (38), one can derive

$$\frac{U_z}{N} = \frac{1}{N}\frac{dZ}{dT} = F\cos\alpha_0 - \frac{[R\cos\theta - (Fn\sin\alpha_0 - \rho_0\cos\alpha_0)][-R\sin\theta 2\pi - F\sin\alpha_0]}{\sqrt{r_0^2 - [R\cos\theta - (Fn\sin\alpha_0 - \rho_0\cos\alpha_0)]^2}} \qquad (42)$$

$$\frac{1}{N}\frac{\partial U_z}{\partial R} = \frac{1}{(\sqrt{\psi})^3}[r_0^2\cos\theta(2\pi R\sin\theta + F\sin\alpha_0) + 2\pi\sin\theta\psi(R\cos\theta - \beta] \qquad (43)$$

and

$$\frac{1}{N}\frac{1}{R}\frac{\partial U_z}{\partial\theta} = \frac{1}{(\sqrt{\psi})^3}[-r_0^2\sin\theta\{2\pi R\sin\theta + F\sin\alpha_0\} + 2\pi\cos\theta(R\cos\theta - \beta)\psi] \qquad (44)$$

Thus

$$\delta = \left\{ \frac{\dfrac{1}{R}\dfrac{\partial U_z}{\partial \theta}}{\dfrac{\partial U_z}{\partial R}} \right\}^2 = \left\{ \frac{2\pi \cos\theta(R\cos\theta - \beta)\psi - r_0^2 \sin\theta\,(2\pi R \sin\theta + F\sin\alpha_0)}{2\pi \sin\theta(R\cos\theta - \beta)\psi + r_0^2\cos\theta(2\pi R\sin\theta + F\sin\alpha_0)} \right\}^2 \quad (45)$$

where

$$\beta = Fn\sin\alpha_0 - \rho_0\cos\alpha_0,$$

and

$$\psi = r_0^2 - [R\cos\theta - (Fn\sin\alpha_0 - \rho_0\cos\alpha_0)]^2 \quad (46)$$

Evaluation of the Power. It now remains to evaluate numerically the spinning power from the following equation:

$$\dot{W}' = (1+\delta)^{1/2}\left\{2\pi R_0 F\cos\alpha_0 + \int_\theta \left(\Delta\frac{\partial Z}{\partial n}\right)d\theta\right\} \quad (47)$$

where δ is defined in Equation (45).

Combining Equations (40) and (41), one has

$$\Delta\frac{\partial Z}{\partial n} = \frac{R_{\text{upper}}\cos\theta - \beta}{\sqrt{r_0^2 - (R_{\text{upper}}\cos\theta - \beta)^2}} - \frac{R_{\text{lower}}\cos\theta - \beta}{\sqrt{r_0^2 - (R_{\text{lower}}\cos\theta - \beta)^2}} \quad (48)$$

and δ is solved as δ_{average} for the area of contact.

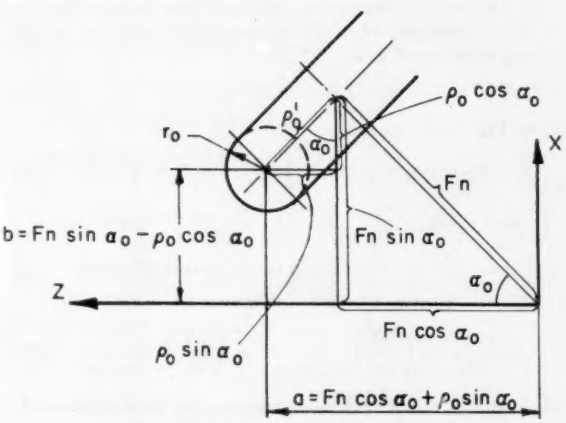

Fig. 7 Approximating the torus by a cylinder

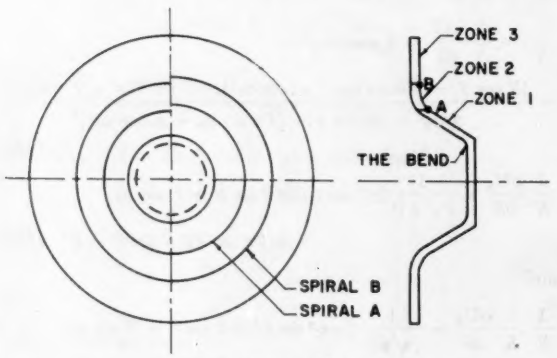

Fig. 8 Zones of the cone

The boundaries of the approximated area of contact, Fig. 6, will now be computed. These boundaries are derived from the intersection of the cone with the roller.

The equation of the toric portion of the roller (see Appendix) is

$$G = [\sqrt{(R\cos\theta\cos\alpha_0 - Z\sin\alpha_0)^2 + R^2\sin^2\theta} - \rho_0]^2 + [R\cos\theta\sin\alpha_0 + Z\cos\alpha_0 - Fn]^2 - r_0^2 = 0 \quad (49)$$

and the equation of the portion of the cone which is in the process of being deformed (zone 2 of Fig. 8) is

$$Z = b + \sqrt{b^2 - c}$$

where

$$\left.\begin{aligned} b &= \rho_0\sin\alpha_0 + F\left(n - \frac{\theta}{2\pi}\right)\cos\alpha_0 \doteqdot \rho_0\sin\alpha_0 + F(n-1)\cos\alpha_0 \\ c &= (R\cos\alpha_0 + \rho_0)^2 + \left[R\sin\alpha_0 - F\left(n - \frac{\theta}{2\pi}\right)\right]^2 - r_0^2 \\ &\doteqdot (R\cos\alpha_0 + \rho_0)^2 + [R\sin\alpha_0 - F(n-1)]^2 - r_0^2 \end{aligned}\right\} \quad (50)$$

Area of Contact. The area of contact between the roller and the cone is shown in Fig. 5 and an approximated one is shown in Fig. 6. The boundaries of the approximate area of contact can now be described line by line as follows:

Line AB

$$\left\{\begin{aligned} &(R\cos\alpha_0 - Z\sin\alpha_0 + \rho_0)^2 + (R\sin\alpha_0 + Z\cos\alpha_0 - Fn)^2 - r_0^2 = 0 \\ &\theta = 0 \end{aligned}\right. \quad (51)$$

Line BD

$$R = R_B = F\left(n - \frac{\theta}{2\pi}\right)\sin\alpha_0 - \rho_0\cos\alpha_0 \doteqdot F(n-1)\sin\alpha_0 - \rho_0\cos\alpha_0 \quad (52)$$

Line DE is computed from the intersection of the roller, $G = 0$, with zone 2 of the cone. G and zone 2 of the cone were defined previously by Equations (49) and (50), respectively.

Line AE

$$R = R_A = R_0 = F\left(n - \frac{\theta}{2\pi}\right)\sin\alpha_0 - (\rho_0 + r_0)\cos\alpha_0 \doteqdot F(n-1)\sin\alpha_0 - (\rho_0 + r_0)\cos\alpha_0 \quad (53)$$

Line EE'

$\theta = \theta_E$ and θ_E is found from the equation of the line DE for the value of $R = R_A$.

The boundary line DE as well as the values of θ_E and δ were computed on the IBM 650 digital computer. The numerical method used is described in Avitzur's thesis [5]. The actual boundaries of the area of contact, Fig. 5, are fully defined in the same reference.

In order to calculate the total energy of deformation under the torus, it is necessary to integrate within the boundaries of R and θ.

Since the boundaries of integration have to be solved numerically, the IBM 650 digital computer was also used for the numerical evaluation of the integrals. Even though a computer was used, it is necessary to simplify the boundaries as shown by the dotted lines in Fig. 6. The programming of the computer is not shown in the paper for obvious reasons.

Forces. The total spinning power can be divided into the feed power and the tangential power, $\dot{W}_F$ and $\dot{W}_T$, respectively. Since $\dot{W}_F$ is small compared with $\dot{W}_T$ as observed from the experiment, the former is neglected here. Thus

$$\dot{W}_T = tU_\theta \tag{54}$$

where t = tangential force.

Numerical calculations of the tangential forces versus feed, included angle and round-off radius were plotted and shown in Figs. 13, 14, and 15, respectively.

Solving the Power by a Simplified but Approximate Method (Deformation Theory). It is seemingly difficult to calculate the spinning power and the tangential force. What is more, the necessity of using a digital computer to evaluate the integrals handicaps one in getting a quick numerical answer. Therefore the following simple method is suggested to obtain an approximate power and tangential force with comparatively little effort.

A cubic block of unit volume as shown in Fig. 9 is subjected to pure shear with load, k psi $\times$ 1 sq in. = k lb

where

shear strain = γ

displacement ξ = 1 tan γ

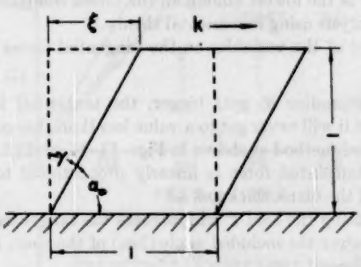

Fig. 9 Deformation of a cube by pure shear

$$\text{work per unit volume} = w = (\sigma_0/\sqrt{3}) \tan \gamma \tag{55}$$

$$\text{total volume worked on cone} = V = 2\pi RNs_0F \sin \alpha_0 \text{ in}^3/\text{min} \tag{56}$$

and

$$\gamma = 90° - \alpha_0 \tag{57}$$

$$\dot{W} = \text{total power} = 2\pi RN \sin \alpha_0 s_0 F \frac{\sigma_0}{\sqrt{3}} \tan \gamma = \frac{2}{\sqrt{3}} \pi \sigma_0 s_0 NFR \cos \alpha_0 \tag{58}$$

Numerical calculations for a few examples of the tangential forces using this simplified method also were plotted in Figs. 13, 14, and 15 in dotted lines.

Experiments and Results

Two types of experiments were conducted. One was designed to study the nature of the deformation in spinning. The other was designed to measure forces between the tool and the work, and also the spinning power.

Investigation of Deformation Pattern. In the original disk 0.0125-in. holes were drilled and plugged with "sculp" metal (aluminum alloy) as shown in Fig. 10. After the cones were spun, the metal was cut and filed carefully until the holes were revealed. From the direction of the plugs, a three-dimensional deformation picture was constructed. A typical picture of the holes is shown in Fig. 11. This cone was spun and checked by the Cincinnati Milling Machine Company as part of a study conducted there. Detailed comparisons between the model cone and actual cones is given in [5].

In Fig. 12 a top view of the radial line of holes shows the shear $\epsilon_{R\theta}$ of the cone. The angle α_θ indicates the extent to which the outer surface slipped over the inner surface of the cone. Numerical measurements of the distortion of the plugged holes can be found in Ref. [5].

In the analytical approach it was assumed that $\alpha_\theta = \alpha_R = 0$. It was observed experimentally that α_θ and α_R do not exceed a few degrees. In standard practice α_0 is not over 75 deg, which

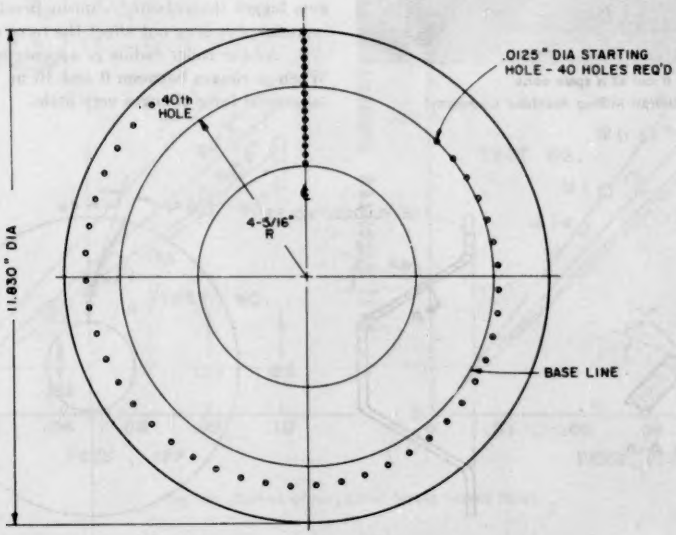

Fig. 10 Drilled holes in original disk to study deformation

means that the minimum shear angle γ is over 15 deg. Since α_θ and α_R are much smaller than 15 deg, it is justified to assume that $\alpha_R = \alpha_\theta = 0$.

In the analytical approach ϵ_{RZ} was further assumed as pure shear, which means that $\alpha = 0$. This assumption does not actually hold. For large α_0, it seems that the deformation is closer to pure bending. For smaller α_0, the deformation is closer to pure shear rather than bending. For simplicity of the computation pure shear has been assumed throughout the study. (For the difference in power consumption between pure shear and bending, see Appendix 2 of [5].)

Measuring Tangential Force and Power. Two sets of experiments were conducted separately at the Cincinnati Milling Machine Company and Spincraft, Inc. At the Cincinnati Milling Machine Company tests were made to measure the forces. On their power-spinning machine the roller is mounted on a three-dimensional dynamometer to measure the forces between the roller and the cone, the feed force, tangential force and the axial thrust. In this study only the tangential force is of interest. The experimental results are given in Table 1. The effect of the parameters, feed, included angle, and the round-off radius on the tangential force was plotted and shown in Figs. 13, 14, and 15. At Spincraft, Inc., the power consumption of a d-c motor which drives the main spindle was measured. The setup is shown in Fig. 16. The tare horsepower and the horsepower for spinning were measured separately. The power consumption for deforming the cone $\dot{W}^0$ is calculated as follows:

$$\dot{W}^0 = \frac{\text{HP with load} - \text{tare HP}}{\text{efficiency}}$$

Since it is not easy to get the efficiency, it was assumed to be 100 per cent for the first approximation. The experimental results are given in Table 2 and plots shown in Figs. 13, 14, and 15. The true stress and strain curves for aluminum specimens were obtained and a typical sample for 1100-H is shown in Fig. 17. The yield strength is taken as an average of the true stresses in the region after yielding. The averages of the yield strengths from several test runs are listed in Tables 1 and 2.

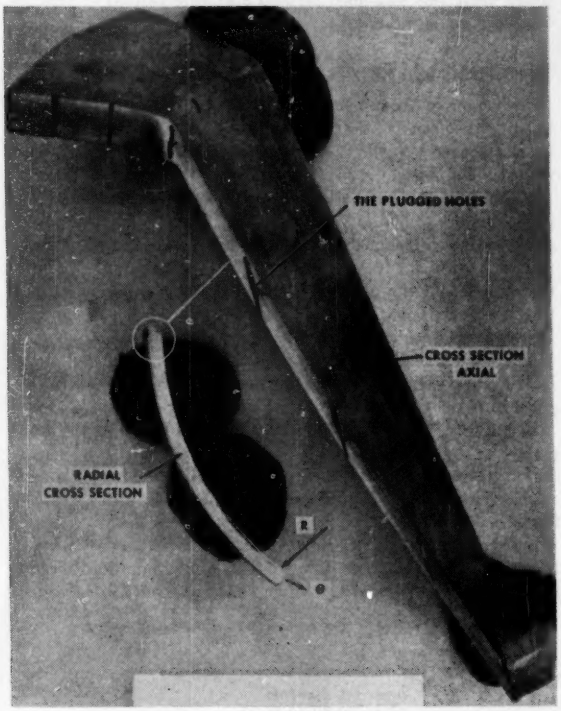

Fig. 11 A cut of a spun cone
(Courtesy of The Cincinnati Milling Machine Company)

Conclusion

Results from theoretical analysis and experimental tests agree fairly well regardless of difficulties involved in the force and power measurement. The forces calculated from the simplified deformation theory is the lowest among all the forces computed from the lengthy analysis using incremental theory.

The effect of the variables on the tangential forces is observed as follows:

1 As the radius R_0 gets bigger, the tangential force is decreased, but it will never get to a value less than that predicted by the simplified method as shown in Figs. 13, 14, and 15.

2 The tangential force is linearly proportional to the yield limit σ_0 and the blank thickness s_0.

3 Increasing the feed F will increase the tangential force.

4 The larger the included angle ($2\alpha_0$) of the cone, the smaller will be the force.

5 As the roller round-off radius r_0 approaches zero, the efficiency approaches its best value; i.e., smallest force. As r_0 gets bigger than about $^1/_4$ in. in practical conditions, a further increase of r_0 does not affect the force appreciably.

6 As the roller radius ρ_0 approaches zero, the force is least. When ρ_0 ranges between 6 and 10 in. ($6 \text{ in.} \leq \rho_0 \leq 10 \text{ in.}$), the tangential force changes very little.

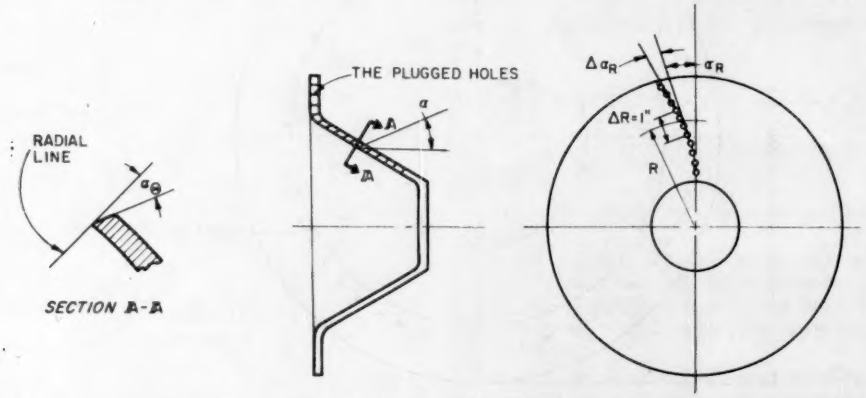

Fig. 12 Distortions of holes in cone

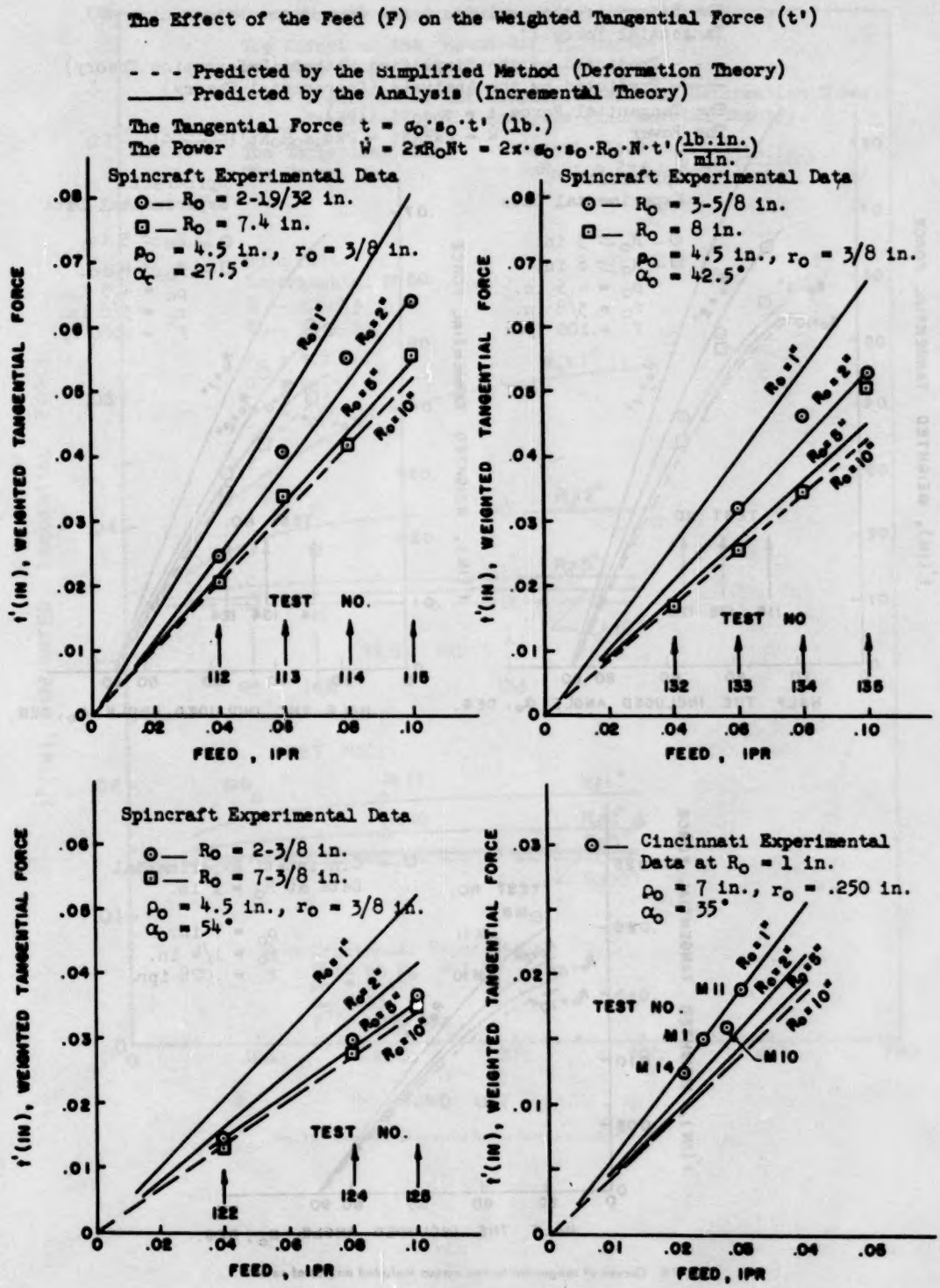

Fig. 13 Curves of tangential forces versus feeds

The Effect of the Included Angle $2\alpha_o$ on the Weighted Tangential Force t'

- - - Predicted by the Simplified Method (Deformation Theory)

——— Predicted by the Analysis (Incremental Theory)

The Tangential Force $t = \sigma_o s_o t'$ (lb.)

The Power $\dot{W} = 2\pi R_o N t = 2\pi\sigma_o s_o R_o N t' \left(\frac{\text{lb.in.}}{\text{min.}}\right)$

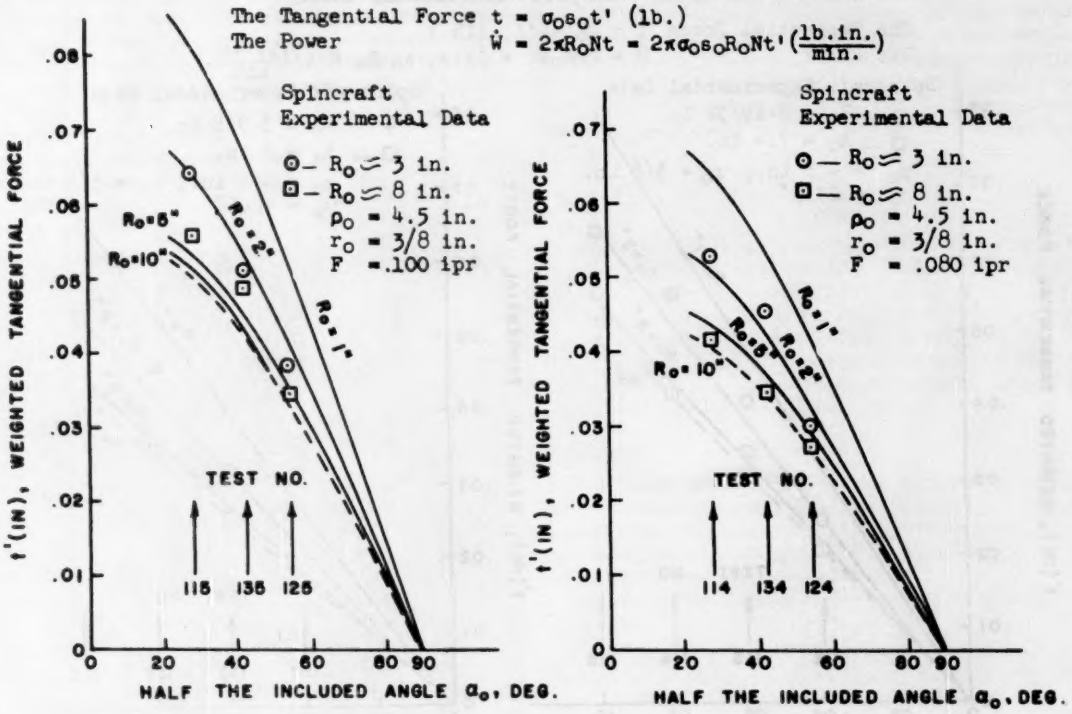

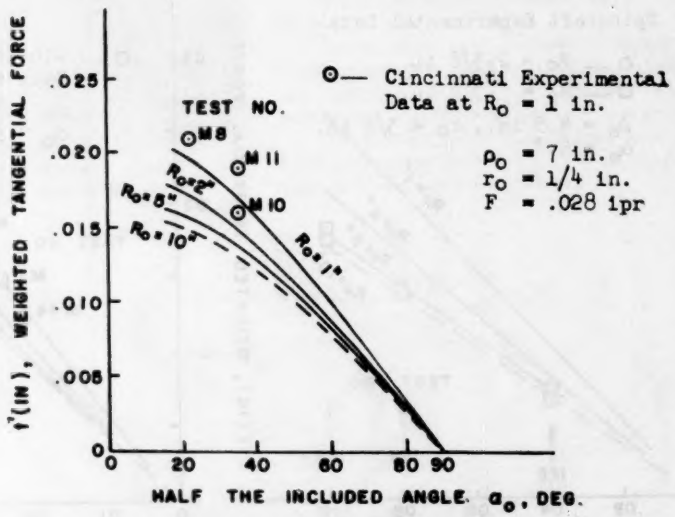

Fig. 14 Curves of tangential forces versus included angles of cones

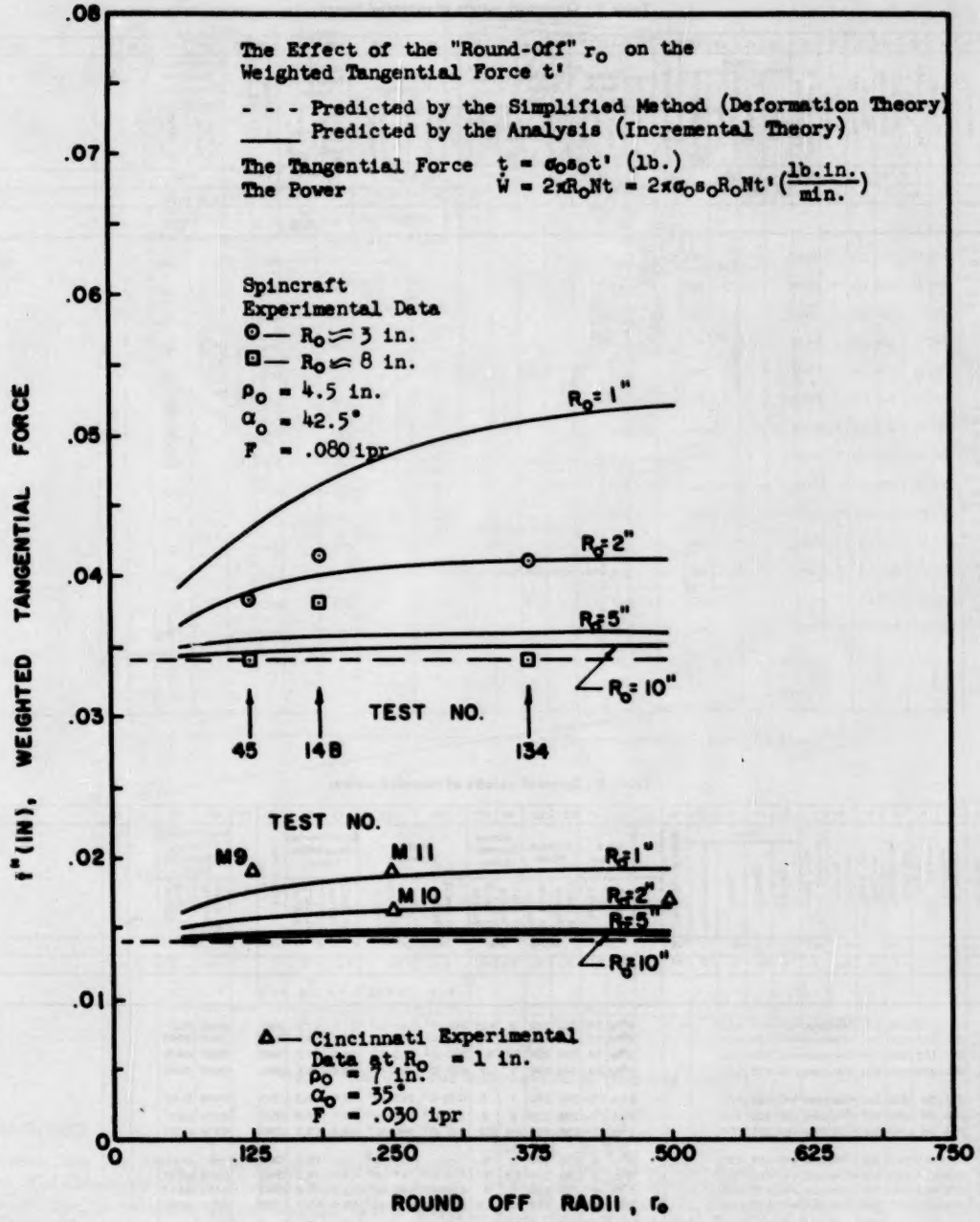

Fig. 15 Curves of tangential forces versus round-off radii

Table 1 Cincinnati results of recorded forces

1	2	3	4	5	6	7	8	9	10	11	12	13	14	15	16	17	18	19	20	21	22	23	24	25	26	27	28	29	30	31	32
	Run Number	Material	Original Thickness	Half Included Angle	Feed per Revolution	Rollers "Round Off"	Rollers Radius	Yield Limit of Worked Cone	Speed				Feed per Minute		Cones Radius		Voltage Drawn		Excess Current Drawn		Power Consumed		Experimental Tangential Force		Weighting Factor		Experimental Weighted Tangential Force				
									Initial	Halfway	Final	Representative			Small	Large	At Small Radius	At Large Radius	At Small Radius	At Large Radius	At Small Radius	At Large Radius	At Small Radius	At Large Radius			At Small Radius	At Large Radius			
			in.	°	ipr	inch		psi	rpm				ipm		inch		volts		amp		lb-in./min		lb		ppi		inch				
			S_0	α_0	F	r_0	ρ_0	σ_0	N_S	N_H	N_F	N	NF		P_1	P_2	V_1	V_2	ΔI_1	ΔI_2	$\dot{W}_1$	$\dot{W}_2$	t_1	t_2			t_1'	t_2'			
																					$\dot{W} = 531 \cdot V \cdot \Delta I$		$t = \frac{\dot{W}}{2\pi RN}$		$\sigma_0 \cdot S_0$		$t' = \frac{t}{\sigma_0 \cdot S_0}$				
	M14	1100 Al	.250	35	.021	1/4	7	25000				300	6.3		1.0								75		6250			.012			
	L2	1100 Al	.250	35	.022	1/4	7	25000				300			1.0								50		6250			.008			
	M1	1100 Al	.250	35	.024	1/4	7	25000				300			1.0								95		6250			.015			
	M10	1100 Al	.250	35	.028	1/4	7	25000				300			1.0								100		6250			.016			
	M11	1100 Al	.250	35	.030	1/4	7	25000				300			1.0								120		6250			.019			
	M5	1100 Al	.250	35	.042	1/4	7	25000				300			1.0								130		6250			.021			
	M4	1100 Al	.250	35	.025	1/8	7	25000				300			1.0								155		6250			.025			
	M9	1100 Al	.250	35	.030	1/8	7	25000				300			1.0								120		6250			.019			
	M5	1100 Al	.250	35	.030	1/2	7	25000				300			1.0								105		6250			.017			
	D30	1100 Al	.375	35	.025	1/4	7	25000				300			1.0								200		9370			.021			
	D42	1100 Al	.485	35	.033	1/4	7	25000				300			1.0								300		12000			.025			
	M8	1100 Al	.250	21	.028	1/4	7	25000				300			1.0								130		6250			.021			
	M7	1100 Al	.250	21	.033	1/4	7	25000				300			1.0								105		6250			.017			
	M12	1100 Al	.250	21	.035	1/4	7	25000				300			1.0								115		6250			.0185			

Table 2 Spincraft results of recorded power

1	2	3	4	5	6	7	8	9	10	11	12	13	14	15	16	17	18	19	20	21	22	23	24	25	26	27	28	29	30	31	32
	Run Number	Material	Original Thickness	Half Included Angle	Feed per Revolution	Rollers "Round Off"	Rollers Radius	Yield Limit of Worked Cone	Speed				Feed per Minute		Cones Radius		Voltage Drawn		Excess Current Drawn		Power Consumed		Experimental Tangential Force		Weighting Factor		Experimental Weighted Tangential Force				
									Initial	Halfway	Final	Representative			Small	Large	At Small Radius	At Large Radius	At Small Radius	At Large Radius	At Small Radius	At Large Radius	At Small Radius	At Large Radius			At Small Radius	At Large Radius			
			in.	°	ipr	inch		psi	rpm				ipm		inch		volts		amp		lb-in./min		lb		ppi		inch				
			S_0	α_0	F	r_0	ρ_0	σ_0	N_S	N_H	N_F	N	NF		P_1	P_2	V_1	V_2	ΔI_1	ΔI_2	$\dot{W}_1$	$\dot{W}_2$	t_1	t_2			t_1'	t_2'			
																					$\dot{W} = 531 \cdot V \cdot \Delta I$		$t = \frac{\dot{W}}{2\pi RN}$		$\sigma_0 \cdot S_0$		$t' = \frac{t}{\sigma_0 \cdot S_0}$				
	112	Aluminum 1100-23-O	.081	27.5	.040	3/8	4 3/32	17,000	439	439	439				2 7/32	7.4	232	232	2	4.25	$247 \cdot 10^3$	$555 \cdot 10^3$	34.4	27.2	1380		.0250	.0197			
	113		.081	27.5	.060	3/8	4 3/32	17,000	440	439	435				2 7/32	7.4	232	232	3.3	7	$407 \cdot 10^3$	$860 \cdot 10^3$	56.7	42.5	1380		.0410	.0340			
	114		.081	27.5	.080	3/8	4 3/32	17,000	440	435	430				2 7/32	7.4	230	228	4.5	9.5	$550 \cdot 10^3$	$1150 \cdot 10^3$	76.5	57.5	1380		.0555	.0416			
	115		.081	27.5	.100	3/8	4 3/32	17,000	440	430	410				2 7/32	7.4	240	236	5	12	$638 \cdot 10^3$	$1500 \cdot 10^3$	89.0	78.5	1380		.0645	.0570			
	122		.077	54	.040	3/8	4 3/32	17,000	440	438	432				2 3/8	7 3/4	240	240	1	3	$1275 \cdot 10^3$	$383 \cdot 10^3$	19.4	18.3	1310		.0148	.0140			
	124		.076	54	.080	3/8	4 3/32	17,000	438	435	432				2 3/8	7 3/4	236	236	2	6	$250 \cdot 10^3$	$750 \cdot 10^3$	38.2	35.8	1290		.0296	.0277			
	125		.076	54	.100	3/8	4 3/32	17,000	438	430	428				2 3/8	7 3/4	236	236	2.5	7.5	$316 \cdot 10^3$	$940 \cdot 10^3$	48.2	45.0	1290		.0374	.0350			
	132		.080	42.5	.040	3/8	4 7/32	17,000	440	438	438				3 3/8	8	236	236	X	4	—	$500 \cdot 10^3$	—	22.7	1360		—	.0167			
	133		.079	42.5	.060	3/8	4 7/32	17,000	440	438	434				3 3/8	8	236	234	3.5	6	$439 \cdot 10^3$	$747 \cdot 10^3$	44.0	34.2	1340		.0328	.0255			
	134		.079	42.5	.080	3/8	4 7/32	17,000	440	435	430				3 3/8	8	234	232	5	8	$620 \cdot 10^3$	$986 \cdot 10^3$	62.0	45.8	1340		.0462	.0342			
	135		.079	42.5	.100	3/8	4 7/32	17,000	440	435	429				3 3/8	8	234	232	5.5	11.5	$685 \cdot 10^3$	$1420 \cdot 10^3$	68.5	65.5	1340		.0510	.0490			
	45		.079	42.5	.080	1/8	4 1/2	17,000	440	435	430				3 3/8	8	236	236	4	8	$503 \cdot 10^3$	$1000 \cdot 10^3$	50.3	46.2	1340		.0375	.0345			
	48		.0805	42.5	.080	3/16	4 1/2	17,000	440	430	430				3 3/8	8	243	243	4.5	9	$580 \cdot 10^3$	$1160 \cdot 10^3$	57.7	53.6	1370		.042	.0390			

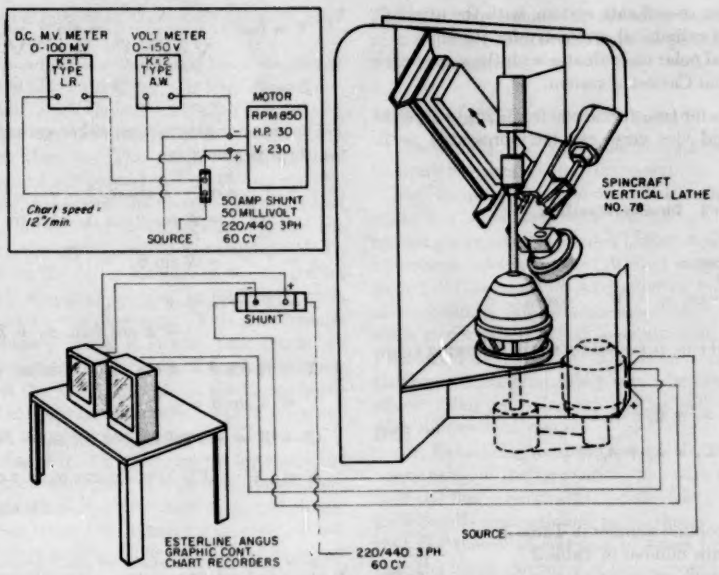

Fig. 1 Spincraft experimental setup

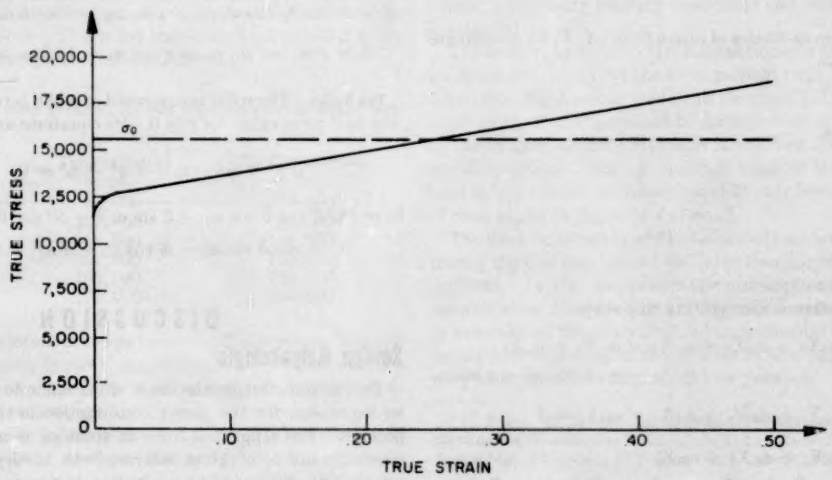

Fig. 17 True stress-true strain curve for Al 1100(25)H

Acknowledgment

Assistance from Mr. Serope Kalpakcioglu, Senior Research Engineer, The Cincinnati Milling Machine Company, and staffs in Spincraft, Inc., in obtaining the experimental data is deeply appreciated. The authors wish to thank also the Army Ballistics Missiles Agency for its support of the present investigation by Project No. DA-11-022-ORD-2542 to the University of Michigan.

References

1(a) B. N. Colding, "Shear Spinning," ASME Paper No. 59—Prod-2, 1959.

1(b) J. N. Feola, "Experimental Analysis of Shear Deformation," MS thesis, Syracuse University, Syracuse, N. Y., January, 1955.

1(c) E. Siebel and K. A. Droge, "Forces and Material Flow in Spinning," *Werkstattstechnik and Maschinenbau*, vol. 45, 1955, pp. 6–9.

2 H. Reicher, "Roll Spinning of Cone Shaped Aluminum Parts," *Fertigungstechnik*, vol. 8, part 1, 1958, pp. 181–184, vol. 8, part 2, 1958, pp. 252–260.

3 H. Rouse, editor, "Advanced Mechanics of Fluids," John Wiley & Sons, New York, N. Y., 1959, p. 204.

4 W. Prager and P. H. Hodge, Jr., "Theory of Perfectly Plastic Solids," John Wiley & Sons, New York, N. Y., 1951, p. 31.

5 B. Avitzur, "Analysis of Power Spinning of Cones," PhD thesis, University of Michigan, Ann Arbor, Mich., June, 1959.

APPENDIX

Transformation of Co-Ordinate Systems and Mathematical Description of Toric Part of Roller

The Sets of Axis and Their Transformation. Consider three co-ordinate systems (see Fig. 4):

1 (x, y, z) Cartesian co-ordinate system, with the origin O'. The axis z is the axis of cylindrical symmetry for the roller, and the origin is the center of the toric portion of the roller.

2 (X, Y, Z) Cartesian co-ordinate system, with the origin O. The axis Z is the axis of cylindrical symmetry for the cone.

3 (R, θ, Z) cylindrical polar co-ordinates with the same origin O and Z-axis as the second Cartesian system.

The directional cosines for transformation from (x, y, z)-system to (X, Y, Z)-system and vice versa can be represented as in Table 3

Table 3 Directional cosines

	x	y	z
X	$\cos \alpha_0$	0	$\sin \alpha_0$
Y	0	1	0
Z	$-\sin \alpha_0$	0	$\cos \alpha_0$

The transformation scheme is according to the following equation:

$$\left.\begin{aligned} x_i &= a_i + a_{ij} X_j \\ X_j &= b_j + a_{ij} x_i \end{aligned}\right\} \tag{59}$$

where

i = 1, 2, 3 denote column number in Table 3
j = 1, 2, 3 denote row number in Table 3
a_i = denote co-ordinates of origin O in (x, y, z) co-ordinate system
$a_1 = a_2 = 0$
$a_3 = -Fn$
b_j = denote co-ordinates of origin O' in (X, Y, Z) co-ordinate system
$b_1 = Fn \sin \alpha_0$
$b_2 = 0$
$b_3 = Fn \cos \alpha_0$
$x_1 = x$
$x_2 = y$
$x_3 = x$
$X_1 = X$
$X_2 = Y$
$X_3 = Z$

The transformation is now getting this shape:

$$x_1 = x = a_1 + a_{11}X_1 + a_{12}X_2 + a_{13}X_3 = a_{11}X_1 + a_{12}X_3 = X \cos \alpha_0 - z \sin \alpha_0$$

$$x_2 = y = a_2 + a_{21}X_1 + a_{22}X_2 + a_{23}X_3 = a_{22}X_2 = Y$$

$$x_3 = z = a_3 + a_{31}X_1 + a_{32}X_2 + a_{33}X_3 = a_3 + a_{31}X_1 + a_{32}X_3 = -Fn + X \sin \alpha_0 + Z \cos \alpha_0$$

And applying the second of Equation (59), one gets:

$$X_1 = X = x \cos \alpha_0 + z \sin \alpha_0 + Fn \sin \alpha_0$$

$$X_2 = Y = y$$

$$X_3 = Z = -x \sin \alpha_0 + z \cos \alpha_0 + Fn \cos \alpha_0$$

The transformation from (R, θ, Z)-system to (X, Y, Z)-system is to be performed by:

$$X = R \cos \theta$$

$$Y = R \sin \theta$$

$$Z = Z$$

and from (X, Y, Z) to (R, θ, Z) is performed through

$$R = \sqrt{X^2 + Y^2}$$

$$\theta = \cos^{-1} \frac{X}{\sqrt{X^2 + Y^2}} = \sin^{-1} \frac{Y}{\sqrt{X^2 + Y^2}} = tn^{-1} \frac{X}{Y}$$

$$Z = Z$$

The transformation from either system to any other system of the three is now given.

$$\left\{\begin{aligned} x &= X \cos \alpha_0 - Z \sin \alpha_0 \\ &= R \cos \theta \cos \alpha_0 - Z \sin \alpha_0 \\ y &= Y = R \sin \theta \\ z &= X \sin \alpha_0 + Z \cos \alpha_0 - Fn \\ &= R \cos \theta \sin \alpha_0 + Z \cos \alpha_0 - Fn \end{aligned}\right.$$

$$\left\{\begin{aligned} X &= R \cos \theta = x \cos \alpha_0 + z \sin \alpha_0 + Fn \sin \alpha_0 \\ Y &= R \sin \theta = y \\ Z &= Z = -x \sin \alpha_0 + z \cos \alpha_0 + Fn \cos \alpha_0 \end{aligned}\right\} \tag{60}$$

$$\left\{\begin{aligned} R &= (X^2 + Y^2)^{1/2} = [(x \cos \alpha_0 + z \cos \alpha_0 + Fn \sin \alpha_0)^2 + y^2]^{1/2} \\ \theta &= \cos^{-1} \frac{X}{\sqrt{X^2 + Y^2}} = \sin^{-1} \frac{Y}{\sqrt{X^2 + Y^2}} \\ &= \cos^{-1} \frac{x \cos \alpha_0 + z \sin \alpha_0 + Fn \sin \alpha_0}{\sqrt{(x \cos \alpha_0 + z \sin \alpha_0 + Fn \sin \alpha_0)^2 + y^2}} \\ Z &= z = -x \sin \alpha_0 + z \cos \alpha_0 + Fn \cos \alpha_0 \end{aligned}\right.$$

The Roller. The roller is composed of a half torus and a cylinder. The half torus exists for $z \geq 0$. Its equations are:

$$G = \left.\begin{aligned} &[\sqrt{x^2 + y^2} - \rho_0]^2 + z^2 - r_0^2 = 0 \\ &[\sqrt{R \cos \theta \cos \alpha_0 - Z \sin \alpha_0)^2 + R^2 \sin^2 \theta} - \rho_0]^2 \\ &+ [R \cos \theta \sin \alpha_0 + Z \cos \alpha_0 - Fn]^2 - r_0^2 = 0 \end{aligned}\right\} \tag{61}$$

DISCUSSION

Serope Kalpakcioglu[2]

This is undoubtedly the finest effort made to date to arrive at an expression for the power consumption in the shear spinning process. The tangential force in spinning is a very important quantity and is of great interest both to designers of power spinning machines and to production engineers faced with problems of sufficient power to carry out a certain spinning operation.

It is encouraging to note that there is excellent agreement between the incremental theory and the simplified deformation theory at large radii of the workpiece. It should be remembered that it is at the higher radii that the tangential force becomes important, thus the simplified deformation theory should prove very useful. The power spinning process is a highly complex one and certain simplifications in any analysis are inevitable. In view of this the good agreement between theory and experiment is noteworthy. In spite of the high strain rate in spinning, the use of average yield stress σ_0 from conventional low strain rate tensile data and its good agreement with experiment appear to be difficult to explain. A similar agreement has been observed by Kobayashi and Thomsen[3] in metal cutting data and this

[2] Senior Research Engineer, The Cincinnati Milling Machine Company, Cincinnati, Ohio.

[3] S. Kobayashi and E. G. Thomsen, "Some Observations on the Shearing Process in Metal Cutting," JOURNAL of ENGINEERING FOR INDUSTRY, TRANS. ASME, series B, vol. 81, 1959, pp. 251–262.

writer agrees with these authors that the reason for such good correlation is indeed not clear.

While both theories state that the tangential force is directly proportional to the original blank thickness s_0 it has been experimentally observed that this is not the case. While the axial and normal forces appear to be directly proportional to s_0 the tangential force increases faster than s_0. This can be seen if points D301 and D427 from Table 1 are plotted in Fig. 13. (Actually, the point D427 will be higher because the material for this point was softer than the rest; Bhn 29 versus 42. Thus, if it had the same hardness as the rest, the experimental force value would be greater.) The tendency for the faster increase of the tangential force with respect to s_0 has also been observed in 1020 steel, while the other forces increase in direct proportion. This phenomenon has been difficult to explain. While it is true that the flange bends forward more and more as s_0 increases, it has been experimentally determined that the energy going into the flange bending is only a few per cent of the spinning energy. The discrepancy may be due to a change in the metal flow pattern as s_0 increases.

A final point concerning Fig. 14: The curves for simplified deformation theory are true cosine curves with σ_0 obtained from Fig. 17 and given a constant value, irrespective of α_0. It should be remembered, however, that the average value of σ_0 will depend on the maximum true strain. Thus the value of σ_0 at any mandrel angle α_0 will be different. While, for a limited range of α_0 and for a relatively low strain hardening material like 1100 aluminum, the error will be small, for high strain-hardening materials, like 304 stainless steel, this error will be considerable, as seen from Table 3. This point should be kept in mind when comparing experimental and theoretical data.

Table 3 Average yield stress σ_0 for 304 stainless steel in tensile test; Bhn = 133

Natural strain, ϵ	True stress, σ, psi	Average stress, σ_0, psi
0.2	93,000	74,000
0.4	127,000	88,000
0.6	141,000	108,000
0.8	152,000	116,000
1.0	163,000	124,000
1.2	174,000	132,000

While the correlation between theory and experiment is good, care should be taken to avoid generalizations by those who use the analytical results, particularly in dealing with new metals so widely used in the present age.

The authors are to be commended for very fine work and it is hoped that they will continue this study toward obtaining analytical expressions for the other forces too, which, while not contributing much to the over-all power consumption, are quite large in magnitude.

Authors' Closure

The authors wish to thank Mr. Kalpakcioglu for his complimentary remarks and fine discussion.

Mr. Kalpakcioglu questioned the fact that a stress-strain curve from a low strain-rate test was used in the analysis, whereas spinning was done at a much higher strain rate. However, good agreement between analytical and experimental results was obtained. This could be attributed to the reason that for copper and aluminum flow stresses are increased merely a few per cent while strain rate is raised to as much as 1000 times according to Professor Fukui, et al.[4] This is because at the high strain rate the strain-hardening effect could be counteracted by the heat effect. This reasoning can also be well applied to metal cutting with similar work metals.

Mr. Kalpakcioglu made a remark that the theory predicts linear relationship of the tengential force with the original blank thickness (s_0) but experimental points D301 and D427 (in Table 1) show results contradictory to the theory. It must be emphasized that the theory of spinning of cones holds under the condition that the blank thickness of those cones is much smaller than the minimum radius of the cone as was stated in the second assumption on page 232. As this assumption was violated for these two points, discrepancy between analytical and experimental results is expected.

The authors agree with Mr. Kalpakcioglu in the statement that for different cone angles the average yield limit is different due to different strain-hardening effect as shown in Table 3. For a more rigorous analysis this should be incorporated in the computation of the tangential force although it will introduce more complicated equations. A single average value of the yield limit was used in this study (see Tables 1 and 2) only because the variation of cone angles in the tests was small.

The work on spinning which the authors reported in this paper is merely the first step toward the understanding of this complicated problem. In the analysis many assumptions were made for simplification of the solution. Therefore caution must be taken in generalizing the analytical and experimental data. To have a better understanding of the process further study both analytically and experimentally should be pursued.

[4] S. Fukui, H. Kudo, and J. Seino, "Study on Impact Extrusion Method for Nonferrous Metals," *Report of the Institute of Science and Technology*, University of Tokyo, vol. 11, no. 9, 1957, p. 98.

A. G. MacDONALD
Graduate Student, University of California, Berkeley, Calif.

S. KOBAYASHI
Assistant Professor, Mechanical Engineering, Doshisha University, Kyoto, Japan; presently Graduate Student, University of California, Berkeley, Calif.

E. G. THOMSEN
Professor, University of California, Berkeley, Calif. Mem. ASME

Some Problems of Press Forging Lead and Aluminum

Several press forgings were made and it was found that the experimental mean forging pressures were in substantial agreement with values predicted by theoretical solutions based on an approximate theory. The forging processes were axial symmetric forging of disks between flat dies and forging in closed dies with several edge effects, such as overhanging flash, with and without flash-edge restriction. The materials were commerically pure aluminum and lead and were chosen because of their respective work-hardening and strain-rate effects at room temperature. It was found further that the local pressures measured in the forging were in good agreement with the theory, but that some local plastic flow tends to equalize the pressure in the body of the forging.

THE problem of press forging of metals has theoretical as well as technological significance in that solutions would help to bring about a better understanding of the behavior of metals during plastic deformation at high pressure. Such solutions would give specific answers to problems actually encountered in practice. It is for these reasons that a number of investigators have dealt with the forging problem and have proposed certain theoretical solutions which are based on a material having the properties of an ideal plastic solid. This leads to so-called slip-line solutions. The work was done by Prandtl [1],[1] Hill, Lee, and Tupper [2], and Green [3].

Other investigators have used more approximate methods for obtaining solutions by assuming the metal of the forging to be a real metal, but assuming that the state of stress in the metal can be simplified. These treatments are given by Siebel [4], Sachs [5], and Stone and Greenberger [6]. Comparison of these ideal and approximate solutions was made by Alexander [7], Bishop [8], and Kobayashi and Thomsen [9], and comparisons of experiment with theory were reported by Watts and Ford [10], Kobayashi, et al. [11], Schroeder and Webster [12], and Kobayashi, MacDonald, and Thomsen [13]. It was found by the latter investigators [11, 12, 13], that the approximate solutions, using a simplified state of stress, give good correlation with experiment. It is the purpose of the present investigation to report additional data and to examine the extrusion of the flash during closed die forging as a possible method for improving the forging process. Some schematic diagrams of the dies for the forging tests to be discussed are shown in Fig. 1.

Forging of Disks

The forging of disks from short cylinders between flat dies has been treated theoretically at length recently by Bishop [8] who proved that the approximate equation

$$\frac{d\sigma_r}{dr} = \frac{d\sigma_z}{dr} = -\frac{2\mu}{h}\sigma_z \qquad (1)$$

must be a good approximation to the state of stress in the disk. In order to solve equation (1), however, the further assumption must be made, that μ is not a function of r and h and that σ_z is constant throughout the thickness h of the disk at any r. The solution for the axial stress component σ_z then is given in dimensionless form by

$$\frac{-\sigma_z}{\bar{\sigma}} = e^{\frac{2\mu}{h}(r_f - r)} \qquad (2)$$

where $\bar{\sigma}$ is the instantaneous yield stress or flow stress The magnitude of $\bar{\sigma}$ depends on whatever effect strain (work-hardening effect), strain rate (dynamic effect), or both, have on the instantaneous yield condition of the metal. These effects must be determined from a property test. If the coefficient of friction becomes large, sticking of the metal in the deformed disk adjacent to the die surfaces may occur. Hence plastic shear deformation in the surface layers near the die surfaces may take place instead of sliding. This condition, in accordance with the accepted von Mises' yield criterion applicable to ductile metals, is given by $-\mu\sigma_z/\bar{\sigma} = 0.577$ [11, 12]. Thus equation (2) for sticking becomes

[1] Numbers in brackets designate References at end of paper.

Contributed by the Metal Processing Activity of the Production Engineering Division and presented at the Annual Meeting, Atlantic City, N. J., November 29–December 4, 1959, of THE AMERICAN SOCIETY OF MECHANICAL ENGINEERS.

NOTE: Statements and opinions advanced in papers are to be understood as individual expressions of their authors and not those of the Society. Manuscript received at ASME Headquarters, July 7, 1959. Paper No. 59—A-164.

Nomenclature

A_0/a = extrusion ratio
C, K = constants
n = exponent
h = instantaneous flash height, in.
h_0 = initial flash height, in.
h_F = instantaneous flash height when $r_f = r_F$, in.
r = instantaneous radius anywhere in flash or body of forging, in.
r_d = die radius, in.
r_f = flash radius, in.
r_0 = critical radius at which sticking occurs, in.
r_F = die-land edge radius, in.
p_a = average forging pressure, psi
p_z = average extrusion pressure, psi
σ_r = normal stress component in r-direction, psi
$(\sigma_r)_{r_F}$ = normal stress component in r-direction at $r = r_F$, psi
σ_z = normal stress component in z-direction, psi
$\bar{\sigma}$ = effective stress, psi
$\bar{\epsilon}$ = effective strain, in/in.
$\dot{\bar{\epsilon}}$ = effective strain rate, in/in. per sec
μ = coefficient of friction

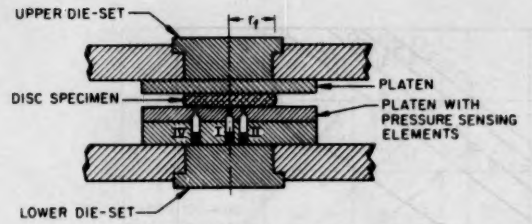

(a) Disk forging between flat dies

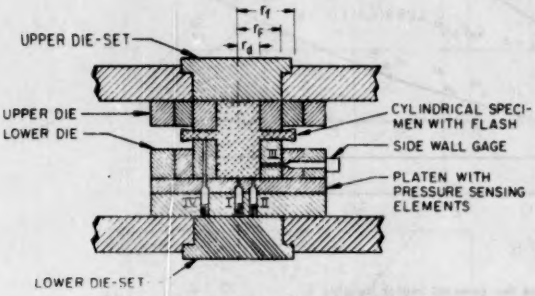

(b) Closed die forging with overhanging flash

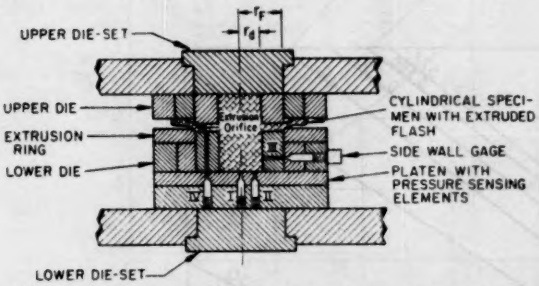

(c) Closed die forging with flash edge restriction (flash extrusion)

Fig. 1 Schematic diagrams of forging processes

r_d = die radius = 1.00 in.
r_F = die-land-edge radius = 1.75 in.
r_f = radius of disk for (a) or flash radius for (b) and (c)

$$-\frac{\sigma_z}{\bar{\sigma}} = \frac{2}{h\sqrt{3}}(r_0 - r) + \frac{1}{\mu\sqrt{3}} \tag{3}$$

for the range of r, $0 \leq r \leq r_0$, where r_0 is the radius at which sticking terminates and is given by

$$r_0 = r_f - \frac{h}{2\mu}\ln\left(\frac{1}{\mu\sqrt{3}}\right) \tag{4}$$

Utilizing the equations (2), (3), and (4), the average dimensionless forging pressures can be determined by integration [12, 13] and are as follows:

$$\frac{p_a}{\bar{\sigma}} = {}^1/_2\left(\frac{h}{\mu r_f}\right)^2\left(e^{\frac{2\mu r_f}{h}} - \frac{2\mu r_f}{h} - 1\right); \quad \text{for} \quad r_0 \leqq 0 \tag{5}$$

and

$$\frac{p_a}{\bar{\sigma}} = {}^1/_2\left(\frac{h}{\mu r_f}\right)^2\left[\left(\frac{2\mu r_0}{h} + 1\right)e^{\frac{2\mu}{h}(r_f - r_0)} - \frac{2\mu r_f}{h} - 1\right] + \left(\frac{r_0}{r_f}\right)^2\left[\frac{1}{\mu\sqrt{3}} + \frac{2\sqrt{3}}{9}\frac{r_0}{h}\right]; \quad \text{for} \quad r_f \geq r_0 \geq 0 \tag{6}$$

The theoretical equations (5) and (6) are plotted in Fig. 2 together with experimental data obtained previously by the authors when compressing commercially pure lead cylinders of several initial heights h_0, which were reported earlier [13]. It is seen that for dry dies and for dies lubricated with petroleum jelly, the data align themselves approximately along the $\mu \simeq 0.577$ and $\mu \simeq 0.05$ to 0.10 curves, respectively. Inasmuch as the instantaneous flow stress for lead is dependent principally on strain rate, it was thought to be of interest to compare the theoretical curves of Fig. 2(*a*) also with a work-hardening material. Consequently, 2-in-diameter bars of commercially pure 1100-F aluminum were annealed in a salt bath at 650 F for 1 hr. The plastic stress-strain property was subsequently determined for the annealed alloy from a compression test with grooved and lubricated end surfaces of short 1-in. × 1-in. cylinders and were found to follow the approximate stress-strain law in the fully plastic region given by the equation $\bar{\sigma} = 22200(\bar{\epsilon})^{0.28}$. The effective strain $\bar{\epsilon}$ in the case of compressing or forging a cylinder is closely given by $\ln(h/h_0)$, while $\dot{\bar{\epsilon}}$ is given by the rate of change of $\bar{\epsilon}$ with respect to time.

The comparison for lead and aluminum using the platens shown in Fig. 1(*a*) for the forging of cylinders having initial heights of $h_0 = 1.01$ in. is given in Fig. 2(*b*). It is seen that the experimental points for dry friction with aluminum are slightly lower than those for lead, while those for aluminum lubricated with graphite in oil are slightly higher than those for lead. Hence forging pressures under the test conditions explored appear to depend to a greater extent on the degree of lubrication in forging lead than do those in forging aluminum.

Inasmuch as the dies were equipped with pressure-sensing elements as shown in Fig. 1(*a*), a comparison of local pressures for lead and aluminum is now also available. Consequently, the dimensionless local forging pressures $-\sigma_z/\bar{\sigma}$ as function of r_f/h for $h_0 = 1.01$ in. are shown for lead and aluminum in Fig. 3 for conditions of dry friction. The solid lines are the predicted local pressures as given by equations (2) and (4) for $\mu \geq 0.577$. A comparison shows, therefore, that the experimental points in general fall reasonably close to the theoretical curves for both lead and aluminum. It was unfortunate, however, that it was not possible to extend the comparison of theory with experiment to the same strain with aluminum as was done with lead. This limitation with imposed by die strength and press capacity.

Closed-Die Forging With and Without Overhanging Flash

The closed-die forging of lead and aluminum was discussed earlier by Kobayashi, et al. [11], and local pressure determinations with lead were reported by Kobayashi, MacDonald, and Thomsen [13]. The present investigation extends the local pressure measurements also to aluminum. In the closed-die forging it is assumed that the metal in an axially symmetric forging, when squeezed between dies in a finishing operation as shown in Fig. 1(*a*), can be treated as a fictitious disk. Hence, a similar analysis as that for forging a disk, discussed in the foregoing section, can be utilized for this process. It is assumed in the analysis [11] that the metal in the disk attached to the body of the forging is subjected to metal shearing, while that in the flash may slide over the dies unless the condition for sticking is satisfied. The equations are as follows:

(*a*) For the case of overlapping dies with the die and flash radii given by r_d and r_f, respectively,

$$\left.\begin{aligned} -\frac{\sigma_z}{\bar{\sigma}} &= e^{\frac{2\mu}{h}(r_f - r)}, \quad \text{when} \quad r_d \leq r \leq r_f \\ -\frac{\sigma_z}{\bar{\sigma}} &= \frac{2}{h\sqrt{3}}(r_d - r_f) + e^{\frac{2\mu}{h}(r_f - r_d)}, \\ &\qquad \text{when} \quad 0 \leq r \leq r_d \end{aligned}\right\} \tag{7}$$

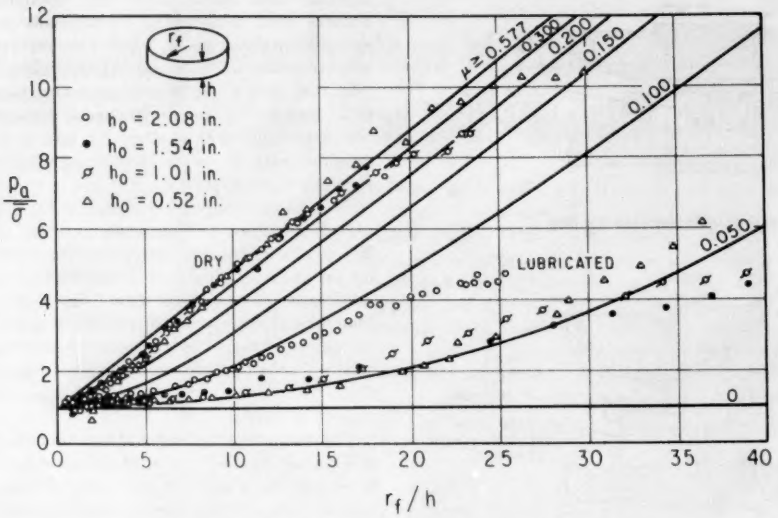

(a) Lead only, dry and lubricated dies for several initial heights h_0

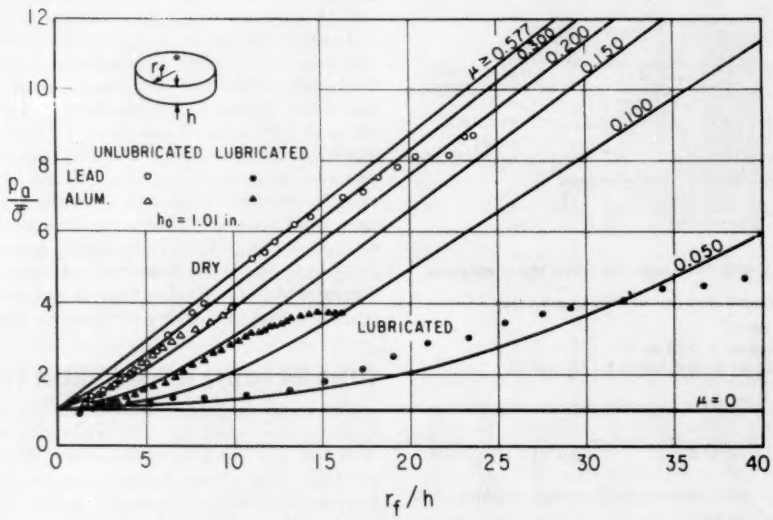

(b) Lead and aluminum, dry and lubricated for h_0 = 1.01 in.

Fig. 2 Theoretical and experimental dimensionless average forging pressures as function of radius to height ratio of disks of commercially pure lead and aluminum

and

$$\frac{p_a}{\bar{\sigma}} = {}^1/_2 \left(\frac{h}{\mu r_f}\right)^2 \left[\left(\frac{2\mu r_d}{h} + 1\right) e^{\frac{2\mu}{h}(r_f - r_d)} - \frac{2\mu r_f}{h} - 1\right] + \left(\frac{r_d}{r_f}\right)^2 \left[e^{\frac{2\mu}{h}(r_f - r_d)} + \frac{2\sqrt{3}}{9}\frac{r_d}{h}\right] \quad (8)$$

In the event that frictional resistance becomes so great that the radius r_0 at which sticking occurs lies within the flash radius, then equations (7) and (8) reduce to those of a disk given previously by equations (2) to (6), inclusive.

(*b*) For the case of overhanging flash, Fig. 1(*b*), assuming that the resulting radial and hoop stresses at the edge of the dies are zero. Strictly this condition applies only at the instant when the flash radius is equal to the die radius r_d; this condition also applies when r_f becomes large and conversely h becomes sufficiently small that the hoop stresses in the overhanging flash can relieve themselves by buckling of the flash. The resulting equations consequently are those of equations (7) and (8) as long as $r_f \leq r_p$ where r_p is the die-land edge radius.

When $r_f \geq r_p$ the equations reduce to the following:

$$-\frac{\sigma_z}{\bar{\sigma}} = e^{\frac{2\mu}{h}(r_p - r)} \quad (9)$$

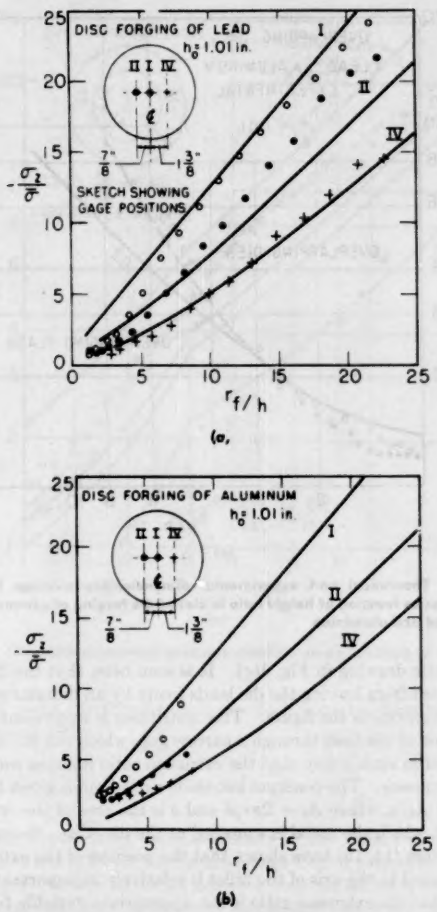

Fig. 3 Local dimensionless axial pressure distribution for lead and aluminum for the condition of forging 2-in. cylinders dry between overlapping flat and parallel dies

and

$$\frac{p_a}{\bar{\sigma}} = {}^1/_2\left(\frac{h}{\mu r_F}\right)^2\left[\left(\frac{2\mu r_d}{h}+1\right)e^{\frac{2\mu}{h}(r_F-r_d)} - \frac{2\mu r_F}{h} - 1\right] + \left(\frac{r_d}{r_F}\right)^2\left[e^{\frac{2\mu}{h}(r_F-r_d)} + \frac{2\sqrt{3}}{9}\frac{r_d}{h}\right] \quad (10)$$

(*c*) For the case of overhanging flash but under the assumption that the resulting hoop stress due to flash overhang is not zero, the equations are the same as those of (7) and (8), as long as $r_f \leq r_F$. When $r_f \geq r_F$ the approximate correction term given by Kobayashi, MacDonald, and Thomsen [13] must be used as given by

$$-\left(\frac{\sigma_r}{\bar{\sigma}}\right)_{r_F} = {}^1/_2\left[\left(\frac{\frac{3h_F}{h}-1}{\frac{h_F}{h}+1}\right)^{1/4} - 1\right] \quad (11)$$

so that,

$$-\frac{\sigma_a}{\bar{\sigma}} = \left[1-\left(\frac{\sigma_r}{\bar{\sigma}}\right)_{r_F}\right]e^{\frac{2\mu}{h}(r_f-r)} \quad (12)$$

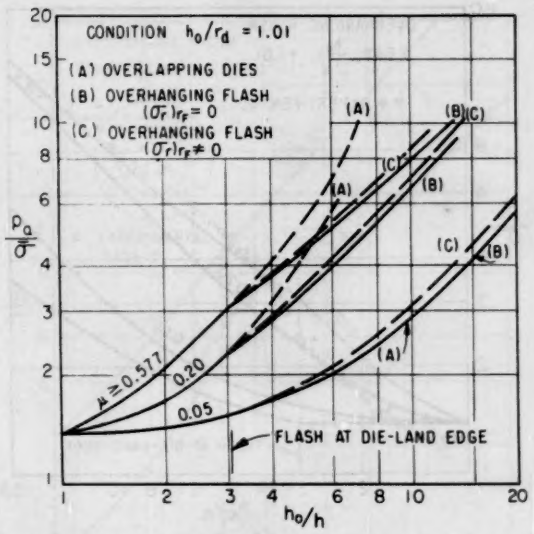

Fig. 4 Theoretical approximate average pressures for closed die forging as function of height ratio for three conditions of surface friction

and

$$\frac{p_a}{\bar{\sigma}} = \left[1-\left(\frac{\sigma_r}{\bar{\sigma}}\right)_{r_F}\right]\left\{{}^1/_2\left(\frac{h}{\mu r_f}\right)^2\left[\left(\frac{2\mu r_d}{h}+1\right)e^{\frac{2\mu}{h}(r_f-r_d)} - \frac{2\mu r_f}{h} - 1\right] + \left(\frac{r_d}{r_f}\right)^2 e^{\frac{2\mu}{h}(r_f-r_d)}\right\} + \left(\frac{r_d}{r_f}\right)^2\frac{2\sqrt{3}}{9}\frac{r_d}{h} \quad (13)$$

where $(\sigma_r)_{r_F}$ is the radial stress in the flash at $r = r_F$.

The theoretical curves of $p_a/\bar{\sigma}$ versus h_0/h, which correspond to the equations given in the foregoing sections (*a*) to (*c*), are plotted in Fig. 4 and have been identified by the same letter for several values of μ. It is seen that the curves for overhanging flash for the two values of $(\sigma_r)_{r_F} = 0$ and $(\sigma_r)_{r_F} \neq 0$ differ only by a relatively small amount. Hence, comparison of theory with experimental data for a forging with overhanging flash is made only with (B) type curves, where $(\sigma_r)_{r_F} = 0$, and is shown in Figs. 5(*a*) and 5(*b*) for lead and aluminum, respectively. The parameters are $h_0 = 1.01$ in. and $r_d = 1.00$ in., thus $h_0/r_d = 1.01$. It is seen that the lead and aluminum curves are nearly identical and agree reasonably well with the theory. However, the comparison was again limited by the extent to which aluminum could be forged with the available die and press capacity. A similar comparison with lead and aluminum for overlapping dies, type A curve of Fig. 4, is given in Fig. 5(*c*). The experimental local pressures of the two metals are also compared with the theory for $\mu \geq 0.577$ and are given in Fig. 6. This is done only for overhanging flash, and it is seen that the pressures in the body of the lead forging, gages I, II, and III of Fig. 6(*a*), lie between the theoretical curves I and II, thus indicating that some plastic flow equalizes the pressure within the body of the forging. This is a fortunate fact in that it permits possibly a more uniform impression of the metal in the whole body of the forging than would be predicted by the theory alone. The agreement between experiment and theory in the flash, however, as given by gage IV is good and indicates that a pressure gradient exists in the flash as predicted by the theory. The comparison between theory and experiment for aluminum was limited to the wall pressure gage III, since the pressure pad containing the remaining pressure-sensing elements could not be used with the high local pressures necessary to forge the aluminum. It is seen, however, that the experimental values

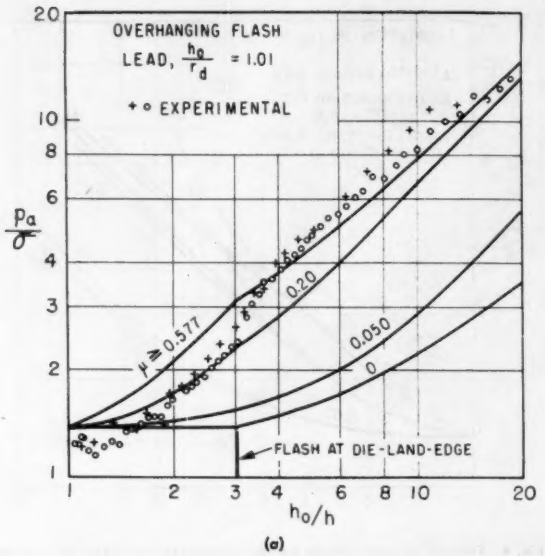

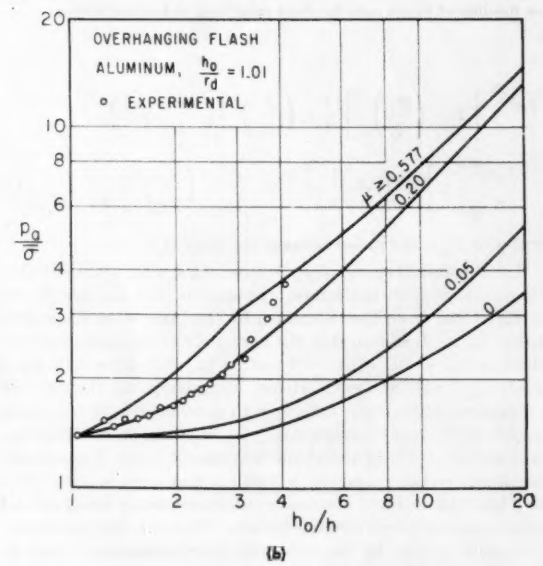

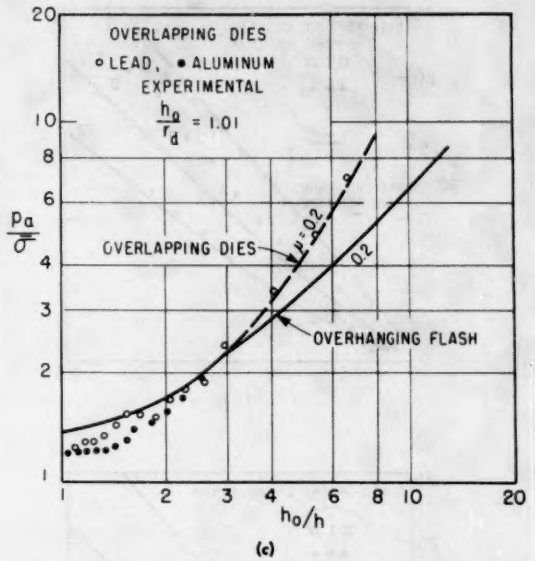

Fig. 5 Theoretical and experimental dimensionless average forging pressures as function of height ratio in closed die forging of commercially pure lead and aluminum

for both lead and aluminum are in general in good agreement with local and average theoretical forging pressures.

Closed-Die Forging With Extrusion of the Flash at Die-Land Edge

Returning momentarily to the theoretical curves of Fig. 4, it is seen that the average forging pressure, say for $\mu = 0.577$, rises fastest with overlapping dies. Overlapping dies, however, have the disadvantage that the forging pressure can only be raised to high values at large h_0/h. This corresponds to large values of r_f for any given h_0 and consequently to large values of total load since with overlapping dies the total load is ever increasing as r_f increases. This disadvantage is not present with the forging processes given by type C or B-curves of Fig. 4, but the pressure can be raised only by significant reductions in flash height. This may be a disadvantage and, hence, an alternate process will be given which is less dependent on h_0/h once the flash radius r_f has reached the die-edge radius r_p. The process is illustrated in the schematic drawing in Fig. 1(*c*). It is seen here, that the flash is prevented from leaving the die lands freely by an annular restriction, as shown in the figure. This restriction is equivalent to an extrusion of the flash through a narrow gap, which can be (or not) designed in such a way that the extrusion ratio remains constant as h decreases. The constant extrusion ratio then is given by the ratio of A_0/a, where $A_0 = 2\pi r_p h$ and a is the area of the opening through which the metal is squeezed at the die edge. Several investigators [14, 15] have shown that the position of the extrusion with regard to the axis of the billet is relatively unimportant, and hence that the extrusion ratio is the appropriate variable for obtaining the extrusion pressure. Thus the pressure required to extrude can be given in several empirical forms [16], but appears to be most readily approximated by a consideration of the work of plastic deformation. The pressure to extrude in an inverted extrusion process is given for work-hardening metals, such as aluminum, by

$$p_e \simeq C \int_{\bar{\epsilon}_1}^{\bar{\epsilon}_2} \bar{\sigma} d\bar{\epsilon} \tag{14}$$

and for metals affected principally by strain rate, such as lead, by

$$p_e \simeq K(\dot{\bar{\epsilon}})^n \tag{15}$$

where the constant $C \simeq 1.5$ is an empirical factor to correct for the work of shear deformation which was neglected in deriving these formulas and K is an empirical factor to correct for the effect of extrusion speed. Thus by rewriting equations (14) and (15) in terms of the dimensionless radial pressures at the die-land edge in the forging process of Fig. 1(*c*) and by setting $-\sigma_r \simeq p_e$, i.e., assuming near hydrostatic conditions at the edge of the flash, yields

$$-\left(\frac{\sigma_r}{\bar{\sigma}}\right)_{r_p} \simeq \frac{C}{\bar{\sigma}} \int_{\bar{\epsilon}_1}^{\bar{\epsilon}_2} \bar{\sigma} d\bar{\epsilon} \tag{16}$$

and

$$-\left(\frac{\sigma_r}{\bar{\sigma}}\right)_{r_p} \simeq \frac{K}{\bar{\sigma}} \left(\ln \frac{A_0}{a}\right)^n \tag{17}$$

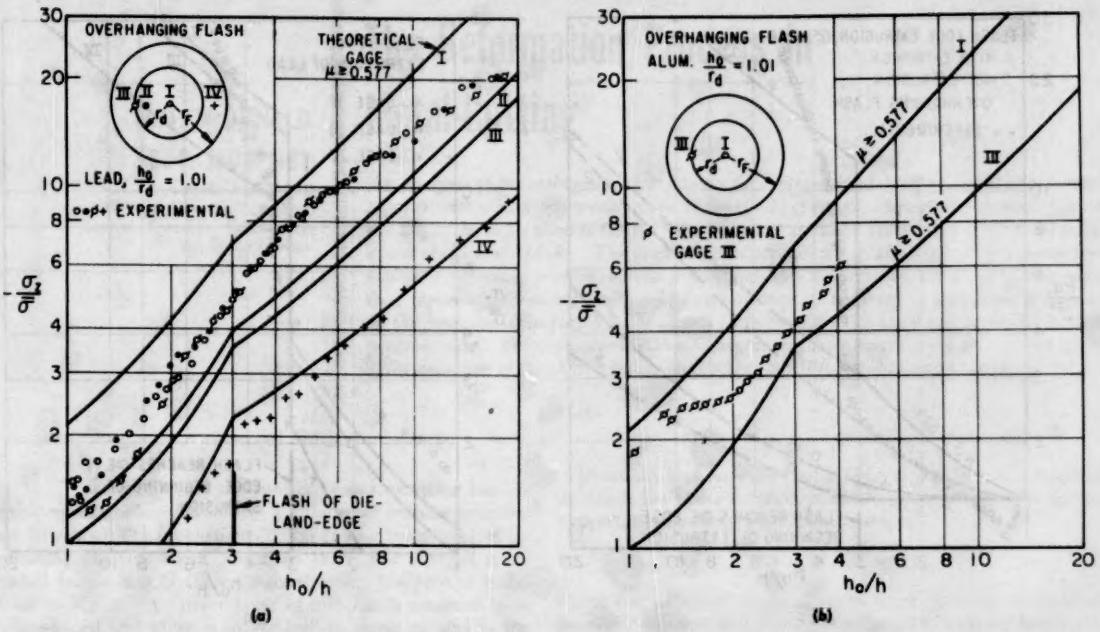

Fig. 6 Local dimensionless pressure distribution as function of height ratio in closed die forging of commercially pure (a) lead and (b) aluminum

where $\bar{\epsilon}$ is the effective strain in the flash upon reaching the die-edge radius and

$$\bar{\epsilon}_2 = \bar{\epsilon}_1 + \ln \frac{A_0}{a}$$

Hence, substituting these equations in the former equations (11), (12), and (13), the local and average forging pressures can be computed. It is to be noted, however, that the solution for these equations will result in different theoretical values for each extrusion ratio for work-hardening metals, and in addition for each strain rate for those metals that are affected by strain rate. In the case of the lead forgings to be discussed the die-land-edge orifice or gap was such as to keep the extrusion ratio $A_0/a \simeq 5.0$. Hence, equation (17) for lead can be evaluated as soon as K and n are known. Thomsen [17] has given the necessary information for inverted extrusions at various speeds and extrusion ratios. Thus the extrusion pressure at an average forging speed of 0.03 ipm required an average forging pressure of 5000 psi in an inverted axial symmetric rod extrusion of commercially pure lead. The average flow stress $\bar{\sigma}$ for this speed is approximately 1700 psi and the magnitude of the radial dimensionless pressure becomes approximately

$$-\left(\frac{\sigma_r}{\bar{\sigma}}\right)_{rr} \simeq \frac{5000}{1700} = 2.94.$$

Assuming that this value can be used for the present extrusion of the flash in our forging, the average forging pressure can now be evaluated by equation (13). The results of such calculations are shown as a solid curve in Fig. 7(*a*), together with the data of two experimental forging tests using commercially pure lead. It is seen again that the theory gives the correct order of magnitude of pressures, even though small differences exist, which may be due to some of the assumptions made, such as the neglect of additional stresses and others, once the flash has been extruded. Actually the neglect of this effect may not be serious in the present case. In fact, it is more likely that contact of the upper forging die with the extruded flash increased the total load some relatively small but unknown amount in the range of pressures investigated. It is also to be noted that the local pressures shown in Fig. 7(*b*) give trends similar to the average forging pressures and that the local pressures tend to equalize in the forging as well as in the flash, as the extrusion of the flash is initiated.

In closing, it may be of interest to compare the effectiveness of the process of extruding the flash of a forging to that of merely forging with overhanging flash as given by curves 1 and 2 in Fig. 7(*a*) for $\mu = 0.577$. Thus if it were desired, for example, to raise the average pressure to a value of 15,000 psi, it would be necessary to reduce the height of the flash to $^1/_4$ of its initial height when using the extrusion process (curve 1), while for the more conventional process (curve 2), the height of the flash would have to be reduced to $^1/_{20}$ of its initial height.

Conclusions

1 The press-forging equations based on simplified states of stress yield predictions of average forging pressures which are in substantial agreement with experimental data obtained with commercially pure lead and aluminum.

2 The local press-forging pressures as determined by pressure-sensing elements were in agreement with those predicted by the theory for the lead and aluminum-disk experiments. For the closed die-forging experiments the local pressures tended to equalize within the body of the forging. This is at variance with the theory but is readily explained by the readjustment of the pressures due to internal plastic flow.

3 The possible increase of forging pressures due to the extrusion of the flash through a restriction at its edge is substantial when compared with conventional processes; it appears to be a feasible forging process for the purpose of improving the impression ability in press forging.

Acknowledgments

The authors wish to thank the National Science Foundation for

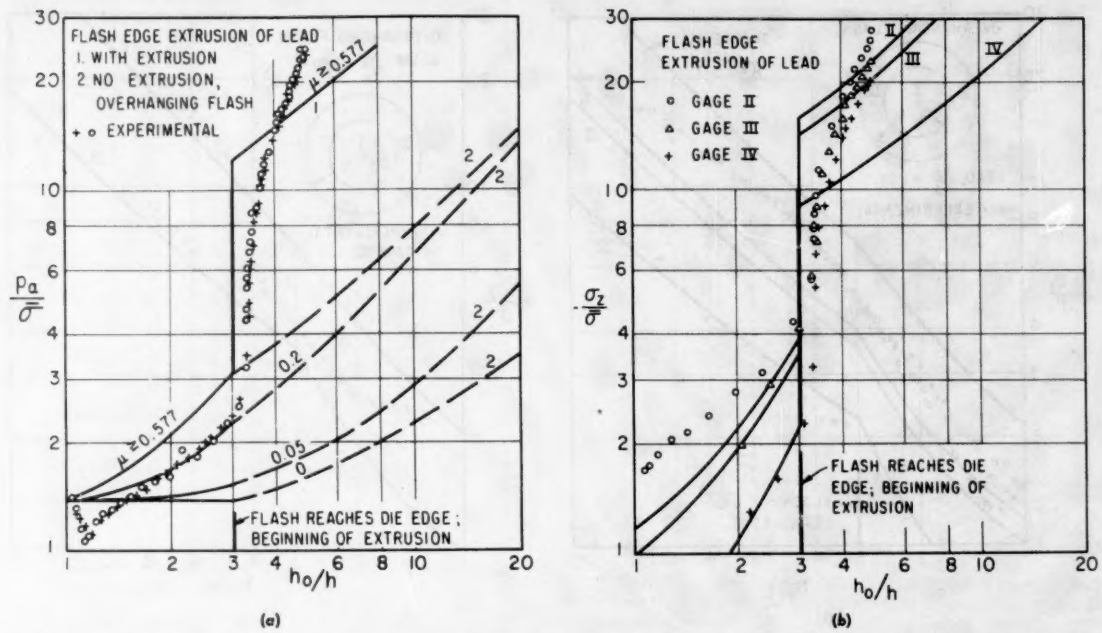

Fig. 7 Dimensionless average and local pressure distribution as function of height ratio in closed die forging with flash edge extrusion of commercially pure lead

its support by its grant and the University of California for the use of laboratory space and equipment. They further wish to thank Messrs. Hall, Harris, Miller, and Woodruff for assisting with the experimental phase of the project, Mr. Kot for preparing all figures, and Mrs. Arneson for typing the manuscript.

References

1 L. Prandtl, "Anwendungsbeispiele zu einem Henckyschen Satz über das Plastische Gleichgewicht," *Zeitschrift für Angewandte Mathematik und Mechanik*, vol. 3, 1923, pp. 401–406.

2 R. Hill, E. H. Lee, and S. J. Tupper, "A Method of Numerical Analysis of Plastic Flow in Plane Strain and Its Application to the Compression of a Ductile Material Between Rough Plates," *Journal of Applied Mechanics*, vol. 18, TRANS. ASME, vol. 73, 1951, pp. 46–52.

3 A. P. Green, "A Theoretical Investigation of the Compression of a Ductile Material Between Smooth Flat Dies," *Philosophical Magazine*, series 7, vol. 42, 1951, p. 900.

4 E. Siebel, "Grundlagen zur Berechnung des Kraft- und Arbeitsbedarfs beim Schmieden und Walzen," *Stahl und Eisen*, vol. 43, 1923, pp. 1295–1298.

5 G. Sachs, "Spanlose Formung der Metalle," Mitteilungen der Deutschen Material Prüfungsanstalten, Supplement 16, Julius Springer, Berlin, Germany, 1931, p. 93.

6 M. Stone and J. Greenberger, "Rolling Pressures in Strip Mill," *Iron and Steel Engineer*, vol. 20, 1943, p. 61.

7 J. M. Alexander, "The Effect of Coulomb Friction in the Plane-Strain Compression of a Plastic Rigid Material," *Journal of the Mechanics and Physics of Solids*, vol. 3, 1955, pp. 233–245.

8 J. F. W. Bishop, "On the Effect of Friction on Compression and Indentation Between Flat Dies," *Journal of the Mechanics and Physics of Solids*, vol. 6, 1958, pp. 132–144.

9 S. Kobayashi and E. G. Thomsen, "Approximate Solutions to a Problem of Press Forging," JOURNAL OF ENGINEERING FOR INDUSTRY, TRANS. ASME, series B, vol. 81, 1959, pp. 217–227.

10 A. B. Watts and H. Ford, "An Experimental Investigation of the Yielding of Strip Between Smooth Dies," *Proceedings of The Institution of Mechanical Engineers*, vol. 1b, 1952–53, pp. 448–453.

11 S. Kobayashi, R. Herzog, J. T. Lapsley, Jr., and E. G. Thomsen, "Theory and Experiment of Press Forging Axisymmetric Parts of Aluminum and Lead," JOURNAL OF ENGINEERING FOR INDUSTRY, TRANS. ASME, series B, vol. 81, 1959, pp. 228–238.

12 W. Schroeder and D. A. Webster, "Press-Forging Thin Sections: Effect of Friction, Area, and Thickness on Pressure Required," *Journal of Applied Mechanics*, vol. 16, TRANS. ASME, vol. 71, 1949, pp. 289–294.

13 S. Kobayashi, A. G. MacDonald, and E. G. Thomsen, "Some Aspects of Press Forging," *Journal of the Mechanical Sciences*, to be pubished.

14 W. Johnson, "Extrusion Through Square Dies of Large Reduction," *Journal of the Mechanics and Physics of Solids*, vol. 4, 1956, pp. 191–198.

15 J. Frisch and E. G. Thomsen, "The Effect of Process-Variables on Extrusion Pressures of Lead," JOURNAL OF ENGINEERING FOR INDUSTRY, TRANS. ASME, series B, vol. 81, 1959, pp. 207–216.

16 M. T. Watkins, K. Ashcroft, and J. McKenzie, "Some Aspects of the Cold Extrusion of Metals," presented at the Conference on Technology of Engineering Manufacture, The Institution of Mechanical Engineers, London, England, March 25–27, 1958, Paper No. 47.

17 E. G. Thomsen, "Plane-Strain and Axially Symmetric Velocities and Pressures in Extrusions," Proceedings of the Conference on the Properties of Materials at High Rates of Strain, The Institution of Mechanical Engineers, London, England, April 30–May 2, 1957, pp. 77–85.

The Deformation Process in Metal-Cutting

W. J. McDONALD

B. F. MURPHEY

Minnesota Mining and Manufacturing Company, Central Research Laboratory, St. Paul, Minn.

An analysis of the orthogonal chip process for a strain-hardening material is presented together with a qualitative evaluation of the effects of temperature increases and of flank rubbing. An expression is derived for the average stress on planes through the tool point ahead of the shear plane. The authors postulate that the strain-hardening requires that a stress-reinforcing phenomenon be present and that this requires the shear to take place in a region of increasing stress. The rate of increase required is postulated to depend on the final strain imparted to the chip. Data from the literature are presented to support this view. The conclusion is drawn that the strain imparted to the chip is a measure of the deviation of the shear angle from the Merchant minimum-energy condition.

HISTORICALLY, the subject of metal-cutting has received considerable attention by a number of authors over the past 20 years. The problem can probably best be introduced by examining the analysis of Merchant [1].[1] The analysis is restricted to the case of the orthogonal tool. The process is depicted in Fig. 1. A surface layer of material is removed by a wedge-shaped tool which is constrained to travel parallel to the surface at a chosen depth. Observation of the process shows that the deformation of the chip takes place abruptly as shear in a plane extending from the point of the tool to the surface of the metal and inclined at an angle ϕ to the horizontal. Essentially, all of the energy involved is expended in two processes—the shear of the metal on the shear plane, and the rubbing of the chip on the tool as it passes up the tool face. The variables involved, together with Merchant's notation, are shown in Fig. 1. They are defined in the nomenclature.

Merchant then derives an expression for the work done in terms of t, τ, α, ϕ, and the shear strength of the metal. He reasons that ϕ will take a value such as to make this work a minimum and works out the condition for this minimum, under the assumption that the shear strength of the material being cut is a true constant. The result is

$$2\phi + \tau - \alpha = 90 \text{ deg}$$

where τ is given by

$$\tan \tau = \frac{F_t + F_c \tan \alpha}{F_c - F_t \tan \alpha}$$

[1] Numbers in brackets designate References at end of paper.

Contributed by the Metal Processing Activity of the Production Engineering Division, and presented at the Annual Meeting, Atlantic City, N. J., November 29–December 4, 1959, of THE AMERICAN SOCIETY OF MECHANICAL ENGINEERS.

NOTE: Statements and opinions advanced in papers are to be understood as individual expressions of their authors and not those of the Society. Manuscript received at ASME Headquarters, August 19, 1959. Paper No. 59—A-165.

Merchant then extends the analysis to the case of a material in which the shear strength is increased proportionally by the hydrostatic pressure on it. This results in

$$2\phi + \tau - \alpha = \theta \qquad (1)$$

where θ is a measure of the effect of the hydrostatic pressure on the shear strength and depends on the material being machined. These derivations make the assumption that the strain-hardening and temperature increases in the metal have negligible or compensating effects. Other theories in the field are reviewed by Shaw [2].

Theory

We propose to carry out an analysis for a material whose shear strength is increased monotonically with strain and to evaluate qualitatively the effects of temperature increases, and of flank wear, on the shear angle.

Shaw [2] has shown that the coefficient of friction μ, and thereby τ, is very dependent on α and does not at all obey Amontons' law; that is to say, the friction force is not independent of the area or proportional to the normal force. For this reason, it was felt best to eliminate μ and τ from the analysis altogether. Let us introduce instead

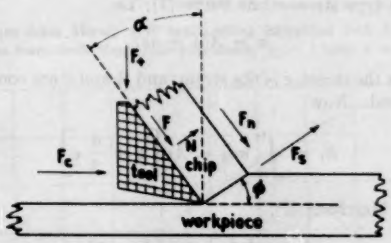

Fig. 1 Side view of chip-cutting process

Nomenclature

α = rake angle of tool
ϕ = shear angle
μ = F/N coefficient of friction
τ = $\tan^{-1} \mu$
E = F_c/A_0 = work per volume of metal removed
F_c = cutting force on tool
F_t = thrust force on tool
ω = F_c/F_t gross apparent coefficient of friction for the entire process
γ = $\tan^{-1} \omega$
ϵ = strain imparted to the chip
F = friction force on tool face
N = normal force on tool face
F_s = shear force on shear plane
F_n = normal force on shear plane
t = thickness of metal being removed
w = width of cut
A_0 = wt = cross-sectional area of chip before removal

$$\omega = F_c/F \qquad \gamma = \tan^{-1}\omega$$

Since

$$\tan\tau = \frac{F_t + F_c\tan\alpha}{F_c - F_t\tan\alpha} = \frac{\cot\gamma + \tan\alpha}{1 - \cot\gamma\tan\alpha}$$

$$\tau = (90 - \gamma) + \alpha$$
$$\gamma = 90 - \tau + \alpha$$

Merchant's equation for the minimum work condition

$$2\phi + \tau - \alpha = 90°$$

becomes

$$2\phi = \gamma, \text{ independent of } \alpha$$

This change of variable does not, of course, change the analysis in any basic way. It is introduced merely to emphasize that the energy-dissipating process on the tool face is not an ordinary friction process, and for general convenience in mathematical manipulation.

Consider Fig. 2 which shows work being done in three processes:

1 Shearing of the metal on the shear plane.
2 Rubbing of the chip over the tool face.
3 Rubbing of the tool flank over the cut surface.

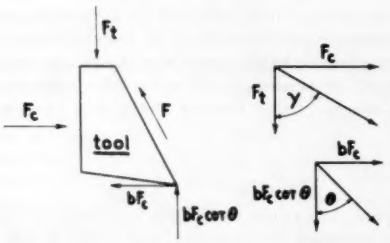

Fig. 2 Forces on tool necessary to calculate energy

Call the work per unit volume of metal removed by each of these three processes E_1, E_2, and E_3, respectively, and call the total external work per unit volume of metal removed, E. Then

$$E = E_1 + E_2 + E_3 \tag{2}$$

To compute E_1, consider a work-hardening material with a Bridgman-type stress-strain curve [3]; i.e.,

$$\sigma = A(1 + a\epsilon),$$

where σ is the stress, ϵ is the strain, and A and a are constants of the material. Now

$$E_1 = \int_0^\epsilon \sigma d\epsilon = A\epsilon\left[1 + \frac{a}{2}\epsilon\right]$$

and from Merchant [1],

$$\epsilon = \cot\phi + \tan(\phi - \alpha)$$

Define l_1 as the length of a unit volume of "uncut" chip, and l_2 as the length of a unit volume of chip after it is cut. Now since F is the friction force on the tool face $E_2 = Fl_2$.

From Merchant:

$$l_2 = \frac{l_1\sin\phi}{\cos(\phi - \alpha)}$$

Consider a force bF_c, due to the rubbing of the flank, which is parallel to F_c and opposing it, and consider the normal force on the flank to be $bF_c\cot\theta$. Then

$$F = F_c(1 - b)\sin\alpha + (F_c - bF_c\cot\theta)\cos\alpha$$
$$F = F_c[(1 - b)\sin\alpha + (\cot\gamma - b\cot\theta)\cos\alpha]$$

Remembering that $F_cl_1 = E$

$$E_2 = E[(1 - b)\sin\alpha + (\cot\gamma - b\cot\theta)\cos\alpha]\frac{\sin\phi}{\cos\phi - \alpha}$$

While $$E_3 = bF_cl_1 = bE$$

Putting the expressions for E_1, E_2, and E into equation (2) and simplifying, one obtains

$$\frac{E}{A} = \frac{1 + \dfrac{a\cos\alpha}{2\sin\phi\cos(\phi - \alpha)}}{\sin\phi\left[\dfrac{\sin(\gamma - \phi)}{\sin\gamma} - b\dfrac{\sin(\theta - \phi)}{\sin\theta}\right]} \tag{3}$$

If $b = a = 0$

$$\frac{E}{A} = \frac{\sin\gamma}{\sin\phi\sin(\gamma - \phi)}$$

and this has a minimum at $\phi = \gamma/2$ (Merchant's result). If a is zero and b is not zero, the condition for the minimum is

$$\cot 2\phi = \frac{\cot\gamma - b\cot\theta}{1 - b}$$

If $b = 0$, this reduces to $2\phi = \gamma$ again; also if $\theta = \gamma$, this reduces to $2\phi = \gamma$. If $\theta < \gamma$, this makes $\phi > \gamma/2$; and if $\theta > \gamma$, this makes $\phi < \gamma/2$.

Since one would normally expect to find $\theta < \gamma$, the effect would be to shift the minimum-energy point to a greater value of ϕ. However, unless b is quite large and θ considerably different from γ, the effect is small, e.g., if $\gamma = 90$ deg, $\theta = 45$ deg, and $b = 0.1$, the minimum-energy point is at $\phi = 48.1$ deg, an increase of 3.1 deg.

If $b = 0$ and $a \neq 0$, the minimum energy point is shifted toward $\phi = \pi/4 + \alpha/2$, and this constitutes an increase in ϕ unless there is zero friction on the tool face. The shift of the minimum-energy point to values of ϕ larger than $\gamma/2$ has interesting implications in the case where $a \neq 0$ and $b = 0$. Describe a plane originating at the tool point and inclined upward at an angle ψ. When $\psi = \phi$, this is the shear plane, Fig. 3. If one computes the average elastic stress on such a plane, there results for ψ less than ϕ:

$$T = \frac{E\sin\psi\sin(\gamma - \psi)}{\sin\gamma} \tag{4}$$

where T is the average elastic stress on such a plane.

Now

$$\frac{dT}{d\psi} = \frac{E\sin(\gamma - 2\psi)}{\sin\gamma}$$

and this has a maximum at $\psi = \gamma/2$.

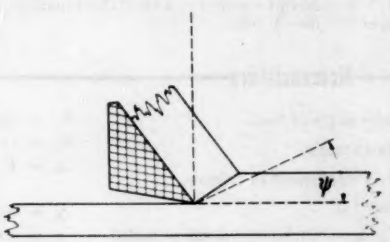

Fig. 3 Diagram showing angle

In other words, if ϕ were to assume the minimum-energy position, the metal would first have to pass through a plane of high shear stress ($\psi = \gamma/2$) without shearing, and then later shear at a lesser stress. Since this cannot happen for a material whose shear strength depends only on the strain, one is forced to conclude that ϕ cannot take on the minimum-energy position for such a material. Instead, it seems logical to postulate that the shear must take place in a region of increasing stress, since some sort of reinforcing phenomenon is needed to compensate for the increased shear strength due to the strain-hardening. Furthermore, if the strain is to be high, the shear should take place in a region where the stress is increasing rapidly, while if the strain is to be low, the shear should be able to take place in a region where the stress is increasing more slowly.

A plot of equation (4) is shown in Fig. 4. This equation, of course, holds only for $\psi < \phi$. We suggest that, for a test where ϵ is large, the value of the observed ϕ will be relatively far to the left of $\gamma/2$ while, if ϵ is small, the observed value of ϕ will be closer to $\gamma/2$. To investigate this possibility, let us first normalize the curves of equation (4). Calling the peak value of average stress T_m, we can normalize by plotting T/T_m versus $2\psi/\gamma$. If we call $T/T_m = z$ and $2\psi/\gamma = x$, equation (4) becomes

$$z = \frac{\sin x(\gamma/2) \sin (2 - x)(\gamma/2)}{\sin^2 (\gamma/2)} \qquad (5)$$

This equation is plotted in Fig. 5. It is seen that z is only slightly a function of γ.

One could use any of several parameters to indicate the deviation of ϕ from $\gamma/2$. Various possibilities are $(1 - z)$, $(1 - x)$, or dz/dx. We have chosen to use $1 - x$, primarily because it is the easiest to calculate. Incidentally, as γ becomes small, $dz/dx = 2(1 - x)$ and in fact $dz/dx \cong 2(1 - x)$ even for $\gamma = 90$ deg.

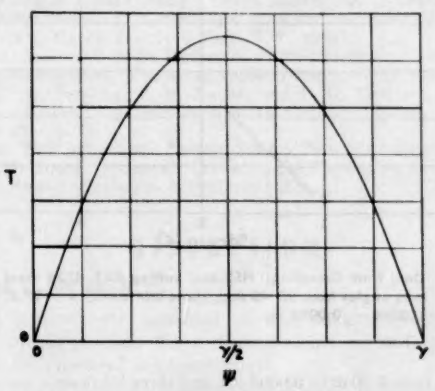

Fig. 4 Plot of Equation (4)

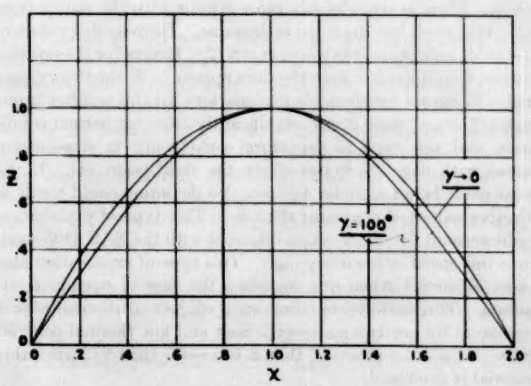

Fig. 5 Plot of Equation (5)

Data

We next require some data to test the theory. Here an important limitation becomes apparent for the analysis is based on a strain-hardening type of stress-strain curve. For most materials, this implies that the test is done at a relatively constant temperature. Unfortunately, the strain rates involved in ordinary machining practice are very high, and this must lead to stress-strain curves which are more nearly adiabatic than isothermal. Zener and Holloman [4] point out that this has drastic effects on the shape of the stress-strain curve.

Shaw, Cook, and Finnie [2] present some data taken at a very low speed ($v = 1$ ipm). These data are tabulated in Table 1 and plotted in Fig. 6. If one calls $\gamma/2 = \phi_0$, then $x = \phi/\phi_0$ and $1 - x = 1 - \phi/\phi_0$. The plot is made of the strain ϵ versus $1 - \phi/\phi_0$. The correlation is seen to be quite good; however, the apparent positive intercept on the strain axis is somewhat puzzling. Another set of slow-speed data (aluminum being cut at 4.85 ipm) is presented by Merchant and Zlatin [6]. The data are given in Table 1 and plotted in Fig. 7. Again the correlation appears to be very good. Creveling, Jordan, and Thomsen [5] present a large number of data taken at speeds of 27.4 and 29.4 fpm. These data are shown in Figs. 8, 9, and 10 for the three different steels investigated. Rake angles varied from 20 to 40 deg, depths of cut

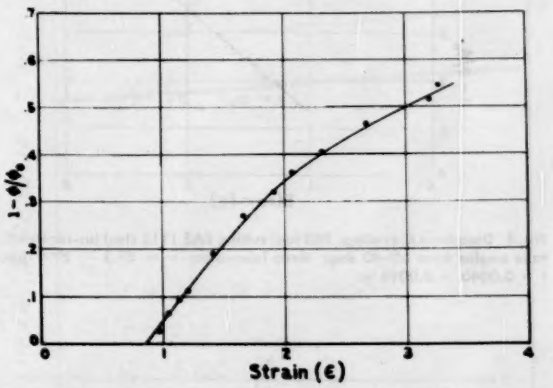

Fig. 6 Data from Shaw; HSS tool cutting annealed SAE 1112 steel; rake angles from 0–45 deg; four lubricants; $v = 1$ ipm, $t = 0.003$ in.

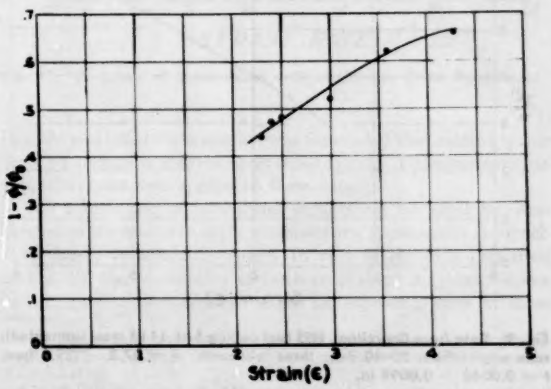

Fig. 7 Data from Merchant; HSS tool cutting aluminum; rake angle = 15 deg; six lubricants; $v = 4.85$ ipm

Table 1 Data from references [2] and [6]

Line	Author	Workpiece	Lubricant	α, deg	t, in.	v, ipm	γ, deg	ϕ_0, deg	ϕ, deg	$1 - \phi/\phi_0$	ϵ
1	S[b]		Benzene	45			82.0	41.0	36.5	0.110	1.20
2	S		Air	45			85.2	42.6	38.6	0.094	1.14
3	S	SAE	Ethanol	45			90.9	45.5	42.7	0.062	1.04
4	S	1112	CCl_4	45			96.9	48.5	47.4	0.023	0.96
5	S	Steel	Benzene	30	0.003	1	74.6	37.3	22.2	0.405	2.31
6	S		Air	30			79.1	39.6	27.0	0.319	1.91
7	S		Ethanol	30			85.8	42.9	31.4	0.269	1.66
8	S		CCl_4	30			94.1	47.1	38.2	0.189	1.41
9	S		Air	16			72.7	36.4	17.5	0.515	3.20
10	S		Ethanol	16			78.8	39.4	21.1	0.464	2.68
11	S		CCl_4	16			88.8	44.4	28.4	0.361	2.07
12	S		CCl_4	0			82.5	41.3	18.8	0.545	3.28
13	M[b]		1[a]				81.8	40.9	15.4	0.623	3.6
14	M		CCl_4				88.9	44.5	24.9	0.441	2.3
15	M	Al	2	15	0.005	4.85	77.5	38.8	13.1	0.662	4.3
16	M		3				88.3	44.2	23.5	0.468	2.4
17	M		4				79.4	39.7	19.0	0.521	3.0
18	M		5				88.9	44.5	23.1	0.481	2.5

[a] 1 Dichloromethane.
2 Ethyl acetate.
3 Hexyl acetate.
4 Ethyl alcohol.
5 Hexyl alcohol.

[b] S = Shaw.
M = Merchant.

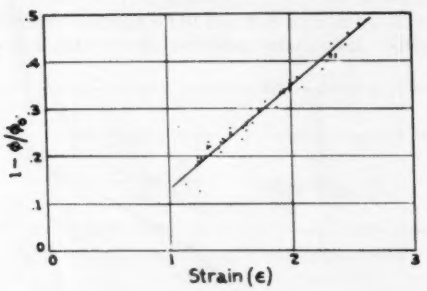

Fig. 8 Data from Creveling; HSS tool cutting SAE 1113 steel (as-received); rake angles from 20–40 deg; three lubricants; v = 27.3 — 29.4 fpm, t = 0.0040 — 0.0098 in.

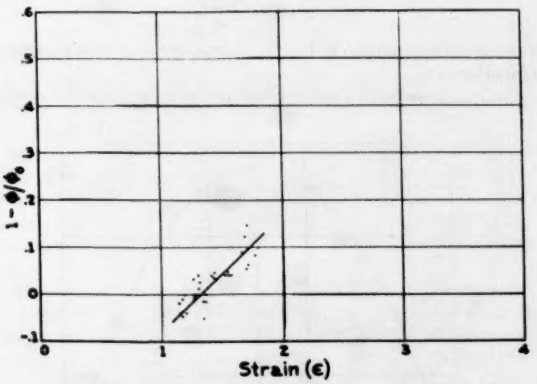

Fig. 10 Data from Creveling; HSS tool cutting SAE 4135 steel (as-received); rake angles from 20–40 deg; three lubricants; v = 27.3 — 29.4 fpm, t = 0.0040 — 0.0098 in.

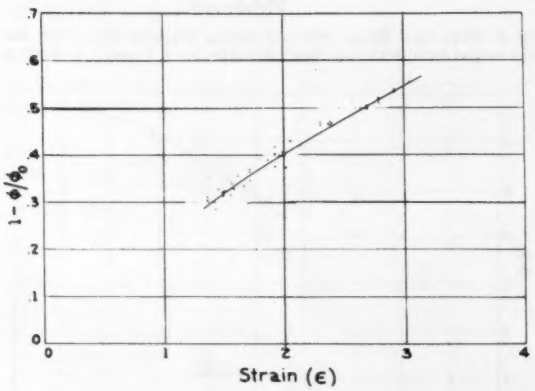

Fig. 9 Data from Creveling; HSS tool cutting SAE 1113 steel (annealed); rake angles from 20–40 deg; three lubricants; v = 27.3 — 29.4 fpm, t = 0.0040 — 0.0098 in.

ranged from 0.0040 to 0.0098 in., and three lubricants were used.

The correlation with SAE 1113 steel, both in the annealed and the as-received condition, is excellent, even at this relatively high speed. There is considerably more scatter with the points from SAE 4135 steel, but the trend is the same. The negative values of $1 - \phi/\phi_0$ indicate points where $\phi > \gamma/2$. Except for the positive intercept on the strain axis, the data appear to fit the theory very well. There are two possible explanations for this positive intercept. The test may depart significantly from isothermal conditions, and this type of departure could result in stress-strain curves with negative slopes above the yield point [4]. If the shear plane is not actually a plane, this deviation could result in effective values of ϕ greater than ϕ_0. This type of explanation could account for the positive intercept with the SAE 4135 steel, since this speed is relatively high. This type of explanation also seems attractive when one considers the case of machining titanium. This material is notoriously subject to thermal effects because of its low-volume specific heat and low thermal conductivity. It is often observed that ϕ is greater than $\gamma/2$ when this material is machined.

However, one feels that this type of reasoning does not give a

satisfactory explanation in the case of Shaw's data, Fig. 6, since this machining was done at the very low speed of 1 ipm. In this regard, let us consider again the effect of rubbing on the tool flank. The equations for T and Z were based on the assumption of no flank rubbing, i.e., $b = 0$. If b is not zero, the maximum of these curves is shifted in the same way as the minimum-energy point previously discussed. As explained previously, this normally would result in shifting the maximum to the right, meaning that our computed value of ϕ_0 was too low. If a larger value of ϕ_0 were used, the value of $1 - \phi/\phi_0$ would be larger, and the difficulty would be resolved. We feel that this is the proper explanation for the intercept with the slow-speed data.

Conclusion

We have examined the case of orthogonal machining of a strain-hardening material. We conclude that the strain imparted to the chip is a measure of the deviation from Merchant's original equation, $2\phi + \tau - \alpha = 90$ deg, provided the temperature increases are not so great as to alter the stress-strain curve drastically. We conclude further that an accurate evaluation of τ in the foregoing equation (or ϕ_0 in terms of our variables) requires an assessment of the forces of rubbing on the tool flank.

References

1 M. E. Merchant, "Mechanics of the Metal Cutting Process," *Journal of Applied Physics*, vol. 16, 1945, pp. 267–275 and pp. 318–324.

2 M. C. Shaw, N. A. Cook and D. Finnie, "The Shear-Angle Relationship in Metal Cutting," TRANS. ASME, vol. 75, 1953, p. 273.

3 P. W. Bridgman, "Large Plastic Flow and Fracture," McGraw-Hill Book Company, Inc., New York, N. Y., 1952.

4 C. Zener and J. H. Holloman, "Effect of Strain Rate Upon Plastic Flow of Steel," *Journal of Applied Physics*, vol. 15, 1944, p. 22.

5 J. H. Creveling, T. H. Jordan, and E. G. Thomsen, "Some Studies of Angle Relationships in Metal Cutting," TRANS. ASME, vol. 79, 1957, p. 127.

6 M. E. Merchant and Norman Zlatin, "New Methods of Analysis of Machining Processes," *Proceedings of The Society for Experimental Stress Analysis*, vol. 3, 1946, pp. 4–27.

DISCUSSION

Fenton L. Bagley, Jr.[2]

The authors have presented an interesting analysis of the metal cutting process. A few of the assumptions used, however, should be considered in greater length.

The first of these is the assumption of strain hardening in the material being cut. As can be seen from the data of Kececioglu[3] shown in Fig. 11 this can, under the unique conditions of metal cutting, be strain softening. Also applicable here is Fig. 12 which shows an increase in shear stress due to increasing strain rate. A statistical analysis[4] of this data reveals the equations stated on each curve. Also included are the correlation coefficient r, standard deviation σ, and the confidence level. The confidence level is the probability that the observed correlation could have been achieved by a sample from a population of random data. The confidence levels of neither Figs. 11 or 12 show the data trends to be highly significant, but neither can they be disregarded. This would imply that the effect of strain rate should also be included in the analysis. In a recent paper by S. Kobayashi and others[5] the opinion was forwarded that neither γ nor $\dot{\gamma} = d\gamma/dt$ had any effect upon shear stress. Unfortunately, no statistical tests were applied to these data.

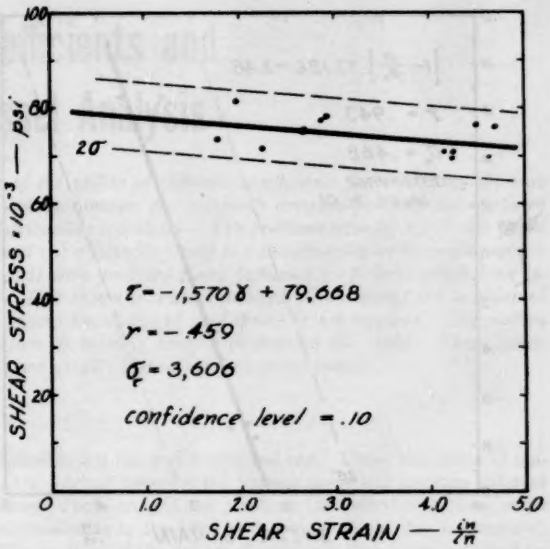

Fig. 11 Variation of shear stress with strain (from Kececioglu)

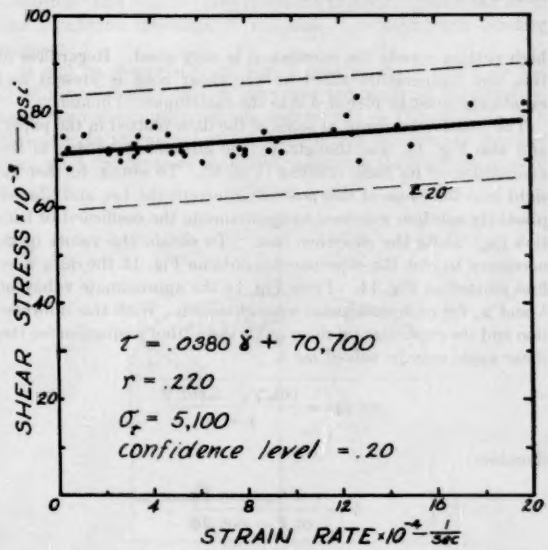

Fig. 12 Variation of shear stress with strain rate (from Kececioglu)

The assumption of isothermal shear must be carefully considered as the majority of the metal cutting applications approach very closely to adiabatic shear. In view of the data presented in Fig. 13[6] the assumption of isothermal shear may not impose as stringent a limitation as might be expected, since at these

[2] Graduate student, Massachusetts Institute of Technology; Mechanical Engineer, Rodman Laboratory, Watertown Arsenal, Mass.

[3] D. Kececioglu, "Shear-Strain Rate in Metal Cutting and Its Effect on Shear-Flow Stress," TRANS. ASME, vol. 80, 1958, pp. 158–168.

[4] A. G. Worthing and J. Geffner, "Treatment of Experimental Data," John Wiley & Sons, Inc., New York, N. Y., chapters 11 & 12.

[5] S. Kobayashi and others, "A Critical Comparison of Metal-Cutting Theories With New Experimental Data," ASME Paper No. 59—A-131.

[6] F. L Bagley and R. Mennell, "Machining Characteristics of Leaded Steel," TRANS. ASME series D, *Journal of Basic Engineering*, vol. 82, 1960, pp. 347–359.

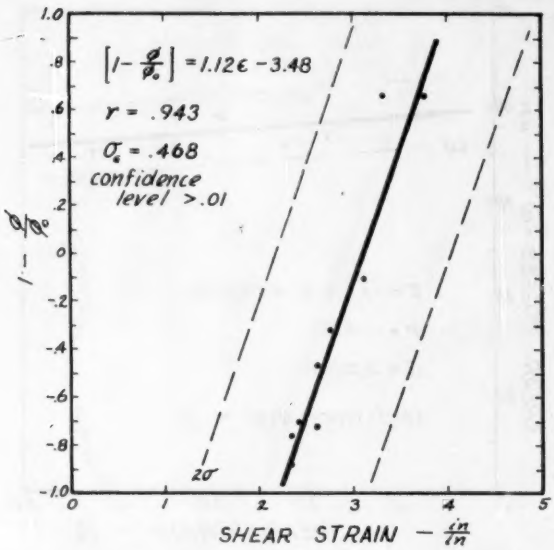

Fig. 13 Data from Bagley and Mennell; C-6 carbide cutting 235 Bhn, 4340 steel; tool signature of 0, 0, 5, 5, 5, 0, 0.020; 0.200 depth, 0.005 feed; dry; V = 50 to 700 sfpm

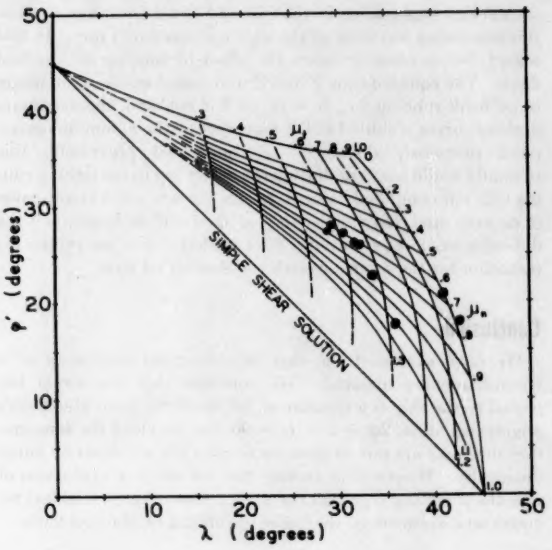

THE FOLLOWING PARAMETERS WERE USED TO PLOT DATA (MERCHANT)

$$\tan \phi' = \frac{\cos \alpha}{\frac{1}{r_c} - \sin \alpha} = r_c \qquad \tan \lambda = \frac{F_n + (F_t \tan \alpha)}{F_t - (F_n \tan \alpha)} = \frac{F_t}{F_t}$$

Fig. 14 Lee and Shaffer plasticity solution for $\alpha = 0$ deg

high cutting speeds the correlation is very good. Regardless of this, the temperature effect on the shear zone is present and eventually must be included into the mathematical model.

The positive intercept of some of the data plotted in the paper, and also Fig. 13, was thought by the authors to be due to the assumption of no flank rubbing ($b = 0$). To obtain further insight into the cause of this positive intercept the Lee and Shaffer plasticity solution was used to approximate the coefficient of friction (μ_n) along the clearance face. To obtain the values of ϕ_0 necessary to plot the experimental data on Fig. 13 the data were first plotted on Fig. 14. From Fig. 14 the approximate values of λ and μ_n for each data point were obtained. With this information and the experimental shear angle the author's equation for the shear angle may be solved for b.

$$\cot 2\phi = \frac{\cot \gamma - b \cot \theta}{1 - b}$$

therefore:

$$b = \frac{\cot \gamma - \cot 2\phi}{\cot \theta - \cot 2\phi}$$

Selecting a data point at random and substituting in the values from the plasticity solution where:

$$\lambda = \gamma$$

$$\lambda_n = \tan^{-1} \mu_n = \theta$$

A value of 3.57 was obtained for b. This is a completely absurd value as these were new, sharp tools. This discrepancy could be due to either the ideal plastic model or the minimum energy approximation as they are both known to be in error.

The value of b was then assumed to be zero and the data plotted in Fig. 13. The correlation is seen to be excellent and the trend shown to have very high significance.

The practical application of Fig. 13 is very difficult as γ is not a constant with respect to cutting speed. Also the introduction of the ideal plastic model is not consistent with the possibility of a shear stress that is a function of shear strain. This is not serious though, since it was necessary later in the analysis to remove the possible variations of the shear stress.

Authors' Closure

We thank Mr. Bagley for his interesting discussion of our paper.

Concerning first the attempt to calculate the quantity b from the equation:

$$\cot 2\phi = \frac{\cot \gamma - b \cot \theta}{1 - b}$$

We do not understand the discusser's use of the plasticity condition to calculate γ, since γ is defined as the angle formed by the resultant of the exterior forces applied to the tool and should simply be calculated from the dynamometer readings. However, we certainly agree that this equation should not be used to calculate b. The equation was in no way intended to predict ϕ in general, but merely points out the effect that flank dragging would have on the original Merchant minimum energy solution for a material whose shear strength was a true constant.

We agree with the discusser concerning the possibility of "strain softening" occurring; in fact, we feel that the entire shape of the stress-strain curve at high strain rates is of paramount importance. Reference [4], by Zener and Holloman, points to this conclusion. We believe that, for heat sensitive materials, or for high speeds, a complex stress-strain relationship could result in rounding of the chip workpiece intersection and consequent values of ϕ greater than ϕ_0.

Influence Coefficients and Pressure Vessel Analysis

G. D. GALLETLY
Engineer, Shell Development Company, Emeryville Research Center, Emeryville, Calif. Assoc. Mem. ASME

A description is given of the utility of influence coefficients for analyzing pressure vessels. To illustrate their advantages two relatively complex problems were selected and their final stress distributions calculated. The problems were (i) a cylinder closed by a torispherical head and (ii) a cylinder joined to a smaller cylinder by an ellipsoidal-toroidal shell. Two vessels were analyzed using influence coefficients which have recently become available. It is shown that accurate stress distributions can be obtained quickly and that a specialized knowledge of shell theory is not required. The method also shows the distribution of bending stresses throughout the shells. These latter, which can be important, are usually ignored by the various codes.

PRESSURE vessels today are usually designed in accordance with the provisions of the ASME Code for Unfired Pressure Vessels [1],[1] and, in so far as pressure loadings are concerned, the code usually attempts to predict only the direct (i.e., membrane) stresses. Examples of such cases are the code's formulas for evaluating the stresses due to internal pressure in cylindrical or spherical shells. The code, of course, recognizes the fact that bending stresses may exist in vessels designed in accordance with its rules. However, usually design rules for details have been written to hold such stresses at a safe level consistent with experience.

The situation with regard to torispherical and ellipsoidal shells appears to be somewhat different from that just outlined. The formulas for these shells, which are based on tests of heads of various geometries, include both bending and direct stresses. However, the accuracy of these formulas, outside the ranges of the tests on which they were based, has not been confirmed. An example of this, for a torispherical head with a large diameter-thickness ratio, was discussed recently in the literature [2].

The reason for not computing the bending stresses in shells is, of course, due to the complex calculations and length of time involved. However, if optimum use of material is desired, plus a realistic knowledge of the elastic stresses in the vessel, then the bending stresses must be calculated. A means is thus required to enable a designer to calculate them quickly and accurately.

One such method is that of using tables of influence coefficients (by "influence coefficient" is meant the stress or deformation at a point in the shell due to unit values of the edge bending loads or unit values of the pressure). These coefficients have been obtained recently for a number of shells of practical interest, Table 1, and it is the purpose of this paper to show how they should be used. Before doing this, however, a brief description will be given of the method used to solve these problems. As an example, a cylindrical pressure vessel with a torispherical head will be considered.

Cylinder-Torispherical Shell Junction

The vessel under consideration is shown in Fig. 1. As shown in this figure, the component parts of the vessel consists of a cylinder, a torus, and a spherical cap. Under the action of uniform internal pressure the various parts will undergo different elastic displacements and rotations (actually for the case under discussion, only the torus will have rotations due to pressure). The position of the deformed shells will then be as indicated by the dashed lines in Fig. 2. In this state no edge bending moments or transverse shears are acting; the shells are in the "membrane condition" and only in-plane forces are present. (Since the torus has membrane rotations, it will also have membrane bending moments.)

It will be observed from Fig. 2 that points 1 and 2 on the original vessel, after cutting the vessel and applying the pressure, have been displaced from one another ($1' \rightarrow 1''$ and $2' \rightarrow 2''$). However, in the actual vessel these points will remain together even after the pressure is applied, assuming there are no gaps in

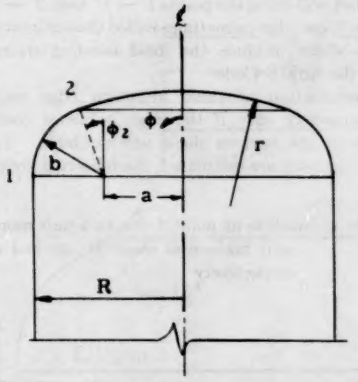

Fig. 1 Cylinder-torispherical shell junction

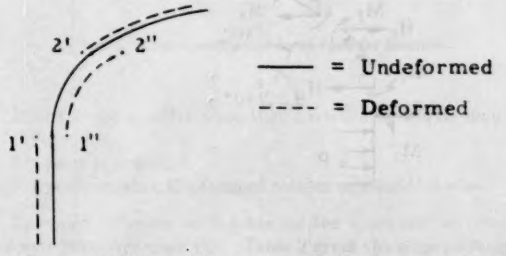

Fig. 2 Deformations due to pressure of the constituent shells

[1] Numbers in brackets designate References at end of paper.

Contributed by the Petroleum Division and presented at the Annual Meeting, Atlantic City, N. J., November 29–December 4, 1959, of THE AMERICAN SOCIETY OF MECHANICAL ENGINEERS.

NOTE: Statements and opinions advanced in papers are to be understood as individual expressions of their authors and not those of the Society. Manuscript received at ASME Headquarters, August 4, 1959. Paper No. 59—A-163.

Table 1 Available tabulations of influence coefficients

Type of Shell	Range of Parameters	Source and Remarks
Open-Crown Hemisphere 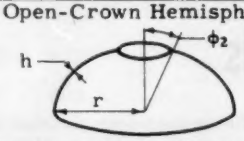	ϕ_2 = 50°, 40°, 30°, 20°, 10° 15 < r/h < 250	Reference 3
Positive-Curvature Toroid 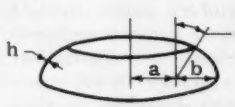	ϕ_2 = 75°, 60°, 45°, 30°, 15° a/b = 4, 5, 6, 7, 8 5 < b/h < 50	Reference 4 See Footnote 2
Negative-Curvature Toroid 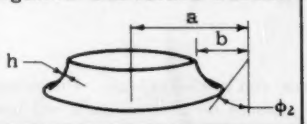	ϕ_2 = 75°, 60°, 45°, 30°, 15° a/b = 3, 4, 5, 6, 7 5 < b/h < 50	Reference 5 See Footnote 2
Open-Crown Ellipsoid 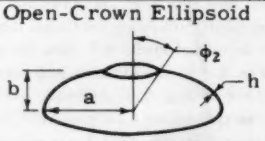	ϕ = 50°, 40°, 30°, 20°, 10° a/b = 2, 3 15 < a/h < 250	Reference 6 See Footnote 2

the vessel. The only way this can be brought about with the shells in their displaced positions of Fig. 2 is to apply axisymmetric edge moments and shears around the cut edges. This system, which is in static equilibrium, is shown in Fig. 3 and, provided the magnitudes and directions of the moments and shears are chosen correctly, they will bring the points $1' \rightarrow 1''$ and $2' \rightarrow 2''$ together again. It is these edge (sometimes called discontinuity) moments and shears which produce the local bending stresses usually ignored by the ASME Code.

The determination of these unknown edge moments and shears is extremely easy if the edge influence coefficients for deformation of the various shells are available. To illustrate how these unknowns are calculated, the following notation will be introduced:

${}_M\theta_{11}$ and ${}_H\theta_{11}$ = rotation at point 1 due to a unit moment M, or unit horizontal shear H, applied at point 1, respectively

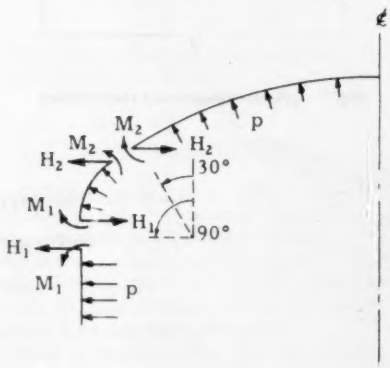

Fig. 3 Axisymmetric edge moments and horizontal shears acting at junctions

${}_M\delta_{11}$ and ${}_H\delta_{11}$ = horizontal displacement at point 1 due to a unit moment M, or unit horizontal shear H, applied at point 1, respectively

${}_M\theta_{12}$ and ${}_H\theta_{12}$ = rotation at point 1 due to a unit moment or unit horizontal shear applied at point 2, respectively

${}_M\delta_{12}$ and ${}_H\delta_{12}$ = horizontal displacement at point 1 due to a unit moment or unit horizontal shear applied at point 2, respectively

The foregoing notation refers to the toroidal transition piece, since it is the only shell element whose two edges will interact with each other (for the shells being considered the cylinder is assumed to be long). The deformations of the torus at point 2 are defined in a similar manner to those at point 1.

The edge rotations and edge horizontal displacements of the spherical cap due to edge moments and edge horizontal shears are defined by:

${}_M\theta_s$ and ${}_H\theta_s$ = rotation at point 2 on the spherical cap due to a unit moment or unit horizontal shear, respectively

${}_M\delta_s$ and ${}_H\delta_s$ = horizontal displacement at point 2 on the spherical cap due to a unit moment or unit horizontal shear, respectively

The edge rotations and horizontal displacements at point 1 on the cylinder are defined similarly. The subscript c, instead of s, is used for these quantities.

The edge rotations and edge horizontal displacements due to pressure will be denoted by capital Greek letters (Θ = rotation, Δ = displacement) with the subscript p to the left. As before, subscripts c and s refer to the cylinder and spherical cap. Subscripts $1t$ and $2t$ will be used to denote the torus at the edges 1 and 2.

The total edge rotations and horizontal displacements of the various shells can then be written as:

(a) Spherical cap

$$\left.\begin{aligned}\delta_e &= {}_M\delta_e M_2 + {}_H\delta_e H_2 + {}_p\Delta_e p\\ \theta_e &= {}_M\theta_e M_2 + {}_H\theta_e H_2 + {}_p\theta_e p\end{aligned}\right\} \quad (1)$$

(*b*) Torus

$$\left.\begin{aligned}\delta_{2i} &= {}_M\delta_{22} M_2 + {}_H\delta_{22} H_2 + {}_M\delta_{21} M_1 + {}_H\delta_{21} H_1 + {}_p\Delta_{2i} p\\ \theta_{2i} &= {}_M\theta_{22} M_2 + {}_H\theta_{22} H_2 + {}_M\theta_{21} M_1 + {}_H\theta_{21} H_1 + {}_p\Theta_{2i} p\\ \delta_{1i} &= {}_M\delta_{12} M_2 + {}_H\delta_{12} H_2 + {}_M\delta_{11} M_1 + {}_H\delta_{11} H_1 + {}_p\Delta_{1i} p\\ \theta_{1i} &= {}_M\theta_{12} M_2 + {}_H\theta_{12} H_2 + {}_M\theta_{11} M_1 + {}_H\theta_{11} H_1 + {}_p\Theta_{1i} p\end{aligned}\right\} \quad (2)$$

(*c*) Cylinder

$$\left.\begin{aligned}\delta_c &= {}_M\delta_c M_1 + {}_H\delta_c H_1 + {}_p\Delta_c p\\ \theta_c &= {}_M\theta_c M_1 + {}_H\theta_c H_1 + {}_p\Theta_c p\end{aligned}\right\} \quad (3)$$

In writing the foregoing equations it was assumed that the edge influence coefficients were obtained with unit values of p and $M_1 \ldots H_2$ and having the directions shown in Fig. 3. Depending on the sign convention used for δ and θ, some of the coefficients in these equations will have negative values. This will be seen later in the numerical examples. There are also certain reciprocal relations between the foregoing edge coefficients but they will not be discussed here.

The next step in the solution is to write the compatibility equations at the cut edges 1 and 2. These equations insure that all the parts of the structure fit together. Thus one has:

$$\left.\begin{aligned}\delta_s &= \delta_{2s}\\ \delta_c &= \delta_{1i}\\ \theta_s &= \theta_{2i}\\ \theta_c &= \theta_{1i}\end{aligned}\right\} \quad (4)$$

Substituting equations (1), (2), and (3) into equations (4), it can be seen that the result will be four linear simultaneous algebraic equations in the unknowns $M_1 \ldots H_2$. Solving this system then gives the edge moments and shears $M_1 \ldots H_2$. Once these have been obtained the stress distributions throughout the various shells can be obtained quickly if the influence coefficients for points away from the edge are known.

This general description of the method of attack used in juncture problems is relatively easy to apply in practice. To illustrate the procedure, two numerical examples will be worked out. The first example will be a torispherical-cylindrical shell junction similar to that just discussed. The second example will deal with a cylinder-ellipsoid-torus-cylinder junction problem, Fig. 5.

Example 1—Cylinder Closed by a Torispherical Head

The vessel under consideration is shown in Fig. 1. The geometric characteristics of the various shells are as follows:

Torus

$a = 131.25$ in.; $b = 18.75$ in.; $a/b = 7$; $b/h = 30$; $\phi_2 = 30$ deg

Cylinder

$R = 150.0$ in.; $R/h_c = 300$; $h_c = 0.5$ in.

Spherical Cap

$r = 281.25$ in.; $r/h_s = 450$; $h_s = 0.625$ in.

where b, R, and r are measured to the middle surface of the shell. It will also be assumed that $p = 60$ psig. The sign convention used is as follows:

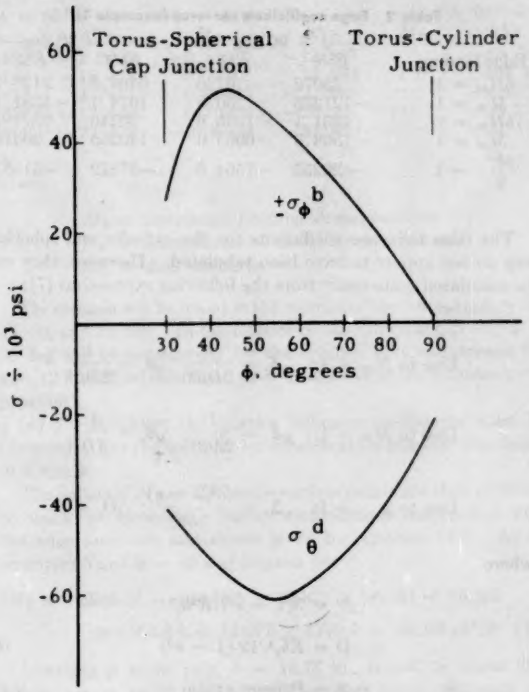

Fig. 4 Stresses in tours, example 1

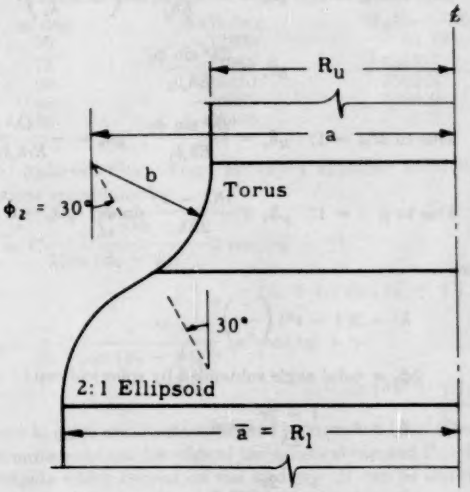

Fig. 5 Cylinder-ellipsoid-torus-cylinder junction

M and H are positive when they have the directions shown in Fig. 3.

δ is positive outward.

θ is positive when the tangent rotates counterclockwise.

The edge influence coefficients for the torus can be obtained directly from reference [4]. Table 2 gives the edge coefficients. There follows (with $\phi = 90$ deg corresponding to subscript 1, and $\phi = 30$ deg to subscript 2).

Table 2 Edge coefficients for torus (example 1)

Edge loading	$\varphi = 90$ deg $Eb^2\theta$	$\varphi = 90$ deg $Eb\delta$	$\phi = 30$ deg $Eb^2\theta$	$\phi = 30$ deg $Eb\delta$
$bH_{90} = 1$.....	25072	−10136	6469.8	2128.7
$M_{90} = 1$.....	−121235	25072	1674.1	−5281.1
$bH_{30} = 1$.....	4951.1	−1995.6	20316	6824.1
$M_{30} = 1$.....	−1568.9	−6065.6	140255	20316
$\frac{pb^2}{2} = 1$.....	−20253	−7564.6	−37872	−31953

The edge influence coefficients for the cylinder and spherical cap do not appear to have been tabulated. However, they can be calculated quite easily from the following expressions [7]:

Cylinder

$$\text{Due to } H_{90} = 1: \quad {}_H\delta_c = \frac{1}{2D\beta^3}; \quad {}_H\theta_c = \frac{1}{2D\beta^2}$$

$$\text{Due to } M_{90} = 1: \quad {}_M\delta_c = \frac{1}{2D\beta^2}; \quad {}_M\theta_c = \frac{1}{\beta D} \tag{5}$$

$$\text{Due to } p = 1: \quad {}_p\Delta_c = \frac{R^2(2-\nu)}{2Eh_c}; \quad {}_p\Theta_c = 0$$

where

$$\beta^4 = 3(1-\nu^2)/R^2h_c^2$$

$$D = Eh_c^3/12(1-\nu^2) \tag{6}$$

ν = Poisson's ratio

Spherical cap

$$\text{Due to } H_{30} = 1: \quad {}_H\delta_s = \frac{-\lambda r \sin^2\phi_2}{Eh_s}\left(k_2 + \frac{1}{k_1}\right);$$

$${}_H\theta_s = \frac{2\lambda^2 \sin\phi_2}{Eh_sk_1} \tag{7}$$

$$\text{Due to } M_{30} = 1: \quad {}_M\delta_s = \frac{2\lambda^2 \sin\phi_2}{Eh_sk_1}; \quad {}_M\theta_s = -\frac{4\lambda^3}{Erh_sk_1}$$

$$\text{Due to } p = 1: \quad {}_p\Delta_s = \frac{r^2(1-\nu)}{2Eh_s}\sin\phi_2; \quad {}_p\Theta_s = 0$$

where

$$\lambda^4 = 3(1-\nu^2)\left(\frac{r}{h_s}\right)^2$$

$2\phi_2$ = total angle subtended by spherical cap

$$k_1 = 1 - \frac{1-2\nu}{2\lambda}\cot\phi_2 \tag{8}$$

$$k_2 = 1 - \frac{1+2\nu}{2\lambda}\cot\phi_2$$

Substituting the numerical values into the foregoing formulas, one obtains the values in Table 3.

From Tables 2 and 3 the edge displacements and rotations of the torus, cylinder, and spherical cap can be obtained. One obtains:

Torus

$$Eb\delta_{90}{}^t = -10{,}136\,(bH_{90}) + 25{,}072\,M_{90} - 1995.6\,(bH_{30}) - 6065.6\,M_{30} - 7564.6\left(\frac{pb^2}{2}\right)$$

$$Eb^2\theta_{90}{}^t = 25{,}072\,(bH_{90}) - 121{,}235\,M_{90} + 4951.1\,(bH_{30}) - 1568.9\,M_{30} - 20{,}253\left(\frac{pb^2}{2}\right) \tag{9}$$

where the superscript t indicates the torus. Inserting the numerical values of b and p in the foregoing equations, one finds for the deformations at $\phi = 90$ deg:

$$E\delta_{90}{}^t = 10{,}136\,H_{90} + 1337.2\,M_{90} - 1995.6\,H_{30} - 323.50\,M_{30} - 4.2551 \times 10^6$$

$$E\theta_{90}{}^t = 1337.2\,H_{90} - 344.85\,M_{90} + 264.06\,H_{30} - 4.4626\,M_{30} - 0.60759 \times 10^6 \tag{10}$$

The relevant equations for $\phi = 30$ deg are found in a similar manner. They are:

$$E\delta_{30}{}^t = 2128.7\,H_{90} - 281.66\,M_{90} + 6824.1\,H_{30} + 1083.5\,M_{30} - 17.974 \times 10^6$$

$$E\theta_{30}{}^t = 345.06\,H_{90} + 4.7619\,M_{90} + 1083.5\,H_{30} + 398.95\,M_{30} - 1.1362 \times 10^6 \tag{11}$$

Cylinder

From Table 3, inserting $h_c = 0.5$ in. and $p = 60$ psig, the following relations are obtained:

$$E\delta_{90}{}^c = 13{,}356\,H_{90} + 1982.6\,M_{90} + 2.295 \times 10^6$$

$$E\theta_{90}{}^c = 1982.6\,H_{90} + 588.56\,M_{90} \tag{12}$$

Spherical cap

With $h_s = 0.625$ in. and $p = 60$ psig, one finds from Table 3:

$$E\delta_{30}{}^c = -6018.9\,H_{30} + 1205.0\,M_{30} + 1.3289 \times 10^6$$

$$E\theta_{30}{}^c = 1205.0\,H_{30} - 467.30\,M_{30} \tag{13}$$

At this stage it is advisable to see if the equations for the various deformations are consistent with the assumed directions of the unknown moments M and horizontal shears H and the sign convention used. As mentioned earlier, the sign convention used herein is that δ is positive outward and θ is positive when the tangent rotates counterclockwise. The directions of the unknown M and H are given in Fig. 3 (subscript 2 corresponds to $\phi = 30$ deg, subscript 1 to $\phi = 90$ deg). It is easily checked that equations (10) through (13) are consistent with the sign convention and Fig. 3. (Note: The displacements of the torus due to the internal pressure may look to be inconsistent but they are not. It is also difficult to decide the signs of the toroidal rotations due to internal pressure. With the H's and M's this indecision does not arise for the toroidal rotations or the displacements, except

Table 3 Edge coefficients for cylinder and spherical cap (example 1)

Cylinder: Edge loading	$E\delta_{90}$	$E\theta_{90}$	Spherical cap: Edge loading	$E\delta_{30}$	$E\theta_{30}$
$H_{90} = 1$....	13356	$991.29/h_c$	$H_{30} = 1$...	−6018.9	$753.10/h_s$
$M_{90} = 1$....	$991.29/h_c$	$147.14/h_c^2$	$M_{30} = 1$...	$753.10/h_s$	$-182.54/h_s^2$
$p = 1$....	$76590h_c$	0	$p = 1$...	$35438h_s$	0

Table 4 Edge and interior coefficients of M_ϕ and bN_θ for torus (example 1)

Edge loading	$\phi = 30°$		$\phi = 45°$		$\phi = 60°$		$\phi = 75°$		$\phi = 90°$	
	M_ϕ	bN_θ	M_ϕ	bN_θ	M_ϕ	bN_θ	M_ϕ	bN_θ	M_ϕ	bN_θ
$bH_{90} = 1$		9.4607	−0.02280	4.6646	−0.08100	−2.9951	−0.11813	−17.807		−42.233
$M_{90} = 1$		−23.471	0.06744	−23.671	0.31149	−18.475	0.71793	12.695	1.0	104.47
$bH_{30} = 1$		30.069	0.08221	16.395	0.07476	4.7611	0.02753	−2.7655		−8.3150
$M_{30} = 1$	1.0	90.293	0.79908	18.677	0.41630	−17.659	0.10904	−26.297		−25.273
$pb^2/2 = 1$		−137.51	−0.06561	−108.00	−0.10271	−77.572	−0.05098	−51.669		−29.119

possibly for the deformations at the edge away from where the load is applied.)

Since the parts of the vessel must fit together with no gaps or discontinuities in slope, the following relations must hold:

$$\begin{aligned} \delta_{90}{}^t &= \delta_{90}{}^c \\ \theta_{90}{}^t &= \theta_{90}{}^c \\ \delta_{30}{}^t &= \delta_{30}{}^c \\ \theta_{30}{}^t &= \theta_{30}{}^c \end{aligned} \tag{14}$$

Substituting equations (10) through (13) into equation (14), the following four equations in the unknowns H_{90}, M_{90}, H_{30}, and M_{30} are obtained:

$$\begin{aligned} 23{,}492\,H_{90} + 654.4\,M_{90} + 1995.6\,H_{30} + 323.50\,M_{30} &= -6.5501 \times 10^6 \\ 645.4\,H_{90} + 933.41\,M_{90} - 264.06\,H_{30} + 4.4626\,M_{30} &= -0.60759 \times 10^6 \\ -2128.7\,H_{90} + 281.66\,M_{90} - 12{,}843\,H_{30} + 121.5\,M_{30} &= -19.303 \times 10^6 \\ -345.06\,H_{90} - 4.7619\,M_{90} + 121.5\,H_{30} - 866.25\,M_{30} &= -1.1362 \times 10^6 \end{aligned} \tag{15}$$

This system of four equations in four unknowns can be solved by various methods. Since a digital-computer program was available, this scheme was employed herein. The results were:

$$\begin{aligned} H_1 &= H_{90} = -440.46 \\ M_1 &= M_{90} = 96.461 \\ H_2 &= H_{30} = 1594.3 \\ M_2 &= M_{30} = 1710.2 \end{aligned} \tag{16}$$

Final Stress Distribution. Having determined the edge moments and shears the next step in the stress analysis is to calculate the stress distributions in the various parts of the structure. If the necessary interior influence coefficients are available this is quite a simple matter.[2]

As the largest stresses are usually the meridional bending stresses, $\sigma_\phi{}^b$, and the circumferential direct stresses, $\sigma_\theta{}^d$, only the stress distributions for these will be computed. The relation between the stresses and the stress resultants are:

$$\begin{aligned} \sigma_\phi{}^b &= \frac{6}{h^2} M_\phi \\ \sigma_\theta{}^d &= \frac{N_\theta}{h} \end{aligned} \tag{17}$$

where

M_ϕ = meridional bending stress resultant
N_θ = circumferential direct stress resultant
h = shell thickness

The stresses will be found in the interior of the torus for $\phi = 30$, 45, 60, and 75 deg. In the interior of the spherical cap only $\phi = 25$ deg will be considered; for the cylinder only the stresses for $x = 12$ in. will be calculated (x = distance from the cylinder-torus junction).

(*a*) *Torus.* First the interior influence coefficients must be obtained. For the torus under consideration one has[2] the values in Table 4.

The values of M_ϕ or bN_θ at the various points are then obtained by using the foregoing influence coefficients in conjunction with the edge moments and shears given by equation (16). As an example, N_θ at $\phi = 45$ deg is given by:

$$bN_\theta = 4.6646 \times -440.46\,b - 23.671 \times 96.461 + 16.395 \times 1594.3\,b + 18.677 \times 1710.2 - 108.00\,pb^2/2 \tag{18}$$

Inserting $p = 60$ psig, $b = 18.75$ in., it will be found that $(N_\theta)_{\phi=45°} = -35{,}085$ lb/in. The other stress resultants are found in a similar manner and one obtains the values given in Table 5.

Table 5 Final N_θ and M_ϕ values in torus (example 1)

ϕ, deg	N_θ(lb/in.)	M_ϕ(lb-in/in.)
90	−12800	96.461
75	−27965	1516.7
60	−36430	2562.5
45	−35085	3326.9
30	−25460	1710.2

(*b*) *Spherical Cap.* From Hetenyi's analysis[3] the following relations are obtained:

$$\begin{aligned} N_\theta &= C \frac{\lambda e^{-\lambda\psi}}{2[\sin(\phi_2 - \psi)]^{1/2}} [2\cos(\lambda\psi + \gamma) - (k_1 + k_2)\sin(\lambda\psi + \gamma)] \\ M_\phi &= \frac{r}{2\lambda} C \frac{e^{-\lambda\psi}}{[\sin(\phi_2 - \psi)]^{1/2}} [k_1 \cos(\lambda\psi + \gamma) + \sin(\lambda\psi + \gamma)] \end{aligned} \tag{19}$$

where λ, ϕ_2, k_1 and k_2 are as defined by equation (8). The angle ψ is measured from the edge of the spherical cap and C and γ are constants which depend on the loading. It can be shown that they have the values given in Table 6.

Table 6 Constants C and γ in spherical cap analysis

Edge loading	C	γ
1 ↺ ↻ 1	$\frac{2\lambda(\sin\phi_2)^{1/2}}{rk_1}$	0
1 → ← 1	$\frac{-(\sin\phi_2)^{1/2}(1+k_1^2)^{1/2}}{k_1}$	$\arctan(-k_1)$

[2] These coefficients have been obtained by the author for the shells shown in Table 1. However, due to the large range of shell geometries investigated, the results are too voluminous to be published in a paper. The author has presented sets of the interior influence coefficients for positive and negative-curvature toroidal shells to the libraries of the following societies: ASME, ASCE, and I. Mech. E. (England). Designers working on a specific toroidal shell will be able to obtain the necessary interior influence coefficients by visiting or contacting one of these libraries.

[3] Reference [7], p. 473.

For $\phi = 25$ deg, $\psi = 5$ deg. Evaluating this one obtains, for $\phi = 25$ deg the values in Table 7.

Table 7 Interior coefficients (at $\phi = 25$ deg) for M_ϕ and N_θ in spherical cap (example 1)

Edge loading	N_θ	M_ϕ
$H = 1$	1.9484	−0.3585
$M = 1$	−0.5305	0.00301

Due to the internal pressure $M_\phi = 0$ and $N_\theta = pr/2 = 8437.5$ lb per in. Using Table 7 and the values of M_2 and H_2 given by equation (16) one finds:

$$N_\theta = 8437.5 - 0.5305 \times 1710.2 + 1.9484 \times 1594.3 = 10{,}637 \text{ lb per in.}$$

$$M_\phi = 0.00301 \times 1710.2 - 0.3585 \times 1594.3 = -566.5 \text{ lb-in/in.}$$

From reference [7],[4] the following expressions for N_θ and M_ϕ due to edge bending loads are obtained:

$$N_\theta = -Ew/R = E/2\beta^3 DR\,[\beta M_1 \psi(\beta x) + H_1 \theta(\beta x)]$$
$$M_\phi = -D\,d^2w/dx^2 = 1/2\beta\,[2\beta M_1 \phi(\beta x) + 2H_1 \zeta(\beta x)] \quad (20)$$

where β and D are defined by equation (6). The functions ψ, θ, ϕ, and ζ are tabulated in Table 45 of reference [7]. Evaluating the foregoing for $x = 12$ in. one finds:

$$N_\theta = -1727.9 \text{ lb per in.}$$
$$M_\phi = -465.84 \text{ lb-in/in.}$$

To the value of N_θ must be added the contribution due to the internal pressure. This latter equals pR; i.e. = 9000 lb per in. Thus, the final N_θ equals 7272.1 lb per in.

The final stress distribution ($\sigma_\theta{}^d$ and $\sigma_\phi{}^b$) in the torus is shown in Fig. 4. The maximum stresses equal:

$$\sigma_\theta{}^d = -61{,}000 \text{ psi at } \phi = 54 \text{ deg}$$
$$\sigma_\phi{}^b = \pm 51{,}000 \text{ psi at } \phi = 44 \text{ deg}$$

It is of some interest to compare the maximum direct stress given with that obtained by using the formula given in Paragraph UG-32(e) of the ASME Code [1]. This can be written, assuming the joint efficiency equals 1, as

$$\sigma = p\left(0.885\,\frac{R}{t} + 0.1\right) \quad (21)$$

where

R = radius of spherical cap, in.

t = thickness of head, in.

Inserting the relevant numerical values it will be found that $\sigma = 23{,}900$ psi. This is very much less than the maximum stress obtained in the foregoing. This deficiency of the ASME Code for thin torispherical shells has been noted before [2].

Example 2—Cylinder-Ellipsoid-Torus-Cylinder Junction

The vessel used for illustrative purposes is shown in Fig. 5. The geometric characteristics of the various shells are:

Upper cylinder: $R_u = 120.94$ in.; $R_u/h_c = 192$; $h_c = 0.625$ in.

Torus: $a = 181.41$ in.; $b = 60.47$ in.; $a/b = 3$; $b/h_t \approx 40$; $h_t = 1.5$ in.; $\phi_2 = 30$ deg

2:1 Ellipsoid: $\bar{a} = 200$ in.; $\bar{a}/h_e = 200$; $h_e = 1.0$ in.; $\phi_2 = 30$ deg

Lower cylinder: $R_l = 200$ in.; $R_l/h_c' = 200$; $h_c' = 1.0$ in.

It will also be assumed that $p = 85$ psig

Table 8 Edge coefficients for torus (example 2)

Edge loading	$\phi = 90$ deg $Eb^2\theta$	$\phi = 90$ deg $Eb\delta$	$\phi = 30$ deg $Eb^2\theta$	$\phi = 30$ deg $Eb\delta$
$bH_1 = 1$	−10620	1845.8	195.52	22.840
$M_1 = 1$	121975	−10620	−43.008	−168.27
$bH_2 = 1$	210.21	−28.504	−12101	−1796.8
$M_2 = 1$	541.45	−244.23	−174120	−12101
$pb^2/2 = 1$	−179.15	−565.60	−6746.4	−2626.8

The edge influence coefficients for the torus and the ellipsoid can be found in references [5] and [6], respectively. The edge coefficients for the torus are given in Table 8.

In Table 8 δ is positive outward from the center line, and θ is positive when the tangent turns clockwise. The pressure p is assumed to act on the concave surface and bending moments are positive when producing compression in the convex fibers of the torus. The moments M_1 and M_2 acting on the torus in Fig. 6 are negative with this convention, which is the same as the one used in reference [5].

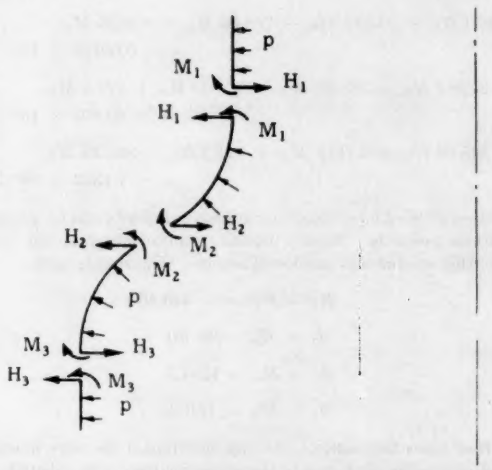

Fig. 6 Axisymmetric edge moments and horizontal shears acting at various junctions

Table 9 Edge coefficients for 2:1 ellipsoid (example 2)

Edge loading	$\phi = 90$ deg $E\theta$	$\phi = 90$ deg $E\delta/h$	$\phi = 30$ deg $E\theta$	$\phi = 30$ deg $E\delta/h$
$\frac{H_1}{h} = 1$	664.73	−7285.1	1.890	0.4769
$\frac{M_1}{h^2} = 1$	−120.40	664.73	0.3264	−1.156
$\frac{H_2}{h} = 1$	0.9282	−0.0797	483.75	3454.4
$\frac{M_2}{h^2} = 1$	0.2687	−1.5137	143.17	483.75
$v = 1$	440.40	−48097	1021.1	−881.48

The sign convention in Table 9 is similar to that for the toroidal shell, except that θ is positive when the tangent turns counterclockwise. M_2 and M_3 on the ellipsoid are positive when acting as shown in Fig. 6.

From the foregoing tabulations it will be observed that the coefficients at the edge away from where the loading is applied

[4] Reference [7], p. 393.

are very much smaller (2 per cent or less) than those at the loaded edge. (The cross coefficients for the 2:1 ellipsoid are actually omitted in reference [6].) In the following calculations these small cross-influence coefficients will be ignored to simplify the calculations. The error introduced by this simplification will not be of any significance.

The edge influence coefficients for the two cylinders can be obtained from equations (5). The edge coefficients are given in Table 10.

Table 10 Edge coefficients for cylinders (example 2)

Edge loading	Upper cylinder $E\delta_{90}$	Upper cylinder $E\theta_{90}$	Edge loading	Lower cylinder $E\delta_{90}$	Lower cylinder $E\theta_{90}$
$H_1 = 1$....	6919.9	1023.1	$H_3 = 1$...	7271.2	660.90
$M_1 = 1$....	1023.1	302.53	$M_3 = 1$...	660.90	120.14
$p = 1$....	19892	...	$p = 1$...	34000	...

The displacements and rotations of points 1, 2, and 3 on the vessel, Fig. 6, can now be written down directly in terms of the unknown edge moments and shears. Thus one obtains, see Fig. 6 for the directions of the forces and moments:

Upper cylinder

$$\begin{aligned} E\delta_{1c} &= 1023.1\,M_1 - 6919.9\,H_1 + 19{,}892\,p \\ E\theta_{1c} &= -302.53\,M_1 + 1023.1\,H_1 \end{aligned} \tag{22}$$

Torus

$$\begin{aligned} E\delta_{1t} &= 10{,}620\frac{M_1}{b} + 1845.8\,H_1 + 565.60\frac{pb}{2} \\ -E\theta_{1t} &= -121{,}975\frac{M_1}{b^2} - 10{,}620\frac{H_1}{b} + 179.15\frac{p}{2} \\ E\delta_{2t} &= 12{,}101\frac{M_2}{b} - 1796.8\,H_2 + 2626.8\frac{pb}{2} \\ -E\theta_{2t} &= 174{,}120\frac{M_2}{b^2} - 12{,}101\frac{H_2}{b} + 6746.4\frac{p}{2} \end{aligned} \tag{23}$$

Ellipsoid

$$\begin{aligned} E\delta_{2e} &= 483.75\frac{M_2}{h} + 3454.4\,H_2 - 881.48\,ph \\ E\theta_{2e} &= 143.17\frac{M_2}{h^2} + 483.75\frac{H_2}{h} + 1021.1\,p \\ E\delta_{3e} &= 664.73\frac{M_3}{h} - 7285.1\,H_3 - 48{,}097\,ph \end{aligned} \tag{24}$$

$$E\theta_{3e} = -120.40\frac{M_3}{h^2} + 664.73\frac{H_3}{h} + 440.40\,p$$

Lower cylinder

$$\begin{aligned} E\delta_{3c} &= 660.90\,M_3 + 7271.2\,H_3 + 34000\,p \\ E\theta_{3c} &= 120.14\,M_3 + 660.90\,H_3 \end{aligned} \tag{25}$$

In the foregoing equations δ was taken positive outward and θ was considered positive when the tangent rotated counterclockwise. The two negative signs on the left side of the torus equations resulted from the coefficients being tabulated for positive θ when the tangent rotated clockwise. The pressure p on the torus was taken to be acting on the convex surface, which changed the sign on the pressure terms.

The compatibility equations for this system are as follows:

$$\begin{aligned} E\delta_{1c} &= E\delta_{1t} \qquad E\delta_{2t} = E\delta_{2e} \qquad E\delta_{3e} = E\delta_{3c} \\ E\theta_{1c} &= E\theta_{1t} \qquad E\theta_{2t} = E\theta_{2e} \qquad E\theta_{3e} = E\theta_{3c} \end{aligned} \tag{26}$$

Substituting the numerical values and solving the resulting three pairs of simultaneous equations one finds:

$$\begin{aligned} M_1 &= 1.4152\,p \\ H_1 &= 0.45524\,p \\ M_2 &= -49.762\,p \\ H_2 &= 17.980\,p \\ M_3 &= 1.74108\,p \\ H_3 &= -5.63962\,p \end{aligned} \tag{27}$$

The directions of these edge moments and shears may be determined from Fig. 6. In terms of the directions given in references [5] and [6], they are as shown in Fig. 7.

Final Stress Distribution. Only the stresses in the ellipsoid and the torus will be calculated as the stresses in the two cylinders are calculated in the same manner as for the previous example. The relevant influence coefficients for the ellipsoid and torus are[3] given in Tables 11 and 12.

Utilizing the influence coefficients given in the tables and the edge moments and shears given in Fig. 7, the stresses in the ellipsoid and torus can be found. As examples N_θ at $\phi = 60$ deg is obtained as follows:

(*a*) Torus

$$\begin{aligned} N_\theta &= -1.1409 \times 0.45524\,p + 8.0948 \times -1.4152\,p/b + 1.5166 \\ &\quad \times 17.980\,p + 21.518 \times 49.762\,p/b - 11.120 \times (-pb)/2 \\ &= 380.48\,p \end{aligned} \tag{28}$$

Table 11 Edge and interior coefficients of M_ϕ and bN_θ for torus (example 2)

Edge loading	$\phi = 90°$ M_ϕ	$\phi = 90°$ bN_θ	$\phi = 75°$ M_ϕ	$\phi = 75°$ bN_θ	$\phi = 60°$ M_ϕ	$\phi = 60°$ bN_θ	$\phi = 45°$ M_ϕ	$\phi = 45°$ bN_θ	$\phi = 30°$ M_ϕ	$\phi = 30°$ bN_θ
$bH_1 = 1$		23.073	−0.03806	0.39219	−0.00218	−1.1409	0.00124	−0.13672		0.22840
$M_1 = 1$	1.0	−132.75	0.23789	26.705	−0.03541	8.0948	−0.01414	−0.69190		−1.6827
$bH_2 = 1$		−0.35630	−0.00191	0.49205	0.01227	1.5166	0.04760	−3.5594		−18.228
$M_2 = 1$		−3.0529	−0.03837	0.86552	−0.00148	21.518	0.50433	21.010	1.0	−121.01
$pb^2/2 = 1$		−7.6700	0.00402	−8.3527	0.01536	−11.120	0.01762	−18.865		−27.768

Table 12 Edge and interior coefficients of $(1/h^2)M_\phi$ and $(1/h)N_\theta$ for 2:1 ellipsoid (example 2)

Edge loading	$\phi = 90°$ M_ϕ/h^2	$\phi = 90°$ N_θ/h	$\phi = 75°$ M_ϕ/h^2	$\phi = 75°$ N_θ/h	$\phi = 60°$ M_ϕ/h^2	$\phi = 60°$ N_θ/h	$\phi = 45°$ M_ϕ/h^2	$\phi = 45°$ N_θ/h	$\phi = 30°$ M_ϕ/h^2	$\phi = 30°$ N_θ/h
$H_3/h = 1$		−36.426	−3.0488	−3.7877	−0.41829	2.2710	0.12705	0.13478		0.00317
$M_3/h^2 = 1$	1.0	3.3236	0.38082	−0.56577	−0.02474	−0.33290	−0.01528	0.02589		−0.00764
$H_2/h = 1$		−0.000399	−0.00898	0.05742	−0.07086	−0.05437	0.20106	−1.3283		22.589
$M_2/h^2 = 1$		−0.00757	0.00065	0.01182	−0.01269	0.02752	−0.03005	−0.28805	1.0	3.1996
$p = 1$		−210.48	1.6031	−181.62	1.4959	−137.80	−0.01207	−64.017		39.525

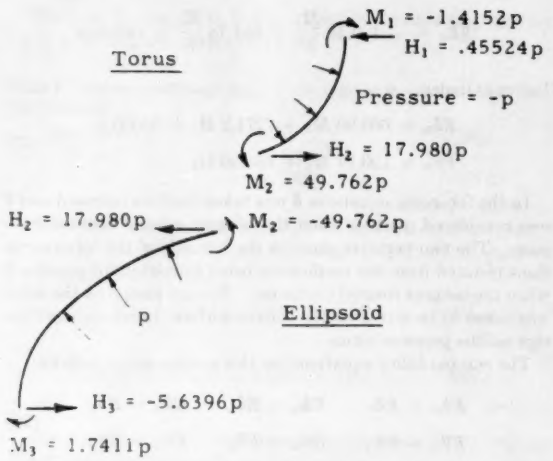

Fig. 7 Edge moments and shears in the notation of references [6] and [7], example 2

(*b*) Ellipsoid

$$N_\theta = 2.2710 \times -5.6396\,p - 0.33290 \times 1.7411\,p/h - 0.05437 \times 17.980\,p + 0.02752 \times -49.762\,p/h - 137.80\,p = -153.54\,p \quad (29)$$

The values for N_θ and M_ϕ are given in Table 13.

Table 13 Final N_θ and M_ϕ-values (example 2)

	Torus		Ellipsoid	
ϕ	N_θ/p	M_ϕ/p	N_θ/p	M_ϕ/p
90	236.59	−1.4152	1.107	1.7411
75	261.65	−12.722	−160.80	19.266
60	380.48	−14.826	−153.54	3.169
45	523.63	−44.690	−74.281	4.355
30	412.38	−49.762	286.42	−49.762

These values are in the sign convention of references [5] and [6], which is:

	Torus	Ellipsoid
N_θ/p	+ = tension	+ = tension
M_ϕ/p	+ = tension on outside fibers of vessel	− = tension on outside fibers of vessel

To make the meridional bending stress ($\sigma_\phi{}^b = 6M_\phi/h^2$) at the torus-ellipsoid junction have the same sign for both the torus and the ellipsoid, the sign of M_ϕ/p for the torus was reversed. Therefore, in the bending-stress values given in Table 14, + indicates tension on the fibers on the inside of the vessel. For the circumferential direct stress ($\sigma_\theta{}^d = N_\theta/h$), + indicates tension.

Table 14 Final stress values (example 2)

		p = 85 psig	
	ϕ	$\sigma_\phi{}^b$, psi	$\sigma_\theta{}^d$, psi
Torus	90	320.8	13407
	75	2883.7	14827
	60	3360.6	21560
	45	−10130	29673
	30	−11280	23369
Ellipsoid	30	−25379	24346
	45	2221	−6313.9
	60	1616.2	−13051
	75	9825.6	−13668
	90	887.96	94.1

The foregoing stresses, for p = 85 psig, are plotted in Fig. 8. The maximum values are as follows:

	Torus	Ellipsoid
Maximum bending stress, psi	16000	25400
Maximum direct stress, psi	30000	24300

The ASME Boiler Code does not give any formulas whereby the stresses in shells which are part ellipsoidal and part toroidal can be calculated. However, if the formula of Paragraph UG-32(d) is used for the ellipsoidal part it yields a stress of 17,000 psi (assuming the joint efficiency equals 1). This is only 70 per cent of the maximum direct stress calculated in the paper for the ellipsoid.

Conclusion

The two illustrative examples have shown the utility of influence coefficients in analyzing pressure vessels of fairly complicated shapes. The results were obtained in a straightforward manner and very little knowledge of shell theory was required. Also, although the numerical examples have only considered internal pressure, the influence coefficients for the edge moments and shears are still valid if the vessels are subjected to axisymmetric temperature distributions.

With regard to the availability of the influence coefficients for the different types of shell, tabulations have been made recently for the following (see Table 1):

1 Positive and negative-curvature toroidal shells.
2 Open-crown hemispheres.
3 2:1 and 3:1 open-crown ellipsoidal shells.

Edge influence coefficients are also available for cylinders, spherical caps, and cones. The interior coefficients for cylinders can quickly be obtained from a tabulation in Timoshenko [7]; those for cones can be obtained as indicated by Taylor [9]; reasonably good approximate values for spherical caps can be obtained as shown in the first numerical example of the paper.

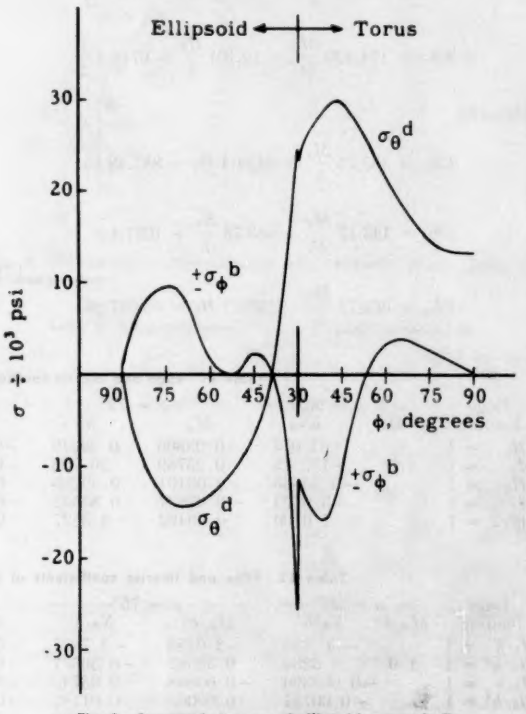

Fig. 8 Stresses in torus and ellipsoid, example 2

The available influence coefficients are primarily for constant-thickness shells. Also, for the shells where tabulations exist, these tables are only available over a certain range of the geometric parameters; e.g., for very thin shells (radius/thickness > 200) they are not available. In these cases resort has to be made to the approximate analytical solutions unless a general program is available for a computer. As far as the author is aware, such a program does not exist as yet. Of course it would be very desirable to have such a machine program since it could be written in such a manner that variable thickness shells could be calculated. The effect of shear deformations also could be taken into account without much difficulty.

Acknowledgment

The author wishes to express his appreciation to Mr. D. R. Snow for his careful checking of the two numerical examples in the paper.

References

1 "Rules for Construction of Unfired Pressure Vessels," ASME, section VIII, 1956 edition, New York, N. Y.

2 G. D. Galletly, "Torispherical Shells—A Caution to Designers," JOURNAL OF ENGINEERING FOR INDUSTRY, series B, TRANS. ASME, vol. 81, 1959, pp. 51–66.

3 G. D. Galletly, "Influence Coefficients for Open-Crown Hemispheres," *Journal of Engineering for Power*, series A, TRANS. ASME, vol. 82, 1960, p. 73.

4 G. D. Galletly, "Edge Influence Coefficients for Toroidal Shells of Positive Gaussian Curvature," JOURNAL OF ENGINEERING FOR INDUSTRY, series B, TRANS. ASME, vol. 82, 1960, p. 60.

5 G. D. Galletly, "Edge Influence Coefficients for Toroidal Shells of Negative Gaussian Curvature," JOURNAL OF ENGINEERING FOR INDUSTRY, series B, TRANS. ASME, vol. 82, 1960, p. 69.

6 G. D. Galletly, "Bending of 2:1 and 3:1 Open-Crown Ellipsoidal Shells," to be published by the Welding Research Council.

7 S. Timoshenko, "Theory of Plates and Shells," McGraw-Hill Book Company, Inc., New York, N. Y., 1940, pp. 393 and 473.

8 C. E. Taylor and E. Wenk, Jr., "Analysis of Stresses in the Conical Elements of Shell Structures," Proceedings of the Second U. S. National Congress of Applied Mechanics, ASME, New York, N. Y., 1955.

9 C. E. Taylor, "Simplification of Analysis of Stress in Conical Shells," University of Illinois, Urbana, Ill., 1958, unpublished.

10 P. M. Naghdi and C. N. de Silva, "Deformation of Elastic Ellipsoidal Shells of Revolution," Proceedings of the Second U. S. National Congress of Applied Mechanics, ASME, New York, N. Y., 1955.

Note: Cylinders and spherical caps can be analyzed quickly using reference [7]. For cones see references [8] and [9], and for ellipsoids see reference [10]. This latter is, however, fairly tedious.

DISCUSSION

S. P. Barton[5]

The author has presented a useful paper describing the influence coefficient approach for analyzing shell structures. The supporting tables of coefficients (published earlier) will certainly be welcomed by designers using the method.

The method is well suited for shells with relatively few discontinuities in load or geometry. However, from a designer's point of view, this type of an approach becomes rather tedious when many discontinuities are present. Another problem arises when the influence coefficients are not tabulated. As the author noted, such tables are available for only a limited number of cases.

A computer solution which simply requires input describing the geometry, loading, and material characteristics appears to be a further simplification. It was with interest that the writer noted the author's closing comment on the subject. A program of this type is used at the Westinghouse Steam Turbine Division and has proved to be a convenient method for analyzing composite structures encountered in our field. It is an elastic, axisymmetrical, thin shell analysis which simultaneously determines the membrane and bending action. It is applicable to shells of arbitrary meridional profile, including varying wall thickness. The loading may be caused by temperature gradients, rotation, bands of moments, or forces between the edges, pressures, or the usual edge loading. The program is rather general and may be used, for example, to analyze rotating disks, turbine casings, expansion joints, etc.

The writer also analyzed the author's first sample problem using this computer method. The following data were obtained throughout the shell: (1) meridional and circumferential bending stresses, (2) meridional and circumferential direct stresses, (3) shear stresses, (4) axial and normal components of deflection, and (5) angular displacement. The location and magnitude of the peak stresses were substantially the same as those shown in the paper. It may be of interest to note that the circumferential bending stress, and the direct meridional stresses were on the order of 14,000 psi and 10,000, respectively, in the same vicinity.

It is planned to describe this method in a forthcoming ASME paper.

[5] Engineer, Steam Division, Westinghouse Electric Corporation, Lester, Pa. Assoc. Mem. ASME.

Harry Kraus[6]

The author has rendered pressure vessel designers a great service in this paper and his many other papers on pressure vessels of various shapes. The data furnished in his papers do indeed allow persons who are not familiar with the details of shell theory to obtain accurate answers to pressure vessel stress problems without expending a great deal of time in the process.

In the nuclear power plant industry, for example, his method should see wide application. As a case in point, stresses in toroidal seal welds used in nuclear reactor pressure vessel closures can be calculated very nicely by using his influence coefficients. Also, a great deal of time and expense which had heretofore been contemplated for the development of design tables for torispherical heads from a consideration of the basic equations of shell theory, can now be avoided.

It should be added that by using the author's influence coefficients design tables for shells made up of a combination of shapes, can now be made up by utilizing a comparatively simple computer routine. With such a routine the computer would solve the compatibility equations[7] for the discontinuity reactions at each joint of the structure, using the influence coefficients as input, and would then calculate the stress distribution due to these reactions. In this manner the high level computer programming talent required for a numerical solution of the basic differential equations of shell theory is no longer required, as it has been provided to industry through the author's papers. The computer routines suggested by the writer can be written by any person with an elementary knowledge of computer programming. Thus, design tables can be quickly generated without the necessity of repeated hand solutions of the four simultaneous equations that obtain at each joint in the structure, and the best design for a particular application can be selected.

Eric E. Ungar[8]

The author is to be congratulated for his useful and lucid exposition of the application of influence coefficients to the stress

[6] Engineer, Westinghouse Electric Corporation, Bettis Atomic Power Laboratory, Pittsburgh, Pa. Assoc. Mem. ASME.

[7] Equations (4) of the subject paper.

[8] Senior Engineering Scientist, Bolt Beranek and Newman Inc., Cambridge, Mass.

and deformation analysis of pressure vessels. The summary presented in his present paper and his previous papers, in which he developed expressions and tables for the influence coefficients of some shell geometries, should prove very useful to designers. The method the author advocates would permit reduction of the now formidable task of stress analysis of pressure vessels with complicated geometries to the stage where it would require only the relatively routine filling in of form sheets. The latter task can be performed by personnel without advanced training, and for some purposes even the form sheet calculations can be programmed on a relatively low capacity digital computor.

It might be pointed out that some influence coefficient form sheet techniques for shells of revolution have been used for several years by Prof. B. W. Shaffer of New York University and his research group. They have dealt mainly with stress analyses of rocket engine chambers, which are of course also a type of pressure vessel.

In the paper under discussion the author implies, but fails to state, that the cylindrical shells he considers are sufficiently long so that edge loadings on one end produce no significant deformations at the other. For many practical vessels this may undoubtedly be a reasonable assumption, but it is useful to know for what conditions it holds, what sort of magnitudes are involved, and what to do if the cylindrical portions are relatively short. These questions are answered in a recent paper by Shaffer, Cochin, and Mantus.[9]

The afore-mentioned paper deals also with several other points which may be of interest to pressure vessel designers and other likely users of Dr. Galletly's work. Convenient extensive tabulations of influence coefficients for cylindrical shells of any length are presented. Coefficients which give the effects of loads applied at one edge on deformations at the other are included. The effect of relatively rigid rings is also discussed, and the corresponding influence coefficients are presented. Finally, the paper applies the methods discussed to a configuration often encountered in rocket engines; by assuming several values of one of the geometric parameters in this configuration, an optimum design is determined.

The discusser should like to suggest two extensions of the author's work, which may be of considerable practical interest. The first is the tabulation of influence coefficients for often-encountered composite structures, such as the toroid-and-hemisphere of Fig. 1 and the torus-and-ellipsoid of Fig. 5 of the subject paper. Of course, this would make sense only for a limited number of common geometries; for example, those where the wall thickness is constant. The second suggestion is to deal again with often encountered configurations, and, following the lead of Shaffer, et al., to perform a series of calculations for various values of one parameter (e.g., ratio of wall thicknesses), and to select an optimum substructure on this basis.

Author's Closure

The author wishes to thank Messrs. Barton, Kraus, and Ungar for their generous comments on his paper.

He was very interested to learn that a general computer program is in use at Westinghouse Electric Corporation. The desirability of having such a program has, of course, been recognized for some time. While it is not a difficult matter for an experienced programmer to code the two second-order, coupled ordinary differential equations describing the behavior of symmetrically loaded shells of revolution of variable wall thickness, information has been lacking regarding the best method to use in so far as accuracy and efficient use of the computer is concerned. A finite-difference formulation of the problem can be used or the two equations can be integrated directly using, say, the Runge-Kutta scheme. However, such an approach does not permit the saving in computer time which can be obtained for shells of constant thickness and constant meridional curvature. For these (spherical segments, tori, etc.), the governing equations reduce to a single, second-order complex equation and only two, rather than four, numerical integrations are necessary to obtain the homogeneous solutions for a shell with a crown-opening.

An additional point, on which very little work seems to have been done, is the utilization of the edge effect which occurs in many shells when they are loaded by axisymmetric edge loads. For instance, in analyzing a thin complete hemisphere, the edge effect may extend only 20 deg from the equator. Yet both methods mentioned analyze the shell from $0 \leq \phi \leq 90$ deg, and ignore any time savings which would accrue through exploitation of the existence of the edge effect. The author looks forward to Mr. Barton's forthcoming paper on the subject, where he hopes the foregoing points are discussed.

It is to be noted that, even with an IBM 704, it is desirable to take some pains to obtain the most economical and accurate computer program. This is because such a program is a precursor to the analysis of shells of revolution subjected to unsymmetric loading. The partial differential equations for these latter can, fortunately, be reduced to ordinary differential equations for each Fourier component of the loading. Depending on the number of components to be considered in the analysis, and the number of times such problems are encountered, an inefficient program can be quite uneconomic.

The author agrees with Mr. Barton that the influence coefficient approach might become rather tedious if there are many discontinuities in the structure. However, with pressure vessels, this is not usually the case. He is also grateful to Mr. Barton for having checked the first example in the paper. The author's program also gives the additional stress and deformation quantities mentioned by Mr. Barton.

The author is grateful to both Mr. Kraus and Dr. Ungar for their suggestions regarding possible further uses of influence coefficients. With regard to Dr. Ungar's comment on composite structures, the author would like to mention that the composite ellipsoid-cylinder problem has recently been solved by Messrs. Kraus, Bilodeau, and Langer. This is to be the subject of a forthcoming ASME paper. It is also the author's understanding that these gentlemen are working on other composite structures, such as torispherical shells, etc. When available, these papers will be of valuable assistance to the designer.

Dr. Ungar's suggestion regarding optimum design is also of interest. Presumably one must decide whether this should be done on a permissible stress basis or using limit design techniques. One must also be careful to avoid circumferential buckling under internal pressure, e.g., in very thin 3:1 ellipsoidal shells.

Dr. Ungar is correct in stating that the cylinders used in the examples are assumed to be long. This is practically always the case with pressure vessels. The assumption was mentioned explicitly in the section "Cylinder-Torispherical Shell Junction," but was not repeated when discussing the examples.

The author was interested to learn of the work of Shaffer, et al. The concept of influence coefficients for structures is, indeed, not new. Müller-Breslau used it many years ago for beams, trusses, etc., and other authors have extended it to plates. The author has never seen, however, any published information on influence coefficients for the shell types discussed in the paper, by Shaffer or anyone else.[10] The paper[9] mentioned by Dr. Ungar will be of only limited applicability in the pressure-vessel field. This is not altogether surprising, however, as the subject of the paper was

[9] B. W. Shaffer, I. Cochin, M. Mantus, "Optimum Length of a Rocket-Wall Extension Beyond Its Circumferential Keyway," *Trans. New York Academy of Sciences*, series II, vol. 21, no. 4, February, 1959, pp. 295–315.

[10] Except as given in the author's references [3 and 4].

rocket casings. One point worth mentioning in connection with the foregoing work is that the differential equations for the axisymmetrical deformations of a cylinder are the same as those for the bending of beams on an elastic foundation. Thus the questions raised in Dr. Ungar's third paragraph can be answered immediately by consulting Hetényi's book, "Beams on Elastic Foundation" (see Chapter III, Section 17, page 46, "Classification of Beams According to Stiffness").

In conclusion, the author would like to mention that the influence coefficient approach can obviously be extended to cases where more than two shells come together at a common junction, e.g., in some nuclear reactors. One has to be a little more careful in setting up the compatibility equations in these cases. However, in general, they will not be any more involved than, for example, those occurring at the junction of a torispherical head with a cylindrical skirt (see author's Reference [2]).

ERIC E. UNGAR

Senior Engineering Scientist, Bolt Beranek and Newman, Inc., Cambridge, Mass. Assoc. Mem. ASME

L. A. MEKLER[1]

Tube Metal Temperatures for Structural Design

A simple procedure is developed for calculating the circumferential temperature distributions in tubes exposed to nonuniform radiation. Convection to the fluid in the tubes and circumferential conduction in the tube walls are accounted for, in addition to radiation. Convenient dimensionless quantities are introduced and used for the presentation of graphs which facilitate rapid calculation of metal temperatures for structural design purposes. A calculation procedure using these graphs and a sample calculation are appended.

Introduction

When a tube bank arranged in a plane is subjected to uniform radiation from a parallel radiating plane, the flux intensity around the circumference of the tubes is not uniform. The flux distribution around a tube of a single row bank, with tubes spaced on two diameters, is shown in Fig. 1 for purposes of illustration [1].[2] The tube shown is assumed to receive direct radiation from a radiating plane, and reradiation from a refractory plane behind the tube bank. Under these conditions the center point on the exposed half of the circumference (point 1 in Fig. 1) receives approximately 1.8 times the average circumferential flux, or about 3.2 times the minimum flux. The positions of minimum flux occur at 60 deg from the center of the shielded half of the circumference (points 5 and 9 in Fig. 1).

The flux distributions shown in Fig. 1 correspond to plane tube banks. However, the distributions obtained with cylindrical tube banks having tube circle diameters which are large compared to the tubes are substantially the same as for tubes arranged in a plane. Therefore, the flux distribution around the tubes of most commercial tubular heaters may be considered as a function of tube spacing only.

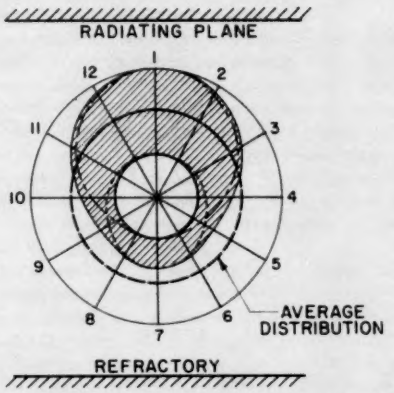

Fig. 1 Radiant heat flux distribution around tube circumference, for single row bank, tube spacing = 2D

If the radiant heat received by the outer surface of a tube were transmitted to the fluid inside the tube in a purely radial direction through the tube metal and the inside film, the temperature differences between the fluid and the outer tube surface at the various points around the tube circumference would be proportional to the flux intensities impinging at these points. However, since the tube metal is a relatively good conductor of heat, there is also a flow of heat in the circumferential direction within the metal; heat then flows from points exposed to a higher radiation intensity to points exposed to a lesser intensity. Thus the temperature of each circumferential tube element (as shown in Fig. 2) depends

[1] Deceased; formerly, Consultant, Petro-Chem Development Company, Inc., New York, N. Y.

[2] Numbers in brackets designate References at end of paper.

Contributed by the Petroleum Division and presented at the Annual Meeting, Atlantic City, N. J., November 29–December 4, 1959, of The American Society of Mechanical Engineers.

Note: Statements and opinions advanced in papers are to be understood as individual expressions of their authors and not those of the Society. Manuscript received at ASME Headquarters, August 4, 1959. Paper No. 59—A-166.

Nomenclature

C_1, C_2 = constants
D = mean diameter of tube
D_o = outside diameter of tube
F_r = Fourier coefficients
h = film coefficient between fluid in tube and wall
K = thermal conductivity of metal
m = number of elements in half tube circumference
q_{R_n} = heat flow into nth element due to radiation
q'_n = heat flow into nth from $(n-1)$st element by conduction
q''_n = heat flow into nth from $(n+1)$st element by conduction
q_{L_n} = heat flow into nth element by convection from fluid
$q(\theta)$ = heat flowing in tube wall at angle θ
R = mean radius of tube
S = center distance of banked tubes
T_n = temperature of nth element
T_L = temperature of fluid in tube
$T(\theta)$ = tube wall temperature at angle θ
t = tube metal thickness
$U = (T - T_L)h/\phi_{avg}$
$\beta = \left(\frac{h\lambda}{K}\right)\left(\frac{\lambda}{t}\right) = \left(\frac{\pi}{2m}\right)^2\left(\frac{hD}{K}\right)\left(\frac{D}{t}\right) = \left(\frac{2\pi}{m}\right)\mu^2$
λ = mean length of element in circumferential direction
ϕ_n = radiation intensity on nth element
ϕ_{avg} = average radiation intensity for entire tube circumference
$\phi(\theta)$ = radiation intensity at angle θ
$\mu^2 = \left(\frac{R}{t}\right)\left(\frac{hR}{K}\right)$
θ = angular co-ordinate

on four possible paths for the flow of heat: Radiation from the outside, convection and conduction to the fluid inside the tube, and conduction to or from the two adjoining tube elements. Under steady-state operating conditions, the element assumes a temperature which permits it to be at thermal equilibrium with its entire surroundings.

The center point of the exposed half of the tube circumference is found to be the hottest, even if the equalizing effect of the circumferential heat flow is considered. However, this point represents a highly localized condition. For purposes of structural design it may be more logical to use, say, the average temperature of the central 60-deg arc of the exposed face (between points 12 and 2 in Fig. 1). It is the purpose of this paper to indicate how the steady-state temperature of the metal in this arc (or in any portion of the tube circumference) may be calculated and to introduce a method for rapid practical calculation of this "design" temperature.

Mathematical Solution

Consider a differential element (Fig. 2) of a tube which is exposed to a known flux distribution $\phi(\theta)$. Curvature effects may be neglected if the tube wall thickness t is small compared to the mean radius R of the tube, and the heat flowing into the element due to radiation is given by

$$dq_R(\theta) = \phi(\theta)\, R d\theta. \tag{1}$$

The heat flowing into the tube element from the fluid in the tube may be expressed as

$$dq_L(\theta) = h(T_L - T) R d\theta, \tag{2}$$

where T is the temperature of the tube element (T being a function of θ), T_L denotes the temperature of the liquid in the tube, and h is the film coefficient on the inside of the tube.

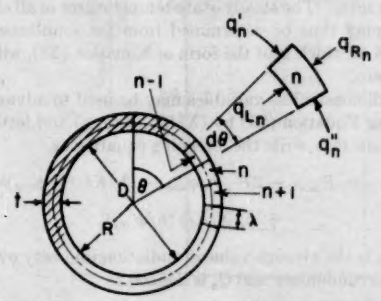

Fig. 2 Nomenclature and tube element geometry

According to Fourier's Law [2] for steady-state conduction, the heat flowing through any radial plane of the tube in the direction of increasing θ is

$$q(\theta) = -Kt \frac{dT}{Rd\theta}, \tag{3}$$

where t is the tube wall thickness and K the thermal conductivity of the tube material. K is henceforth assumed to be independent of temperature. The foregoing equation gives the heat flow into the differential element at the angle θ. The heat flowing into the element at the angle $(\theta + d\theta)$, on the other hand, is

$$-q(\theta + d\theta) = Kt\left(\frac{dT}{Rd\theta} + \frac{d^2T}{R^2d\theta^2} Rd\theta\right). \tag{4}$$

In the steady state the net heat flow into the element must vanish, or

$$dq_R(\theta) + dq_L(\theta) + q(\theta) - q(\theta + d\theta) = 0 \tag{5}$$

Substitution of Equations (1) through (4) into Equation (5) leads to the differential equation

$$Kt \frac{d^2T}{R^2d\theta^2} - h(T - T_L) + \phi(\theta) = 0. \tag{6}$$

Solution of this type of equation, i.e., determination of $T(\theta)$, may readily be accomplished for many functions $\phi(\theta)$. However, because of the many quantities affecting the analysis, it is easier to solve the problem in dimensionless form. Division of Equation (6) by ϕ_{avg}, the average radiation intensity, permits rewriting of this equation as

$$\frac{Kt}{\phi_{avg}R^2} \frac{d^2}{d\theta^2}(T - T_L) - \frac{h(T - T_L)}{\phi_{avg}} + \frac{\phi(\theta)}{\phi_{avg}} = 0, \tag{7}$$

where each term is dimensionless. By introduction of a dimensionless temperature parameter, defined by

$$U = (T - T_L)h/\phi_{avg}, \tag{8}$$

Equation (7) may be rewritten as

$$\frac{d^2U}{d\theta^2} - \mu^2 U = -\mu^2 \frac{\phi(\theta)}{\phi_{avg}} \tag{9}$$

where

$$\mu^2 = \left(\frac{R}{t}\right) \cdot \left(\frac{hR}{K}\right) \tag{10}$$

is a dimensionless quantity involving the geometry-dependent ratio (R/t) and the ratio (hR/K) comparing the convective and conductive heat-transfer mechanisms.[3]

The general solution of Equation (9) is of the form

$$U(\theta) = C_1 \sinh(\mu\theta) + C_2 \cosh(\mu\theta) + \text{p.i.}, \tag{11}$$

where C_1 and C_2 are constants of integration and p.i. is a particular integral which may be evaluated from the known function $-\mu^2\phi(\theta)\phi_{avg}$, using any of the standard methods. The constants may be evaluated from any suitable boundary conditions. For the case most often encountered in practice where the radiation intensity distribution is symmetric about $\theta = 0$, as in Fig. 1, symmetry demands that

$$q(0) = q(\pi) = 0; \tag{12}$$

or, in view of Equations (3), (8), and (11),

$$\left.\begin{aligned} \frac{dU(0)}{d\theta} &= \mu C_1 \cosh(0) + \mu C_2 \sinh(0) \\ &\quad + \frac{d}{d\theta}(\text{p.i.})\bigg|_{\theta=0} = 0 \\ \frac{dU(\pi)}{d\theta} &= \mu C_1 \cosh(\mu\pi) + \mu C_2 \sinh(\mu\pi) \\ &\quad + \frac{d}{d\theta}(\text{p.i.})\bigg|_{\theta=\pi} = 0. \end{aligned}\right\} \tag{13}$$

Because the p.i. corresponding to a symmetric $\phi(\theta)$ is symmetric [which may easily be proved from a Fourier series expansion of

[3] The six quantities which affect the analysis (T, K, t, h, ϕ, and R) may be expressed in terms of a total of four dimensional parameters (length, time, temperature, and energy; in, say, feet, hours, deg F, and Btu). According to the Buckingham Pi theorem, then, only two (6 − 4 = 2) independent dimensionless quantities may be found. The solution of the problem then involves finding the relation of a third dimensionless parameter to two others. In the problem as posed, we wish to find a distribution of U for given μ^2 and $\phi(\theta)/\phi_{avg}$.

$\phi(\theta)$ as will be shown here, in view of the linearity of the differential equation], the first derivatives of the particular integral must vanish at $\theta = 0$ and $\theta = \pi$, so that one finds

$$C_1 = 0, C_2 = 0 \tag{14}$$

whence, clearly,

$$U(\theta) = \text{p.i.} \tag{15}$$

A general symmetric intensity distribution may be expressed in terms of a Fourier cosine series

$$\phi(\theta) = \frac{1}{2} F_0 + F_1 \cos\theta + F_2 \cos 2\theta + F_3 \cos 3\theta + \ldots \tag{16a}$$

$$= \frac{1}{2} F_0 + \sum_{r=1}^{\infty} F_r \cos(r\theta),$$

where the F's are Fourier coefficients, which may be evaluated from

$$F_r = \frac{2}{\pi} \int_0^{\pi} \phi(\theta) \cos r\theta \, d\theta, \; r = 0,1,2 \ldots \tag{16b}$$

Equation (15) then becomes

$$U(\theta) = \frac{1}{\phi_{avg}} \left[\frac{1}{2} F_0 + \sum_{r=1}^{\infty} \frac{F_r \cos(r\theta)}{1 + r^2/\mu^2} \right] \tag{17}$$

For example, if the radiation intensity distribution in Fig. 1 may be approximated by

$$\phi(\theta) = \phi_{avg} (1.00 - 0.40 \cos\theta - 0.10 \cos 2\theta)$$

for an installation for which

$$\left(\frac{hD}{K}\right)\left(\frac{D}{t}\right) = 4\mu^2 = 40, \text{ or } \mu^2 = 10,$$

the temperature distribution, according to Equation (17), is given by

$$U(\theta) = 1.00 - \frac{0.40}{1 + \frac{1}{10}} \cos\theta - \frac{0.10}{1 + \frac{4}{10}} \cos 2\theta$$

$$= 1.00 - 0.364 \cos\theta - 0.0715 \cos 2\theta.$$

The general analytical solution for temperatures in tubes subject to symmetric radiation distributions, and the results as presented by Equation (17), may be used to obtain the desired temperature distributions if the functions $\phi(\theta)$ are available in analytical form or in terms of Fourier series approximations. Occasionally, however, the radiation distributions around the tubes are obtained by numerical or graphical, rather than by mathematical, means. Under such conditions the computation of Fourier coefficients would be either exceedingly tedious or inaccurate, so that a more suitable alternate procedure would be desirable.

Finite-Difference Solution

When the basic data are available in numerical form, numerical solution methods based on finite differences rather than on differentials are more suitable. The governing differential Equation (9) can be transformed directly into difference form [3]. However, the same results can be obtained by a more basic approach which permits a better insight into the interrelation of the various parameters.

If the tube is divided into $2m$ equal elements (that is, m elements in each symmetric half), the mean circumferential length of each element is

$$\lambda = \pi D/2m. \tag{18}$$

With a mean radiation intensity ϕ_n on the nth element the heat flowing into this element due to radiation is

$$q_{R_n} = \phi_n \lambda. \tag{19}$$

The heat flowing into the nth element by conduction is

$$q'_n = (T_{n-1} - T_n) Kt/\lambda \tag{20}$$

from the adjoining $(n - 1)$st element, and

$$q''_n = (T_{n+1} - T_n) Kt/\lambda \tag{21}$$

from the $(n + 1)$st element. The symbols T_n, $T_{(n-1)}$, and $T_{(n+1)}$ represent the respective mean temperatures of elements n, $n - 1$, and $n + 1$; K is the thermal conductivity of the tube material and t the thickness of the tube. In Equations (20) and (21) the effect of curvature of the tube walls has been neglected; this is permissible for tubes with a ratio of D/t greater than 10.

If the mean temperature of the inside surface of the nth tube element is assumed to be T_n (that is, if the radial temperature variation in the tube wall is neglected as a first approximation), then the heat flowing into element n from the fluid in the tube is

$$q_{L_n} = (T_L - T_n) h\lambda, \tag{22}$$

where T_L is the temperature of the fluid and h is the film coefficient on the inside of the tube.

The total heat flowing into element n is obtained by adding all four effects. From Equations (19) through (22),

$$q_{tot_n} = q_{R_n} + q'_n + q''_n + q_{L_n}$$

$$= (T_{n-1} + T_n - 2T_{n-1}) Kt/\lambda + (T_L - T_n)\lambda h + \phi_n \lambda. \tag{23}$$

Under steady-state conditions the total heat flowing into each element is zero. The steady-state temperatures in all elements of the tube may thus be determined from $2m$ simultaneous equations, each of which is of the form of Equation (23), with q_{tot_n} set equal to zero.

Again, dimensionless variables may be used to advantage. By multiplying Equation (23) by $(\lambda/Kt)\,(h/\phi_{avg})$ and letting $T'_n = T_n - T_L$, one may write the foregoing equation as

$$Q_n = (T'_{n-1} + T'_{n-1} - 2T'_n) h/\phi_{avg} - (\lambda/Kt)\,(h/\phi_{avg}) h\lambda T'_n + \phi_n (\lambda/Kt)\,(h/\phi_{avg}). \tag{24}$$

where ϕ_{avg} is the average value of radiation intensity over the entire tube circumference and Q_n is defined as

$$Q_n = (\lambda/Kt)\,(h/\phi_{avg}) q_{tot_n}. \tag{25}$$

By defining a dimensionless temperature parameter similarly to that of Equation (8) by

$$U_n = (T_n - T_L) h/\phi_{avg}, \tag{26}$$

and by introducing another dimensionless parameter,[4] defined as

$$\beta = (h\lambda/K)\,(\lambda/t) = (\pi/2m)^2\,(hD/K)\,(D/t), \tag{27}$$

one may rewrite Equation (24) as

$$Q_n = U_{n-1} - (2 + \beta) U_n + U_{n+1} + \beta \phi_n/\phi_{avg}. \tag{28}$$

With a given radiation distribution, one may compute ϕ_n/ϕ_{avg} for each element, and if the dimensions and heat-transfor properties are known the value of β may also be determined. In the steady state, q_{tot_n} must be equal to zero at each point. There-

[4] Note: β is related to the dimensionless parameter μ^2 of Equation (10) as $\beta = \frac{\pi^2}{m^2} \mu^2$.

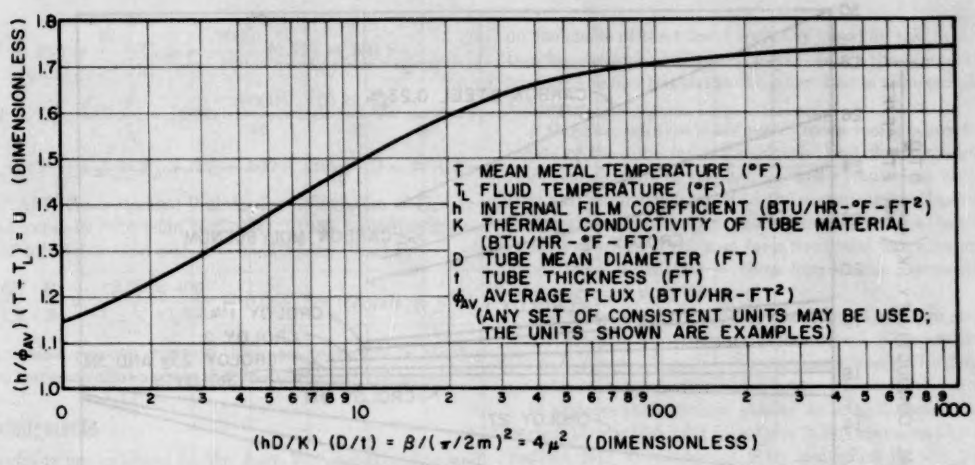
(h/φAV) (T - TL) = U (DIMENSIONLESS)
T MEAN METAL TEMPERATURE (°F)
TL FLUID TEMPERATURE (°F)
h INTERNAL FILM COEFFICIENT (BTU/HR-°F-FT²)
K THERMAL CONDUCTIVITY OF TUBE MATERIAL (BTU/HR-°F-FT)
D TUBE MEAN DIAMETER (FT)
t TUBE THICKNESS (FT)
φAV AVERAGE FLUX (BTU/HR-FT²)
(ANY SET OF CONSISTENT UNITS MAY BE USED; THE UNITS SHOWN ARE EXAMPLES)
(hD/K) (D/t) = β/(π/2m)² = 4μ² (DIMENSIONLESS)

Fig. 3 Variation of average temperature over hottest 60 deg of tube with heat-transfer properties and tube geometry, for tube spacing = 2D

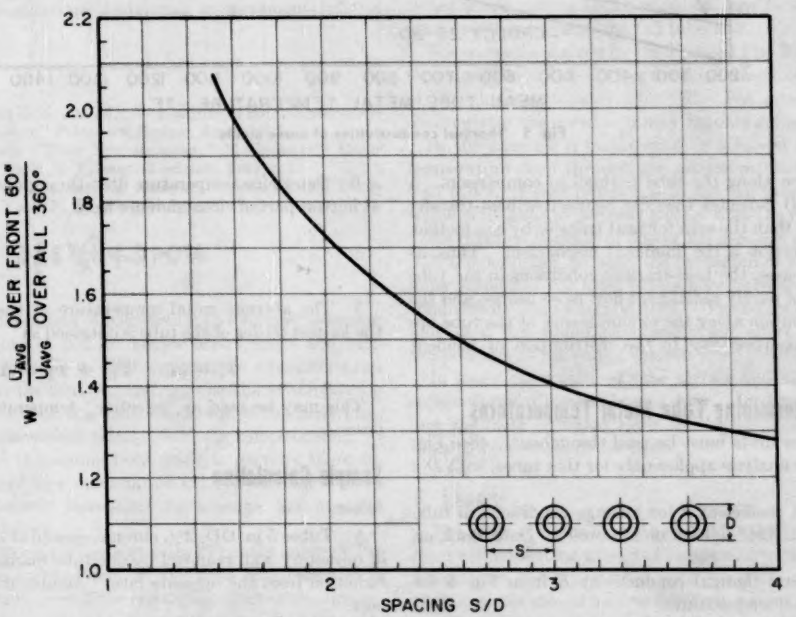

Fig. 4 Effect of tube spacing, for (hD/K) (D/t) = 400

fore, in view of Equation (25), all the Q_n's must be zero also. By applying the relations of Equation (28) to each of the $2m$ points on the tube circumference a total of $2m$ equations in terms of the $2m$ unknown dimensionless U_n's is obtained.

The set of $2m$ simultaneous equations, which reduces to a set of m equations in m unknowns if the radiation distribution is symmetric, may be solved by the usual methods for simultaneous linear algebraic equations. However, if for accuracy a large number of points on the tube circumference is used, the large number of equations may require a prohibitive amount of labor unless automatic computing equipment is available. Fortunately, the form of Equation (28) lends itself to solution by relaxation methods. These consist of assuming a value of U_n for each tube element, computing Q_n for each element, and then making the necessary adjustments in the assumed values of the U_n's until all the Q_n's are made as close to zero as one desires.

Results

The results of a series of calculations are shown in Figs. 3 and 4. Fig. 3 shows how the average value of the dimensionless temperature parameter U over the hottest 60 deg of the tube varies with $(hD/K)(D/t) = 4\mu^2$, for a tube spacing of two diameters. Fig. 4 shows how the ratio of the average value of U over the front 60 deg to the average value of U over the entire circumference varies with tube spacing, for a fixed value of $(hD/K)(D/t)$ of 400. However, since the curve in Fig. 3 is nearly horizontal for $(hD/K)(D/t)$ greater than about 150, Fig. 4 can be used with reasonable accuracy for the entire range of values of this parameter from 150 to 1000, which includes nearly all cases commonly encountered in practice.

The curve in Fig. 3 behaves asymptotically for large values of μ^2, or large ratios of (hD/K) and/or (D/t). A large value of (hD/K) indicates that the convection into the fluid is dominant,

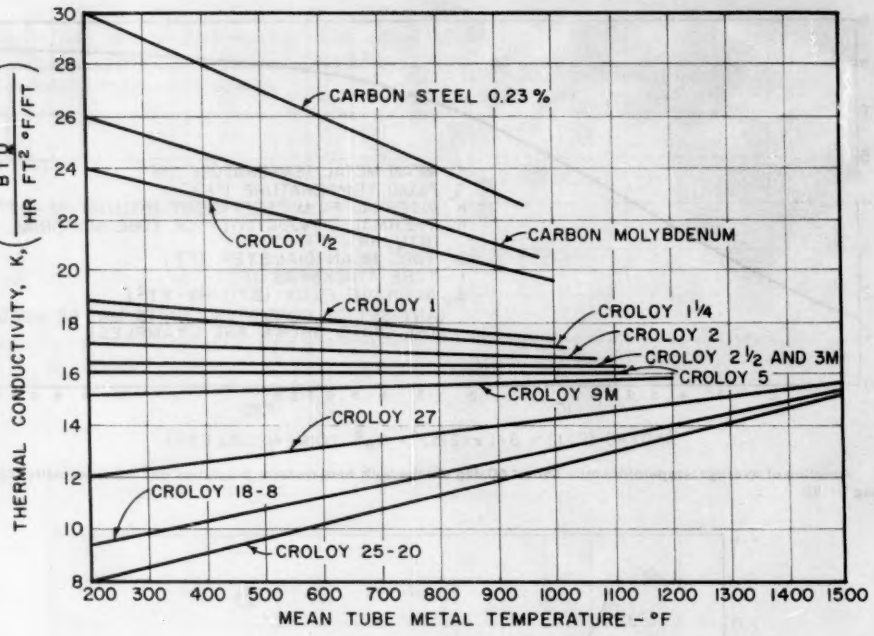

Fig. 5 Thermal conductivities of some steels

and that conduction along the tube is small in comparison. A large value of (D/t) indicates that the convective heat-transfer area is much larger than the area for heat transfer by conduction, so that again convection is the dominant mechanism. Thus, as $(hD/K)\,(D/t)$ increases, the heat-transfer conditions in the tube approach the case of purely radial heat flow more nearly, and the temperature distribution along the circumference of the tube approaches exact proportionality to the distribution of incident radiation.

Procedure for Determining Tube Metal Temperatures

NOTE: Consistent units must be used throughout. (See Fig. 3.) Caution: This analysis applies only for thin tubes, with $D/t > 10$.

1 Calculate film coefficient h for average conditions in tube from relation p. 211, 1955 edition of Maxwell's "Data Book on Hydrocarbons."

2 Read tube metal thermal conductivity K from Fig. 5 for estimated mean metal temperature.

3 Calculate $(hD/K) \cdot (D/t)$. D is mean tube diameter, = (ID + OD)/2. If $(hD/K) \cdot (D/t) < 150$, find U from Fig. 3. If $(hD/K) \cdot (D/t) > 150$, take $U = 1.73$.

U is a dimensionless temperature difference factor, defined in Fig. 3.

4 Fig. 3 applies for 2-diameter spacing. Obtain corrected U for other spacings from

$$U_{corr} = U\left(\frac{W}{1.73}\right)$$

where W is ratio read from Fig. 4.

5 Compute temperature difference between fluid and metal at mean tube diameter at hottest part of circumference from

$$(T - T_L) = \frac{\phi_{avg}}{h}\, U_{corr}$$

ϕ_{avg} is average circumferential rate determined from design conditions.

6 Determine temperature drop through half thickness of tube at hottest part of circumference from

$$\Delta T = U_{corr}\,\frac{\phi_{avg}}{K} \cdot \frac{t}{2}.$$

7 The average metal temperature at the outside surface of the hottest 60 deg of the tube is obtained as

$$T_e = (T - T_L) + T_L + \Delta T.$$

This may be used as "effective" temperature for design purposes.

Sample Calculation

Assume:

A Tubes 5 in. OD, 2¼ chrome, spaced at 9 in. centers in front of refractory wall removed by one tube diameter and exposed to radiation from the opposite face. Assume 0.25-in. M.W. thickness.

B Fluid temperature and pressure (determined from process conditions): 900 deg F and 400 psi.

C Average circumferential rate 9000 Btu/sq ft/hr determined from design furnace operating conditions.

D Film coefficient as calculated from heat-transfer equations = 160 Btu/hr deg F ft².

Then:

1 $h = 160$ Btu/hr deg F ft² (given).

2 $K = 16$ Btu/hr ft² deg F/ft from Fig. 5.

3 $\left(\frac{hD}{K}\right)\left(\frac{D}{t}\right) = \left(\frac{160 \times 4.75/12}{16}\right)\left(\frac{4.75}{0.25}\right) = 75.1$; since $75.1 < 150$, read $U = 1.69$ from Fig. 3.

4 Spacing $S/D_o = 9/5 = 1.8$. Read $W = 1.825$ from Fig. 4.

Then $U_{corr} = U\,\frac{W}{1.73} = 1.69\,\frac{1.825}{1.73} = 1.78$

5 $(T - T_L) = \frac{\phi_{avg}}{h} U_{corr} = \frac{9000}{160} (1.78) = 100$ F

6 $\Delta T = U_{corr} \frac{\phi_{avg}}{K} \frac{t}{2} = (1.78) \frac{(9000)}{16} \cdot \frac{(0.25/12)}{2} = 10.4$ F

7 $T_s = (T - T_L) + T_L + \Delta T = 100 + 900 + 10 = 1010$ F

Using "API Recommended Practice for Calculation of Heater-Tube Thickness in Petroleum Refineries," 1958, assuming life to rupture of 100,000 hr, find with $S = 13{,}000$ from Chart F,

$$t = \frac{(D/2) \cdot P}{1.2 \cdot S} = \frac{(2.5) \times 400}{1.2 \times 13{,}000} = 0.064 \text{ (See formula, p. 6)}$$

For practical reasons, retiring thickness minimum is $^1/_8$ in.; therefore corrosion allowance with 0.25-in. wall is 0.125 in.

Acknowledgments

The authors are indebted to Mr. John W. Throckmorton and Petro-Chem Development Corporation for continued interest and assistance in the preparation of this paper, and to Mr. E. H. TenBroeck for his suggestions concerning improvements of the manuscript.

References

1 L. A. Mekler and R. S. Fairall, "Evaluation of Heat Absorption Rates in Tubular Heaters," *Petroleum Refiner*, June, 1952.

2 W. H. McAdams, "Heat Transmission," McGraw-Hill Book Company, Inc., New York, N. Y., second edition, 1942, p. 6.

3 S. H. Crandall, "Engineering Analysis," McGraw-Hill Book Company, Inc., New York, N. Y., 1956, chapter 1.

DISCUSSION

D. J. Bergman[5]

This paper provides means of calculating an average maximum tube wall temperature in radiant heater banks where the tube wall thickness is sufficient so that appreciable circumferential heat transfer reduces the heat flux through the film to the flowing fluid immediately back of the central portion of the fired face. It also furnishes a convenient tabular form for computation.

However, some of the assumptions made to simplify the complex mathematics lead to a reduction of tube surface for a given duty without apparently increasing the average heat-transfer rate or metal temperature.

The following statement is made on page 271 of the paper: "The center point of the exposed half of the tube circumference is found to be the hottest, even if the equalizing effect of the circumferential heat flow is considered. However, this point represents a highly localized condition. For purposes of structural design it may be more logical to use, say, the average temperature of the central 60-deg arc of the exposed face."

In the case where this becomes important the tube is unfortunately unable to do this averaging and the central hot spot develops oxidation, or swelling, or both. It would appear safer to correct for the circumferential flow of heat but still use maximum wall temperature for structural design.

Another assumption is, "Curvature effects may be neglected if the tube wall thickness t is small compared to the mean radius R of the tube, . . ." "In Equations (20) and (21) the effect of curvature of the tube walls has been neglected; this is permissible for tubes with a ratio of D/t greater than 10."

For the above limit the ratio of outside to inside periphery is 5/4 for a 5-in. OD tube. The crowding of flux (without considering circumferential flow of heat) is 25 per cent—and the film drop on the inside of the tube is normally based on this rate. Correction for circumferential flow would reduce the temperature drop through the film but not to the point used in the example given in the paper.

A third assumption is the use of mean temperature for the elements of the tube for calculation of heat flow circumferentially from one element to another. When extended to radial flow of heat this assumption leads to the surprising conclusion that the temperature drop through the inside half of the tube thickness is at least constant if not zero for a fixed heat flux rate and a range of thickness up to $D/t = 10$ as long as the parameter (hD/K) (D/t) is greater than 150.

This seems to be checked by the relation given in step 5 of the Procedure for Determining Tube Metal Temperature, where $(T - T_L) = \phi_{avg} U_{corr}/h$. No allowance is made for flow through metal with a conductivity K.

It appears that a curve similar to Fig. 3 should be used to correct the proportional inside flux rate (determined by maximum radiant rate at outside of tube multiplied by OD/ID). This corrected rate should then be used to obtain the film drop.

The average between outside maximum radiant rate and corrected inside rate as above would be used to determine the temperature drop through the full tube wall.

The corrections given by the changed Fig. 3 are relatively small for values above $D/t = 10$ or for the example of a $^1/_4$-in. tube wall of $2^1/_4$-chrome material 5-in. OD. For greater thickness and conductivity the correction may become appreciable.

In the example a minor error is involved by calculating the temperature drop through the minimum thickness of minimum wall tubes. Usual practice is to use the average wall thickness which is roughly 10 per cent greater than the minimum wall.

No mention is made of one of the greatest causes of high tube wall temperature; namely, the formation of coke or scale on the inner surface of the tube. This may have an appreciably lower conductivity than the tube itself. The temperature at the beginning of a run would have much less effect on tube life than temperature at the end of the run when scale is present.

In many cases reduced tube surface and higher heat rates are satisfactory for a given heater duty. In that case it is better to face the facts of higher rates and higher tube wall temperature than to keep them under cover.

F. Landis[6]

The authors are to be commended for their simple and effective means of predicting tube wall temperatures in tubes subjected to nonuniform radiation. For most practical design applications their analysis should lead to excellent results. There may, however, be a few instances where the assumed conditions lead to errors in prediction.

The authors specify a single known tube-to-fluid film coefficient. Most experimental data on which film coefficients are based were determined with uniform tube wall temperatures and little detail is known on the variation of the average film coefficient with nonuniform surface temperatures, although this may lead to significant changes.

Furthermore, the radiation heat flux to a row of tubes backed by a refractory is normally computed with the aid of a radiation shape factor as presented by Hottel.[7] For these factors to be directly applicable, the external tube temperature must be uniform.

Both of the above deviations would become important for thin

[5] Chief Engineer, Engineering and Development Department, Universal Oil Products Company, Des Plaines, Ill. Mem. ASME.

[6] Associate Professor of Mechanical Engineering, New York University, New York, N. Y. Mem. ASME.

[7] See, for instance, W. H. McAdams, "Heat Transmission," McGraw-Hill Book Company, Inc., New York, N. Y., third edition, 1954, Figs. 4–12, p. 69.

and very closely spaced tubes, and caution should be employed when using the authors' conclusions for such a case. However, even under these conditions, the method proposed by the authors appears to be the best available technique.

Authors' Closure

The discussers' cogent comments are greatly appreciated. It is hoped that the following paragraphs will shed further light on the applicability of the results by answering the various questions that were raised.

As both discussers pointed out, the results presented apply only for those physical situations in which the assumptions underlying the analysis are satisfied. Mr. Bergman's comment concerning coke or scale deposits on tube surfaces is a particularly important case in point. If the nature of a given installation is amenable to the formation of such deposits, they must certainly be considered. Similarly, Professor Landis' note of caution concerning the possible circumferential variation of film coefficient is very significant, especially for configurations where large circumferential tube wall temperature gradients occur and where the film coefficient is strongly influenced by surface temperature.

Although, as Professor Landis mentions, the development of Hottel's charts (and the method of Reference [1]) assumes uniform tube surface temperature, use of these charts and methods is justified for most practical cases. The difference of the fourth powers of the radiator and receiver absolute temperatures, which enters all radiation calculations, is generally dominated by the radiator temperature term and is relatively insensitive to variations in receiver temperature like those generally encountered in practice around tube circumferences. If one computes shape factors for circumferential area increments, multiplies each by its appropriate fourth power temperature difference, and then combines the results to obtain the total radiation on the entire circumference, one obtains very nearly the same effect as if one would have initially assumed uniform surface temperatures and simply added the incremental shape factors to obtain the over-all shape factor.

One certainly cannot disagree with Mr. Bergman's remark that designing on the basis of hottest point temperatures is somewhat safer than using the hottest 60 deg or average temperatures. However, the second alternative may also represent a reasonable design philosophy, particularly since the differences in the two cases tend to be relatively small. A curve corresponding to the hottest point temperature would lie only about 0.05 unit above the one shown in Fig. 3 pertaining to the hottest 60 deg average temperature and would approach the value of 1.8 asymptotically. The curve corresponding to the hottest point would also lie about 0.05 unit above the curve shown in Fig. 4.

It must be pointed out that the use of mean wall temperatures does not imply zero radial gradient and that the thin tube assumption is not very stringent. This assumption permits the radial temperature distribution in the tube wall to be approximated by a linear one whose mean value occurs at the mean radius. It further permits the circumferential heat flow to be determined in terms of only the mean temperatures, since for thin tubes the circumferential heat flow path lengths do not vary much across the tube thickness. Thus, Equations (20) and (21) do not require the radial gradients to be zero; in fact, Step 6 of the design procedure shows how one may compute the temperature drop through half the tube thickness in order to obtain the temperatures of the tube surfaces.

On the other hand, Equation (22) does neglect radial temperature variations. Although their effect can be included without a great deal of additional effort, it was thought desirable to avoid this added complication in this study, particularly since the thermal resistance of a half thickness of tube wall is in general much smaller than that of the film. Of course, the film coefficient should ideally be computed on the basis of the best possible information, including flux crowding if this is significant, as Mr. Bergman points out.

In closing, it may be worth while to reiterate that the finite difference approach used is a very powerful one. Without a great deal of added complication it can be made to account also for the effect of deposits, for variable film coefficients, and even for lengthwise heat flow in the tube walls. It is hoped that this method will be useful for the development of further, more accurate, and more detailed design charts.

T. W. MACIOS
Mechanical Engineer, Sverdrup and Parcel Engineering Company, St. Louis, Mo.

Supersonic-Wind-Tunnel Air-Drying-System Design

Air-drying system design for supersonic wind tunnels entails many complexities. These complexities are discussed in this paper with the express intention of establishing criteria for air-drying-system design. Various types of systems are examined and a method of drying-system selection is presented.

SPACE travel can never become a reality until existing high-speed and temperature problems are overcome. Because of the ever persistent research and test procedures constantly and vigorously being conducted, these problems will, without a doubt, soon become solutions of the past.

One of the most essential methods of testing known today is the highly regarded wind tunnel. Shortly after the origin of the wind tunnel, when full-scale prototypes were tested, its usefulness concerning future design information was quickly realized. The speed requirements of the tunnel increased amazingly fast. This acceleration was brought about by the advent of World War II and the Korean War, when superiority depended largely upon faster airplanes traveling at higher altitudes. As a result, the present period is commonly called the "Jet Age."

As progress continues to advance in the fields of jets and rockets, the hypersonic wind tunnel ($M > 4.5$) becomes more and more important. However, testing at speeds of Mach 1 to 4.5 (supersonic conditions) is still the prime investigation area and will be for many years to come. The need for greater participation in the field of research is presently being met by more and more industries throughout the country, thus requiring new and additional test facilities. Therefore supersonic wind tunnels will have to be designed to meet these new facility requirements.

The design of a supersonic wind tunnel entails many difficult problems. Air-drying-system design for the supersonic wind tunnel is one of the more critical barriers that must be overcome.

Test measurements taken in a wind tunnel will be usable only if the desired simulated flight conditions are obtained. It is therefore necessary to maintain uniformity of flow.

Contributed by the Aviation Division and presented at the Annual Meeting, Atlantic City, N. J., November 29–December 4, 1959, of The AMERICAN SOCIETY OF MECHANICAL ENGINEERS.

NOTE: Statements and opinions advanced in papers are to be understood as individual expressions of their authors and not those of the Society. Manuscript received at ASME Headquarters, March 30, 1959. Paper No. 59—A-161.

Air-Drying Requirements

Some common nomenclature may be introduced at this time which will be used in the discussion of wind-tunnel operation and performance.

Stagnation condition refers to the physical properties of air (pressure, temperature, and so on) when at rest. For example, the pressure of a certain quantity of air, measured after its velocity has been decreased from 1 fps to 0 fps, is called the *stagnation pressure* for that particular quantity (mass) of air. This stagnation pressure is sometimes referred to as the total pressure and is a result of two conditions. One condition, referred to as the static condition, pertains to the pressure of the quantity of air when in motion (called the *static pressure*). The second condition, referred to as the dynamic condition, pertains to the amount of pressure additive to the static pressure, as a result of the quantity of air speed (called the *dynamic pressure*). The summation of the static pressure and the dynamic pressure equals the stagnation pressure (total pressure) of the quantity of air.

If the air flow of the tunnel is a combination of water vapor and air, the static pressure is the sum of the water vapor pressure and the air pressure. The two pressures are referred to as the *partial pressures* of the mixture.

To maintain flow quality requirements, a working knowledge of the air-water vapor mixture flow is needed. Air-water mixture

Nomenclature

A = outside-surface area, sq ft
G = mass velocity of air, lb/hr sq ft face area
h = absolute humidity of moist air, grams water vapor/gram dry air
h' = absolute humidity after compression and cooling
h_E = inlet absolute humidity
h_f = outlet absolute humidity
h_o = outside surface coefficient, Btu/hr sq ft deg F
h_i = refrigerant, (inside) surface coefficient, Btu/hr sq ft deg F
$h_{s,a}$ = absolute humidity corresponding to atmospheric saturation
M_c = Mach number at which condensation shock is expected to occur
N = number of rows of coil depth
P = air pressure
P_a = atmospheric pressure
P^* = vapor pressure (partial pressure of water vapor)
$P_s^*(T)$ = saturation vapor pressure at temperature T
Q_s = sensible heat transfer, Btu/hr sq ft of face area
Q_t = total heat transfer, Btu/hr sq ft of face area
R = ratio of air-side to refrigerant-side surface
t_1 = entering dry-bulb temperature, deg F
t_2 = exit dry-bulb temperature, deg F
t_o = outside-surface temperature, deg F
t_r = refrigerant temperature, deg F
T_c = temperature of air-water, deg F, vapor mixture at which shock occurs
T_0 = initial air-water vapor temperature, deg F

may become saturated upon expansion through a nozzle. According to the adiabatic law, the partial pressure of a vapor decreases with a decreasing temperature. Therefore the amount of expansion at which saturation will be reached can be associated with each value of initial humidity. Expansion beyond this point will result in either condensation or supersaturation of the air-water vapor mixture. Flow in a supersonic wind tunnel results in rapid expansions and short transit times, therefore, large amounts of supersaturation may be expected to occur without condensation. However, beyond a certain degree of supersaturation, which depends on the initial condition of the air, a strong condensation, often called a condensation shock, will occur.

In supersonic nozzles this type of condensation is usually rather sharply defined. The heat released by the condensation produces an increase of static pressure and a decrease in the Mach number.

The condensation shock has a detrimental effect on the uniformity of flow in a supersonic wind tunnel. Therefore it is necessary to prevent such a condensation shock or reduce its effect to such a point that measurements taken in the tunnel are unimpaired.

The criteria for condensation free flow are given in Fig. 1, and were obtained from experimental data of Head [8].[1] The graph allows prediction of the stagnation dewpoint of the tunnel air required to delay the onset of condensation up to a Mach number M_c. If condensation free flow is desired, M_c must be larger than the test section Mach number.

The use of the graph is very simple. Draw a horizontal line through the stagnation temperature T_0 which is shown on the scale at the left in Fig. 1. Let A be the point of intersection of this horizontal line with the curve of the lower set which corresponds to the Mach number at which condensation occurs. Now draw a vertical line through point A. Let point B be the intersection of the vertical line with the curve of the upper set which corresponds to the temperature gradient of the nozzle under consideration.

[1] Numbers in brackets designate References at end of paper.

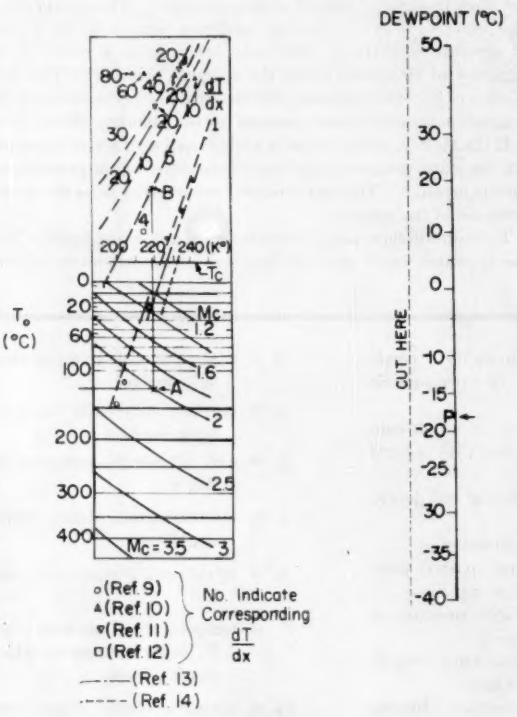

Fig. 1 Criterion for condensation free flow

The dewpoint scale in Fig. 1 must either be cut out or reproduced on a transparent paper. If the scale is then placed along A-B, with point P of the scale coincident with A, the dewpoint can be read at point B. Also, the temperature at which the condensation shock occurs, T_c, can be read at the intersection of A-B with the T_c-scale. The dewpoints on the scale are the saturation points for water above 0 C, for ice below 0 C.

The criteria just discussed will determine the requirements imposed on a particular drying system designed to prevent condensation shock.

Experimentation shows that a small uniform deviation from undisturbed flow in the test section can be obtained by keeping the absolute humidity of the tunnel air to the order of 4 grains of water per pound of dry air [15].

The upper set of curves in Fig. 1 is to be chosen according to the temperature gradient (dT/dx)-deg C/cm, in the nozzle considered.

If the shock is allowed to occur upstream of the test section, Fig. 1 may be used to determine the shock location.

The temperature gradient, in the test section where the occurrence of condensation shock must be prevented, is zero. As a result, the choice of dT/dx equal to 1 deg C/cm should be used irrespective of the nozzle temperature gradient.

Because of further expansions around test-section models, the choice of M_c is difficult. The temperature gradients, in these expansion, also must be taken into account when the choice of M_c is made. No generalization can be stated concerning this, because of the number of parameters involved and lack of experimental information.

Design Procedure

The design of an air-drying system offers many courses of action. There are several systems, physical and chemical, that may be used for drying air. They are generally classified as either *condensation* or *adsorption*.

Condensation is a thermodynamical process in which the air-water vapor mixture is brought to a state of supersaturation, so that the moisture will condense and be separated out. The following systems, (*a*) cooling, (*b*) compressing, or a combination of the two can produce condensation of the water vapor.

(*a*) *Drying by Cooling.* This system is based on air-water vapor mixture passing over cooling coils (usually the finned type). The result is condensation on the walls and coil surfaces of the drier.

Condensation also may occur as water droplets or ice crystals in the form of a mist. This takes place when the saturation pressure (corresponding to the outlet temperature) is higher than the vapor pressure (corresponding to the final humidity that can be achieved in the absence of mist).

Experiments conducted [1] show that much lower humidities at the drier outlet are obtained at higher cooler temperatures for a given range of inlet humidities. This is because operation without mist is possible for much higher inlet humidities at the higher cooler temperature.

Driers operating with mist present may require glass or felt filters at the drier outlet. Periodic reactivation of the filters is necessary to maintain the desired performance of the drier.

This system is relatively difficult to design since the manner in which condensation occurs is not easily predicted. The process depends upon the number of condensation nuclei present and the contact time.

Many methods have been devised to predict the performance of a dehumidifying coil but the one developed by G. L. Tuve [2] is generally acceptable for design criteria.

Tuve uses the over-all heat-transfer coefficient to determine the surface coefficients. The outside surface coefficient, in this method, is a coefficient of sensible heat only. The relationship is expressed by the following equation:

$$h_o = \frac{0.243}{AN} G \log_e \left(\frac{t_1 - t_s}{t_2 - t_s}\right) \tag{1}$$

The relationship is derived by setting sensible heat transfer per square foot of face area, $C_p G(t_1 - t_2)$ equal to $h_o \Delta t_m AN$, where the mean temperature difference is

$$\Delta t_m = \frac{t_1 - t_2}{\log_e \left(\frac{t_1 - t_s}{t_2 - t_s}\right)}, \text{ deg F} \tag{2}$$

The average temperature of the external surface of the cooler cannot be found by direct measurements, and therefore is commonly a calculated value determined from test data [2], or a fictitious value found graphically [3]. The graphical method requires the use of a nonlogarithmic psychrometric chart. Graphically, the average temperature is the point of intersection of the saturation curve with a straight line starting from the point representing the condition of the air that enters the coil and extending at an angle corresponding to the ratio of sensible to total heat load.

The refrigerant temperature may be found by solving the following equation for (t_r):

$$QT = \frac{h_i}{R} (t_s - t_r) AN \tag{3}$$

$$t_r = t_s - \frac{RQT}{h_i AN} \tag{3a}$$

(*b*) *Drying by Compression.* Drying air by compression is usually used in conjunction with cooling. If compressed air is needed for tunnel operation, compression followed by cooling down to initial temperature is a natural way of drying. This situation exists for blow-down-type, intermittent wind tunnels, or for continuously operated, closed wind tunnels with high stagnation temperatures. Predrying by compression is realized when high-pressure reservoirs are used to obtain flexible operation of a closed wind tunnel that requires a dry air supply. Generally, an additional drier is needed to satisfy the requirements. Since adsorption driers give a higher adsorbent capacity with high operating pressures, a desirable combination of compression and after cooling followed by adsorption drying may be realized.

The power required to operate and regenerate this type of drying system is much higher than any of the other types of drying plants. An economic argument against the use of such a system may exist if (*a*) compressed air is not used for tunnel driving or, (*b*) the installed power is high and the compressors operated intermittently. The following conditions will hold true for drying by compression:

After initial compression, the partial vapor pressure of the moisture is raised for a given value, h, of the absolute humidity to

$$P^* = 1.6ph \tag{4}$$

If the temperature is lowered downstream to its initial value T_0, the air may become saturated and condensation may take place. Therefore the vapor pressure decreases to the value $P_s^*(T_0)$. As a result of this, the absolute humidity is consequently lowered to the value

$$h' = (0.625) P_s^*(T_0) P^{-1} \tag{5}$$

Equation (5) can be expressed in terms of the absolute humidity $(h_{s,a})$ corresponding to atmospheric saturation.

$$h' = (h_{s,a})(P_a/P) \tag{6}$$

Adsorption is a process which involves the chemical or physical action of water vapor on the surface of some substance. The chemical adsorption of the water vapor by some agent such as sulfuric acid or phosphorous pentoxide is not generally used for drying in supersonic wind tunnels owing to both the low capacity of the chemical adsorbers and the difficulty involved in regenerating them. The following is a discussion of systems based on the physical action of this process.

(*a*) *Drying by Adsorption.* The use of adsorption for dehumidification in wind tunnels is a dynamic adsorption process. It involves the flow of humid air through a solid granular adsorbent. The porous surfaces of the solid granular adsorbents derive their adsorbing potential from an intermolecular attraction of the water-vapor molecules. A schematic diagram illustrating a typical working arrangement of a two-adsorber silica-gel unit, is shown in Fig. 2.

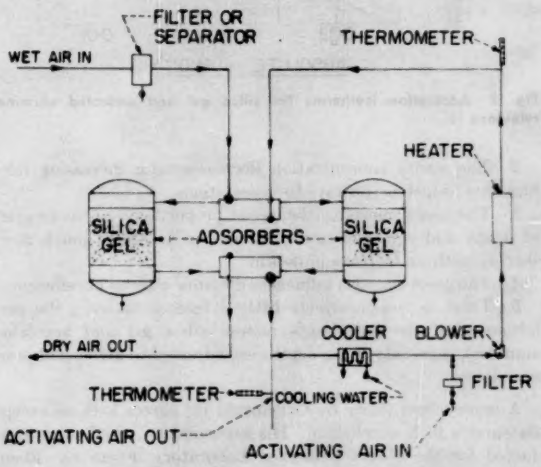

Fig. 2 Schematic diagram of typical two-adsorber silica-gel unit, reference [7]

Silica gel and activated alumina are the granular adsorbents generally used for wind-tunnel drying. The ratio of mass of water vapor adsorbed to mass of adsorbent is called concentration or percentage adsorption. The adsorbent can be described by one of its three dependent parameters; (*a*) its concentration at a given temperature and partial pressure, (*b*) its temperature, and (*c*) the absolute humidity or the partial pressure. Silica gel is more commonly used because it has a higher adsorbing capacity for most conditions of temperature and pressure.

Fig. 3 shows a graph illustrating the amount of water concentration in a silica-gel and an activated-alumina adsorbent for a specific absolute humidity range, at various isotherms (constant-temperature lines).

Bateman [4] conducted experiments on adsorption driers considering various values of the three fundamental parameters; inlet humidity, grain size, and contact time. Five conclusions were made from these tests:

1 The maximum temperature rise in the drying unit is remarkably independent of grain size, depth of adsorbent layer, and contact time. It can be expressed by

$$\Delta t = \text{const } (h_g - h_f) \tag{7}$$

where

const = 30 deg C × 10^3 per g/g for silica gel
const = 34 deg C × 10^3 per g/g for activated alumina

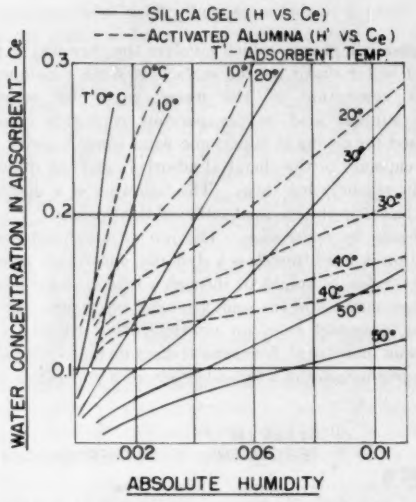

Fig. 3 Adsorption isotherms for silica gel and activated alumina, reference [1]

2 The useful concentration decreases with increasing inlet humidity, which is contrary to expectations.

3 The useful concentration is not proportional to the product of depth and constant contact time, but increases much more sharply with an increase in depth.

4 The grain size also influences dynamic adsorption efficiency.

5 There is comparatively little difference between the performance of the adsorbents tested (silica gel and activated alumina), especially if the depths are adjusted to give equal pressure losses.

A more recent study by Gruenwald [5] agrees with all except Bateman's fifth conclusion. His experiments, which were conducted for the Naval Ordnance Laboratory 40-cm by 40-cm wind tunnel, indicates that silica gel is superior to alumina and Sova bead (a product of the Socony Vacuum Oil Company of New York).

Procedure for the design of a silica-gel drying plant is outlined for practical application in literature on silica gel published by the Davidson Chemical Corporation of Baltimore, Md. A design of a full-flow drier (charging drier), expressed in terms of wind-tunnel characteristics, has been outlined by Smolderen.[2] Fig. 4 shows the results of the dynamic adsorption of water vapor from air containing 5 grains and 10 grains per cu ft (50 and 100 per cent saturation, respectively) at a rate of flow of 0.8 cfm per lb of silica gel at 77 F (25 C) under isothermal conditions.

Wind-tunnel running times or number of runs between successive reactivation periods are important factors of desiccant reactivation. By installing two or more driers, interruption of tunnel operation can be avoided. However, it may be a costly operation in terms of heating power, if the amount of time allowed for reactivating the drier(s) not being used is small.

Drying-System Selection

The designers selection of a particular system will depend principally upon the comparative evaluation of the following factors: (*a*) Desired performance; (*b*) adaptability; (*c*) reactivation required; (*d*) initial cost; (*e*) operating cost.

It is important that all of these factors be considered in a comparative sense. Therefore the following discussion is intended to serve as a guide for this purpose.

[2] Reference [1], p. 38.

(a) Desired Performance. It is, of course, necessary for the drying system to meet certain stipulated requirements. For instance, a supersonic wind tunnel requires its drying unit to perform two design functions: (i) The tunnel or upstream reservoir must be filled with sufficiently dry air. (ii) The humidity must be kept low during tunnel operation. (Intermittent wind tunnels are exceptions and only require the performance of the first function.) Therefore it should be determined if stipulated requirements are realized and which drying system performs more efficiently.

(b) Adaptability. This factor is self-explanatory and will depend upon the particular application characteristics of a drying system in relation to the wind tunnel under consideration. For example, a dusting effect (erosion of an adsorbent which results in flaking) may not be acceptable for a specific installation.

(c) Reactivation Requirements. Air-drier systems discussed herein all require reactivation of one type or another. The ease with which this is accomplished determines the criterion for comparison. For example, physical adsorbers can be regenerated simply by heating and therefore are very popular. Also, cooling and compression-type systems may be regenerated by allowing the water vapor condensed on the walls to flow out of the drier continuously.

Regeneration becomes more complicated when ice forms on coil walls. In this situation, it may be necessary to melt the ice and allow the condensate to run off, creating undesirable requirements.

(d) Initial Cost. Although, the foregoing discussion of influencing factors is important, it may be necessary at times to alter (when possible) their results in order to justify system selection from an initial-cost standpoint. Therefore it is important that the initial-cost analysis should be made with performance, adaptability, and reactivation in mind.

(e) Operating Cost. The operating cost of an air-drying system will be the cost of maintaining system operation. This, of course, will include the cost of regeneration. Again, as in the case of initial cost, it is necessary to consider all influencing factors of selection in this comparative analysis.

Summary

Design of an air-drying system for supersonic wind tunnels is an essential and critical part of the over-all tunnel design. The foregoing is a summary type discussion intended to provide criteria for air-drying-system design. The information and conclusions

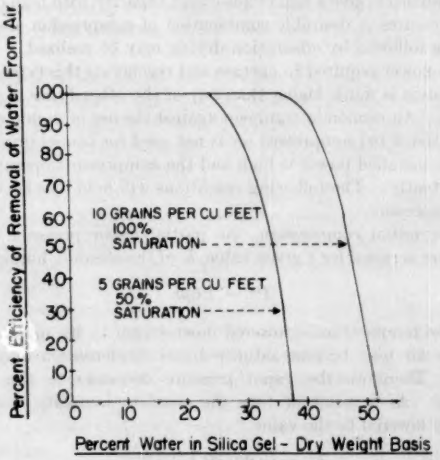

Fig. 4 Dynamic adsorption of water vapor under isothermal conditions at 25 per cent c (77 F). Air flow rate of 0.8 cfm per lb silica gel, reference [7].

are based on the research and experimentation conducted on this subject (see list of references). The various types of air-drying systems were examined in terms of their characteristics, performance, and application; and the method of selection evaluated in terms of desired performance, adaptability, required reactivation, initial and operating cost.

References

1 J. J. Smolderen, "Condensation Effects and Air Drying Systems for Supersonic Wind Tunnels," AGARDograph, No. 17, July, 1956.

2 G. L. Tuve and L. J. Seigel, "Performance of Surface-Coil Dehumidifiers," *Heating, Piping and Air Conditioning*, vol. 10, 1938, pp. 605–612.

3 "Heat Transfer Surface Coils—'ASHVE' Guide," American Society of Heating and Ventilating Engineers, 1941, pp. 473–500.

4 P. J. Bateman, "Drying Air by Solid Granular Adsorbents," Great Britain Aeronautical Research Council, Current Paper No. 79, February, 1951.

5 K. H. Gruenwald, U. S. Naval Ordnance Laboratory, Silver Spring, Md., Memorandum No. 10518.

6 A. I. Brown and S. M. Marco, "Introduction to Heat Transfer," McGraw-Hill Book Company, Inc., New York, N. Y., 1951.

7 F. C. Dehler, "Silica Gel," The Davison Chemical Corporation, Baltimore, Md.

8 R. M. Head, "Investigations of Spontaneous Condensation Phenomena," GALCIT Dissertation, California Institute of Technology, 1949.

9 W. C. Burgess, Jr., and F. L. Seashore, "Criterions for Condensation-Free Flow in Supersonic Tunnels," NACA TN 2518, December, 1951.

10 P. Wegener and R. Smelt, "Summary of Naval Ordnance Laboratory Research on Liquefaction Phenomena in Hypersonic Wind Tunnels," U. S. Naval Ordnance Laboratory Memorandum 10772, Silver Spring, Md.

11 K. L. Oswatitsch, "Kondensationserscheinungen in Überschalldüsen," *Zeitschrift für angewandte Mathematik und Mechanik*, vol. 22, 1942, pp. 1–14.

12 St. Genese Rhode.

13 Adolf Sander and Gerhard Damköhler, "Supersaturation in the Spontaneous Formation of Nuclei in Water Vapor," NACA TN 1368, November, 1953.

14 J. V. Charyk and L. Lees, "Condensation of the Components of Air in Supersonic Wind Tunnels," Princeton University Aeronautical Engineering Laboratory, Report 127, 1943.

15 O. W. Eshbach, "Handbook of Engineering Fundamentals," second edition, John Wiley & Sons, New York, N. Y., 1952.

Journal of ENGINEERING FOR INDUSTRY

Information for Authors

• Manuscripts should be submitted in final form to the Editor. Each manuscript must be accompanied by a statement that it has not been published elsewhere nor has it been submitted for publication elsewhere. A paper which would occupy more than 8 pages of the Journal may be returned to the author for abridgment.

• The author should state his business connection, the title of his position, and his mailing address. A short abstract (50 to 100 words) should be included on the first page immediately preceding the introductory paragraph of the paper.

Three copies of the manuscript are required. One of these must be a carefully prepared printer's copy, typed in double spacing, on one side of the page only, with wide margins, on $8^1/_2$ by 11-in. opaque white paper. Mimeographed manuscripts, if prepared with exceptional care, can be accepted provided they are completely edited.

• As far as possible, all mathematical expressions should be typewritten. Greek letters and other symbols not available on the typewriter should be carefully inserted in ink. Care should be taken to distinguish between capital and lowercase letter, between zero (0) and the letter (*O*), between the numeral (1) and the letter (*l*), etc. A letter representing a vector cannot be printed with an arrow above or below it. The letter should be underscored with a single wavy line, wherever it appears in the text, to designate boldface type.

• A list of symbols carefully marked for the use of the editor (thus: κ, Greek l.c. kappa), if it has not been included in the body of the paper, should accompany the manuscript on a separate page.

• Before preparing a manuscript the author should study printed articles in the Journal, with special attention to the form and style of mathematical expressions, tables, footnotes, references, and abstract. Numbers that identify mathematical expressions should be enclosed in parentheses. Numbers that identify references at the end of the paper should be enclosed in brackets. Care should be taken to arrange all tables and mathematical expressions in such a way that they will fit into a single column when set in type. Equations that might extend beyond the width of one column (fractions that should not be broken or long expressions enclosed in parentheses) should be rephrased to go on two or more lines within column width. Fractional powers are preferred to root signs and should always be used in more elaborate formulas. The solidus should be used instead of the horizontal line for fractions wherever possible.

• A normal paper should not exceed 8 pages in the Journal. It is about 8000 words or 20 double-spaced typewritten pages exclusive of drawings. A Technical Brief should not exceed 750 words or about one page in the Journal inclusive of drawings.

• Originals and two copies of figures must accompany the manuscript. Line drawings should not be larger than $8^1/_2 \times 11$ in. and should be planned for reduction to column width. Lettering should be large enough to be clearly legible when the illustration is reduced. The originals of line drawings must be in India ink on white or pale blue tracing paper or tracing cloth. Photographs of equipment or test specimens must be glossy prints and should be used sparingly. Captions for figures should be typed double-spaced and included as the last page of the manuscript. The figure number and author's name should be written in the margin or on the back of each illustration.

• Titles of papers should be brief.

• Authors can obtain copies of the ASME Manual MS-4, "An ASME Paper," from the Editor and are urged to do so before drafting their papers in final form.

• Papers published in Journals of the Transactions of the ASME must be presented at a Meeting, either in person or by title. Scheduling of papers is in the hands of the Publications Committee.

• An author is entitled to 25 preprints free of charge (in the case of two authors, 15 each; three or more authors, 10 each). Larger quantities of preprints or reprints can be ordered from Editorial Department, The American Society of Mechanical Engineers, 29 West 39th Street, New York 18, N. Y. Quotations will be sent on request.

Please address all communications to:

Editor, ASME,

29 West 39th Street,

New York 18, N. Y.

ASME Publications Committee